UNIVERSITÀ DEGLI STUDI DI PAVIA
DOTTORATO DI RICERCA IN FISICA – XXXV CICLO

Beam-test results of a capillary based dual-readout fibre-sampling calorimeter prototype

JINKY AGARWALA

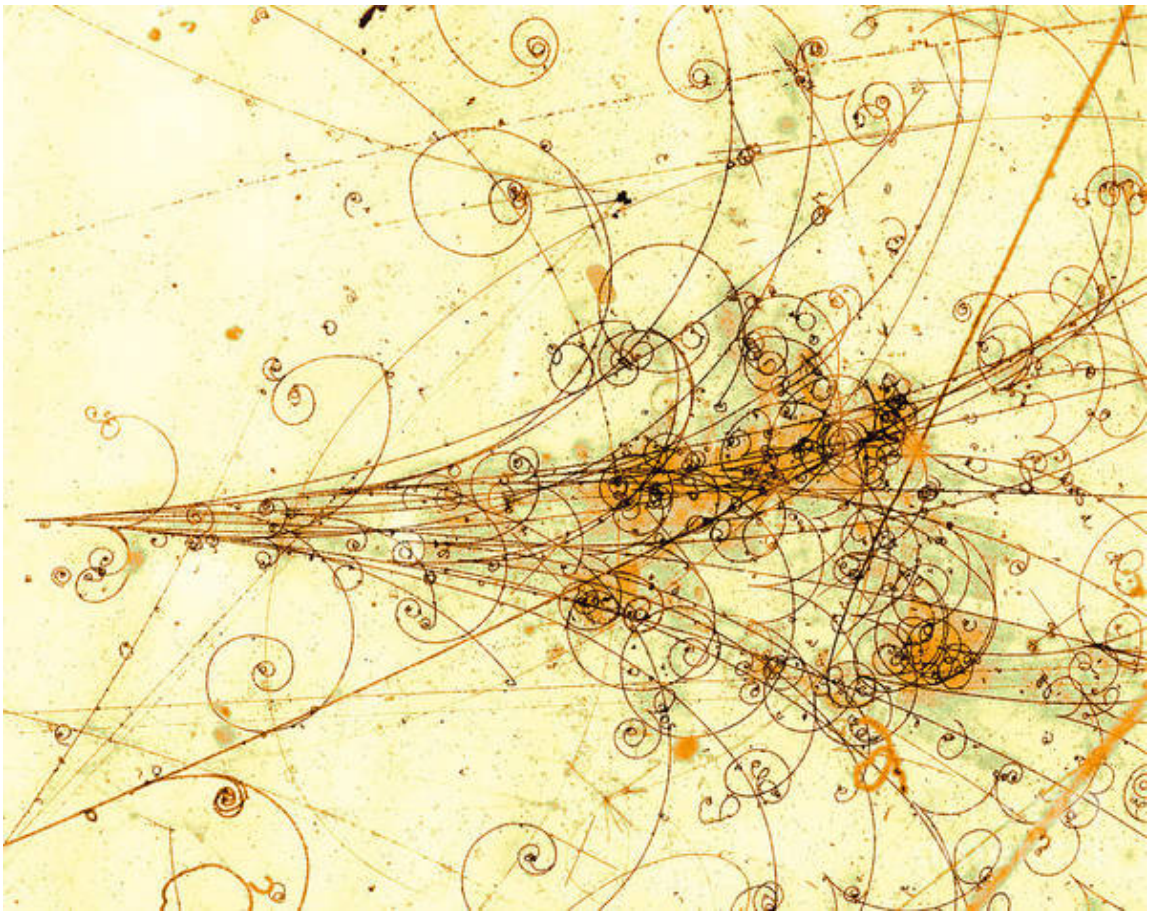

Tesi per il conseguimento del titolo

Beam-test results of a capillary based dual-readout fibre-sampling calorimeter prototype

Jinky Agarwala

2022

Università degli Studi di Pavia
Dipartimento di Fisica

DOTTORATO DI RICERCA IN FISICA – XXXV CICLO

Beam-test results of a capillary based dual-readout fibre-sampling calorimeter prototype

Jinky Agarwala

Submitted to the Graduate School of Physics in partial
fulfilment of the requirements for the degree of
DOTTORE DI RICERCA IN FISICA
DOCTOR OF PHILOSOPHY IN PHYSICS
at the
University of Pavia

Supervisor: Roberto Ferrari

Cover: **Electromagnetic shower** (fineartamerica collection)

Beam-test results of a capillary based dual-readout fibre-sampling calorimeter prototype

Jinky Agarwala

PhD thesis - University of Pavia
Pavia, Italy, December 2022

To Maharaj

Acknowledgements

Thank you Bob! I express my deepest and sincere gratitude for your guidance, invaluable feedback on my analysis and nevertheless the discussions and your patience on me. I feel that from all these I have learnt a significant amount that will stay with me. From the detailed corrections, suggestions and explanations you have provided on the thesis manuscript, I have gained further clarity on the subject. Though I could have better utilised the opportunity of having you as my supervisor by taking initiatives for arranging frequent virtual meetings during the first one and a half year of my PhD. In fact, the pandemic started before I had the third, in-person conversation with you after I arrived in Pavia.

I would like to thank a group of people for their constant help in my work for the ATLAS collaboration. I will start by thanking Athina and Gabriella for their guidance during my shifts for the quality control tests concerning the construction of Micromegas readout panels. I would like to thank Simone who had been a great assistance during the initial setting up of the partition and continued helping until I got primarily accustomed with the online Data Quality Monitoring Framework of the ATLAS experiment. Thanks to Michael Schernau for all the discussions that immensely helped me in better understanding the database of the monitoring framework, the algorithms behind the GNAM histograms for Micromegas and many technical issues. Thanks to the Micromegas experts for all the discussions on the logic of Data Quality Algorithms that I developed. My sincere gratitude goes to Serguei Kolos for providing the excellent and detailed tutorial aimed to introduce the new developers to the ATLAS online Data Quality Monitoring tools. Besides, he was always prompt in responding to my queries.

I express my gratitude to the technicians (Alessandro, Claudio, Filippo, Samuel) for their effort on building the fibre-sampling, dual-readout calorimeter prototype and to Romualdo Santoro who was the main responsible for the SiPM readouts. I convey special gratitude to Marco Prata and Massimo Rossella for providing the equipment for testing the photomultiplier tubes, their kind instructions and time. I thank everyone who participated in our CERN SPS beam test. Thanks to Lorenzo Pezzotti for providing the simulated data that I analysed to understand the detector performances. I sincerely appreciate the effort of the software group (Edoardo, Iacopo, Lorenzo) for handling the raw data taken with the test beams and providing ready-to-analyse physics data. Thanks to Giacomo for his analysis contribution from which I have profited in enhancing my knowledge on the subject. I would like to pay my special regards to Johannes Bernhard for providing information promptly to my queries regarding the SPS beams we used and the experimental setup.

I express my deepest regards to Prof. Alberto Rotondi for offering the course on Information and Data Analysis. This introduced me to statistics for HEP. Thank you Gabri for all your help and time throughout the three years! Besides, I am extremely grateful for your valuable corrections and feedback on the chapters of the thesis. Thank you Agostino! I appreciate your good will of inspiring younger members of the group towards the work. You have given me the opportunity to visit CERN many times for taking part in ATLAS activities and stimulating in-person discussions. I highly appreciate your decisive team leadership! Thank you Emanuele for being a stunning guide during my first and so far the only visit to the ATLAS cavern! It is, indeed, an unforgettable memory.

Thank you Lucio for being more than a PhD coordinator. I always felt at ease to ask for any help literally from the day one. Apart from following closely and helping in the bureaucratic matters concerning my staying in Italy, you introduced me to many good shops of local products in Pavia. I remember that wonderful morning when I had the privilege to have a glance at your personal book collection.

Finally yet most importantly, I express my hearty gratitude to my mother and my sister, Jina. Thank you for always giving me the freedom to do what I want, the priceless support, and never complaining about anything! Thank you Renato for always staying connected. The in-person time spent with you in Pavia was splendid and so was the sudden Verona trip and the opera, in the middle of the thesis writing. Thank you Christophe for always being there to care and for everything! I managed to finish writing the thesis timely because I have a wise best friend like you.

Contents

List of abbreviations

γ photon

$-\frac{dE}{dX}$ stopping power

ϵ_c critical energy

f_{samp} sampling fraction

f_{em} electromagnetic fraction

X_0 radiation length

R_M Molière radius

λ_{int} nuclear interaction length

ACR ATLAS Control Room

ADC Analogue-to-Digital Converter

BCID Bunch Crossing IDentifier

BGO Bismuth Germanate

BSM Beyond Standard Model

COG Centre Of Gravity

CDR Conceptual Design Report

CEPC Circular Electron Positron Collider

C-CCDs Contact-CCDs

CLD CLIC-Like Detector

CLIC Compact LInear Collider

C.p.e. Cherenkov photoelectrons

CR Control Room

CSCs Cathode Strip Chambers

DM Dark Matter

DREAM Dual-REAdout Module

DRO Dual-ReadOut

DNN Deep Neural Network

DQM Data Quality Monitoring

DQMD Data Quality Monitoring Display

DQMF Data Quality Monitoring Framework

DWCs Delay Wire Chambers

ECAL Electromagnetic CALorimeter

EM electromagnetic

ESPP European Strategy for Particle Physics

EW ElectroWeak

FCC Future Circular Collider

FEE Front End Electronics

GPN General Public Network

GRL Good Runs Lists

HCAL Hadron CALorimeter

HEP High Energy Physics

HiDRa High-Resolution Highly granular Dual-Readout Demonstrator

HG High Gain

HL High-Luminosity

HLT High Level Trigger

HNL Heavy Neutral Leptons

IDEA Innovative Detector for Electron-positron Accelerator

ILC International Linear Collider

IP Interaction Point

IS Information Service

L1 Level-1

LBs Luminosity Blocks

LEP Large Electron Positron collider

LEMMA Low EMittance Muon Accelerator

LINACs LINear ACcelerators

LG Low Gain

LHC Large Hadron Collider

LHS Left Hand Side

LS2 Long Shutdown 2

LY Light Yield

MAPS Monolithic Active Pixel Sensors

MC Muon Counter

MDTs Monitoring Drift Tubes

Micromegas Micro mesh gaseous structure

MIPs Minimum Ionising Particles

MM MicroMegas

MPGD Micro Pattern Gaseous Detector

MPV Most Probable Value

NA Numerical Aperture

NP New Physics

NSW New Small Wheel

OH Online Histogramming service

PCBs Printed Circuit Boards

PDE Photon Detection Efficiency

PDFs Parton Distribution Functions

PDG Particle Data Group*

PFA Particle Flow Analysis

PID Particle IDentification

PMTs PhotoMultiplier Tubes

*https://pdg.lbl.gov/2020/AtomicNuclearProperties

PS PreShower

QAQC Quality Assurance and Quality Control

QTs Qualification Tasks

RHS Right Hand Side

RBI Ruđer Bošković Institute

RF Radio Frequency

RO ReadOut

RPCs Resistive Plate Chambers

SiPMs Silicon PhotoMultipliers

SM Standard Model

SPACAL SPAghetti CALorimeters

SPPC Super Proton Proton Collider

SPS Super Proton Synchrotron

SRF Superconducting Radio Frequency

sTGC small-strip Thin Gap Chamber

SW Small Wheel

TDAQ Trigger and Data Acquisition

TDC Time-to-Digital Converter

WIMPs Weakly Interacting Massive Particles

Introduction

I joined the RD_FCC[†] group of INFN[‡]-Pavia in November 2019, to pursue studies and frontier research on the Dual-Readout calorimetry and its application in experiments proposed at future circular lepton colliders. The motivation behind was to understand how particle detectors together with modern technology are used for searching basic building blocks of the universe.

The journey of calorimetry in particle physics from a crude apparatus for stopping particles to an instrumentation for precision measurements has taken place over several decades. Understanding the physics of energy deposition of particles via interactions with matter and developing techniques for conversion of deposited energies into human readable signals have been crucial features for learning. Monte Carlo based simulations provided inputs in understanding the nature of electromagnetic showers. Hadronic showers are even more complex and are fully explored with simulation models. The non-relativistic component of the shower that is dominated by processes at the nuclear level, is still poorly described by the hadronic shower development package provided by Geant4. Therefore, the construction and characterisation of calorimeter prototypes becomes an excellent way to learn more about hadron showers.

The INFN-Pavia group has been developing prototypes of novel modular structures of Dual-Readout calorimeters in order to finalise the design and concept of calorimeters aimed to perform precision measurements in experiments proposed at future circular lepton colliders. I spent one half of the first year familiarising myself with the activities of our group and then performed simulation studies on an electromagnetic-scale Dual-Readout calorimeter. The construction of the electromagnetic-scale novel module started at the beginning of the second year of my doctoral studies. It took eight months for the detector to be ready for tests with beams at two facilities, DESY[§] and the Super Proton Synchrotron at CERN[¶]. During the final year of my PhD, I analysed data samples taken with the CERN test beams.

Chapters 1 and 2 are dedicated to describe concepts of calorimetry in particle physics and the state-of-the-art of the Dual-Readout calorimetry, respectively. Chapter 3 outlines possible scenarios of the post-LHC era, i.e., the future projects for high-energy collider physics. This chapter also elaborates on the physics potential at the FCC-ee

[†]Research & Development for Future Circular Lepton Colliders (https://web.infn.it/RD_FCC/)
[‡](Italian) National Institute of Nuclear Physics
[§]Deutsches Elektronen-SYnchrotron
[¶]European Council for Nuclear Research

collider, the IDEA detector concept that has been proposed by the researchers of various INFN groups and the role of Dual-Readout calorimetry in precision measurements. Chapter 4 provides the designs and dimensions of the two fibre-sampling calorimeter modules, an electromagnetic-scale and a hadronic-scale, with detailed description of the construction steps of the electromagnetic-scale module and some additional work required for the construction of the hadronic-scale module. On the other hand, Chapters 5 and 6 are dedicated to describe the simulation studies of the electromagnetic-scale module along with the Geant4 geometry of the hadronic-scale module and the analysis work related to the CERN beam test of the electromagnetic-scale module, respectively.

Members of the Pavia RD_FCC group are also part of the ATLAS[‖] experiment at the LHC and hence, I had the chance to join the ATLAS collaboration too during my PhD. As a result, in addition to the above mentioned work, I had the opportunity to participate in the ongoing construction activities for the Micromegas chambers for the ATLAS New Small Wheel and software tool development for the online Data Quality Monitoring for the Micromegas. When the construction activities on the Micromegas were completed, I started working on the software tool development and continued for one year. This participation allowed me to qualify as an ATLAS author in January 2021 and become a Muon Desk Shifter in the ATLAS Control Room during the test runs of 2021 and the LHC Run 3 of 2022. Appendix A begins with a short introduction of the ATLAS experiment and is dedicated to describe the mentioned ATLAS activities.

Conclusions on the lessons from the electromagnetic-scale prototype tests have been drawn in Chapter 7. Some objectives on the readout of the upcoming significant containment prototype are also shortly discussed in this chapter. The Bibliography [1] to [79] concern calorimetry and future collider projects, whereas the rest corresponds to the ATLAS experiment and aspects related to it.

[‖] A Toroidal LHC ApparatuS

Chapter 1

Calorimetry in particle physics

1.1 Basic concept

Historically, a calorimeter is a device that measures all heat* released in a reaction. In chemistry, calorimeter measures the heat exchange, typically in a volume of liquid, due to the energy released by a chemical reaction. In particle physics, calorimeters [1, 2] constitute an important class of detectors for measuring the energy of particles. The particles interact within the detector volume (a block of dense material) via electromagnetic or strong processes and transfer all or part of their energy to the material. Typically, calorimeters are designed such that particles are almost completely absorbed (exceptions: muons and neutrinos) and hence, the process is regarded as a *destructive* phenomenon. As a result of interactions, a shower of secondary particles is produced. Finally, all or part of the energy of the particle is converted into measurable detector response. Ideally, the detector dimensions are large enough to absorb most of the energy of the particle and this energy is converted into a signal directly proportional to it. In reality, this is normally the case for high-energy electron and photon (γ), but it hardly happens for single hadron and jet (discussed in Section 1.4). Calorimeters detect both charged ($e^{\pm}$s, charged hadrons, i.e., protons, pions, etc.) and most neutral particles (γ's, neutrons). A calorimeter is at the heart of a modern high-energy collider experiment. The primary roles of calorimeters are Particle IDentification (PID) (electrons, muons, γ's, single hadrons and jets), generation of trigger signals, energy measurements of particles developing electromagnetic (EM) showers i.e., electrons, γ's, π^0s, and/or energy measurements of hadrons and jets.

1.2 Classifications

Depending on detector construction strategy, there are two types of calorimeters: *homogeneous* and *sampling*. In a homogeneous calorimeter, the volume where the shower develops is itself, the body of the detector to detect the final products (γ's, e^{-}s, ions). So, the deposited energy is fully detected and as a consequence the calorimeter provides potentially the optimal energy resolution (discussed in Section 1.5). Sampling calorimeters are comprised of alternating layers of dense absorbers (such as copper, lead,

*'Calor' in Latin

uranium, etc.), called *passive* medium, where the showers develop, and light detector structures, called *active* medium, where particles are actually detected. The schematic of a sampling calorimeter is shown in Figure 1.1. The very essential parameter, the *sampling fraction (f_{samp})*, is the fraction of the total deposited energy that is released (or sampled) in the active media:

$$f_{samp} = \frac{energy\ \ deposited\ \ in\ \ the\ \ active\ \ media}{total\ \ energy\ \ deposited\ \ in\ \ the\ \ calorimeter} \tag{1.1}$$

The choice of sampling fraction is driven in opposite directions by the experimental needs. The resolution is improved by increasing the sampling fraction, in order to limit the effects due to sampling fluctuations. On the other hand, increasing the passive medium reduces the detector dimensions and costs as well as the shower dimensions, i.e., it improves the capability to resolve nearby showers. Hence any actual choice is a compromise between different requirements. In practice, the sampling fraction is usually small with the consequence that the resolution of sampling calorimeters is much worse than the resolution of homogeneous calorimeters. Usually, the sampling fraction is calculated for Minimum Ionising Particles (MIPs) that are ideal particles interacting with matter only through ionisation with a constant energy loss rate or stopping power ($-\frac{dE}{dX}$) equal to the minimum possible value. In many practical cases, relativistic heavy particles (e.g., cosmic-ray muons) can be considered as MIPs. Another important parameter is the *sampling frequency* that is defined by the thickness of the layers. Increasing the sampling frequency improves the resolution at the cost of a more complex mechanics and/or electronics. Almost all calorimeters operating in collider experiments are sampling calorimeters, with the $PbWO_4$ crystal calorimeter of the CMS[†] experiment [3] as a notable exception.

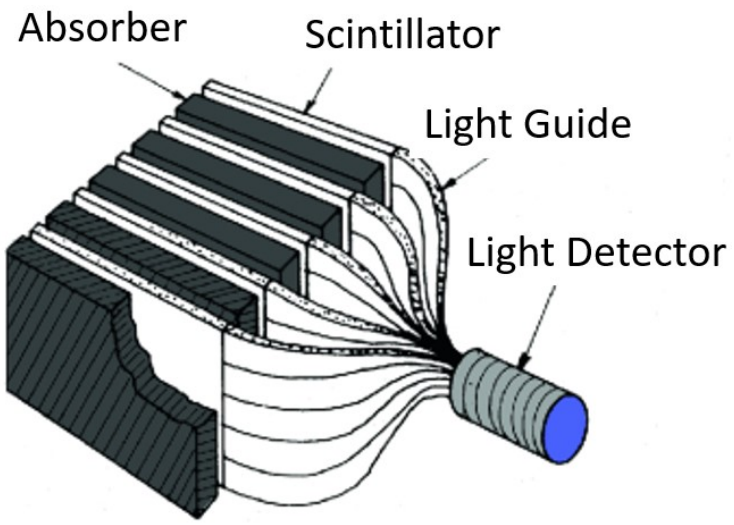

Figure 1.1: Schematic of a sampling calorimeter which has alternating layers of scintillators as active media in between passive absorber plates. Ref. [1]

Depending on the incoming particle type, there are two types of calorimeters: electromagnetic and hadronic. In next Sections, 1.3 and 1.4, physics behind the EM and hadronic cascades are described, respectively.

[†]Compact Muon Solenoid

1.3 Physics of electromagnetic showers

An EM cascade [1, 2] is developed by the interaction of electrons, positrons and γ's with the detector material. e^- and e^+ lose their energies by ionisation and bremsstrahlung radiation. Bremsstrahlung arises when e^- and e^+ are decelerated in the Coulomb fields of nuclei with subsequent emission of photons. The process is governed by the following expression:

$$-\frac{dE}{dx} = 4\alpha N_A \frac{Z^2}{A} \cdot \left(\frac{1}{4\pi\epsilon}\frac{e^2}{mc^2}\right)^2 \cdot E \cdot ln\frac{183}{Z^{\frac{1}{3}}} \tag{1.2}$$

where the left hand side of Equation 1.2 represents, as mentioned before, the stopping power of the material and in the right hand side, α is the fine structure constant, Z and A are the atomic number and the relative atomic mass of the material, respectively, N_A is the Avogadro number, c and ϵ are the velocity of light and the vacuum permittivity, e, m and E are the charge, rest mass and energy of the electron, respectively.

On the other hand, photons have to create charged particles or transfer energies to charged particles in order to be detected. Photons interact with matter through the photoelectric effect, Compton scattering and pair production. The cross sections for these processes vary with Z^5, Z^2 and Z, respectively.

At high energies, the EM showers are dominated by bremsstrahlung radiation and pair production, whose diagrams are shown in Figure 1.2. On the other hand, ionisation, the photoelectric effect and Compton scattering are dominant at low energies. The *critical energy* (ϵ_c) can be defined as the energy at which the loss due to ionisation and the loss due to radiation have the same intensity, see Equation 1.3 and Figure 1.3.

$$\left(\frac{dE_{ion}}{dx}\right)_{\epsilon_c} = \left(\frac{dE_{rad}}{dx}\right)_{\epsilon_c} \tag{1.3}$$

ϵ_c is roughly inversely proportional to the atomic number of the absorber and for solids

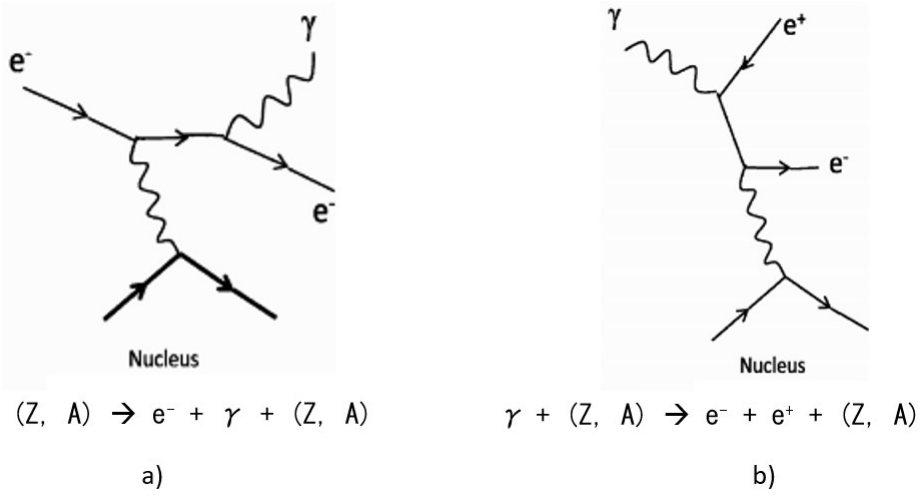

Figure 1.2: Feynman diagrams for the bremsstrahlung radiation (a) and pair production (b).

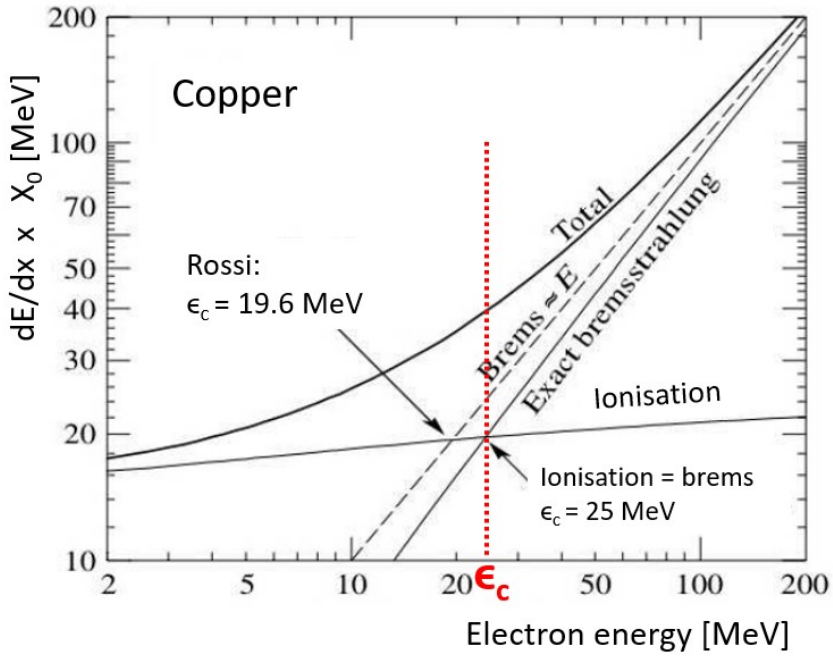

Figure 1.3: Energy losses through ionisation and bremsstrahlung by electrons in copper. The value of the critical energy is indicated by the vertical red line. Ref. [1]

and liquids can be parameterised as [1]:

$$\epsilon_c = \frac{610\ MeV}{Z + 1.24} \tag{1.4}$$

Depending on materials, at energies above $\mathcal{O}(10MeV)$, electrons start producing energetic bremsstrahlung photons that in turn are converted into $e^+ - e^-$ pairs. These $e^+ - e^-$ pairs release energies through radiation of further photons and this way particle multiplication happens. Maximum number of particles is produced at a certain shower depth called as the *shower maximum*. Its depth becomes higher with an increase in energy of the incoming particle. The shower maximum is reached when the average energy of the shower particles equals ϵ_c. Beyond this depth the number of particles in the multiplication process decreases gradually and a longitudinal shower tail is produced. The lateral profile of an EM shower is caused by two phenomena: a) e^-s and e^+s move away from the shower axis because of multiple scattering and b) γ's and e^-s produced in the Compton scattering and photoelectric effect move away from the shower axis. Two parameters, driving the EM shower development, need to be introduced. One, the *radiation length* (X_0), defines the longitudinal shower dimension, while the lateral dimension is defined by the *Molière radius* (R_M). The first is defined through Equation 1.2 that can be rewritten as:

$$\begin{aligned} -\frac{dE}{dx} &= \frac{E}{X_0}, \\ E &= E_0\, e^{-x/X_0} \\ E &\approx 37\% \cdot E_0 \ \ at \ \ x = X_0 \end{aligned} \tag{1.5}$$

So, a high-energy electron loses $\sim 63\%$ of its energy when it traverses one radiation length of material. X_0 is a characteristic of a material. It is slightly less ($\frac{7}{9}$) than the mean free path for pair production of high-energy photons. On the other hand, R_M can be expressed in terms of X_0 and ϵ_c [4]:

$$R_M = \frac{21\ MeV}{\epsilon_c} \cdot X_0 \quad [g/cm^2] \tag{1.6}$$

On average, 90% of an EM shower energy is contained within a cylinder of radius R_M around the shower axis. The longitudinal and lateral EM shower profiles, as a function of X_0 and R_M from EGS4 simulation [5, 6] calculation, are shown in Figures 1.4a and 1.4b, respectively. In Figure 1.4b, the lateral shower profiles indicated by the three legends are at different longitudinal depths. An EM calorimeter is intrinsically linear, i.e., the detector response is directly proportional to the deposited particle energy.

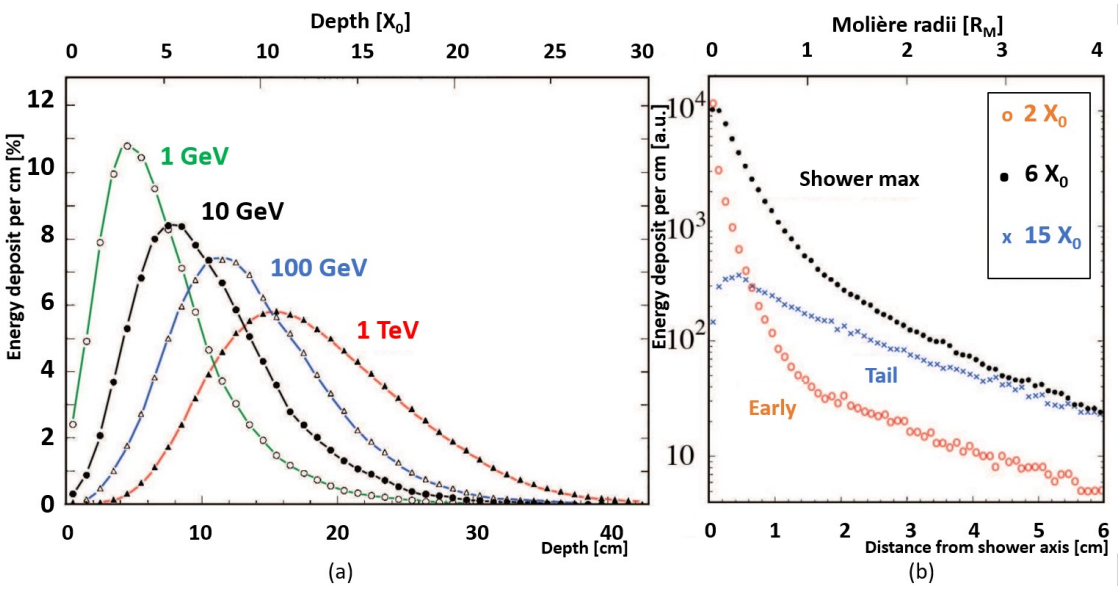

Figure 1.4: Percentage of energy deposited per unit length in a copper block as a function of the longitudinal depth (bottom X axis) and X_0 (top X axis) for 1, 10, 100 and 1000 GeV electrons (a). Energy deposited per unit length by 10 GeV electrons as a function of the radial distance from the shower axis and Molière radius (R_M) (b). Ref. [1]

Some important features that make EM shower profiles complicated are the followings:

- The behaviour of high-energy electrons and photons is not the same. A high-energy electron interacts with the detector material immediately after entering and may radiate thousands of bremsstrahlung photons in few mm lengths. But a high-energy photon may or may not interact immediately after entering the material due to lower probability of interaction compared to that of a high-energy electron [1].

- The scaling of EM showers with X_0 and R_M is not perfect [4]. The amount of particle multiplication through different processes with Z-dependent cross sections

are not same in high-Z and low-Z materials. As a result more X_0 are needed to contain EM showers in high-Z than in low-Z materials.

- The photoelectric effect and Compton scattering that produce soft particles of energy $\mathcal{O}(\sim\ MeV)$ or less, deposit shower energy far below ϵ_c and the effects are not well described by the X_0 and R_M scaling.

- A significant fraction of the shower energy is deposited by soft photoelectrons and Compton electrons [1]. For instance, these soft particles account for $\sim 40\%$ of the energy deposit in high-Z materials (Pb, U, etc.). As these particles have broad angular distributions, the correlation with the incoming particle direction is lost or very weak. So, it is not necessary that the sampling detector geometry has a segmentation orthogonal to the shower axis. The active medium can run parallel to the direction of the incoming particle. This approach, referred to as *longitudinal unsegmentation*, has opened the way for energy measurements with *SPAghetti CALorimeters (SPACAL)* [7, 8] i.e., the usage of long fibres as active detector elements, running parallel to the shower axis, immersed in a much denser passive medium. Electrons with energy of around 1 MeV are the most typical components of an EM shower and their *range*, i.e., the distance they travel from the source through matter before releasing all the energy, is typically $\sim$1 mm.

1.4 Dual nature of hadronic showers

Spallation plays an important role in hadronic cascades [1, 2, 9, 10]. Spallation occurs when an energetic hadron undergoes strong nuclear interaction with an atomic nucleus of the absorber. It is a two-stage process. The primary hadron interacts with nucleons inside the nucleus. The reactions that follow creates a fast intranuclear cascade of high-energy protons, neutrons and pions within the nucleus. During this, some of the energetic hadrons may escape the nucleus as secondary particles. Others deposit their kinetic energy in the nucleus leaving it in an excited state. In the second stage, a slower evaporation takes place when the excited nucleus relaxes by emitting low-energy neutrons, protons, alpha particle, etc., with the majority of the particles being neutrons. The secondary high-energy particles, produced during the intranuclear cascade and escaped, collide with other nuclei in the absorber. A series of secondary spallation reactions follow that generate more secondary particles and low-energy neutrons. The hadronic cascade is an accumulation of all the interactions caused by the primary and secondary particles in the absorber. Break up of nuclei also produces nucleon fragments (quarks and gluons)[‡].

Nucleons (neutrons (n) and protons (p)) are released from the nuclei and the nuclear binding energy of these nucleons is compensated at the expense of a fraction of the shower energy. This fraction of the shower energy can not contribute to any calorimeter signals. This, referred to as the *invisible energy* component of hadronic showers, varies widely from one event to the next. As a consequence, the calorimeter signal is typically

[‡]In high-energy proton-proton collision experiments, these quarks and gluons take part in *hadronisation* and produce *jets*, which are narrow cones of hadrons and other particles. Jets are produced also in high-energy e^+-e^- collisions. An e^+- e^- pair annihilates into a quark-antiquark pair that further produces hadrons and jets as a result of *colour confinement*.

substantially smaller compared to that from an EM shower of same energy and the event-to-event variation in the calorimeter signal is much larger than that for an EM shower of comparable energy.

In the absorption of high-energy hadrons typically some fraction of the energy is used for the production of neutral pions (π^0). These decay almost instantaneously into two high-energy γs that initiate EM showers. So, a hadron shower possesses both an EM component and a non-EM component.

The fraction of the shower energy carried by the EM component in a hadronic shower, generally referred to as the *electromagnetic fraction (f_{em})*, fluctuates strongly event by event (Figure 1.5a). Due to the suppression of the production of a leading π^0 (due to the baryon number conservation), the average of f_{em} is smaller in proton induced showers than in pion induced ones. $< f_{em} >$ is a function of the incoming particle's energy and can be parameterised as:

$$< f_{em} >= 1 - \left[\frac{E}{E_0}\right]^{(k-1)} \tag{1.7}$$

where k (~ 0.82) is a material dependent constant related to the average particle multiplicity in the nuclear interactions and E_0 represents the average energy meeded for the production of one pion (varying from 0.7 GeV to 1.3 GeV for $\pi-$induced reactions on Cu and Pb, respectively) [11]. According to Equation 1.7, the higher the particle energy (E) is, the more π^0 production happens, the larger $< f_{em} >$ becomes. The energy dependency of f_{em} makes (traditional) calorimeters non-linear for hadron detection.

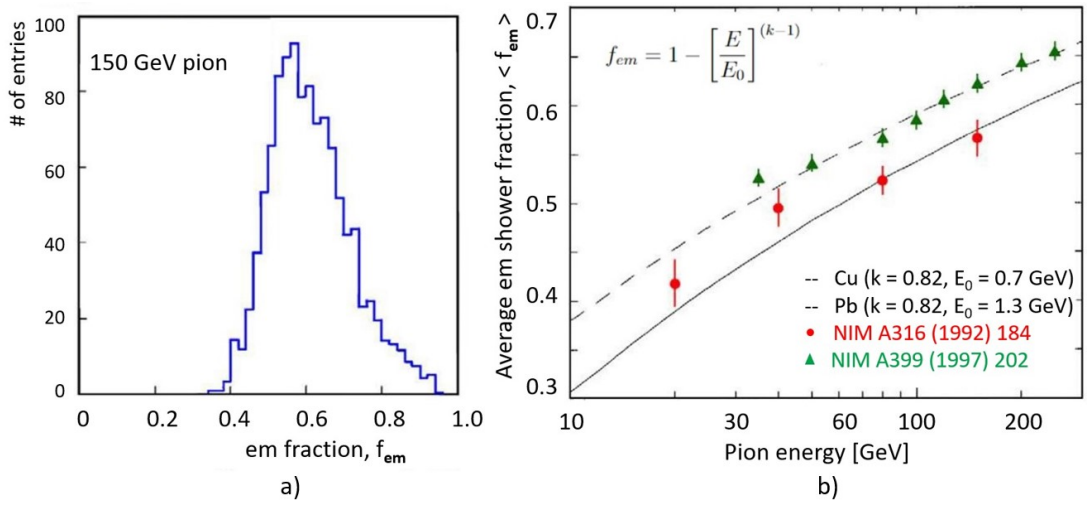

Figure 1.5: Event-to-event asymmetric fluctuation of f_{em} for a hadronic shower produced by 150 GeV pions (a). The average electromagnetic fraction, $< f_{em} >$, increases with the pion energy for hadronic showers developed in copper and lead (b). Ref. [12]

Almost 19% and 37% (total 56%) of the energy carried by the non-EM shower component is deposited in the form of ionisation by pions and protons, respectively. The invisible energy component represents $\sim$34% of the energy and the neutrons carry the remaining $\sim$10%. The percentages reported [1] are the energy containment in a lead absorber for 1.3 GeV pions. Protons, produced by nuclear spallation, are the most dominant signatures of the non-EM shower component.

Hadronic shower shapes scale longitudinally with the *nuclear interaction length (λ_{int})*, i.e., the average distance traversed by a hadron before undergoing a nuclear interaction:

$$\lambda_{int}\ [g/cm^2]\ \simeq\ 35 \cdot A^{1/3} \tag{1.8}$$

λ_{int}, depending on the material (A) and hence, on the number of neutrons, can be a factor $10-30$ larger than X_0. Thus, hadronic showers are larger and more diffuse than EM showers.

Some important features of hadronic shower profiles are the following:

- Hadron calorimeters need more material laterally to contain low-energy hadron showers than high-energy ones. This is because the EM components tend to develop close to the shower axis and, as mentioned earlier, f_{em} is larger for high-energies.
- The longitudinal leakage may play an important role for hadronic showers as the longitudinal fluctuations in the shower development are quite large.
- 50-100 MeV spallation protons are the main component of hadronic showers and their range is typically $\sim$ 1 cm.

1.5 Energy Resolution

The energy resolution is defined as the precision with which the energy of an unknown particle can be determined from the signals it produces in the calorimeter. It is one of the most important criteria for selecting a given type of calorimeter for a particular application. The calorimenter performance is controlled by the statistical fluctuations due to the underlying physical processes. In EM and hadronic calorimeters fluctuations may come from:

- signal quantum statistics (governed by Poisson statistics);
- sampling (governed by Poisson statistics);
- shower leakage;
- instrumental effects e.g., electronic noise, etc.

In an EM calorimeter, one of the above four contributions usually dominates. Event-to-event fluctuations in the signal (S) correspond to Poissonian fluctuations in the number of signal quantum (n). The relatve width of the signal distribution, i.e., the relative precision of the energy measurement can be expressed as:

$$\frac{\sigma_E}{E} \sim \frac{\sqrt{n}}{n} = \frac{1}{\sqrt{n}} \sim \frac{1}{\sqrt{E}} \tag{1.9}$$

Production of more signal quanta (photoelectrons, e^- - hole/ion pairs) leads to better energy resolution for higher energy particles. Both sampling fraction and sampling frequency define the level of sampling fluctuations. Fluctuations in the number of shower particles contributing to the calorimeter signals give rise to this component

that also scales with $1/\sqrt{E}$. For EM sampling calorimeters, in most cases, the energy resolution is dominated by the sampling fluctuation term. For active media made of solid or liquid material, the contribution to the energy resolution due to the sampling fluctuations is estimated to be:

$$\frac{\sigma}{E} = 2.7\% \sqrt{\left(\frac{d}{f_{samp}}\right)} \cdot \frac{1}{\sqrt{E}} \tag{1.10}$$

where d is the dimension of the active medium and f_{samp} is the sampling fraction for MIPs. Fluctuations in longitudinal leakage, lateral leakage and backward leakage (*albedo*) are non-Poissonian in nature and these leakage contribution to the energy resolution roughly scales with $E^{-1/4}$. The noise term scales with E^{-1}. This term dominates at very low energies, where E^{-1} dependence overtakes $E^{-1/2}$. On the other hand, the shower containment dominates at very high energies. At intermediate energies, usually, it is a combimation of the first two terms, in the mentioned list, that determine the energy resolution. There may be some effects that contribute to the energy resolution in an energy-independent way. Usually, all these contributions are uncorrelated and hence, the EM energy resolution is expressed as a quadratic sum[§] of all these terms:

$$\frac{\sigma}{E} = a \cdot \frac{1}{\sqrt{E}} \oplus b \cdot \frac{1}{\sqrt[4]{E}} \oplus c \cdot \frac{1}{E} \oplus d \tag{1.11}$$

As an example, the total EM energy resolution and the contributions from the different terms to the total resolution for the ATLAS EM calorimeter [4] is illustrated in Figure 1.6. The red line shows the contribution to the EM energy resolution due to a stochastic term with $\sigma/\mathrm{E} = 10\%/\sqrt{E}$. The data (black points) show that, between 10 and 100 GeV, the dominating factor is the stochastic term i.e., the contribution of sampling fluctuations. On the other hand, above 100 GeV, an energy-independent constant term, measured to be 0.35%, saturates the energy resolution. This arises due to the impact point dependency of the signal. Below 10 GeV, the electronic noise term is dominating.

On top of the mentioned sources of measurement uncertainties, two additional (mostly non-Poissonian) contributions play an important role in limiting the energy resolution of hadronic calorimeters. These are the fluctuations in:

- the visible energy;
- f_{em}.

The signal produced by the visible non-EM shower component, fluctuates event-to-event. For a non-compensating calorimeter (Section 1.7), the large non-Poissonian fluctuations in the EM shower component (Figure 1.5a) may be the single most important dominating factor that limits the hadronic performance. This is true, in particular, at high energies, where the contributions of stochastic fluctuations, i.e., the $E^{-1/2}$ term, vanish. For non-compensating calorimeters, the hadronic energy resolution can be expressed as:

$$\frac{\sigma}{E} = a \cdot \frac{1}{\sqrt{E}} \oplus b \cdot \left(\frac{E}{E^0}\right)^{\ell-1} \tag{1.12}$$

[§] $\sigma_1 \oplus \sigma_1 = \sqrt{(\sigma_1)^2 + (\sigma_2)^2}$

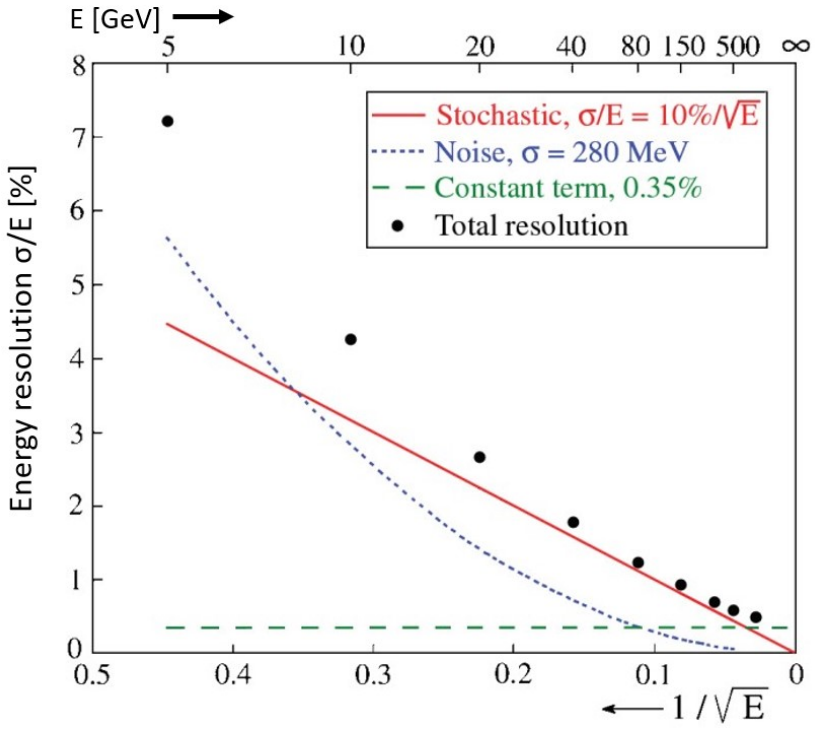

Figure 1.6: The EM energy resolution of the ATLAS EM calorimeter. Different contributions to the total EM resolution are shown separately. Ref. [4]

So, the contribution of fluctuations in f_{em} to the hadronic energy resolution of non-compensating calorimeters is more accurately determined by adding an energy dependent term to the stochastic term which includes the contributions by the sampling fluctuations, signal quantum statistics, etc. that affect the resolution at low energy. The expression is written in Equation 1.12[¶]. The value of b depends on e/h (Section 1.7). However, these intrinsic fluctuations can be eliminated by a clever design of readout and eventually, better hadronic energy resolution can be achieved. This aspect has been discussed in Section 1.8 and Chapter 2.

1.6 PID and position resolution

Not only good energy resolution, but also good position resolution and efficient PID capabilities [2, 13] make calorimeters one of the most important instruments in High Energy Physics (HEP) experiments. An example of γ/jet or γ/π^0 separation is described here. A high rejection factor for jets is required for selecting photons for physics studies at HEP experiments. If the constituents of a jet are a hard π^0 and other soft particles, the two γ's from the π^0 are very close to each other. Hence, these γ's can be misinterpreted as a single γ. A *highly granular* calorimeter, with excellent position resolution, can easily resolve the two closely spaced showers and enable γ/π^0 discrimination.

There are many features of showers and the corresponding signals that are exploited for performing PID. For instance, the shower dimensions, the contribution of shower particles to Cherenkov light production (i.e., the EM shower component), the time

[¶]Experimental estimation: $E_0 = 0.7$ GeV; $\ell = 0.72$ [1]

structure of signals, signal-generation timing, etc., can discriminate between showers produced by an e^- or a hadron. Sampling calorimeters offer better position resolution and PID capabilities than homogeneous ones. The reason is the longitudinal and lateral segmentation of the former. An extensive discussion on the spatial resolution and the powerful PID performance achieved with the ATLAS EM calorimeter can be found in Ref. [14].

1.7 Limitations of traditional hadronic calorimeters

Many factors, originated from the dual nature of hadron showers, limit the performance of hadronic calorimeters in terms of response linearity, energy resolution and detector calibration [1, 2]. The main ones along with the possible solutions, are discussed here.

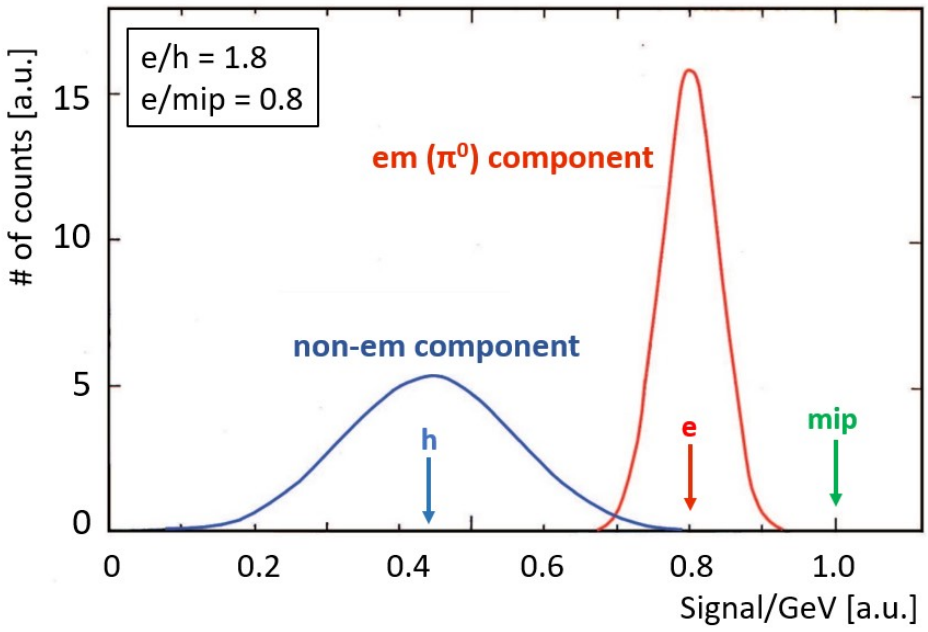

Figure 1.7: Illustration of the e/h and e/mip values of a non-compensating (undercompensating) calorimeter. The distributions show the signal per unit of deposited energy for the EM and non-EM components of a hadron shower. The average values of the EM and non-EM distributions are referred to as the EM response (e) and non-EM response (h), respectively. These distributions are normalised to the response for MIPs. Ref. [1].

The calorimeter *response* is defined as the signal per unit of deposited energy. For a hadronic shower, the average response to the EM component (e) is usually larger than that for the non-EM component (h). This is mainly due to the presence of the invisible energy, as discussed in Section 1.4, but also because of the differences in interactions of electrons and hadrons with matter. This is the *non-compensation* ($h \neq e$) problem of traditional hadronic calorimeters. The distribution of the signal per unit of deposited energy around the mean value is referred to as a *response function*. In Figure 1.7, the response functions for the EM and non-EM components of a hadron shower are illustrated, where e is larger than h. This is true for most (but not all) cases. Moreover, both e and h are usually smaller than the calorimeter response for MIPs because of

inefficiencies in the shower sampling process [15]. A calorimeter can be characterised in terms of both the e/h and e/mip ratios. In Figure 1.7, these numbers are 1.8 and 0.8, respectively. The broader non-EM response function, compared to the EM one, is related with the event-to-event fluctuations in the invisible energy fraction. In other words, as already mentioned, the calorimeter signals for hadrons are smaller than those for electrons of the same energy. Also, we have seen that $< f_{em} >$ increases with the energy of the incoming particle (Equation 1.7). The two features, $\frac{e}{h} \neq 1$ and the energy dependence of $< f_{em} >$ for hadronic showers, make the (non-compensating) calorimeters non-linear.

Let us write the calorimeter response to a charged pion as π:

$$\begin{aligned} \pi &= e < f_{em} > + h\ (1 - < f_{em} >) \\ \frac{\pi}{e} &= \frac{h}{e} + < f_{em} > (1 - \frac{h}{e}) \end{aligned} \tag{1.13}$$

i.e., it changes with the pion energy following the changes of $< f_{em} >$. In non-compensating calorimeters, as already mentioned in Section 1.5, the contribution of fluctuations in the energy-dependent $< f_{em} >$ is the dominating factor that limits the hadronic energy resolution.

The calibration of a calorimeter system [15, 16, 17] is a crucial ingredient for correctly determining the energy of the absorbed particle. The calibration constants establish the correlation between the measured signal and the deposited energy that has generated the signal. The computation of these calibration constants is of great importance and can be critical for calorimeter systems longitudinally segmented in two or more compartments. Other difficulties arise from the need to keep under control the calorimeter system for verifying that the calibration (i.e., the response) is correct and stable (or not).

The complications for calibrating a longitudinally segmented calorimeter arise from:

- non-compensation ($h \neq e$).

- the fact that the response varies with the shower depth. For example, in lead/LAr calorimeters, the response (i.e., the sampling fraction for EM showers) decreases by about 30% from the first few radiation lengths to the shower tail region (> 20 X_0).

The best procedure is to calibrate the individual sections of a longitudinally segmented calorimeter system in exactly the same way. Electrons can be used if the sections can be separated and are deep enough to contain the showers. This may be non-trivial. An alternative way is to intercalibrate the sections with muons traversing the entire depth of the calorimeter. However, if the calorimeter is not compensating, an overall correction factor will have to be applied for hadronic showers. A variety of calibration methods that are used in practice to deal with the mentioned problems are reviewed in Ref. [16].

1.8 Candidates as solutions

Extensive R&D are being carried out in three directions in order to improve the performance of hadronic calorimeters:

- Compensation.
- Particle Flow Analysis.
- Dual-Readout method.

In this chapter, we will discuss the first two approaches. Chapter 2 is dedicated to describe the Dual-Readout method and its state-of-the-art.

1.8.1 Compensation

In compensating calorimeters, the invisible energy component is compensated by amplifying neutron signals, because there is a strong correlation between the nuclear binding energy in spallation reactions and the number of neutrons produced in these reactions as depicted in the two plots of Figures 1.8a and 1.8b. Another strong correlation, therefore, exists between the nuclear binding energy and the kinetic energy transferred by neutrons [10]. The response to the non-EM shower component is boosted by neutron

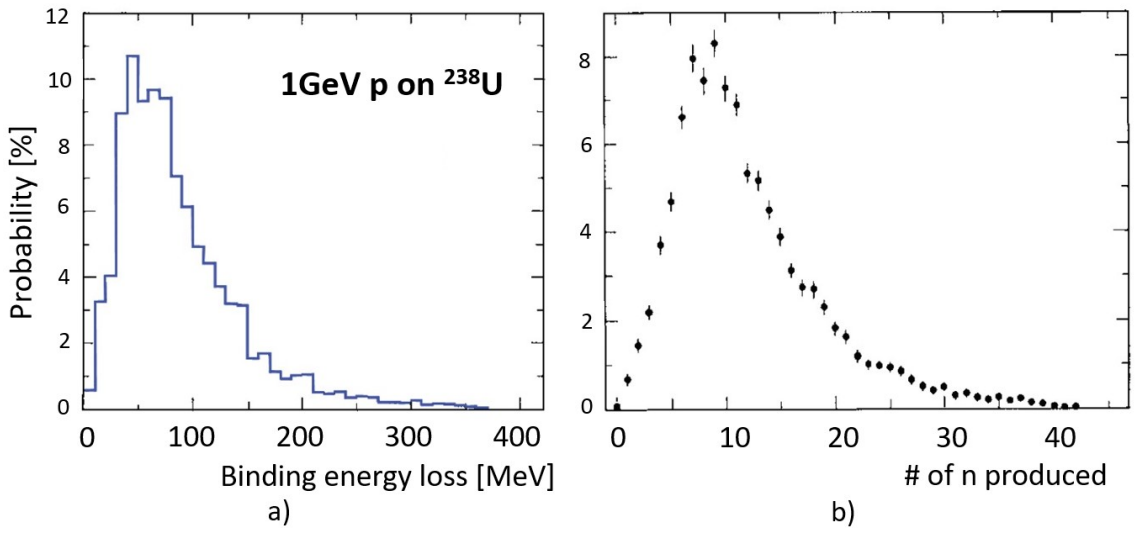

Figure 1.8: Strong correlation is observed between the nuclear binding energy lost in spallation reactions induced by 1 GeV protons on ^{238}U nuclei (a) and the number of neutrons produced in such reactions (b). Ref. [1]

detection in order to make e/h = 1. As mentioned in Section 1.4, 10% of the non-EM shower energy is deposited by neutrons, whereas more than 10% of non-EM signal comes from neutrons in compensating calorimeters. The low-energy eveporation neutrons, which are the most abundantly produced nucleons in hadron showers, transfer their kinetic energy either by elastic or inelastic scattering off nuclei in the absorber medium. The transferred energy fraction in elastic scattering is given by:

$$E_f = \frac{2A}{(A+1)^2} \tag{1.14}$$

This fraction, for hydrogen, is 50%, whereas in any denser material this fraction is very small. That is why hydrogenous active materials are used and neutrons transfer most of their kinetic energy to hydrogen nuclei and the protons recoil. These protons directly contribute to calorimeter signals by ionising the medium.

In order to achieve e/h = 1, precise tuning of the sampling fraction is needed too. In Equation 1.13, e/π, at the left hand side, becomes 1, when h/e, at the right hand side, is equal to 1. So, the hadron response equals to the electron response for the same energy. Figure 1.9 depicts the pion response as a function of the incoming pion energy for three conditioning of e/h. It is clearly visible that response linearity is achieved in compensating calorimeters. Compensation also facilitates simplicity in calibration. Calibration with electrons can be used for hadron energy reconstruction also.

On the other hand, there are some disadvantages and challenges in compensating calorimeters:

- Compensation is achieved with low f_{samp} by paying a price for the EM energy resolution. Low f_{samp} increases fluctuations in f_{em}.
- Neutron detection needs long integration time ($>$ 50 ns) and large integration volume. These are not feasible always.
- Jet energy resolution is not as good as that for a single hadron in lead, uranium calorimeters.

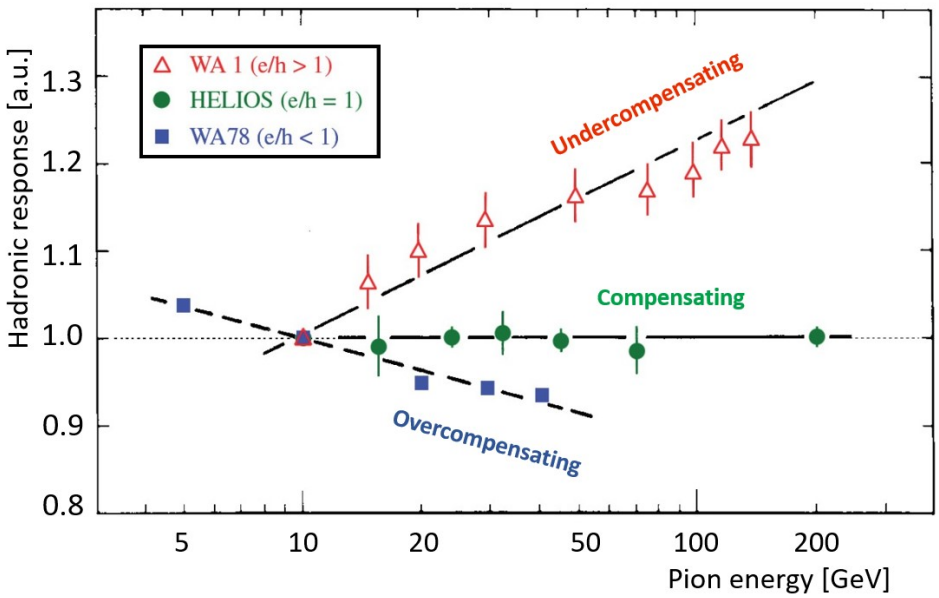

Figure 1.9: Pion response as a function of energy for three different calorimeters with e/h less than, equals and greater than 1. The values are normalised to 10 GeV π^- response. Response linearity is achieved with compensation. Ref. [1]

To overcome such limitations there are some other methods. One of these methods is discussed here.

1.8.2 Particle Flow Analysis

The Particle Flow Analysis (PFA) [13] approach was designed in order to significantly improve the performance for jet detection in HEP experiments. The method is based on the combination of the information from a precision tracker and a highly granular calorimeter. The motivation lies in the fact that the charged jet particles are more precisely measured by the tracking system, whereas the neutral particles can only be measured in the calorimeters. Ideally, the showers originated by charged particles (measured by the tracker) are removed from the calorimeter measurement matrix, and what remains is associated to neutral particles (photons or neutral hadrons). The lack of information from the calorimeter about the nature (charged or neutral) of the particle that it absorbs and the ambiguities in assigning an energy deposit to a well identified impinging particle, limit the success of this method. As the key to the solution of the problem of the correct track-cluster association, the use of calorimeters with a very high granularity has been proposed by the developers of this method. This will improve the identification of the showering fragments. Though the argument against is that, in a compact 4π experiment, high granularity may be largely irrelevant because of the large overlap between showers from different jet components. Moreover, reading millions of electronic channels as a consequence of the high granularity and then discarding the information about the charged-particle shower components are challenging.

The detector systems, based on the PFA algorithm, rely on exploiting strong solenoidal magnetic fields of strength 4-5 T in order to increase the spatial separation between showers introduced by the various jet particles. Such fields may open up the collimated beam of particles, especially at large distances from the vertex. It is important to be quantitative in this matter, because the trajectories of charged particles may bend causing a relatively large transverse momentum with respect to the jet axis.

In this context, the quality of the calorimeter is relevant. About 2/3 of the final-state particles constituting a jet are electrically charged and their momenta can be extremely precisely measured by the trackers. For just 1/3 of the jet energy, it is necessary to rely on the calorimeter measurement only. But in the absence of calorimeter information, the jet energy resolution would be dominated by the fluctuation in the fraction of total energy carried by the charged jet fragments. So, for the PFA algorithm to work, a good precision of the calorimeter measurements is important. Apart from that, the contributions of charged shower particles in calorimeter signals have to be identified and discarded for which a high granularity is the recipe. An energy resolution of 4-5% in resolving hadronically decaying W and Z bosons is the present benchmark requirement. This is a major design goal of experiments envisaged at future e^+e^- collider facilities.

ALEPH, one of the Large Electron Positron collider (LEP) experiments, was the first to apply the PFA algorithm. ALEPH had excellent tracking systems but the hadron calorimeter was not designed for high performance. Using a specific subsample of hadronically decaying Z^0s, an energy resolution of 6.2 GeV was achieved by exploiting the tracking information. It was an improvement of about 25% with respect to the hadronic energy resolution of the stand-alone calorimeter system [18]. Also the CMS experiment [19] took advantage of the silicon tracking system to the fullest and the fine-granular Electromagnetic CALorimeter (ECAL) to improve the jet energy resolution.

Chapter 2

Dual-readout calorimetry

The drawbacks of compensating calorimeters led to searches for further approaches to achieve compensation. The Dual-ReadOut (DRO) method [11, 20] exploits the fact that only the charged particles from the EM component, i.e., e^- and e^+, of a hadronic shower produce Cherenkov light. These particles are, in fact, relativistic in the medium down to kinetic energies of only 200 keV. On the other hand, the dominating spallation protons of the non-EM shower component are typically non-relativistic. While the Cherenkov light is solely related to the EM component of hadronic showers, the scintillation light is sensing the shower visible energy. Hence, the two types of lights provide complementary information about the particles that generate them. The use of both the Cherenkov and scintillation light as signal sources allows to compare the strengths of these two signals and estimate the EM fraction of the hadronic shower, event by event. The total shower energy is then reconstructed correctly for the actual value of f_{em}. Thus the EM and non-EM responses are equalised (condition of compensation) offline and the effect of fluctuations in f_{em} is eliminated. A step-by-step way to reconstruct the hadronic shower energy using this method is described in the following section.

2.1 Analysis method

The two independent signals from a DRO calorimeter can be expressed in terms of the total shower energy (E), the EM shower fraction (f_{em}) and the non-EM shower fraction (1 - f_{em}):

$$S = E \cdot \left[f_{em} + \left(\frac{h}{e}\right)_S (1 - f_{em}) \right] \tag{2.1}$$

$$C = E \cdot \left[f_{em} + \left(\frac{h}{e}\right)_C (1 - f_{em}) \right] \tag{2.2}$$

where S and C are the energies reconstructed by the scintillation and Cherenkov channels, respectively, $\left(\frac{h}{e}\right)_S$ is the ratio between the non-EM response and EM response for the scintillation channels and so is $\left(\frac{h}{e}\right)_C$ for the Cherenkov channels. Both S and C are measured at the EM scale (i.e., the calorimeter response is calibrated with electrons). For EM showers, S = C = E, while for hadronic showers, usually $E > S > C$, since (usually) $1 > (h/e)_S > (h/e)_C$. By solving the two Equations 2.1 and 2.2, f_{em} can

be written independent of shower energy and in terms of the ratio of the two signals:

$$f_{em} = \frac{\left(\frac{h}{e}\right)_C - \frac{C}{S} \cdot \left(\frac{h}{e}\right)_S}{\frac{C}{S}\left[1 - \left(\frac{h}{e}\right)_S\right] - \left[1 - \left(\frac{h}{e}\right)_C\right]} \tag{2.3}$$

where $\left(\frac{h}{e}\right)_S$ and $\left(\frac{h}{e}\right)_C$ are detector-dependent parameters. If they are known, for each hadron event, f_{em} can be determined and the hadron shower energy can be correctly reconstructed. This allows to eliminate the effect of fluctuations in f_{em} and hence the calorimeter performance for hadron detection is improved. In the scatter plot in Figure 2.1, the blue and red points are simulated data points for hadrons from a DRO calorimeter. The linear fit (red line) connects the coordinates $(\left(\frac{h}{e}\right)_S, \left(\frac{h}{e}\right)_C)$ and (1, 1). At these two points the value of f_{em} is 0 and 1, respectively. The slope of the fit line is given by

$$cot\theta = \frac{1 - (\frac{h}{e})_s}{1 - (\frac{h}{e})_c} \equiv \chi \tag{2.4}$$

Note that the χ *factor* can be estimated as soon as E is known (for instance in a beam test) and once one of the two h/e values is known, the last missing h/e is constrained. Moreover, the hadron energy can be reconstructed using only the two signals and the χ value, while the f_{em} can be reconstructed only if both h/e values are known.

$$E = \frac{S - \chi \cdot C}{1 - \chi} \tag{2.5}$$

The fact that θ and χ are independent of energy and particle type gives a possibility to reconstruct the hadron energy with unprecedented precision.

The following are some key advantages of DRO calorimeters over compensating calorimeters:

- High-Z absorbers (like U, Pb) are not mandatory, because low f_{samp} is not required in order to achieve compensation.
- Value of f_{samp}, which is offered by the detector design, can be a choice. This offers the possibility to achieve an excellent EM energy resolution (Equation 1.10).
- Large detector volumes and long signal integration time, for neutron detections, are not necessary for the DRO method. Efficient neutron detection can be performed with DRO calorimeters. It offers complementary information to f_{em} detection and is extremely beneficial for high-precision measurements with calorimeters. This is discussed at the end of Section 2.2.1.
- A DRO calorimeter is composed of towers, i.e., several longitudinally unsegmented sections where groups of same type of fibres are read out typically with single light sensors (e.g., photomultiplier tubes). The number of towers is a choice. Hence, fine lateral segmentation of showers can be achieved. It can provide an excellent PID performance. The experimental verification of this aspect is discussed in Section 2.2.2. However, the granularity of the readout system may not be tuned with the total number of towers. Single tower may have several channels of same type of fibres where each channel represents a group of fibres.
- The DRO modules can simply be calibrated with electrons also for hadron detection.

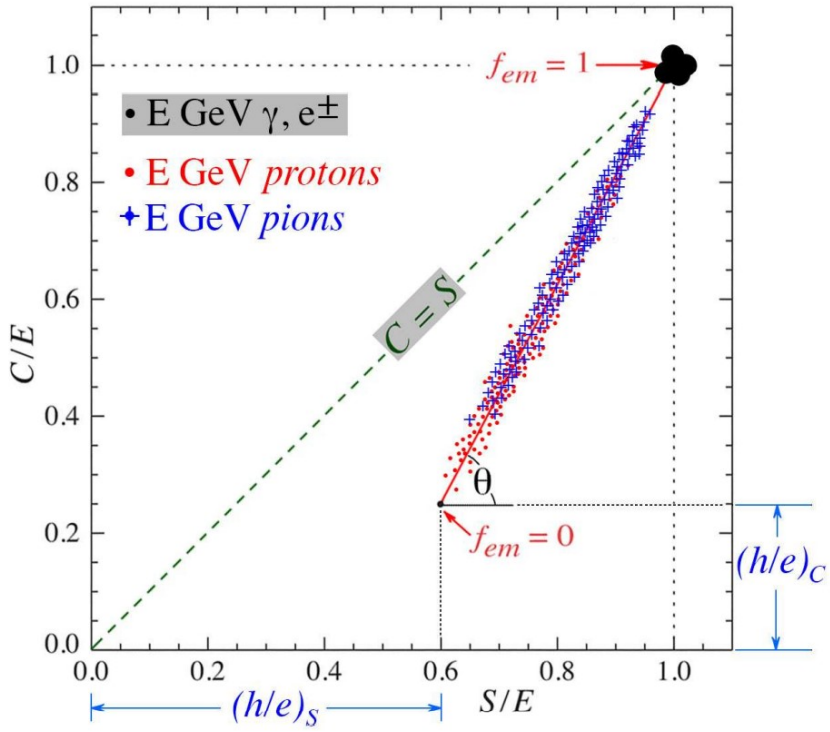

Figure 2.1: Scatter plot of simulated Cherenkov and Scintillation responses for a generic DRO calorimeter. The electron events are accumulated at (1, 1). The hadron events are accumulated along the red straight line. See text for further details. Ref [11]

2.2 State-of-the-art

2.2.1 DREAM calorimeter

The first proof-of-technique detector was a $2\lambda_{int}$ instrument, for ACCESS [21], a high-energy cosmic-ray experiment proposed for the International Space Station. The success of ACCESS inspired the collaboration to build a $10\lambda_{int}$ Dual-REAdout Module (DREAM). The building block of the DREAM calorimeter (Figure 2.2c) was an extruded, hollow, 2 m long copper rod of cross section $4 \times 4\ mm^2$. Seven optical fibres (3 scintillating and 4 quartz or clear fibres) were inserted, inside the central cylinder of 2.5 mm diameter, for light detection. 5130 rods composed 19 hexagonal tower structures (Figure 2.2a) with an effective radius of 16.2 cm. At the rear end of hexagonal towers the two types of fibres were well-separated into bundles and coupled with PhotoMultiplier Tubes (PMTs) (Figure 2.2b) to get two independent signals.

Some performances of the DREAM calorimeter [22, 24] are discussed here. Figure 2.3a depicts the Cherenkov signal distribution for 100 GeV π^- raw data. The asymmetry of the distribution is a reflection of asymmetric fluctuation in f_{em} values. The DRO method, i.e., the estimation of f_{em}, event by event, allows to restore Gaussian distributions for subsamples of events selected based on fixed intervals of f_{em}. Figure 2.3b manifests how the effect of fluctuations in f_{em} is eliminated during data analysis.

For the DREAM calorimeter structure, h/e values are 0.21 and 0.77, assuming 94% containment [11], for the Cherenkov and scintillation channels, respectively. These

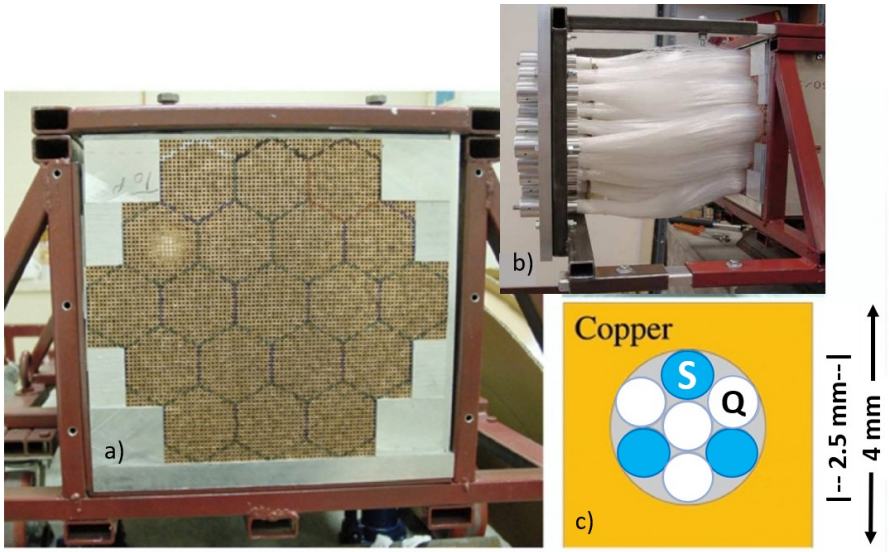

Figure 2.2: The DREAM calorimeter. The hexagonal structure is indicated (a). The grouped fibres at the detector rear-end (b). Dimension of a single unit made of 3 Scintillation and 4 quartz fibres extruded in a copper rod (c). Ref. [22, 23]

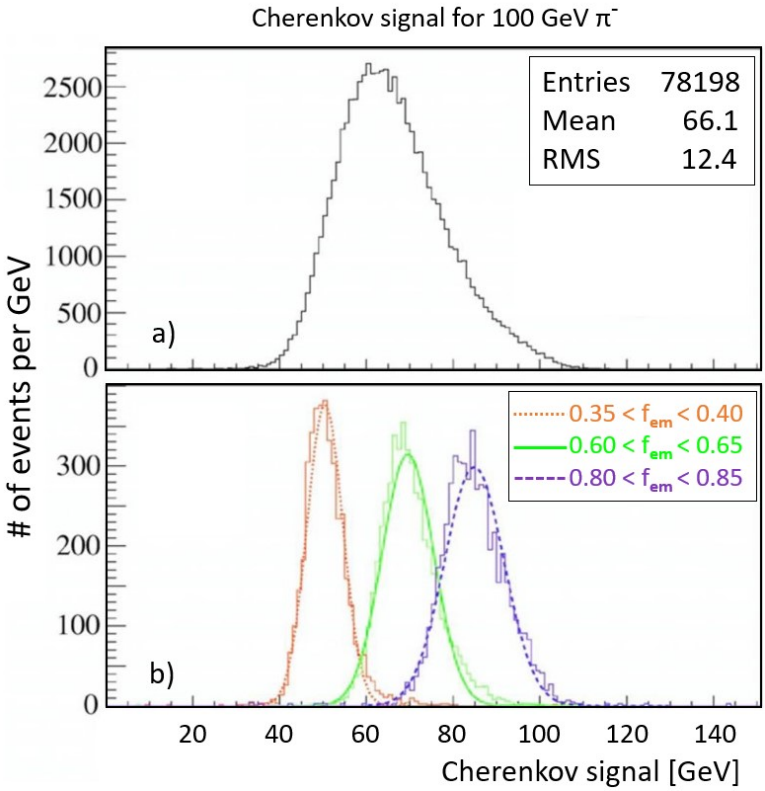

Figure 2.3: Asymmetric Cherenkov signal distribution for 100 GeV π^- raw data from the DREAM calorimeter (a). The total distribution is dissected based on event selection by measured f_{em}. Distributions of sub-samples of events are Gaussian (b). Ref. [11]

values and the value of C/S from experimental data obtained with the DREAM module are plugged in Equation 2.3 to measure f_{em} for each event. An event-by-event correction is applied to reconstruct 200 GeV multi-particle events from raw data. This improves the reconstructed energy (with Cherenkov channels) from ∼133 GeV to ∼190 GeV and the resolution (σ/mean) from ∼14% to ∼5% as shown in Figures 2.4a and 2.4b. A further significant improvement has been achieved by applying a correction for the shower leakage. It correctly reconstructs the energy of the multi-particle events (∼202 GeV) and a 2% energy resolution is achieved (Figure 2.4c). A ± 3% response linearity for hadrons (π^-) has been restored with reconstructed data (Figure 2.4d). Figure 2.4e shows that the energy resolution for multi-particle events improved considerably for the two combined signals than that derived with individual scintillation or Cherenkov signals.

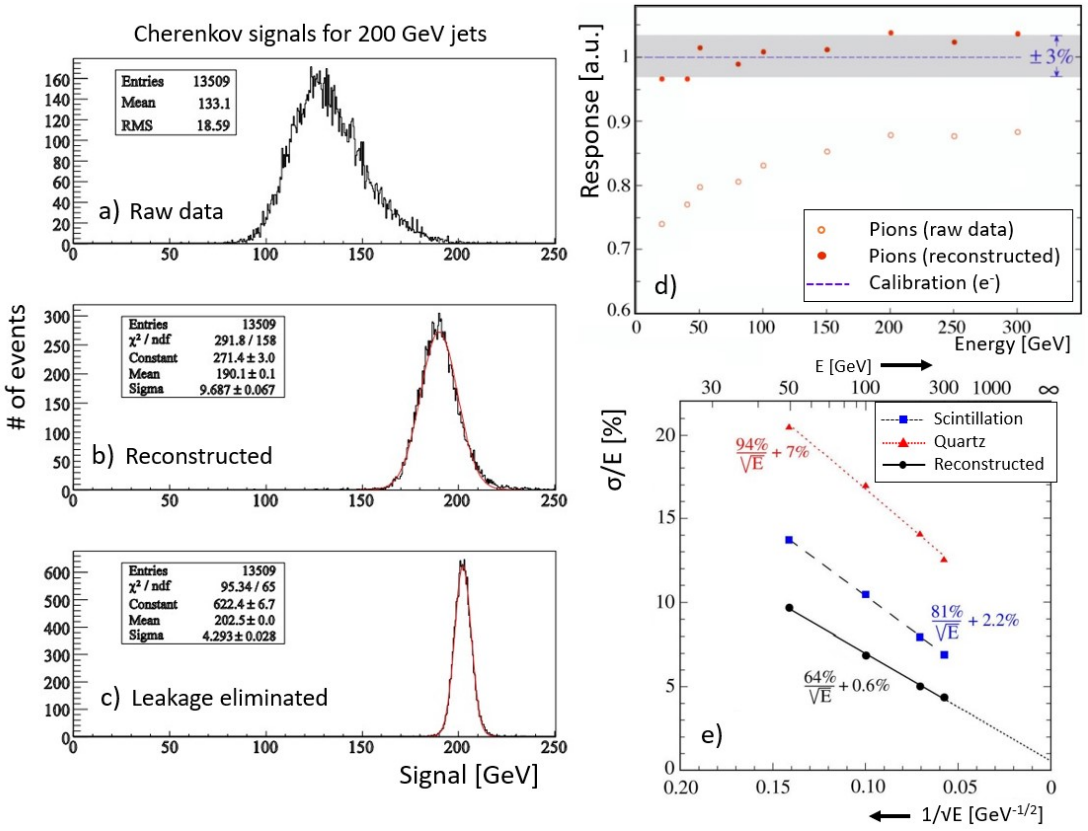

Figure 2.4: Results of DREAM calorimeter. Signal distribution for high-multiplicity jets from raw data (a), after event-by-event reconstruction made on the basis of Cherenkov and scintillation signal ratio (b), after correcting for the leakage fluctuation (c). Pion responses for raw data and reconstructed data are shown. A ± 3% hadron response linearity is achieved (d). The energy resolution for multiparticle events measured independently with scintillation, quartz fibres and after the correction with DRO method (e). Ref. [11]

Neutron detection

We have discussed elimination of fluctuations in f_{em} by the DRO method. Reduction of sampling fluctuation and fluctuations in photoelectron statistics will be discussed in the next Section 2.2.2. The remaining hurdle towards the ultimate hadronic resolution is the fluctuations in the invisible energy (Section 1.5). We have seen that the elimination of fluctuations in f_{em} takes care of the effects of the average contribution of invisible energy. However, for a fixed value of f_{em}, the invisible energy has fluctuations around the average. Efficient neutron detection of hadron showers not only allows to achieve compensation, but also can reduce the contribution of fluctuations in invisible energy. Monte Carlo simulation (HETC/MORSE package [25, 26]) allows to derive the strong correlation, as shown in Figures 2.5a and 2.5b, between the kinetic energy of soft neutrons produced in the shower and the energy loss in the shower due to the binding energy of nucleons, which can not contribute to the signal.

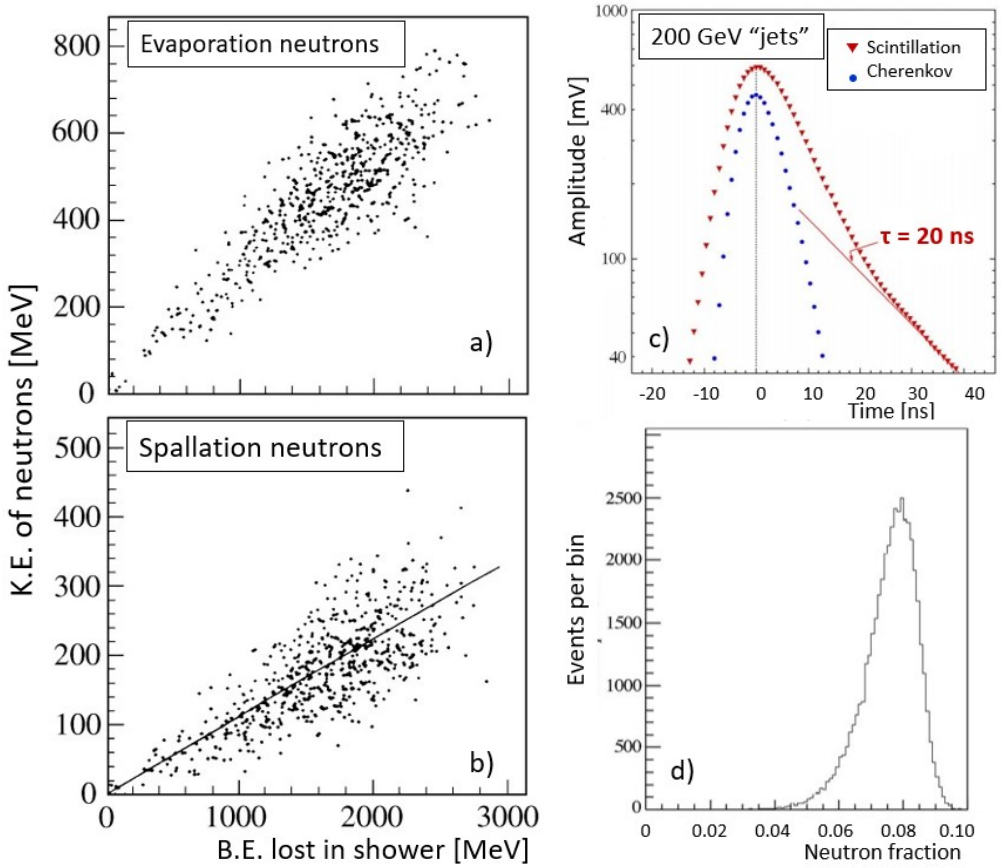

Figure 2.5: The correlation, established by Monte Carlo data, between the kinetic energy of evaporation neutrons (a) and spallation neutrons (b) under 20 MeV and the binding energy lost in 5 GeV π^- shower. The average time structures of scintillation and Cherenkov signals for showers of 200 GeV multi-particle events, measured with the DREAM calorimeter, are shown. A tail that is attributed to the non-relativistic neutrons, is present for scintillation signal (c). Event-by-event distribution of the fraction of scintillation signals due to neutrons is shown (d) Ref. [27]

Data obtained with the DREAM calorimeter have been used both for identifying neutrons and then improving the hadronic energy resolution [27]. The time structures of the scintillation and Cherenkov signals for 200 GeV multi-particle events, measured with a sampling oscilloscope, are shown in Figure 2.5c. The scintillation signal has an exponential tail that can be attributed to the non-relativistic neutrons produced in the shower. The tail, indeed, is absent for the Cherenkov signal. An event-by-event distribution of the contribution of this tail to the hadronic scintillation signal (f_n) is shown in Figure 2.5d. For both the scintillating and Cherenkov signals of EM showers, this kind of tail was found to be absent. It was observed that f_n had an anti-correlation with f_{em}. This implies that measurements of f_n in DREAM-like fibre calorimeters provide complementary information to measurements obtained from ratios of the Cherenkov and scintillation signals.

2.2.2 RD52 calorimeters

The fluctuations that limited the energy resolution of the DREAM calorimeter were the lateral leakage fluctuation, sampling fluctuation and fluctuations in the Cherenkov Light Yield (LY)* (only 8 photoelectrons/GeV by quartz fibres). A detector with larger dimension can reduce the first contribution, whereas crystals are one of the solutions for efficient reduction of the latter two. This option has been explored thoroughly by the CERN RD52 collaboration (2011 - 2017).

Use of crystals

The material properties of high-Z crystals (e.g., $PbWO_4$, Bismuth Germanate (BGO)) ensure potentially higher Cherenkov LY. Hence the sampling fluctuation and fluctuations in Cherenkov light production are controlled. The challenge is to identify, and then effectively separate, the Cherenkov light from the dominant scintillation light. To make the distinction, the following are some efficient ways studied by the RD52 collaboration.

1. Directionality of Cherenkov light.
2. Difference in signal time structures.
3. Difference in spectral compositions.
4. Use of polarisation filters.

Some of the tests are briefly mentioned here.

$PbWO_4$ crystal produces relatively little scintillation light and its large refractive index (n = 2.2) promises a substantial Cerenkov light. Cherenkov light is emitted at a characteristic angle, θ_C ($\cos\theta_C = 1/(\beta n)$), with respect to the momentum vector of the particle that generates it, while the scintillation light is isotropically emitted. To detect the contribution of Cherenkov light to signals from $PbWO_4$, it was rotated (Figure 2.6) in such a way that the crystal axis is oriented at θ_C with respect to the incoming particles. Two PMTs were equipped at the two ends of the crystal and Cerenkov lights, produced by the cosmic rays and after traversing the trigger counters, were detected in either PMTs. The measure of Left(L)-Right(R) response asymmetry, (R-L)/(R+L),

*number of photons or photoelectrons per unit of energy deposited

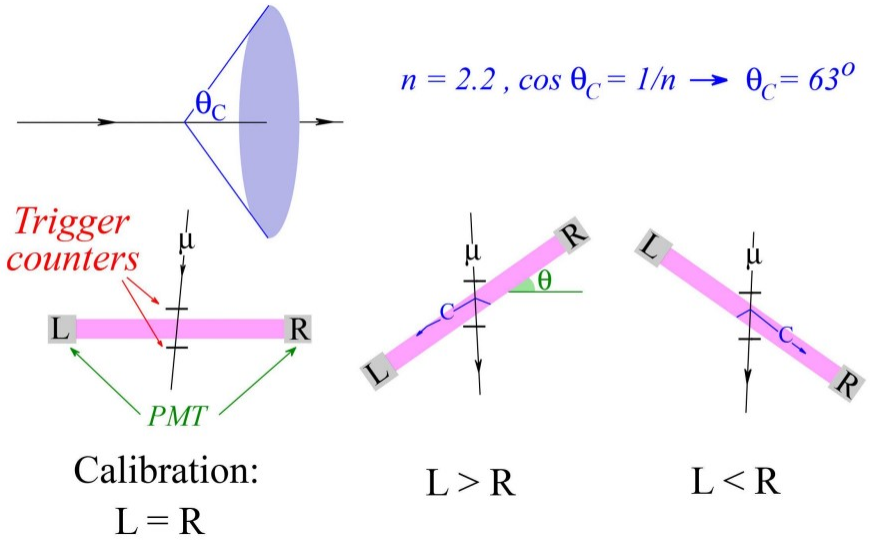

Figure 2.6: Principle of the asymmetry measurement used to establish the contribution of Cherenkov light to the signals from the $PbWO_4$ crystals. Depending on the orientation of $PbWO_4$, this directionally emitted light contributes differently to the signals either from the left or from the right photomultiplier tubes. Ref. [28]

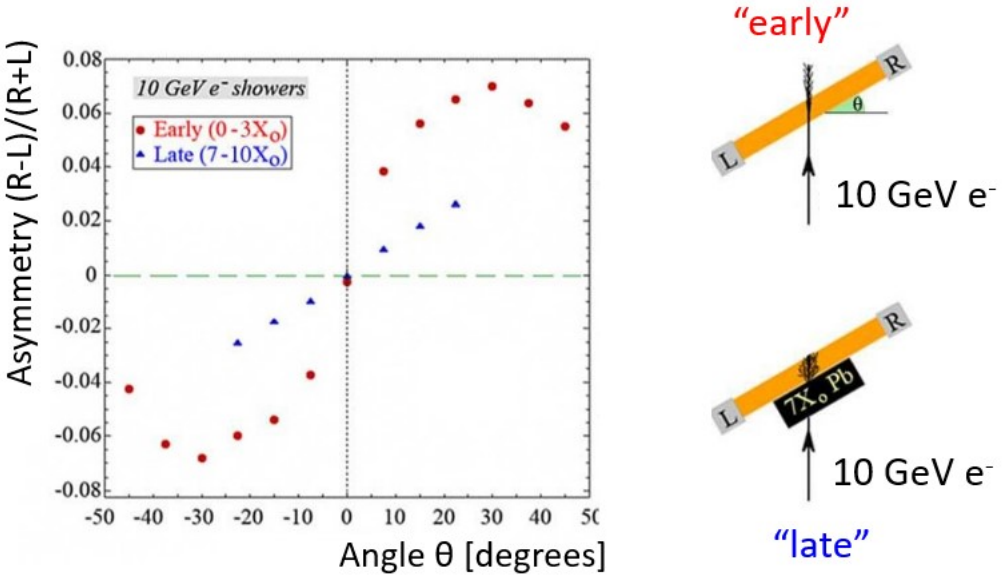

Figure 2.7: Left–right response asymmetry measured for 10 GeV electrons showering in a 2.5 X_0 thick $PbWO_4$ crystal, as a function of the orientation of the crystal with respect to incoming particles. Results are shown for the "early" and the "late" components of the showers. See text for details. Ref. [28]

as a function of orientation of the crystal (Figure 2.7), provided the contribution of Cherenkov light to signals. Results are shown for the "early" and the "late" components of the showers. The latter measurements were performed by placing a 4 cm of lead brick upstream of the crystal as shown in the sketch of Figure 2.7. A detailed overview of these tests is available in Ref. [28]. These tests were performed only to assess the capability of distinguishing Cherenkov lights by their directionality. When tests of crystals along with the DREAM fibre module were performed, the mentioned other three ways to separate the Cherenkov light from the scintillation light, were tested.

The applicability of $PbWO_4$ crystals for the DRO calorimetry was improved by doping them with small amounts, $\mathcal{O}(1\%)$, of molybdenum [29]. As beneficial effects, the decay-time of scintillation light increased and the spectrum of emitted scintillation light had been shifted to larger wavelengths. Calorimeter signals generated by 50 GeV electrons traversing this crystal were measured. The crystal was oriented in such a way to maximize the relative fraction of the Cerenkov light in the detected signals. Almost the entire detected signal was due to prompt Cherenkov light when only UV components were selected by means of an optical filter. On the other hand, the use of a yellow transmission filter allowed to select only scintillation light with larger decay time (∼26 ns) as an effect of Mo doping. This is illustrated in Figure 2.8. Other tests with BGO crystals for recognition of differences in signal time structures and spectral compositions are described in Ref. [11].

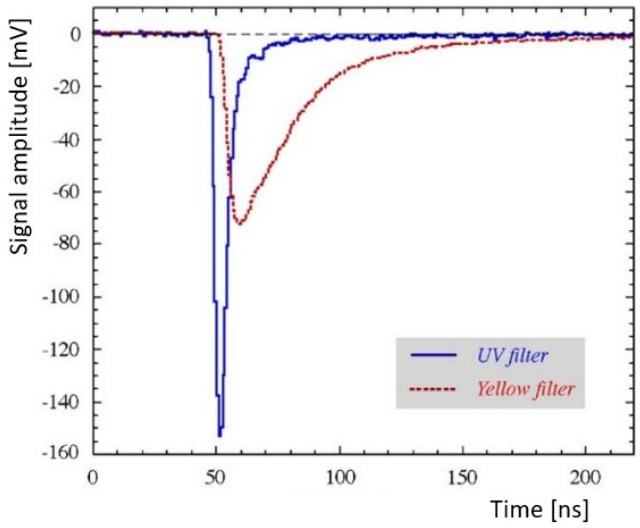

Figure 2.8: Average time structure of the signals, generated by 50 GeV electrons, developed in $PbWO_4$ crystal doped with ∼1% Mo. The orientation of the crystal with respect to incoming particles was 30° in these measurements. The blue and red spectra were obtained with UV and yellow filters, respectively. Ref. [29]

After obtaining positive results from the tests of single crystals, the RD52 collaboration tested calorimeter systems with 19 $PbWO_4$ crystals and 100 BGO crystals, forming two matrices as EM section, and the DREAM calorimeter, serving as hadronic section [30, 31]. The DRO method worked (Figure 2.9) for this combined system. Yet, after many studies, use of crystals was not likely the most promising solution to achieve improvement in performance compared to that of the DREAM calorimeter. The main problem observed was the attenuation of short-wavelength Cherenkov light

due to absorption properties of crystals. Short λ_{att} of Cherenkov light caused dependency of signals on the location of Cherenkov light production. Also, a large fraction of light was sacrificed for sufficient Cherenkov signal extraction. These are the sources of event-to-event fluctuations in signals due to low photostatistics. Studies showed that for 50 GeV electrons, Cherenkov photoelectron (produced in $PbWO_4$ doped with 0.3% Molybdenum) statistics allowed to achieve a resolution of $13.5\%/\sqrt{E}$ (Figure 2.10). Details of this analysis can be found in [30]. This result showed that with crystals the DRO calorimeter performance can not go beyond that with fibres. Apart from above mentioned sources of fluctuations, high-costs of crystals do not make it an option for doing precision measurements with calorimeters in next generation collider experiments. Rather, fibres are cost-effective solutions for scaled-up DRO calorimeters.

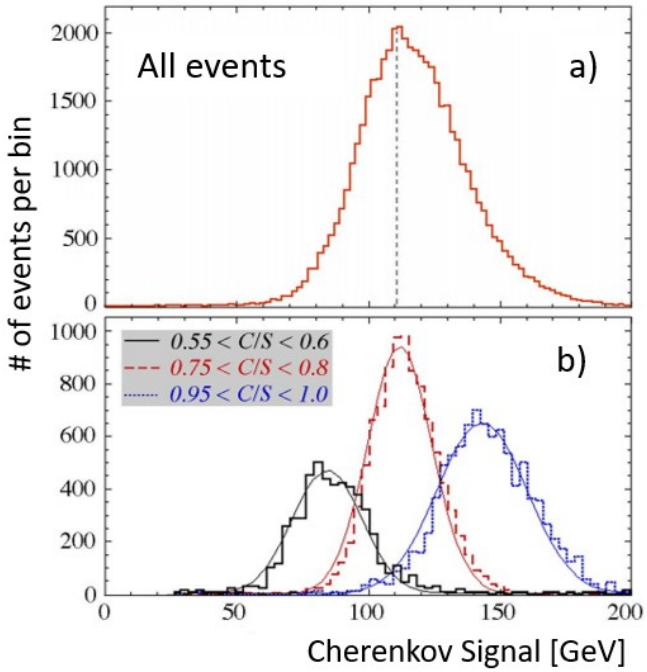

Figure 2.9: The Cerenkov signal distribution for 200 GeV multi-particle events detected in both BGO crystal and fibre calorimeter system (a). The distributions for subsets of events selected on the basis of the ratio of the total Cerenkov and scintillation signals in this detector combination (b). Ref. [11].

Use of fibres

Detector performance concerning the hadronic energy resolution had been significantly improved in the RD52 fibre calorimeter (nine Pb based modules and two Cu based modules) [32, 33] from the DREAM calorimeter by adopting several changes, listed below, that were keys to reduce the lateral leakage fluctuation, Cherenkov LY limitation and sampling fluctuation.

- Bigger detectors (of 9×∼150 Kg + 2×∼120 Kg instrumented mass compared to ∼1030 kg of the DREAM calorimeter) offer better containment.

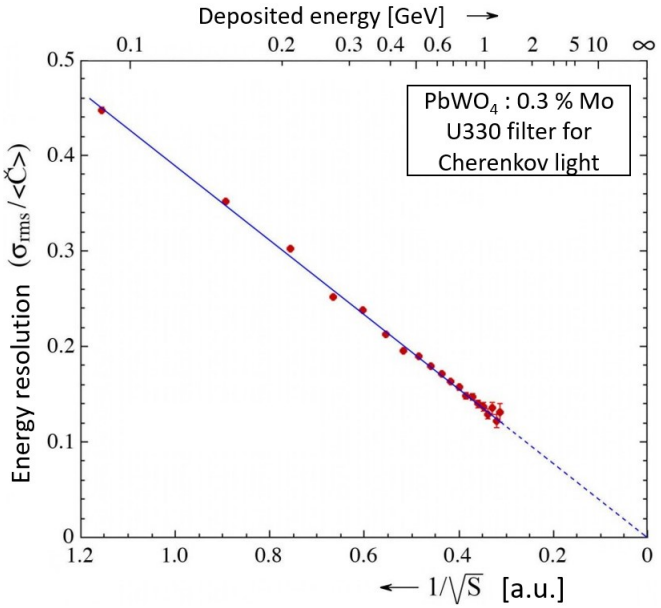

Figure 2.10: The fractional width of the Cherenkov signal distribution, for 50 GeV electrons traversing $PbWO_4$ crystal at 30 ° with the beam line, as a function of amount of energy deposited in the crystal, as derived from the scintillator signal. The $PbWO_4$ crystal was doped with 0.3% Mo. Ref. [30].

- Replacement of quartz fibres by clear fibres with larger Numerical Aperture (NA)[†], because the LY increases with the square of NA; Use of super bialkali PMTs with a factor 4 rise in quantum efficiency (33 C.p.e./GeV from 8 C.p.e/GeV); ∼65% increment in Cherenkov fibre density; Aluminized upstream ends of ∼1000 Cherenkov fibres in one Cu based module.

- A factor two increment in f_{samp} and considerable increment in sampling frequency by individual embedding of fibres in absorber structure.

Tests with e^-: RD52 fibre patterns (Figure 2.11) i.e., the individual embedding of fibres in the absorber structure, offers two completely independent sampling structures of showers with the scintillation and clear fibres. The phenomena underneath the light production and collection for the two types of fibres are completely different [34, 35]. The combination (weighted mean) of the two signals provide significantly improved response and energy resolution [32] compared to the ones obtained with the DREAM calorimeter. Figure 2.12 shows the EM energy resolution measured with the RD52 fibre-sampling Cu module. The fit for the EM energy resolution obtained with the Cherenkov channels shows a very small constant term. But for the combined signal, which is the weighted average of the scintillation and Cherenkov signals, the slight deviation has been caused by the impact point dependency of the scintillation signals i.e., an energy-independent effect. The stochastic term for the combined EM energy resolution is measured to be 13.9 $\%/\sqrt{E}$. Other interesting RD52 EM performances and results can be found in Ref. [11, 32].

[†]NA $= \sin\theta = \sqrt{(n_{core}^2 - n_{clad}^2)}$, where θ is the largest angle an incident particle can have for total internal reflection in the fibre core.

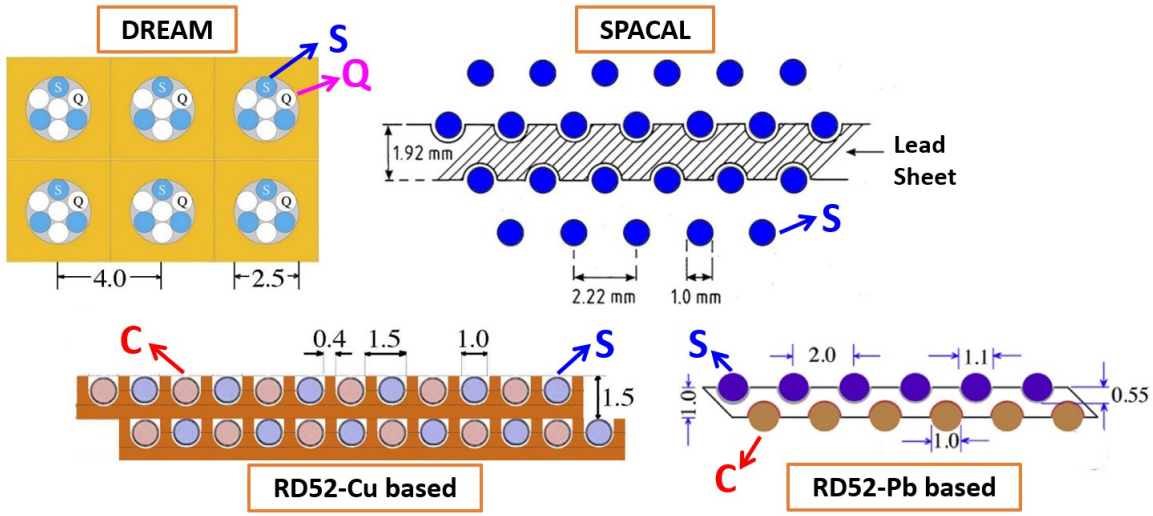

Figure 2.11: Distinct fibre patterns at the detector transverse planes for the DREAM, RD52 copper and lead based fibre DRO calorimeters are shown. For comparison, the fibre patterns of the SPACAL is also shown. S, C and Q stand for scintillation, Cherenkov and quartz fibres, respectively. All the distances (fibre pitch, dimension of geometry, etc.) are in mm. Ref. [7, 8, 32, 33]

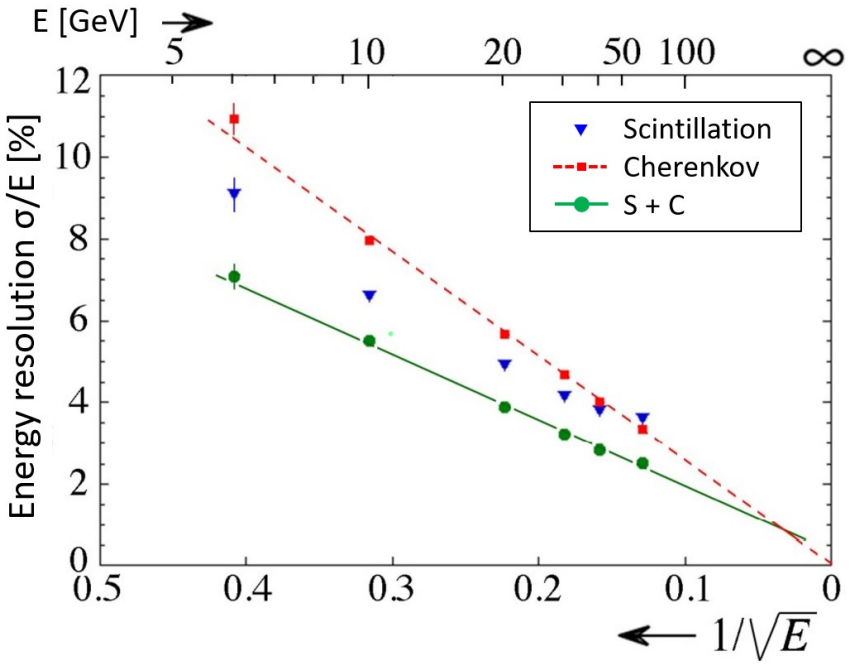

Figure 2.12: The energy resolution obtained with the Cherenkov channels scales with $E^{-1/2}$. But for the scintillation and combined signals constant terms (intercepts in vertical axis) are present. This has been caused by the impact point dependency of the scintillation signals. The stochastic term for the combined EM energy resolution is measured to be $13.9\,\%/\sqrt{E}$. These are measured with the RD52 fibre-sampling Cu module. Ref. [32]

Tests with π^-: The hadronic performances of the RD52 fibre calorimeter were in-

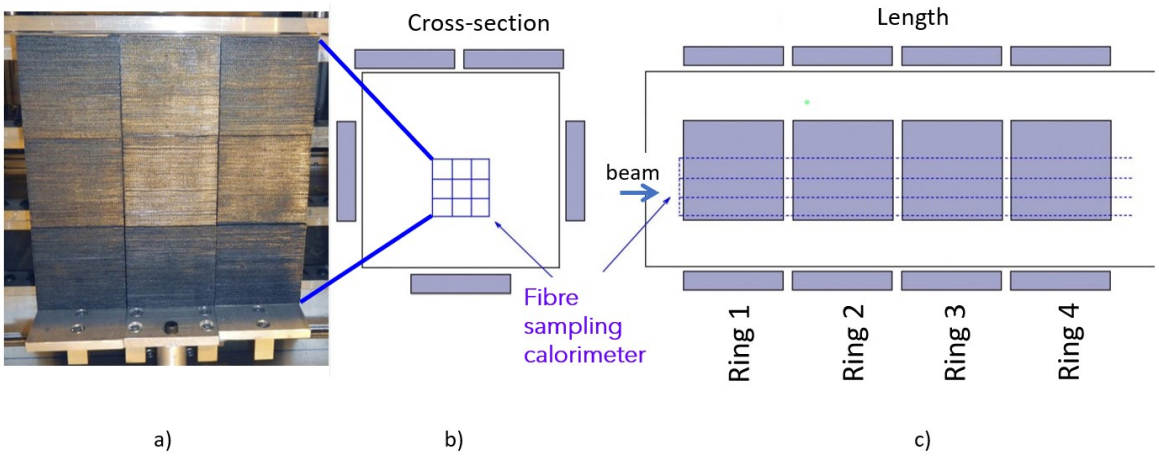

Figure 2.13: Front face of the RD52 fibre-sampling Pb module based on modular structure (a). Schematic representation of the cross section view of the module shows a ring of five grey slabs, i.e., the leakage counters (b). Schematic representation of the side view of the module shows four rings (c).

vestigated with Pb module based on modular structure, each of cross section (9.2 × 9.2) cm^2 and 2.5 m long. Nine modules, each sub-divided in four towers, constitute 36 towers, each of size (4.6 × 4.6 × 250) cm^3. In order to measure the shower leakage, the calorimeter, on four sides, was surrounded by an array of 20 plastic scintillation counters, each of (50 × 50 × 10) cm^3. Figure 2.13 shows the front face of the modular structure and two schematic sketches that illustrate locations of leakage counters around the calorimeter. Each tower had two independent readouts, one for the scintillation fibres and another for the PMMA based clear fibres. In total, 72 PMT signals per event were generated. These signals were calibrated with electrons, whereas the surrounding leakage counters were calibrated with muons. The energy escaped from the calorimeter structure was partially measured in the leakage counters.

Energy reconstructed from raw data with the scintillation and Cherenkov channels are asymmetric and indeed, much lower than the beam energy. These distributions are shown (Figures 2.14a and 2.14b) for 60 and 100 GeV π^-s. For same mentioned energies, the distributions of the combined energy reconstructed with the DRO method (Equation 2.5), with $\chi = 0.45$, are shown in Figures 2.14c and 2.14d.

Figure 2.15 shows that the hadronic energy resolution is significantly improved with DRO corrections than that for individual Cherenkov signals and scales with $E^{-1/2}$ without any energy-independent term. Though a stochastic term of $\sim 70\%/\sqrt{E}$ is quite large, but further improvement has been observed in analysis where energy deposited in the leakage counters has been taken into account.

Particle identification: The traditional way of incorporating the EM section (ECAL) and the hadronic section (HCAL) longitudinally in a calorimeter system allows identification of electrons and photons that are contained, fully, in ECAL. Hence, a separation between electrons and hadrons is possible. This option for the PID is absent in the DRO

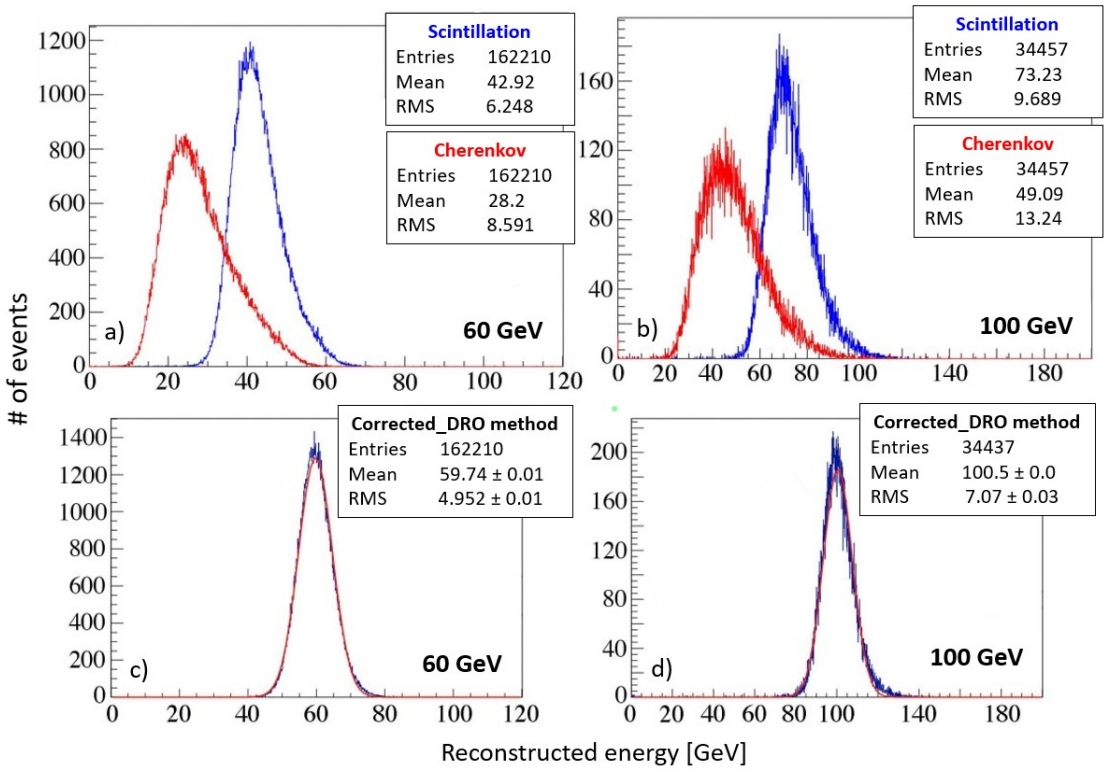

Figure 2.14: Event-by-event distributions of energies reconstructed with the scintillation and Cherenkov channels for 60 GeV (a) and 100 GeV (b) π^-s. Gaussian energy distributions, reconstructed with the DRO method, peak at 59.7 GeV with a resolution of 8.3% (c) and at 100.5 GeV with a resolution of 7% (d). Ref. [11]

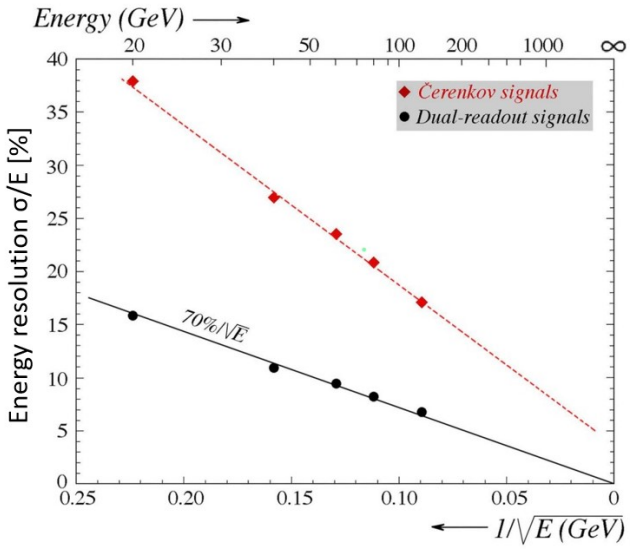

Figure 2.15: The hadronic energy resolution of RD52 fibre-sampling Pb module is far better for the combined signals reconstructed with the DRO method. High lateral leakage fluctuation is the dominant limitation to the energy resolution. Ref. [36]

method, since the calorimeter is longitudinally unsegmented. But there are several fascinating ways to effectively distinguish electrons from hadrons with DRO fibre-sampling calorimeters. Some of these methods, tested extensively with RD52 modules [33], are listed here.

- **Lateral shower profile:** Unlike hadron showers, an EM shower is narrower and confined near the shower axis. The fraction of total shower energy deposited in the central tower, where the beam particles hit, is different for electrons and hadrons (Figure 2.16a).

- **Two independent signals:** Only ultra relativistic particles (e^-, e^+) contribute to the Cherenkov signals. On the other hand, both electrons and hadrons contribute to the scintillation signals. So, an estimation of the ratio of the two signals can separate electrons ($C/S = 1$) from hadrons ($C/S < 1$) (Figure 2.16b).

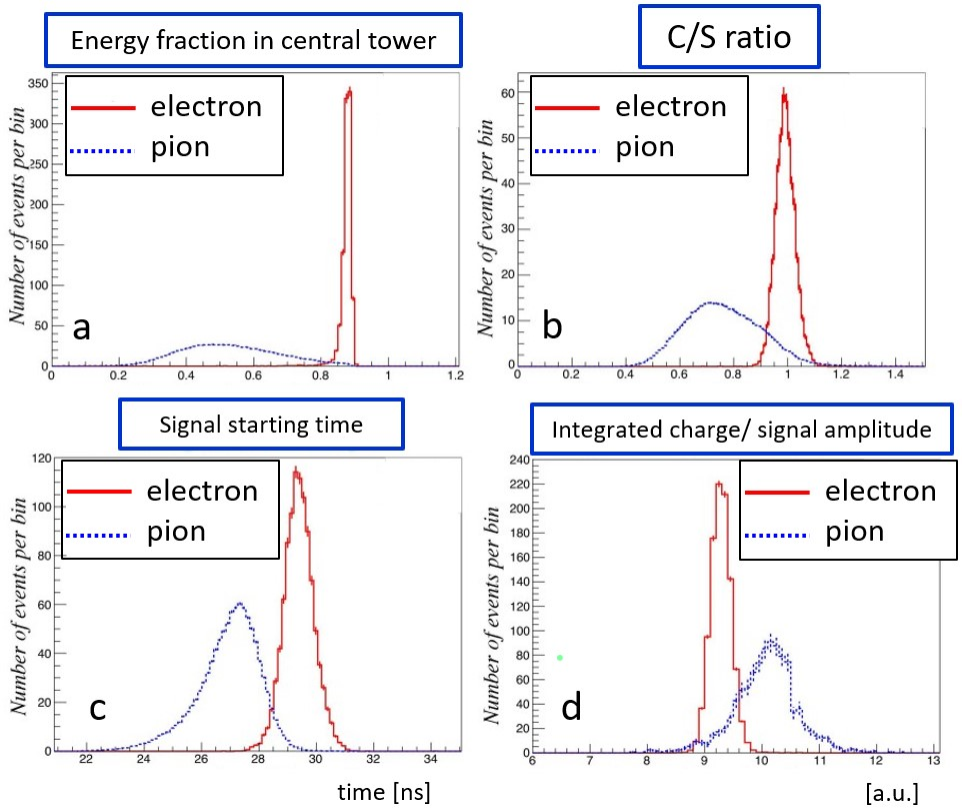

Figure 2.16: Particle identification studies, for 60 GeV electrons and pions, performed with the RD52 fibre calorimeter. The distributions are a fraction of the total signal recorded by the tower in which the particle entered (a), ratio of the Cerenkov and scintillation signals (b), starting time of the scintillation signal in the PMT, measured with respect to an upstream trigger signal (c), and ratio of the total integrated charge and amplitude of the signal (d) Ref. [33]

- **Signal starting time:** The speed of light produced in fibres is lower than the speed of particles that generate the light. Therefore, the deeper the light produced inside a calorimeter, the faster it arrives to the photosensors. The starting time

of a signal at the photosensors identifies the type of particle. Hadrons produce light deeper inside a calorimeter, so the corresponding signals are initiated earlier than that of electrons (Figure 2.16c).

- **Integrated charge over signal amplitude:** The light is produced over a larger region in depth for hadrons. So, the distribution of the integrated charge over signal amplitude is broader for hadrons than that for electrons (Figure 2.16d).

The four methods consider different aspects of the shower and signal generation. Hence, the cuts applied to these four distributions to flag electrons are not correlated with each other. A combination of cuts provides high degree of accuracy in electron identification with very little pion contamination wrongly identified as electrons. The particular combination, ($f_{lat.leak} > 0.70$ AND $f_{C/S} >0.85$ AND $f_{time} >28$ ns), for 60 GeV particles, selects more than 99% of electrons and less than 0.5% of pions.

Tests with SiPMs: Finer granularity of calorimeter system, for measuring lateral components of showers, is a criterion in experiments at future Higgs factories. Silicon PhotoMultipliers (SiPMs) [37, 38] are appropriate candidates to substitute PMTs as photodetectors for the detection of the scintillation and Cherenkov lights, independently, from corresponding fibres.

Potential advantages of using SiPMs are listed:

- Independence of magnetic fields.
- Low operating voltage (compared to PMTs).
- Compact readout.
- At detector rear end, getting rid of unnecessary extra fibres (Figure 2.2) that may catch particles unrelated to particle showers and hence, develop false signals.
- Cost-effective solution for large area application.

Some disadvantages are:

- Saturation effects (being a digital device) i.e., many photons for limited number of pixels.
- Occurrence of *optical crosstalk* (contamination between scintillation and Cherenkov lights), because the two types of fibres with totally different LYs are closely spaced (∼1-2 mm). An example of the detector geometry and readout is given in the following paragraphs.
- Challenging design of the front-end electronics that has to be compatible with the dimension of fibre spacing.

A very small, $(15 \times 15)\ mm^2$ in cross section (i.e., $0.22{\cdot}R_M$) and ∼112 cm deep (i.e., $39{\cdot}X_0$), fibre-sampling prototype, first time coupled with SiPM sensors was constructed. It was tested with beams in 2017. Only a fraction (46%) of the EM shower, contained within 22% of R_M, was sampled with 32 polystyrene based scintillation and 32 PMMA based clear fibres. These fibres were embedded in brass (Cu260) absorber structure. Chessboard-like fibre patterns in the detector transverse plane is shown in Figure 2.17a.

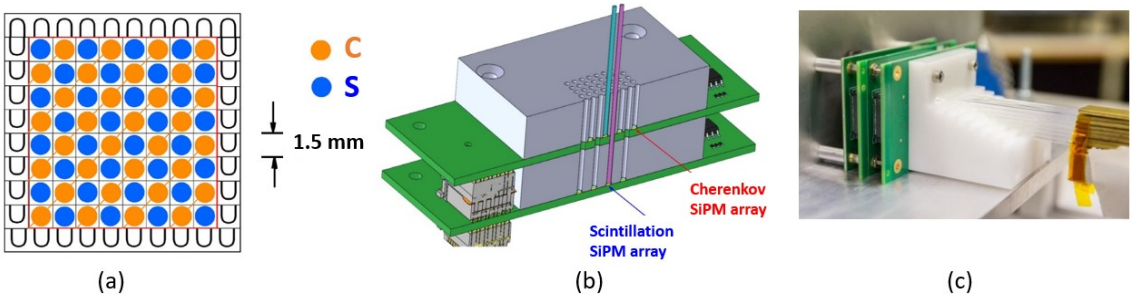

Figure 2.17: The pattern shows arrangement of the two types (2×32) of optical fibres at the detector transverse plane. The fibre pitch is 1.5 mm (a). The two tier structure with two separate arrays of SiPMs coupled with the Cherenkov fibres and scintillation fibres (b). The fibres at the rear end of the brass module are coupled with the two tier readout structure (c).

Each fibre was read with a single SiPM sensor (HAMAMATSU S13615-1025) with an active area of $(1 \times 1)\ mm^2$, 1584 cells and a cell size of $25\mu m$. The photosensors were mounted on a two tier structure (Figure 2.17c) in order to avoid optical crosstalk between the two types of fibres. On the front-tier, SiPMs were connected to the Cherenkov fibres. The scintillation fibres were channelised through holes interleaved with other 32 sensors equipped on the back-tier (Figure 2.17b). Some results from the laboratory tests and beam tests are discussed here. A detailed overview can be found in Ref. [39].

Optical crosstalk: This test was carried out in the laboratory, where all except one fibre tips at the front face of the calorimeter were masked. The unmasked fibre was illuminated with a LED light and the signals in all 64 SiPMs were measured. The signal distribution was obviously concentrated around the illuminated fibre as displayed in Figure 2.18 for 100k events. Similar were the observations for illumination of alternate fibre tips. Analysis showed that when a scintillating fibre was illuminated, the distribution of sum signals in the 32 Čerenkov fibres had a mean value of 0.3% of the scintillation signal, and a rms value of 0.1%. These values set an upper limit to the crosstalk, because it could have happened that a small fraction of the LED light directly entered a neighboring Cherenkov fibre. Another set of tests were performed with 125 GeV μ^+ beams extracted from the SPS at CERN. These measurements exploited the observations from studies of muons with the DREAM calorimeter, as references for calculations. The observations of this set of tests with beams [39] were compatible with that of the previous mentioned laboratory tests. The value $0.3 \pm 0.1\%$ has been considered as a measurement of crosstalk.

Light Yield: The Cherenkov LY measured with the SiPM sensors is 28.5 ± 2 Cpe/GeV (Figure 2.18b). Taking into account the containment of this detector of only 46%, the LY for the complete EM shower is estimated to be 64 ± 2 Cpe/GeV. Excluding the light contributon due to crosstalk this number is reduced to 54 ± 5 Cpe/GeV, i.e., almost twice compared to that measured with PMTs for the RD52 Cu-based module. Plugging this higher LY in the measurement of the EM energy resolution obtained with the RD52 Cu-based module (Figure 2.12), a better stochastic term ($12.5\%/\sqrt{E}$ vs. $13.9\%/\sqrt{E}$) would have been achieved.

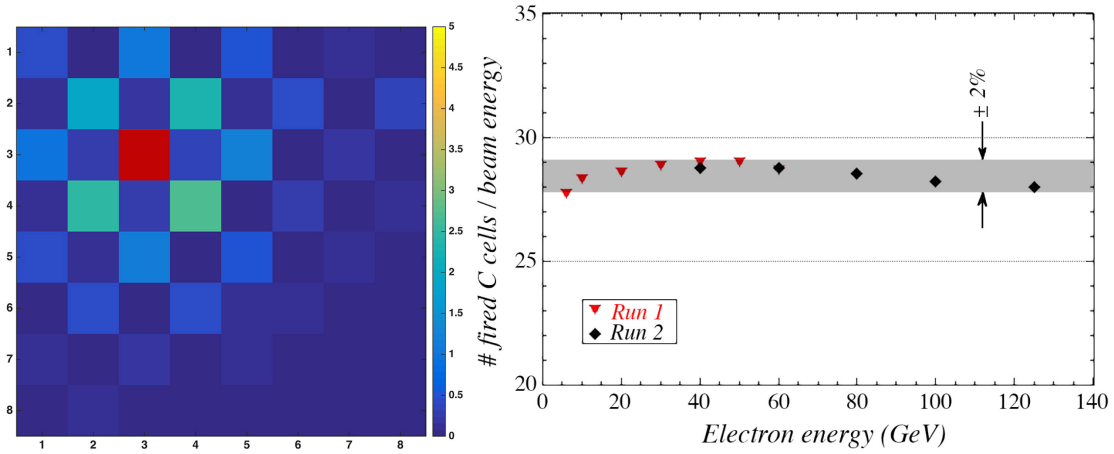

(a) (b)

Figure 2.18: Signals (colour axis) in 64 SiPM sensors due to illumination of single scintillation fibre with LED light at the detector front-face. Rest of 63 fibre tips are masked. The red box shows the maximum signal at the sensor connected to the illuminated fibre (a). The average Cherenkov LY, measured in the SiPMs, as a function of electron beam energy is constant within a band (shaded area) of $\pm\,2\,\%$. This shows that the average shower containment is independent of the electron energy (b). Ref. [39]

Lateral shower profile: The narrow profile of an EM shower was a known fact. Stud-

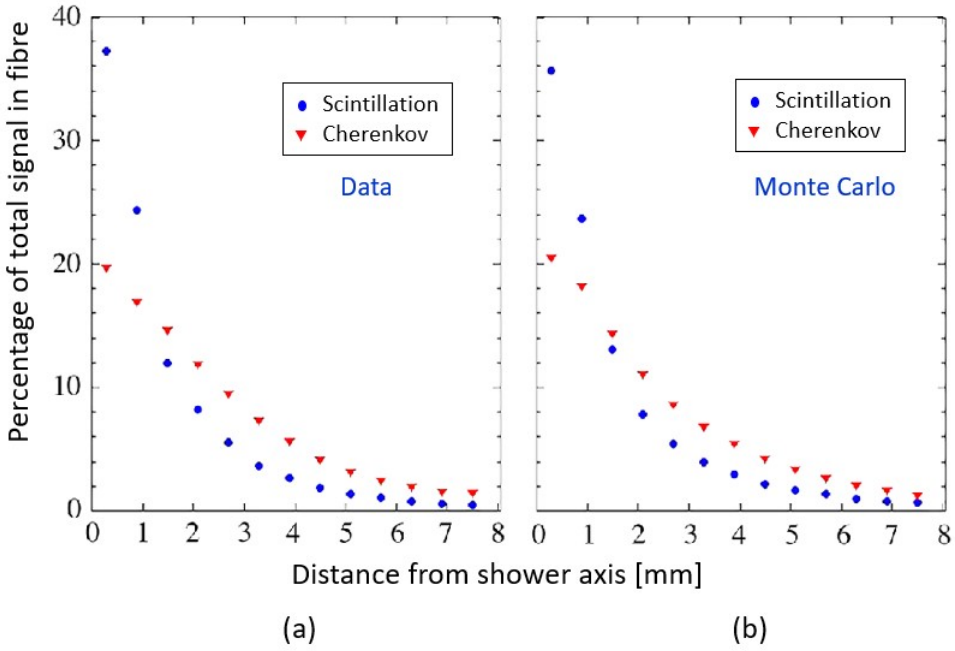

Figure 2.19: Percentage of total signal in fibre as a function of distance from shower axis. The signals from individual fibres located in the same r-bin (e.g., 2–3 mm from the shower axis) are summed, and the average value of these summed signals is plotted as a function of r. Results, independently for both fibres, are from the test beam data (a) and Geant4 simulation (b). Ref. [39]

ies pursued with the SiPM equipped module, thanks to the excellent spatial resolution, reveals that ∼10% of the total shower energy is contained within ∼ 1 mm from the shower axis i.e., a significant percentage of particles' energy is deposited in a single fibre. This fact also points to a problem concerning the *dynamical range* (number of cells/sensor) of the SiPM sensors, because it is a great deal to handle high single signal in the very core of the shower (because of signal saturation) and a long tail of comparatively low signal in the hollow. 40 GeV and 10 GeV electron beams were used to examine the lateral shower profiles (Figure 2.19a), separately and respectively for the Cherenkov and scintillation channels. These results are in good agreement with the simulation studies (Figure 2.19b).

2.2.3 State-of-the-art summary

The main problem of traditional hadronic calorimeters, e/h $\neq$ 1, has been solved by compensating calorimeters (Section 1.8.1). But the limitations in the energy resolution for both the EM and hadronic showers and the challenges concerning the calibration remain in this type of calorimeters. Longitudinally unsegmented, fibre-sampling DRO calorimetry provides solutions to all these problems: (i) responses to the EM and non-EM components of hadron showers are equalised offline, thus, the condition of compensation (e/h ∼1) is achieved; (ii) the effect of fluctuations in f_{em} is eliminated with an event-by-event measurement of the C/S ratio (Section 2.1), hence, a better hadronic performance has been assured; and (iii) calibration constants, which are established with electrons, also provide the correct energy for hadronic showers. Apart from these, both f_{samp} and the sampling frequency can be tuned in a DRO calorimeter. This may offer an adequate EM energy resolution. Excellent e^-/hadron discrimination was also

Calorimeter	Fibres	Dimension	f_{samp} [%]	Beam test
DREAM Cu	∼36k inside extruded rods	$\sim 10\lambda_{int}$	∼2	2003
RD52 Cu	∼4.1k embedded in sheets	$\sim 10\lambda_{int}$	∼4.6	2012
RD52 Pb	∼18.5k embedded in sheets	$\sim 10\lambda_{int}$	∼5.3	2012
RD52 SiPM Brass (Cu260)	64 embedded in sheets	$\sim 39X_0$	5-6	2017
Novel EM-scale Brass (CuZn37)	∼3k loaded in capillaries	$\sim 53X_0$, $\sim 44X_0$	∼3	2021

Table 2.1: A list of prototype detectors tested with beams in the last 20 years for assessing the DRO calorimetry capabilities. The basic structures, lengths, sampling fractions and testing times are listed. This thesis concerns the last one in the list.

demonstrated (Section 1.6). Further, excellent PID capabilities can be achieved with a highly segmented measurement of the lateral shower profiles. The feature, better granularity with more number of towers, is opening high possibility for longitudinally

unsegmented, fibre-sampling DRO calorimeters to be important detectors in experiments proposed at future circular e^+e^- collider facilities (Chapter 3, Section 3.4).

In the last 25 years, R&D on the DRO calorimetry capabilities has achieved major milestones towards fulfilling detector requirements imposed by the physics goals of experiments envisaged at future circular e^+e^- collider facilities. A concise, recent review of the workflow is well demonstrated in Ref. [40]. Table 2.1 lists the hardware R&D activities conducted so far. The search for a cost-effective solution for large area coverage led to the design and construction of a novel prototype calorimeter module with fibre-sampling, DRO tower structures. In principle, the ultimate fine sampling could be reached by individually reading out each fibre in a full containment module, nevertheless a coarser granularity would likely be implemented by combining the analog signals of 8 fibres before digitisation. Chapter 4 is dedicated to describe these projects, recent work status and upcoming activities.

Chapter 3

Calorimetry in future colliders

3.1 Post-LHC era

In 2022, the Large Hadron Collider (LHC) [41] has started its last data taking before upgrading to its High-Luminosity (HL) programme [42] and particle physicists are celebrating the tenth anniversary of the Higgs boson. It is the time to plan about next collider facilities on which depends the future of collider particle physics. The Standard Model (SM) [43], a theory behind the known elementary particles and three fundamental interactions, has been settled with the discovery of Higgs boson. But some questions still remain after this discovery. These questions point to:

- Lack of description about one of the four fundamental forces, gravitation.
- Unexplained mass hierarchy of three generations of matter.
- Masses of neutrinos.
- Matter/anti-matter unbalance found in the universe.
- Origin of dark matter as well as of dark energy.

Intensity and energy frontier collider facilities (may) have the key to answer some of these questions. There are few candidates on the table based on:

- Different beam configuration - linear or circular colliders.
- Different objectives - precision measurements and/or new discoveries.

For the first time in history of collider physics we don't have a clear target towards the energy scale but a versatile and as powerful as possible accelerator facility is of great interest.

3.2 Circular over linear

In ***linear colliders*** two lepton (e^-, e^+) beams are accelerated in LINear ACcelerators (LINACs) and made interact at one Interaction Point (IP). Superconducting Radio Frequency (SRF) is the key technology for this. The main purpose of a linear

e^+e^- collider is to serve as factories for mass-production of the Higgs boson as well as top quark. The two candidates for future e^+e^- linear colliders are the International Linear Collider (ILC) [44] and the Compact LInear Collider (CLIC) [45]. ILC features 17000, 1.3 GHz SRF cavities with 31.5 MV/m acceleration field. A global international collaboration has been working on this project since two decades. The approach of CLIC is different. It adopts a drive beam scheme to produce the main LINAC Radio Frequency (RF). It has a design to operate in stages to reach 3 TeV energy.

The main advantages of a linear accelerator over a circular one [46] are (i) the absence of *synchrotron radiation*, discussed later in this section, and hence comparatively less electrical power consumption to reach the desired energy and larger $\sqrt{s}$ reach and (ii) easier longitudinal beam polarisation. The main challenge is the cost. It increases proportionally with the center-of-mass energy and hence with the length. For different physics programmes (at 250 GeV or 500 GeV) the costs of construction of LINACs and associated power consumption will increase. One of the limitations of a linear e^+e^- machine is the fact that it can not be used to smash protons at a later stage. Protons have to travel long enough through the machine to reach higher energies (around 100 TeV). To serve the purpose an estimated length of ILC is $\sim$ 3000 km which is not feasible. The independent focusing system with high degree of accuracy in calibration is another challenge for linear colliders.

Lepton collider	Centre-of-mass energy ($\sqrt{s}$) [GeV]	Dimension [Km]	Proposed location
ILC	250 GeV-1 TeV	20.5 (length)	Japan
CLIC	380 GeV-3 TeV	11-50 (length)	CERN
μ-collider	126 GeV-10TeV	0.3 (circumference)	CERN
FCC-ee	88-365 GeV	$\sim$ 100 (circumference)	CERN
CEPC	90-250 GeV	100 (circumference)	China

Table 3.1: Future linear and circular lepton collider candidates with planned centre-of-mass energies, dimensions and locations. The last two in the list can be upgraded to hadron machines, namely, FCC-hh and SPPC.

The future ***circular colliders*** are synchrotron accelerators, inspired by the LEP-LHC programme. These machines can work as precision instruments, like LEP, by colliding two lepton beams and later, in the same tunnel, as hadron colliders, like LHC, by colliding two proton beams. The two possible candidates are the Future Circular Collider (FCC) and the Circular Electron Positron Collider (CEPC) [47]/Super Proton Proton Collider (SPPC). It is important to understand the basic difference between a lepton (e, μ) and a hadron (proton) collider.

Leptons, being elementary particles, interact with precise initial states. So the energy involved in a collision is precisely known allowing to measure decay products accurately. So these machines (FCC-ee, CEPC) work as precision instruments. Whereas protons are composite particles made of partons (quarks, glouns). The center-of-mass energy of an interaction is only a fraction of the beam energies. The cross section of the interaction is determined by statistical distributions called as the *Parton Distribution Functions (PDFs)*. On the other hand, hadrons have advantages over leptons in high-

energy reach and new discovery. A charged particle while rotating in an orbit, radiates energy in proportion to the inverse fourth power of the mass of the particle:

$$\triangle E \cong \left(\frac{E}{m}\right)^4 \times \frac{1}{R} \tag{3.1}$$

where E is the energy of the particle and R is the radius of the orbit. This is called the *synchrotron radiation* loss. So, for a given radius of the collider, particles with lighter masses e.g. e^- or e^+ can not reach higher energies as it requires huge electrical power to compensate this loss. On the other hand, protons are 2000 times heavier than electrons. So this loss is reduced by a factor of $(2000)^4$ compared to that in electron machines. As a result, proton collisions can reach higher energies for same R of an electron machine and have potential for direct discoveries. On the other hand, because of the large value of R in FCC-ee and CEPC, $\triangle E$ will be moderate and the required electrical power will be affordable. Both FCC and CEPC/SPPC are designed to work in two stages: as lepton (e^+-e^-) colliders and as hadron (p-p) colliders with ∼100 TeV energy reach. All possible candidates for future lepton colliders with dimensions, operational range of the centre-of-mass energies and planned locations are listed in Table 3.1. The dependency of the integrated luminosity per beam power on the center-of-mass energy, for all proposed machines, are shown in Figure 3.1.

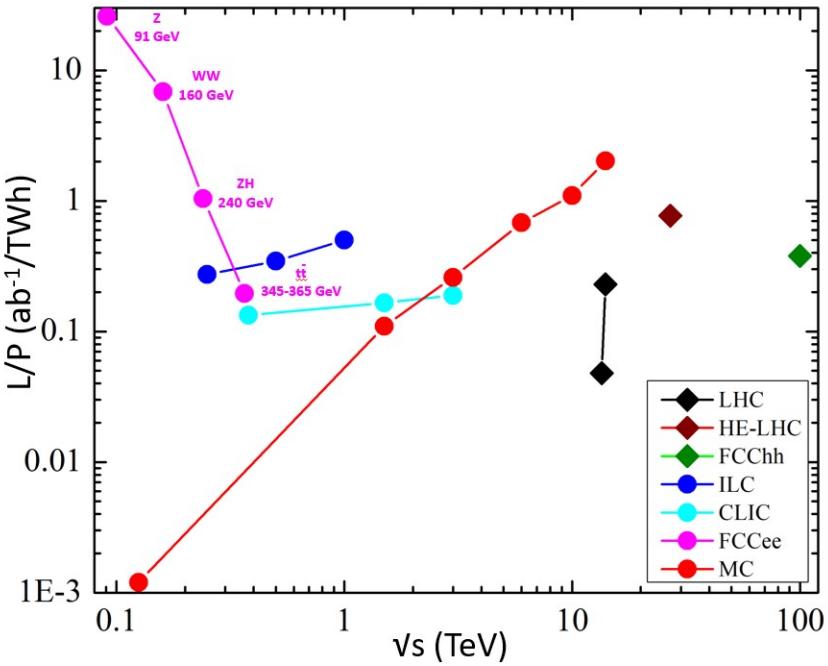

Figure 3.1: Integrated luminosity per beam power as a function of the center-of-mass energy for different linear and circular colliders - present, upcoming and future candidates. In the legend MC refers to the μ-collider. Ref. [48]

The main advantages of circular over linear e^+e^- machines are (i) much larger luminosity below $\sqrt{s} \approx 400$ GeV (Figure 3.1), because of much higher collision rates by adding continuous top-up injection to compensate for luminosity burn-off (i.e., the number of protons that are lost in collisions), (ii) a very precise measurement of the beam energy [49], and (iii) the possibility to collect more data by having several interaction

points. So these machines will be factories for mass-production of heavier particles, i.e., H, Z, W and t, of the SM. Also circular collider projects are being developed based on mature technology.

Option with muons
The fact that muon (μ) is 200 times heavier than e^- adds some attractive features to the μ-collider [48, 50, 51]. The synchrotron radiation loss is reduced by a factor of $(200)^4$ compared to that in e^- machines. The s-channel cross section of $\mu^+\mu^- \rightarrow$ H is also $(200)^2$ times larger than that of $e^+e^- \rightarrow$ H. In Figure 3.1 we can see the rising trend of the luminosity per beam power as a function of $\sqrt{s}$ for the μ-collider. Collisions of 14 TeV muons are comparable to 100 TeV proton collisions [48]. The larger mass makes muons interesting but unstable too, whereas an e^- lives forever. The need for high luminosity faces technical challenges which arise from the short muon lifetime and the difficulty of producing large numbers of muons in bunches with small emittance. A proton-driven μ-collider project, where muons are produced from pion decays, is under studies. The cooling procedure before the muons decay is its biggest challenge. In Low EMittance Muon Accelerator (LEMMA) project muons are produced with low emittance using positron beams. The cooling is not required and the beam background is lower. The muon current is $\mathcal{O}(10^{-3})$ smaller than that in proton scheme. Significant R&D is ongoing to reach an optimised design of the μ-collider that will be a very high energy lepton collider.

3.3 Future Circular Collider

FCC [52, 53, 54] is planned to be installed in a tunnel of about 100 km circumference at CERN. The idea is to take maximum benefits from the existing infrastructures (SPS, LHC, etc.). It will operate in two stages. The first, FCC-ee, is a luminosity frontier electron-positron collider for precision studies and the second, FCC-hh, is an energy frontier proton-proton collider for discovering new particles. High-temperature magnets are the key technology for the second stage. The larger magnets will fit in the 5.5 m inner diameter of the tunnel. Common experimental points are envisioned with large enough caverns from the beginning, i.e., stage 1, to house larger detectors of FCC-hh. FCC-ee and FCC-hh are highly synergic - these will share a common civil engineering and technical infrastructures as illustrated in Figure 3.2. The figure shows that the beams coming toward the IPs are straighter than the outgoing ones in order to reduce the synchrotron radiation at the IP. The 2020 Update of the *European Strategy for Particle Physics (ESPP)*[*] prioritised the necessity of an electron-positron circular collider as a first step towards highest energy hadron collisions and provided a momentum in this project by highlighting the necessity of high precision measurements of the properties of the Higgs boson. As a result, eventually, the FCC Feasibility Study has been launched in 2021 and will continue for 5 years. In case of approval the construction will start at the beginning of 2030s. FCC-ee will operate for 15 years from 2045 to 2060 and FCC-hh will start its operation around 2070 for the following 25 years. FCC-hh will be followed by FCC-eh (ep, ePb) allowing heavy-ion collisions

[*] https://europeanstrategy.cern/home

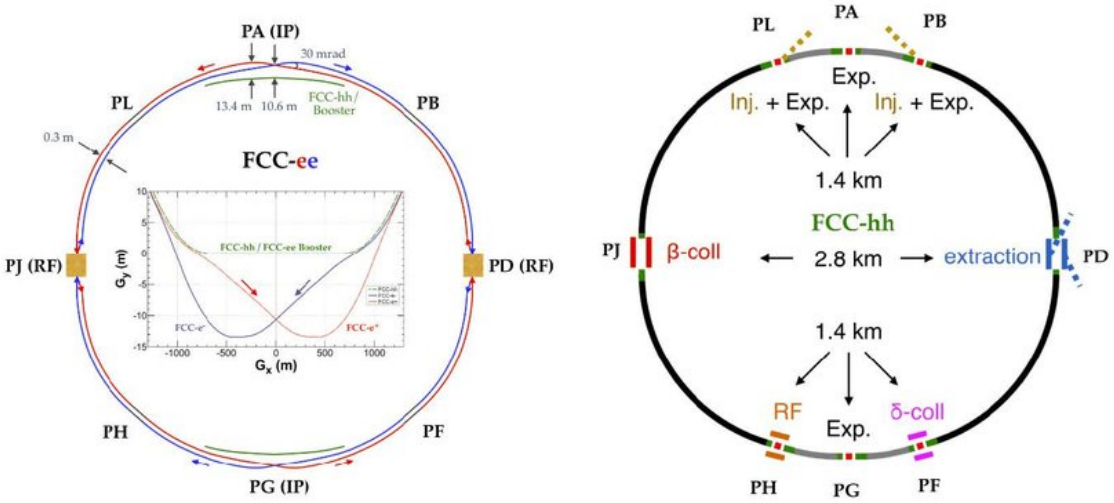

Figure 3.2: The layouts of FCC-ee (left), FCC-hh (right), and a zoomed view of the trajectories across the interaction point PG (left middle). In the arc the e^+ and e^- rings are horizontally separated by 30 cm. Ref. [52]

and electron-proton collisions at few TeV energies. So this facility has the potential to serve the particle physics community till the end of 21st century.

3.3.1 Programme at FCC

FCC-ee [55], along with the Higgs boson (∼125GeV), will also explore other heavier particles (Z, W, t) of the SM and will act as Higgs, ElectroWeak (EW) and top factories to study these particles with unprecedented precision. It will be designed to achieve the highest luminosity and will operate at different centre-of-mass energies for different programmes. In Table 3.2, the high statistics of produced particles (events/year) are listed along with the centre-of-mass energy, the target luminosity, the integrated luminosity and the run time to complete the W, Z, H and top-quark programmes. Two or four IPs are proposed for FCC-ee.

FCC-hh [57] will run with an order of magnitude performance increment than LHC that is running at 14 TeV and ∼0.4 ab^{-1} in integrated luminosity (per experiment over 15 years). So, these parameters for FCC-hh will be 100 TeV and ∼20 ab^{-1} (per experiment over 25 years), respectively. It has direct search potentials and can produce new particles with masses upto few tens of TeV. There will be a 100 times more Higgs events with respect to the number expected in the HL-LHC programme. All decay channels, in particular, $H \to \gamma\gamma$, $H \to ZZ^* \to 4l$, $H \to \mu^+\mu^-$, $H \to Z\gamma \to l^+l^-\gamma$ are foreseen to be investigated. Four IPs are proposed for FCC-hh.

3.3.2 Physics potential at FCC-ee

In this section, a brief overview of different measurements foreseen at FCC-ee will provide a flavour of its extraordinary physics potential [55, 56, 58].

High-precision EW and top physics

$\sqrt{s}$ [GeV]	90 (Z)	125 (eeH)	160 (WW)	240 (HZ)	350 ($t\bar{t}$)	350 (WW→H)
$\mathcal{L}$/IP $[cm^{-2}s^{-1}]$	$2.2{\cdot}10^{36}$	$1.1{\cdot}10^{36}$	$3.8{\cdot}10^{35}$	$8.7{\cdot}10^{34}$	$2.1{\cdot}10^{34}$	$2.1{\cdot}10^{34}$
$\mathcal{L}_{int}$ $[ab^{-1}$ $/yr/\text{IP}]$	22	11	3.8	0.87	0.21	0.21
Events/yr (4 IPs)	$3.7{\cdot}10^{12}$	$1.2{\cdot}10^{4}$	$6.1{\cdot}10^{7}$	$7.0{\cdot}10^{5}$	$4.2{\cdot}10^{5}$	$2.5{\cdot}10^{4}$
Time [yr] (4 IPs)	2.5	1.5	1	3	0.5	3

Table 3.2: Centre-of-mass energy, foreseen luminosity, integrated luminosity, statistics of produced particles (events/year) and run time for W, Z, H and top-quark programmes at FCC-ee. Ref. [56]

FCC-ee will collect multi-ab^{-1} (Table 3.2) of data at $\sqrt{s} \approx 91$ GeV (Z pole), 160 GeV (WW threshold), and 350 GeV ($t\bar{t}$ threshold) in order to measure key properties of the W and Z bosons and of the top quark, as well as other fundamental SM parameters, with unprecedented precision. Numerically, FCC-ee is foreseen to deliver $\sim 10^5$ times the luminosity collected by LEP at the Z pole, i.e., about 1.5×10^{11} $Z \to \mu^+\mu^-$ or $\tau^+\tau^-$ decays and 3×10^{12} hadronic Z decays. The huge data samples available at each $\sqrt{s}$ and the exquisite control of the centre-of-mass energy (at the ± 100 keV level) leading to very accurate energy threshold scans, allows the experimental precision of many SM parameters to be improved by a factor better than 25 with respect to the current state of the art [56]. Some experimental precision targets at FCC-ee are ± 100 keV for m_Z, ± 500 keV for m_W, ± 10 MeV for m_t, $3{\cdot}10^{-5}$ for QED coupling α, one-permil for the QCD coupling α_s etc. These levels of precision can not be achieved at the LHC or other e^+e^- machines. Physics Beyond Standard Model (BSM) can therefore be probed, indirectly, through loop corrections induced by possible new heavy particles [55]. At LEP, BSM physics were bound at the New Physics (NP) scale $\Lambda \approx 7$ TeV, whereas FCC-ee will have a reach of up to $\Lambda \approx 100$ TeV for some operators. High luminosity $e^+e^- \to Z$ can produce 15 times the statistics of Belle-II, for what concerns the B physics. Eventually, FCC-ee can cover the full programme of Belle-II and LHCb [59].

High-precision Higgs physics

The Higgs sector of the SM can be probed at FCC-ee with a unique precision. The Higgs production cross-section peaks at $\sqrt{s} = 240$ GeV dominated by Higgs-strahlung ($e^+e^- \to HZ$). At $\sqrt{s} \approx$ 340-365 GeV, Higgs production can occur by vector boson fusion ($e^+e^- \to (VV \to H)\nu_e\bar{\nu}_e$) and the top Yukawa coupling ($e^+e^- \to t\bar{t}$, with a virtual Higgs exchanged among the top quarks). The Feynman diagrams for the Higgs-strahlung and the vector boson fusion, the two most important mechanisms for Higgs production at FCC-ee, are shown in Figures 3.3a and 3.3b, respectively. The total cross section as a function of $\sqrt{s}$ for these two processes is displayed in Figure 3.4. The foreseen Higgs production at FCC-ee amounts to ~2 million at 240 GeV, 75 000 in vector boson fusion at 350 GeV, 19 000 in the s-channel ($e^+e^- \to H$) at $\sqrt{s} = 125$ GeV

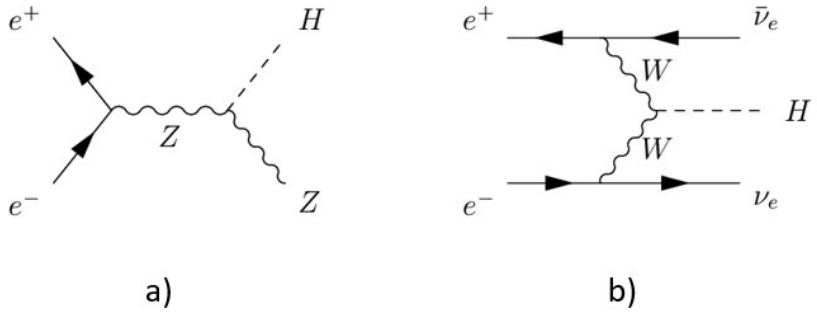

Figure 3.3: Higgs production channels at FCC-ee: Higgs-strahlung (a) and WW fusion (b).

(Table 3.2). The large data samples will allow a unique investigation of Higgs physics topics, e.g., high-precision model-independent determination of the Higgs couplings, Higgs self-coupling through loop corrections in HZ production, etc., to be carried on.

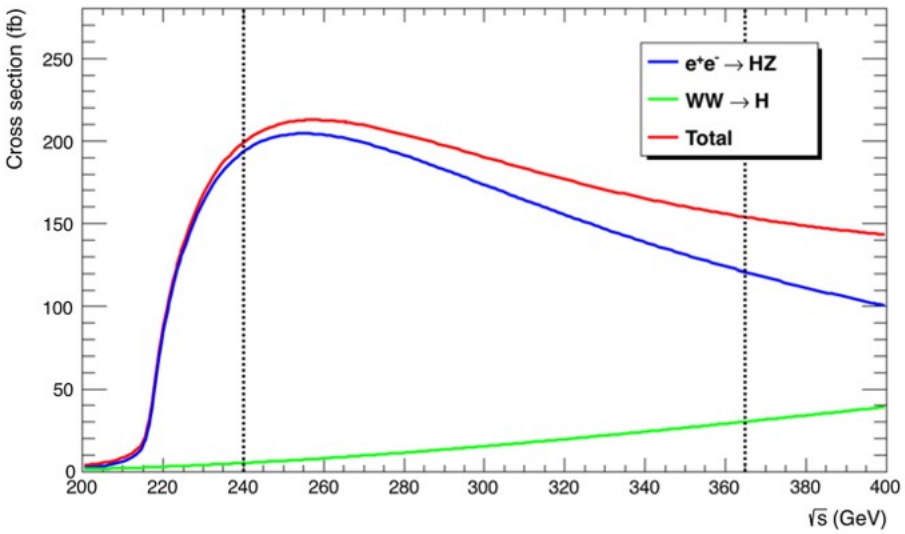

Figure 3.4: The Higgs boson production cross section as a function of the centre-of-mass energy in unpolarised e^+e^- collisions. The blue and green curves represent the Higgs-strahlung and WW fusion mechanisms, respectively, whereas the red one stands for the total production cross section. The two vertical dashed lines indicate the centre-of-mass energies of choice at the FCC-ee for the measurement of the properties of the Higgs boson. Ref. [55]

The total Higgs production cross section is determined from counting $e^+e^- \to ZH$ events tagged with a leptonic Z decay, independently of the Higgs boson decay ($ZH \to \ell^+\ell^- X$). Such an event with $Z \to \mu^+\mu^-$ and the Higgs boson decaying hadronically is displayed in Figure 3.5a. The mass (m_{Recoil}) of the system recoiling against the lepton pair can be measured with precision from the lepton momenta and the total energy-momentum conservation:

$$m^2_{Recoil} = s + m^2_Z - 2 \cdot \sqrt{s} \cdot E_Z \tag{3.2}$$

where $\sqrt{s}$ is the centre-of-mass energy while m_Z and E_Z are the mass and energy of the Z boson reconstructed with the two lepton tracks. m_{Recoil} of the system is equal to the Higgs boson mass and can be measured as shown in Figure 3.5b. This allows a precise determination of the HZ cross section (σ_{HZ}) in a model-independent fashion. Under the assumption that the coupling structure is identical in form to the SM, this cross section is proportional to the square of the Higgs boson coupling to the Z (g^2_{HZZ}). The Higgs boson width can then be inferred by counting the number of HZ events with $H \to ZZ$. Under the same assumption, this number is proportional to $\sigma_{HZ} \times \Gamma_{H\to ZZ}/\Gamma_H$, hence to g^4_{HZZ}/Γ_H. Therefore, Γ_H is extracted from the measurement of g_{HZZ}. A segmented crystal calorimeter may play a crucial role in determining the recoil mass resolution of $Z \to \ell^+\ell^-$ decays. A comparison of the foreseen relative uncertainties for the Higgs boson couplings at HL-LHC, ILC and FCC-ee is shown in Figure 3.6.

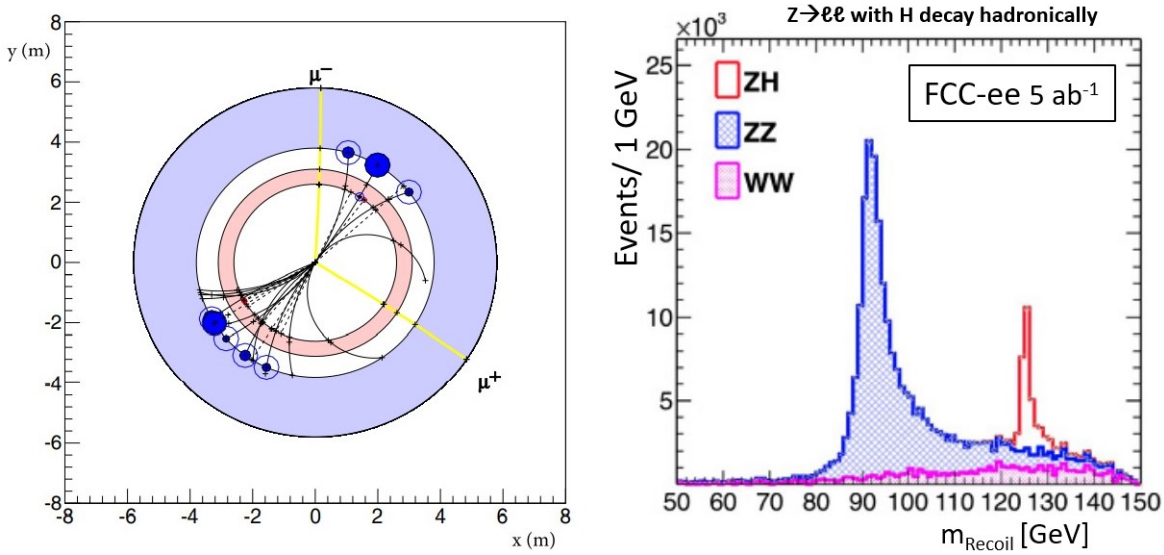

Figure 3.5: A schematic view, transverse to the detector axis, of an $e^+e^- \to$ HZ event with $Z \to \mu^+\mu^-$ and with the Higgs boson decaying hadronically (a). Distribution of recoil mass against $Z \to \mu^+\mu^-$ determined from total energy-momentum conservation, with an integrated luminosity of 500 fb^{-1}. The peak around 125 GeV (distribution in red) consists of HZ events. The backgrounds (distributions in blue and pink) originate from ZZ and WW production (b). Ref. [55]

Loop corrections to the Higgs-strahlung cross sections at different centre-of-mass energies are sensitive to the Higgs self-coupling. The effect is tiny but visible at FCC-ee. At the energy frontier, only the FCC-hh has the potential to reach a precision of the order of ±5% in the determination of the trilinear g_{HHH} coupling, in combination with the precise Higgs decay branching ratio and top-quark EW coupling measurements from the FCC-ee. The large Higgs data samples open up the way for studies of exotic (e.g. flavour-violating Higgs decays) and very rare SM decays. The Higgs couplings to the first- and second-generation fermions, that may reveal new dynamics on the flavour structure of the SM, can be accessed via the exclusive decays $H \to V\gamma$ (vector meson, $V = \rho, \omega, \phi$), with sensitivity to the u, d, s quark Yukawa couplings [60]. The most promising channel is $H \to \rho\gamma$, with $\mathcal{O}(50)$ events expected.

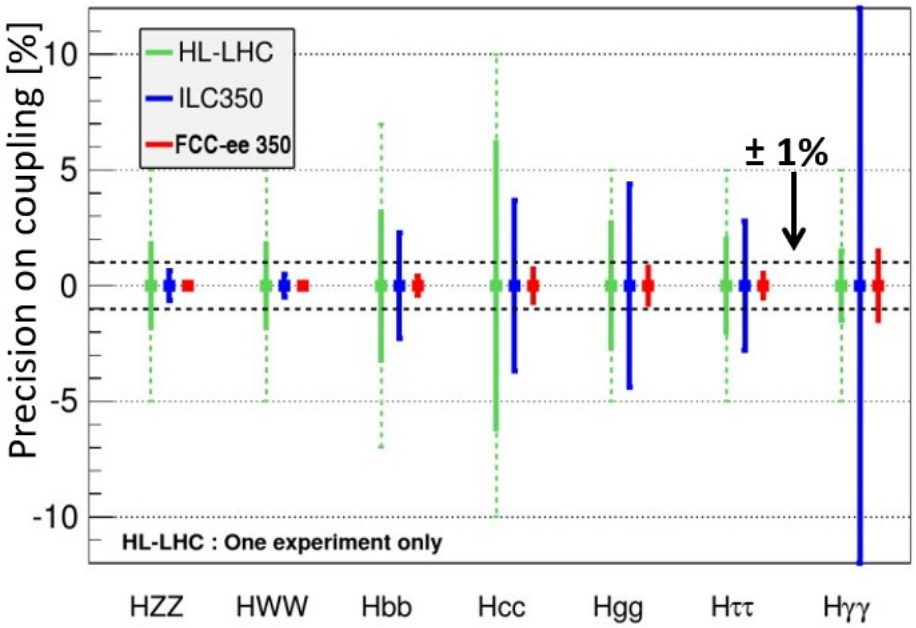

Figure 3.6: Comparison of the expected relative uncertainties for the Higgs boson couplings at HL-LHC, ILC and FCC-ee facilities. Ref. [56]

Direct searches : Dark Matter and Heavy Neutral Leptons
FCC-ee has a strong discovery potential in direct collider searches of possible BSM signatures such as Dark Matter (DM) and right-handed neutrinos i.e., Heavy Neutral Leptons (HNL) [56]. The invisible and very rare decay, Z,H $\rightarrow$ DM DM, provides the best collider option to test DM lighter than $m_{Z,H}/2$. Similarly, measurements of rare decays of the Z boson will enable direct searches for right-handed neutrinos with masses below 60 GeV.

On the other hand, the main goal of the FCC-hh [57] collider is to push the energy-frontier for direct searches. Apart from measuring the Higgs self-coupling, it will explore the dynamics of the EW symmetry breaking. The high-statistics programme will allow to search for decays with violations of the lepton number conservation, for H/Z invisible decays and for decays where Weakly Interacting Massive Particles (WIMPs) are produced. WIMPs can be linked to DM, neutrino masses or baryon asymmetry. The FCC-hh may say final words about the thermal DM candidates - they either should be discovered or ruled out. Single HNL produced in W or Z decays will also be studied at FCC-hh.

3.3.3 Detector requirement

The precision physics programme at FCC-ee demands stringent requirements [61, 62] for detector performances. The performance of heavy-flavour tagging, of particle identification, of tracking and particle-flow reconstruction, and of lepton, jet, missing energy and angular resolution, need to match the physics programme and the exquisite statistical precision offered by FCC-ee. For tracking performance a large solid angle coverage

for Higgs decay products are needed as these are uniformly distributed over the full solid angle because the scalar nature of Higgs boson. The requirements on the resolutions on the track impact parameter are currently estimated to be about, or better than $\sigma = a \bigoplus b/sin^{3/2}\theta$, where θ is the polar angle from the beamline, a ≈ 5 μm and b ≈ 15 μm. In addition to the measurement of the Higgs couplings to pairs of b quarks, c quarks and gluons (high-performance flavour tagging) requirements on the vertex detector will come from the measurement of heavy-quark electroweak observables for which a huge improvement is expected compared to LEP. These measurements will benefit from the large luminosity increase and improved detector technology.

The photon energy resolution of $\sim \frac{15\%}{\sqrt{E}}$ is required for measuring $H \to \gamma\gamma$ channel. Since about 25% of the jet energies is carried by photons, a good energy resolution, a stochastic term of 15–20% for a resolution better than 3% for 50 GeV jets, for photons is needed for a good measurement of jets. It is important to fully explore the hadronic decays of Z, W and H. To clearly discriminate $H \to ZZ^* \to 4j$ and $H \to WW^* \to 4j$ final states a jet energy resolution of $\sim \ 30 - 40\%\sqrt{E}$ is needed. This improvement by a factor of 2 with respect to the traditional hadronic calorimeters running at LHC machines is challenging.

A good separation of e/γ , γ/π^0, e/π, and an excellent separation of photons from neutral hadrons are key ingredients for an effective particle-flow reconstruction. The critical requirements, with the associated detectors, are listed in Table 3.3.

Benchmark physics process	Measured quantity	Required performance	Critical detector
$ZH \to \ell^+\ell^-$X	m_H, cross section	$\Delta(\frac{1}{p_T}) \sim 2 \times 10^{-5} \bigoplus \frac{1\times10^{-3}}{p_T sin\theta}$	Tracker
$H \to \mu^+\mu^-$	BR($H \to \mu^+\mu^-$)		
$H \to b\bar{b}, c\bar{c}, gg$	BR($H \to b\bar{b}, c\bar{c}, gg$)	$\sigma_{r\phi} \sim 5 \bigoplus \frac{10}{psin^{3/2}\theta}\mu$m	Vertex
$H \to \gamma\gamma$	BR($H \to \gamma\gamma$)	$\frac{\sigma_E}{E} = \frac{15\%}{\sqrt{E}} \bigoplus 1\%(GeV)$	ECAL
$H \to ZZ^* \to 4\ell$	BR($H \to ZZ^* \to 4\ell$)	$\frac{\sigma_{E_{jet}}}{E_{jet}} \cong \frac{30\%}{\sqrt{E_{jet}}}$	ECAL
$H \to WW^* \to 4\ell$	BR($H \to WW^* \to 4\ell$)		HCAL

Table 3.3: Detector requirements, with respect to some benchmark physics processes, at FCC-ee.

3.4 IDEA

CLIC-Like Detector (CLD) [63] and Innovative Detector for Electron-positron Accelerator (IDEA) are the two detector concepts that have been envisaged for evaluating

detector performances, cost estimation and technical feasibility at future circular lepton colliders i.e., FCC-ee and CEPC. They are typical detectors used in collider experiments, with a cylindrical barrel region closed at the extremities by two endcaps, and with an onion-like structure consisting of sub-detectors. IDEA [64] is proposed in the Conceptual Design Report (CDR) of FCC and CEPC. The concept is innovative but has been developed based on proven technologies over years of R&D and prototyping. IDEA approaches to optimise standalone hadronic resolution by sampling the showers with fibres exploiting the DRO method. On the other hand, CLD, based on the work done for a detector for the CLIC collider, aims to explore the particle flow approach i.e., to optimise the calorimeter granularity and complement energy measurements with tracking information.

CLD is composed of silicon pixel vertex detector, silicon trackers, highly granular calorimeter (tungsten-silicon ECAL, steel-scintillator Hadron CALorimeter (HCAL), superconducting solenoid (2T), yoke and muon detectors made of Resistive Plate Chambers (RPCs).

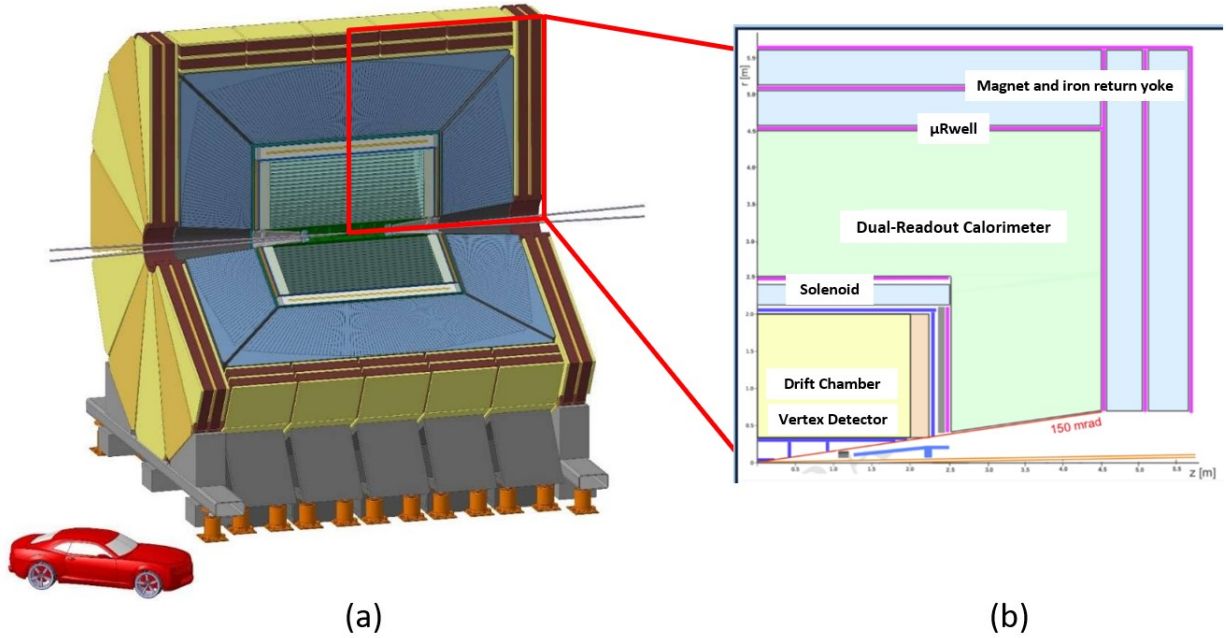

Figure 3.7: Isometric view of IDEA - more than one quarter removed (a). A vertical cross section showing the top right quadrant (b).

An isometric view of IDEA is shown in Figure 3.7a. A concise description of its sub-detectors is pictured here.

- The innermost silicon vertex detector [65] is based on Monolithic Active Pixel Sensors (MAPS) technology. It has a thickness of 0.15-0.30% X_0, a low-power dissipation of 20 mW/cm^2 and a high-resolution of a few μm. The state-of-the-art is adapted from ALICE inner tracker upgrade. Also INFN ARCADIA[†] has performed several R&D activities on this type of detectors.

- An ultra-light drift chamber [65] surrounded by silicon micro strip wrapper will serve the tracking purpose. To minimise multiple scattering in order to perform

[†]INFN CSN5 Call Project

best possible momentum measurements only 2% X_0 material is added in the volume. A very light gas mixture (90% Ar 10% iC_4H_{10}He) fills the chamber. The maximum drift timing is $\sim$ 400 ns. Cluster counting/timing technique improves PID (K/π separation).

- A 5m long, 4.2 m inner diameter, ultra-light (30 cm radial envelop) 2T solenoid [65] surrounds the tracking system. With these dimensions, a yoke thickness of less than 100 cm of iron is sufficient.

- Preshower detectors made of μ-RWELL chambers [66], a Micro Pattern Gaseous Detector (MPGD) technology, are placed before IDEA calorimeter. In barrel region magnet coils amount to 0.7 X_0 absorber and a layer of μ-RWELL chambers sit immediately after to detect the signals. In endcaps 1 X_0 Pb absorber and a layer of μ-RWELL chambers compose the preshower detectors.

- Fibre-sampling, capillary based, DRO tower structures constitute the IDEA calorimeter [67]. Capillary tubes made of copper and scintillation and clear fibres are cho-

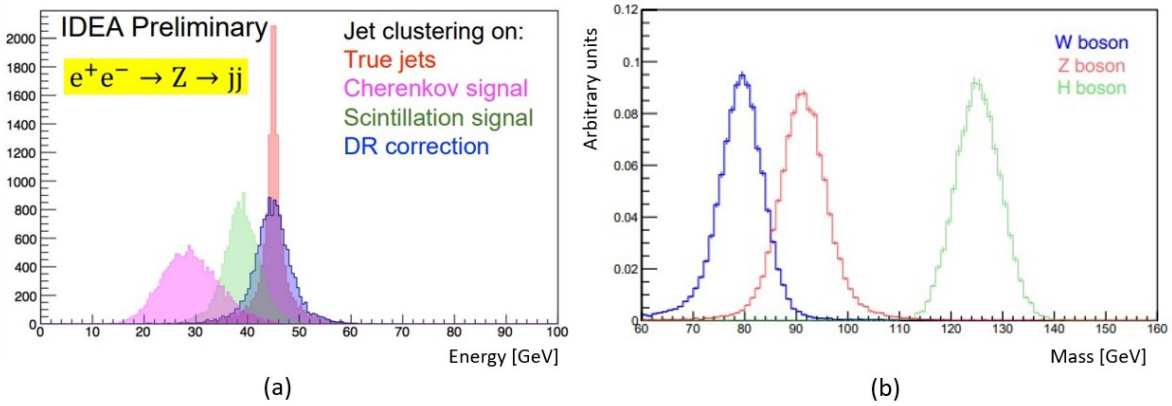

Figure 3.8: IDEA calorimeter standalone simulation studies. Jet energy reconstruction with DRO method (a). Ref. [65]. Separation of peaks of the W and Z bosons (b). Ref. [67].

sen as passive and active materials, respectively. The calorimeter, that surrounds the preshower, can measure, simultaneously, the electromagnetic and hadronic components of particle showers. It foresees a good EM energy resolution of $\sim$10%/$\sqrt{E}$ and a good resolution around 30%/$\sqrt{E}$ for hadronic jets. Figures 3.8a and 3.8b illustrate jet energy reconstruction with DRO method and separation of the W and the Z bosons, respectively, obtained by IDEA calorimeter standalone simulation studies. The transverse granularity of around 1 mm allows for a good separation capability also in the case of two close showers generated by the decay of neutral pions ($\pi^0 \to \gamma\gamma$). Figure 3.9 represents simulation studies that show the separation of two closely spaced showers produced by two γ's. The option of incorporating a homogeneous DRO ECAL section made of crystals is also largely considered [67, 68]. While the fibre-sampling DRO HCAL allows to maintain the hadronic energy resolution, the crystal option allows to improve the EM energy resolution.

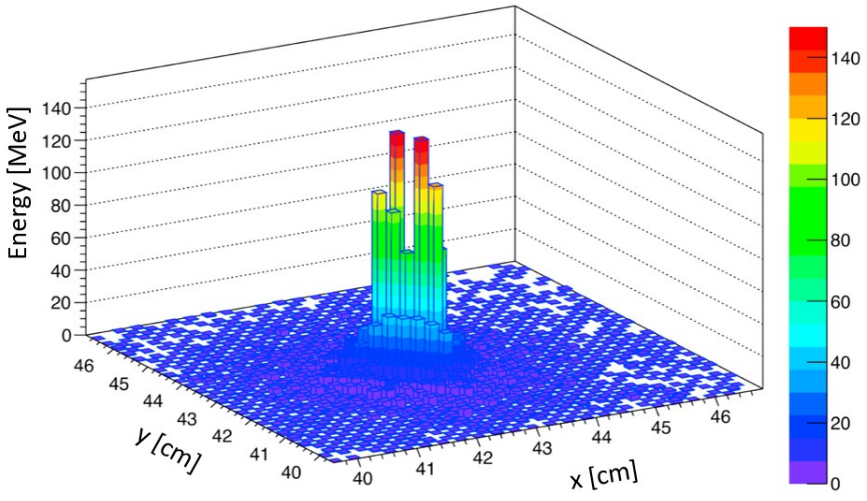

Figure 3.9: IDEA calorimeter standalone simulation studies. Event displays of two closely spaced showers produced by two γ's from the decay of 100 GeV π^0. Ref. [13]

- To cover large areas for muon systems, μ-RWELL detectors [66] have been chosen as a cost-effective solution. It provides good tracking efficiency, precise spatial and time resolution.

Chapter 4

Novel capillary-based tower structures

An EM-scale calorimeter has been built, partially in Pavia, during the end of 2020 and the beginning of 2021. The motivation to construct this module, instead of a hadronic-scale one, has been to establish the proof-of-concepts for the construction technique of a capillary-based tower structure and for building a highly granular module with SiPM sensors. The EM-scale tower structures is a potential first step towards a capillary-based, DRO, fibre sampling calorimeter for the IDEA detector at future circular e^+e^- collider facilities.

In Sections 4.1, 4.2, 4.3, and 4.4.1 design and dimension of the EM-scale calorimeter, its Quality Assurance and Quality Control (QAQC) tests, readout and mechanical construction in Pavia are described, respectively. On the other hand, in Section 4.4.2, the ongoing activities on the production of scaled-up significant containment module is reported.

4.1 Design and Dimension

The EM-scale calorimeter is an assembly of 2880 capillary tubes. Each capillary tube, made of Brass (CuZn37), has an inner diameter of 1.1 mm with tolerance of + 0.1 mm and - 0 mm and an outer diameter of 2 mm with tolerance of ± 0.05 mm. As a consequence of capillary dimensions the sampling fraction of ∼3% is slightly worse than that of RD52 modules [32, 36] and the small Brass module with SiPM sensors [39]. The EM-scale module consists of nine towers forming a 3×3 matrix in the transverse plane of the detector. It has a transverse cross section of ∼(10×10) cm^2, where each tower is ∼(3.5×3.3) cm^2. The eight surrounding towers are 1 m long, whereas the central tower is 1.2 m long on purpose as described in Section 4.4.1. The module constitutes of ∼2·R_M, where R_M is 23.8 mm and ∼44·X_0 for surrounding towers and ∼53·X_0 for the central tower, where the effective X_0 is 22.7 mm.

Each tower, that produces two independent signals formed by scintillation light and Cherenkov light, consists of 2 × 160 capillary tubes loaded with plastic scintillation fibres and clear fibres, that act as active media. 320 capillaries, arranged in a staggered architecture of 20×16 matrix, distribute the same type of fibres in alternate layers forming 10 rows for each type of channel as shown in Figure 4.1. The tube pitch, 2

mm, is the side of an equilateral triangle, whereas the distance between two consecutive sampling layers is determined by the height ($\frac{\sqrt{3}}{2} \cdot side \sim 1.73$ mm) of the triangle as illustrated in the inset image of Figure 4.1.

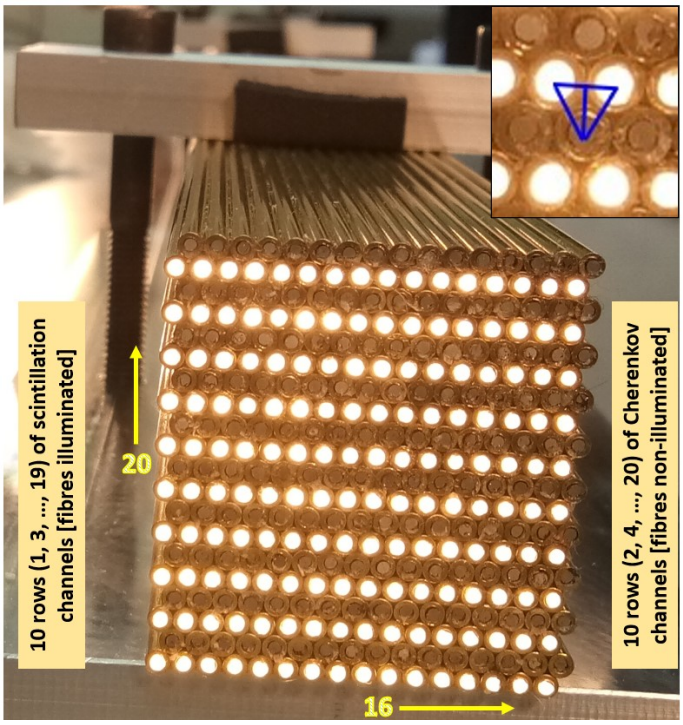

Figure 4.1: A single tower loaded with two types of fibres inside brass capillary tubes in a 20 × 16 staggered arrangement. 160 fibres in ten rows of scintillation channels are illuminated from rear end. The inset image shows that the geometrical dimensions of the staggered structure, tube pitch of 2 mm and distance between sampling layers of ∼1.73 mm, have been calculated by drawing an equilateral triangle.

4.2 Quality control

The tower structures were primarily constructed at Ruđer Bošković Institute (RBI), Zagreb. The brass capillary tubes were glued together with radiation resistant epoxy to form the tower structures. An extensive description of the procedure taken place at RBI for assembling the capillaries and the corresponding measurements can be found in Ref. [69]. Dimensions, deformation and twisting of the tower structures were measured in Pavia as a step of quality control. These measurements were performed with high-performance linear height gauge*. These measurements were taken on a granite planar table. The height of a ceramic gauge block, while placed on this planar table, was calibrated to zero and it was the reference for our measurement system. In particular, following quantities were measured on individual tower:

- Dimensions (both height and width).

*https://www.mitutoyo.com/products/small-tool-instruments-and-data-management/height-gages-2/

- Bending.
- Torsion.

For surrounding towers, height and width measurements were taken at 12 different points on each side. For the 20 cm extra long central tower this number was 15. The mean height and width of each tower are calculated as shown in Figure 4.2. The measurements on one side of the central tower are shown in Figure 4.3. The nominal values of heights and widths of the towers were calculated to be 34.91 mm and 33.00 mm, respectively. A maximum variation in tower to tower dimension of 220 μm was measured. The maximum standard deviation in measurements of any individual tower was 50 μm that guaranteed the required mechanical precision of the prototype detector. Obtained numbers from these measurements are reported in Table 4.1. These values are compatible with expected values and show a good dimensional uniformity throughout all tower structures. Figures 4.4a and 4.4b gives an overview of these measurements.

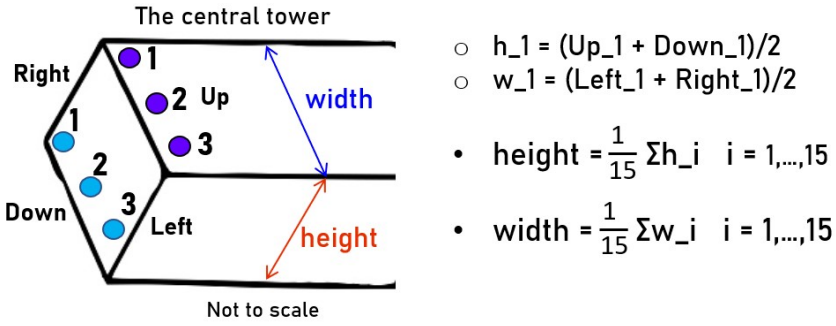

Figure 4.2: 30 measurements are taken on both sides of the central tower to calculate the mean height as well as the mean width.

Tower	mean height(mm)	RMS(mm)	mean width(mm)	RMS(mm)
nominal	34.91	-	33.00	-
T0	34.95	0.05	33.01	0.03
T1	35.00	0.05	33.07	0.02
T2	34.98	0.04	33.07	0.04
T3	34.96	0.04	33.06	0.02
T4	34.92	0.05	33.25	0.05
T5	34.95	0.05	33.23	0.10
T6	35.08	0.04	33.18	0.04
T7	35.08	0.03	33.19	0.04
T8	35.14	0.05	33.21	0.05

Table 4.1: Dimension measurements of nine tower structures.

Deformation and twisting of the towers, along heights as well as widths, were also measured. Bending, a measure of deformation, is the difference between the maximum and the minimum values taken on either sides. Torsion, a measure of twisting, is the

difference between average values at two diagonal corners. The mean values turned out to be a few hundreds and a few tens of μm, respectively, for bending and torsion. The values are reported in Table 4.2. Finally, nine towers were arranged in such a way that maximum uniformity in heights and widths could be achieved for the whole module before interlocking the towers.

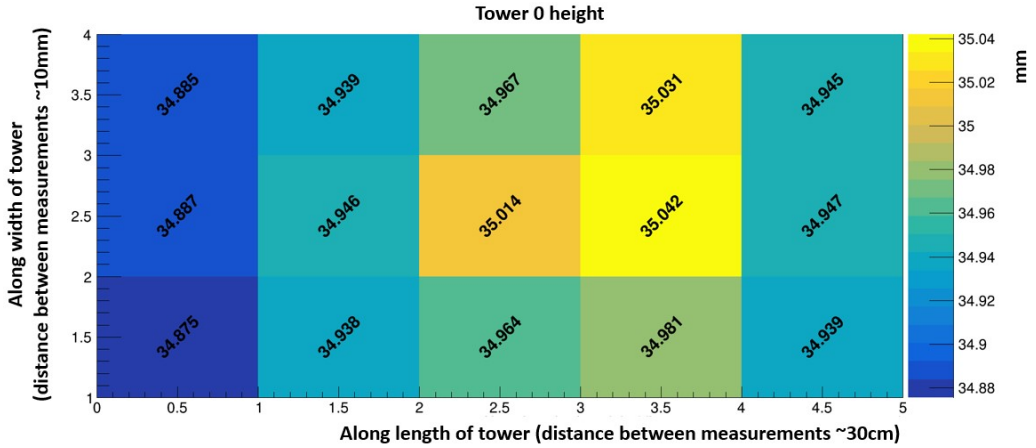

(a)

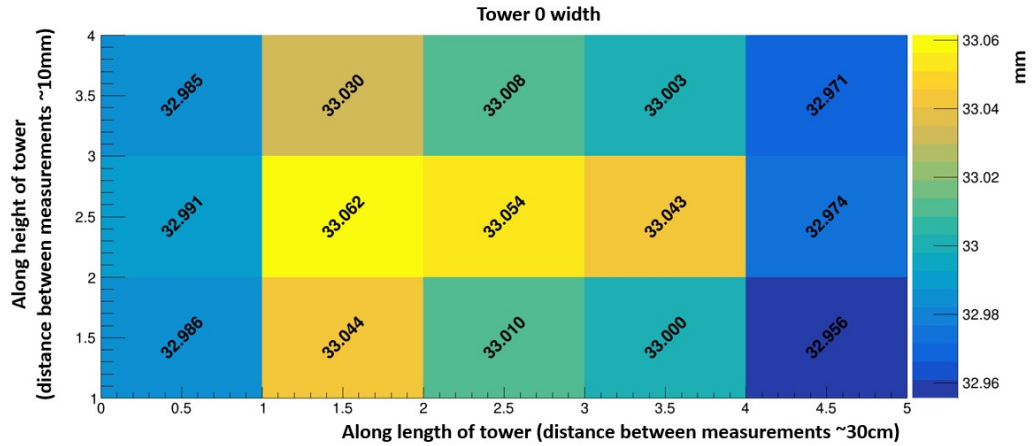

(b)

Figure 4.3: Height (a) and width (b) measurements at 15 points on one side of the central tower.

4.3 Readout

Position sensitive R8900 and extended UV sensitive R8900-100 PMTs from Hamamatsu [70], with tapered voltage-divider bases (Figure 4.5 inset image), were used to read eight surrounding towers. Sixteen PMTs were mounted forming eight scintillation and eight Cherenkov channels. Before mounting, PMTs were qualified in Pavia. An experimental set up (Figure 4.5) was prepared in order to perform linearity tests for PMTs. The

Tower	height		width	
	bending(μm)	torsion(μm)	bending(μm)	torsion(μm)
T0	160	6	119	51
T1	154	20	128	26
T2	121	28	159	1
T3	113	2	129	9
T4	149	62	285	27
T5	158	15	288	104
T6	161	14	121	6
T7	148	54	125	24
T8	265	81	136	10

Table 4.2: Bending and torsion measurements along heights and widths.

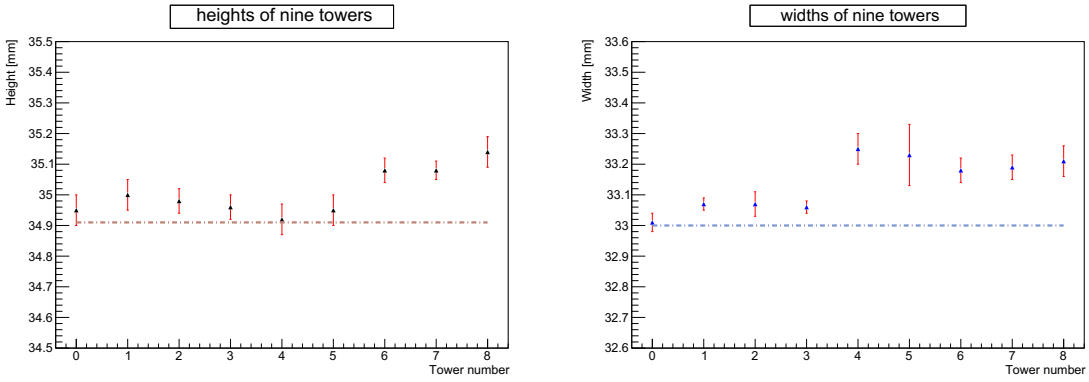

(a) (b)

Figure 4.4: Mean heights (a) and mean widths (b) of the nine tower structures. The horizontal lines refer to the nominal values.

light, produced by a light source (M10306-30)[†] and propagated through an optical fibre, was received by a PMT window. In this chain a software-controlled attenuator was used to tune the light intensity. The signal at PMT output was measured with an oscilloscope. The signal amplitude as a function of ten different values of the attenuator, i.e., corresponding light intensities ($I = I_0 \cdot 10^{-dB/20}$ [in arbitrary unit]) were measured. These measurements were repeated for three operating high voltages (550, 600, 650 V) of the PMT. Figure 4.6 shows three sets of measurements for a particular PMT. These measurements were performed for all sixteen PMTs. PMTs were found to be linear within 1%.

Kodak Wratten 2 nr. 3 yellow filters with optical coupling compounds on both sides were mounted between Scintallation fibre bundles and PMT windows to cut off the yellow component of light that were more affected by attenuation in fibres. An attenuation plot of these filters is shown in Figure 4.7. Figure 4.8 shows the module

[†] https://www.hamamatsu.com/content/dam/hamamatsu-photonics/sites/documents/99_SALES_LIBRARY/sys/SOCS0003E_PLP-10.pdf

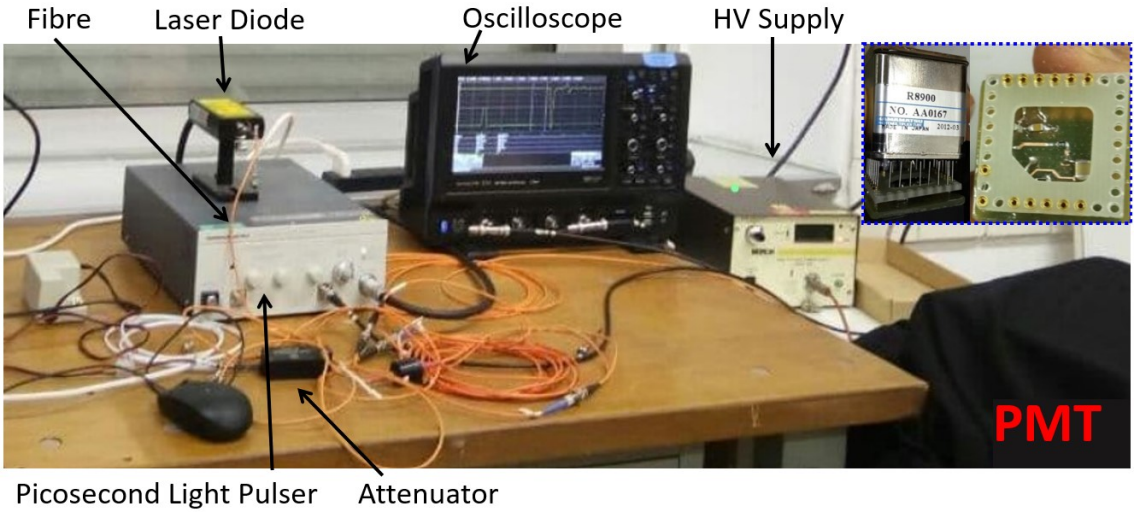

Figure 4.5: The experimental set up for qualifying the PMTs in Pavia laboratory. One R8900 PMT with its tapered base is shown in the inset image.

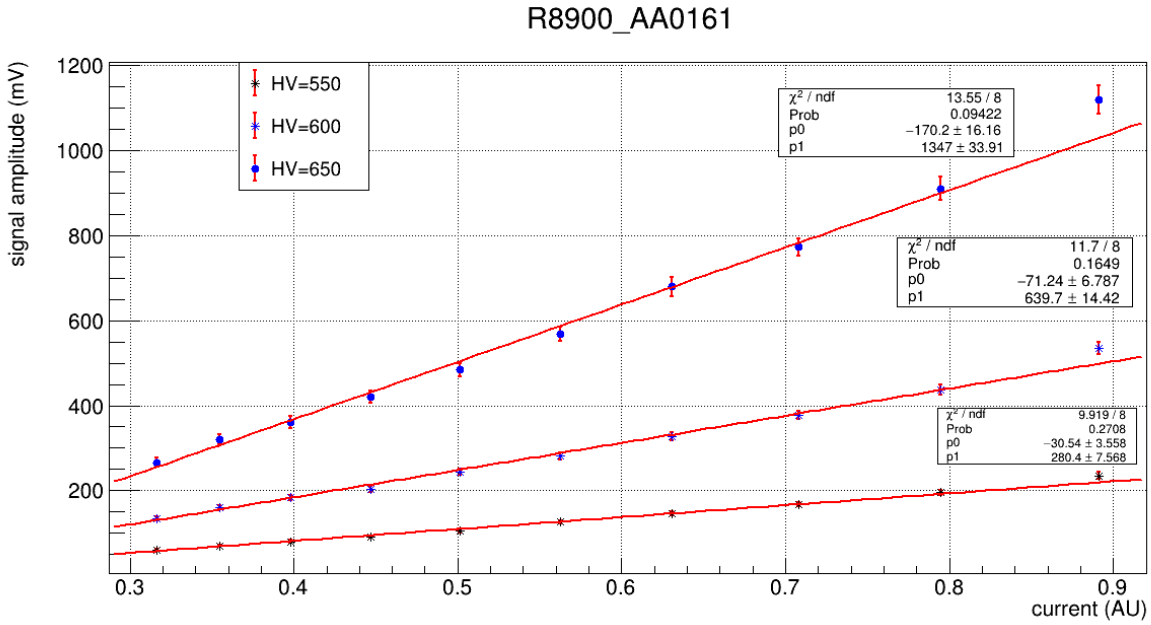

Figure 4.6: Measurement of the signal amplitude of a PMT as a function of the light intensity.

Operating HV [V]	550	600	650
p1 [mV/AU]	280.4 ± 7.6	639.7 ± 14.4	1347.0 ± 33.9
p0 [mV]	-30.5 ± 3.6	-71.2 ± 6.8	-170.2 ± 16.2

Table 4.3: The fitting parameters of Figure 4.6 for the measurements of the signal amplitudes as a function of the light intensities controlled by the attenuator for a R8900-type PMT.

coupled with PMTs. 16 PMT outputs were fed to two Front End Electronics (FEE) boards mounted on two patch panels. Fibres coming out of the central tower were shielded inside a coverage (Figure 4.8 inset image) to be protected from accidental damage by PMT cabling.

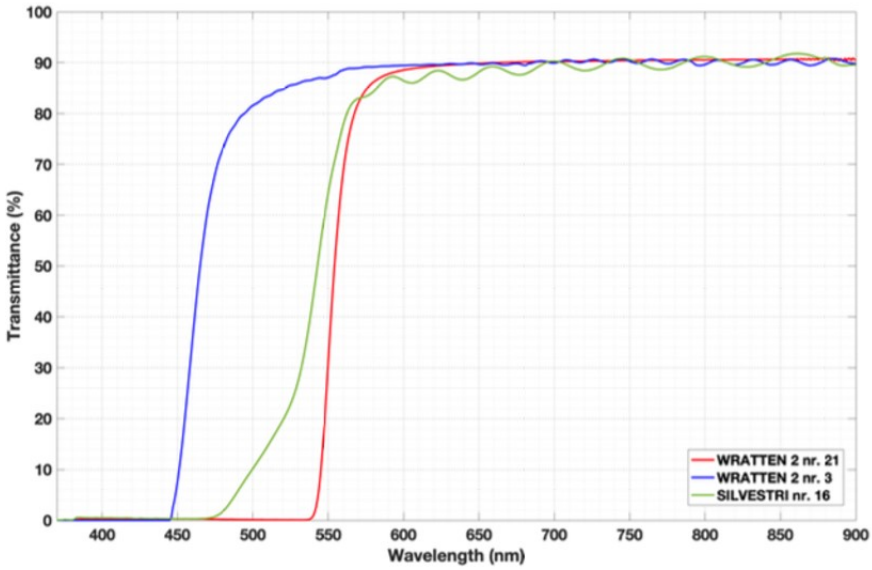

Figure 4.7: The transmittance as a function of wavelength for Kodak Wratten 2 nr. 3 is shown (curve in blue). Ref.[71]

Figure 4.8: Sixteen PMTs are mounted on the module. Patch panels and electronic boards are not yet mounted. The inset image shows the isolation of central tower fibres from PMT cabling.

SiPMs were chosen to read out the central tower that has been configured as a highly

granular tower. Each fibre of this tower, coupled to a single SiPM sensor, was read out independently. The aim was to test an innovative readout technique for large number and high density of channels. In the previous prototype of dimension $\sim (1.5\times1.5\times100)$ cm^3 [39], SiPM sensors, with a dynamical range of $\mathcal{O}$(1k) and of 25 μm cell size, were used. It was definitely too limited, because 10% of the EM shower energy comes from the very core of the shower, i.e., within $\sim$ few mm from the shower axis. This time the new SiPM sensors (S14160-1315 PS) from Hamamatsu had a dynamic range of about a factor 5 larger (7800 cells/sensor vs. 1584 cells/sensor) and a cell size of 15 μm. At the time of integration, dimensions of available packages of SiPM sensors that came with 15 μm pixel size, were not compatible with fibre pitches. This problem was addressed by increasing the fibre pitches, thanks to the adoption of an interface. The design is illustrated in the description of detector construction (Section 4.4). Figure 4.9 illustrates a mechanical drawing of the design of the full module which shows two separate spaces allocated for the readouts of PMTs and SiPMs.

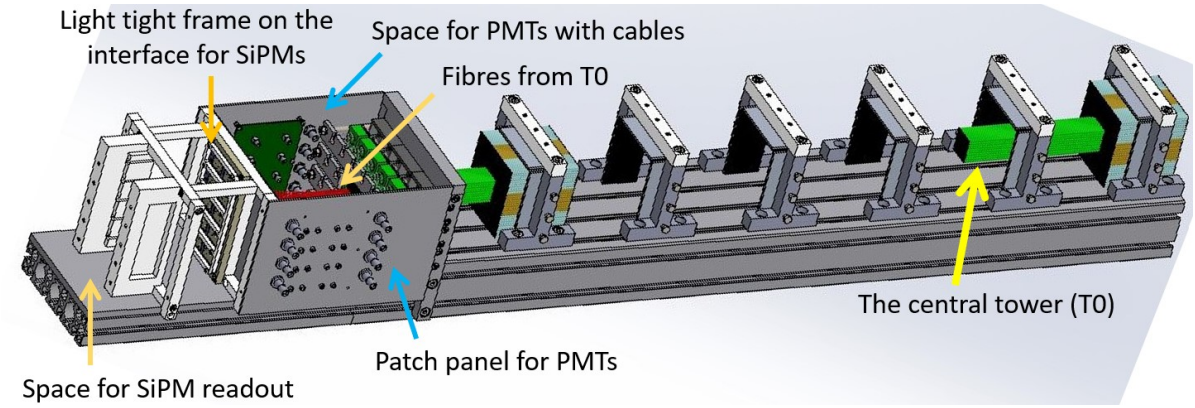

Figure 4.9: A mechanical drawing of the design of the EM-scale calorimeter prototype. The extra long central tower (in green) is indicated. The fibres from the central tower (in red) reach the FEE boards for SiPMs through the space allocated for PMTs and their cabling.

Five FEE boards, each having 64 SiPMs, were attached to the interface of the central tower. The optical cross talks between two types of lights reaching the same electronic board and between lights in two consecutive electronic boards were avoided by a light tight frame (Figure 4.10). Each FEE board was connected, via cables, to a FERS* readout system, a product by CAEN. Two CITIROC1A† chips of each readout board (A5202) was fed by 64 SiPMs i.e., 32 scintillation channels and 32 Cherenkov channels. Each SiPM provided signals to two tunable gain charge amplifiers, namely High Gain (HG) and Low Gain (LG). The HG spectra have been used to analyse the multi-photon spectra and calculate the calibration constants (number of photo-electrons per ADC counts), whereas the LG spectra have been used to extend the overall dynamic range. In Figure 4.11a one FEE board cabled with one readout FERS board is depicted. In Figure 4.11b the FERS system mounted to the EM-scale module is shown. The FEE boards and the readout boards that operate the SiPM sensors have been developed by the group from the University of Insubria, Como.

*https://www.caen.it/products/a5202/
†https://www.weeroc.com/my-weeroc/download-center/citiroc-1a/

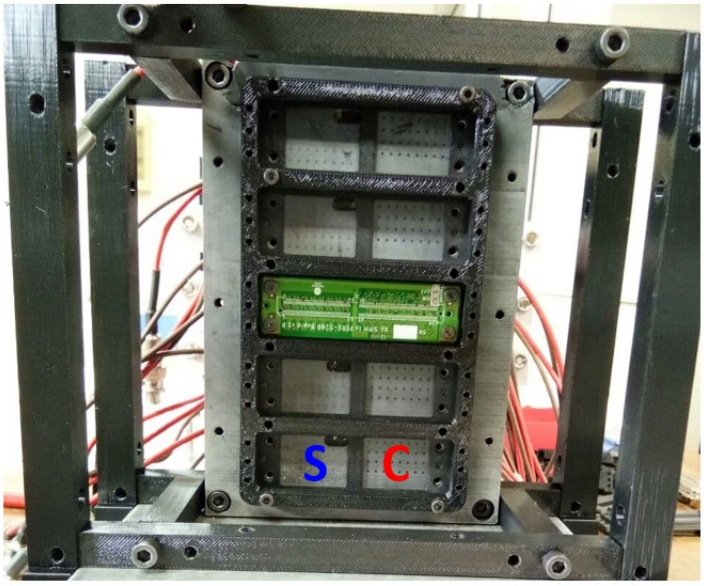

Figure 4.10: The light tight frame is mounted on the interface for SiPMs to stop light contamination between two FEE boards and two types of lights on each board. FEE board, the middle one, is mounted.

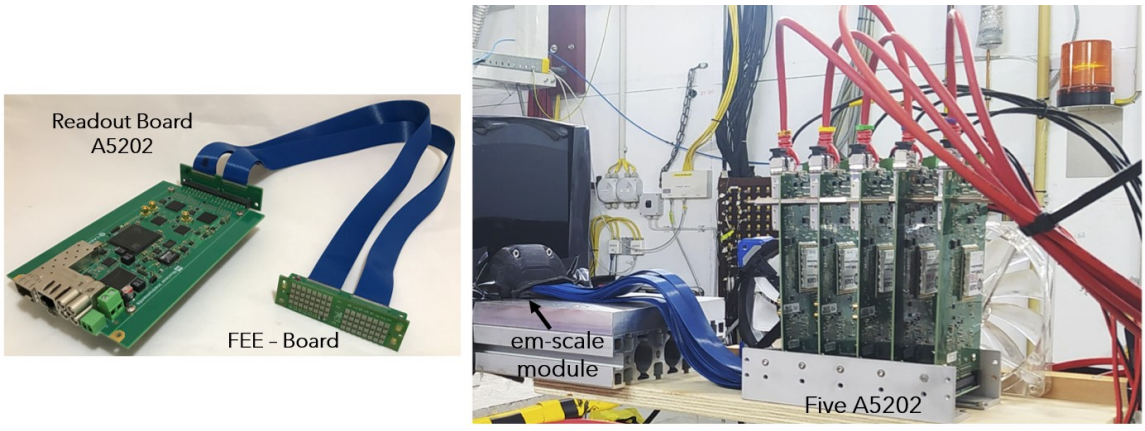

Figure 4.11: A5202 electronic board reads 64 SiPMs via FEE board (a). The prototype detector is connected to the five A5202 readout boards that read out the SiPM signals from the central tower (b).

4.4 Mechanical construction and integration

4.4.1 Tower structures

We used BCF-10 plastic scintillating fibres from Saint-Gobain and SK - 40 plastic clear fibres from Mitsubishi, both of diameter 1 mm. Using a rotary cutter tool clear fibres were polished at the upstream ends i.e., the ends that were supposed to get exposed to beam particles. Polishing was necessary to increase the NA of clear fibres, so that the produced Cherenkov photons can fall inside the aperture and are captured inside fibres. Nine towers, one by one, were prepared in Pavia and finally interlocked together to form the compact module. Preparation of individual tower involved following procedures:

- **Fibre insertion into capillary tubes:** This step was performed manually. The fibres were inserted into the capillary tubes, row by row, from the tower front face. A little amount of instant adhesive was applied at the tips of the fibres (Figure 4.12a) just before pushing them completely inside the tubes. This was needed in order to block fibre positions inside the capillaries. Loading of a single tower with fibres took on average 3 hours.

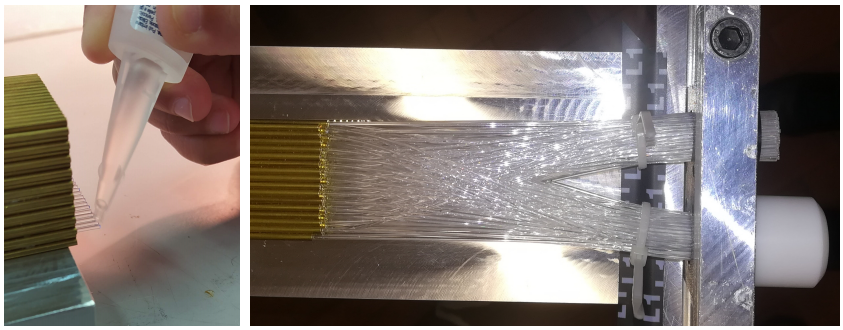

(a) (b)

Figure 4.12: Application of instant adhesive at the tips of the fibres for blocking their positions inside capillaries (a). At the rear end two types of fibres are well separated by a 3D printed holder with two holes (b).

- **Separation and grouping:** Fibres from each tower were separated at the rear end to form two bundles, one of scintillation fibres and the other of clear fibres as shown in Figure 4.12b. Eight 3D printed holders with two holes were prepared for positioning of the bundles. Two bundles from each tower were inserted into the holes of one holder and thus, were differentiated from each other. The bundles were cut in short to get rid of extra fibres (Figure 4.12b).

  A special treatment was required for the central tower that was 20 cm extra long. As mentioned in Section 4.3, the fibre pitches had to be compatible with that of SiPM sensors. To serve the purpose, an interface, made of Delrin®, with 320 holes (Figure 4.13) was prepared. It was a temporary solution for the EM-scale calorimeter. For a scaled up full containment prototype module a different approach will be adapted (Chapter 7). The above mentioned treatment also allowed to keep the 320 fibres well isolated from each other and to separate the readout for SiPMs from the PMTs.

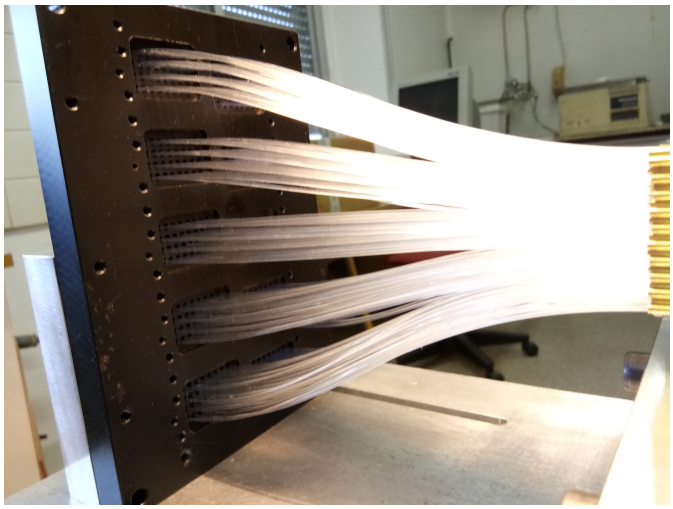

Figure 4.13: Rear end of the central tower. 320 fibres are well separated using an interface for one to one correspondence with SiPM sensors. Fibres are distributed in five layers. Each layer has 32 scintillation and 32 Cherenkov channels.

- **Gluing:** Each tower was aligned vertically, with rear end fibres pointing downwards, using a metallic support. Small teflon containers were used for application of glue at edges of fibre bundles. We used BC-600 optical cement [72] from Saint-Gobain that is a clear epoxy resin formulated specifically for making optical joints with plastic scintillators. This low viscosity adhesive was pushed inside the containers with syringes (Figure 4.14a). Due to viscosity the glue rose up (Figure 4.14b) and was set in 24 hours. The containers were then removed (Figure 4.14c). This process was repeatedly performed for eight surrounding towers.

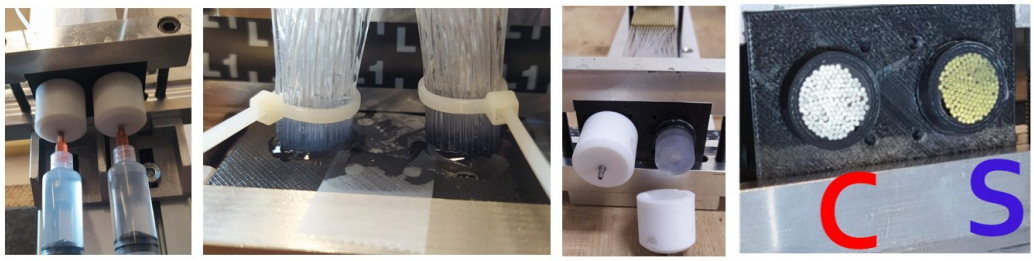

Figure 4.14: Application of optical cement using syringes while tower is aligned vertical (a). Rising up of glue due to viscosity (b). Removal of teflon containers after setting up of glue (c). Grouped, glued fibres after milling are ready to be coupled with PMT windows (d).

Again, a special treatment was required for the central tower. The distribution of glue, in this case, took two days. Optical cement was applied on both sides of the interface with 320 holes. Firstly, dips at one side of the interface were filled up with the glue (Figure 4.15a) and left for 24 hours to set. Then the tower was turned upside down and ten small white frames, were installed around the holes.

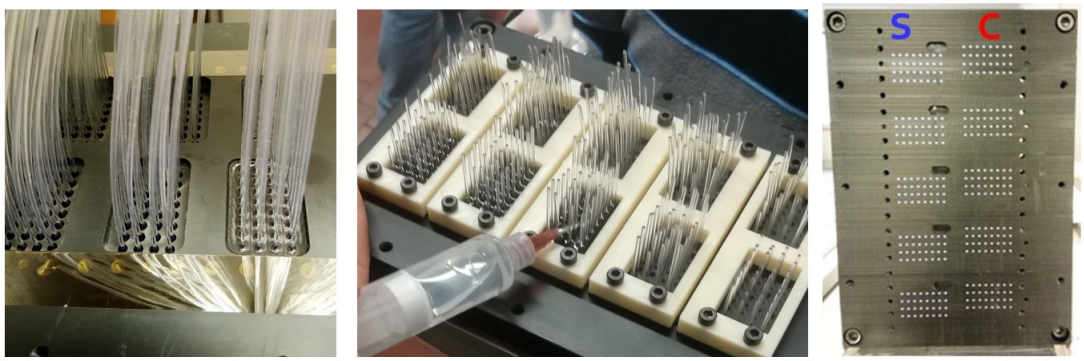

Figure 4.15: Special treatment for the central tower: Application of glue into the dips (a). Application of glue inside frames (b). Polished surface after machining. 2 × 160 fibres, arranged in 2 columns (S and C channels) with adjusted gaps, are ready to be coupled with SiPM sensors (c).

The optical cement was distributed inside these frames (Figure 4.15b) and left for another 24 hours to set. This procedure ensured that fibres were well glued inside the holes. Another reason was to develop some material around the fibres on the back surface of the interface in order to perform milling (next step) for smoothing the surface without damaging the fibres.

- **Machining:** It was the final important step towards the preparation of individual towers. 16 glued bundles of fibres inside the holders and the back surface of the interface in the central tower were milled to remove unnecessary materials (white frames, glued fibres). Polished, smooth surfaces were obtained for efficient coupling with PMT windows and SiPM sensors as shown in Figures 4.14d and 4.15c, respectively.

The design of the mechanical supports were finalised both for the module and FEE for the light sensors to sit. The mechanical finishing was done by bringing all nine towers together on the support and interlocking them in a compact structure (Figure 4.16).

4.4.2 Hadronic-scale module

After testing the EM-scale module with beams (Chapter 6), the next obvious step is the construction of a module with a similar design, i.e., use of capillary tubes and highly granular readout, for a significant containment of hadron showers. Several steps have already been taken in that direction. This project is referred to as High-Resolution Highly granular Dual-Readout Demonstrator (HiDRa) [73]. So far, the prototype modules, built by DREAM and RD52 collaborations, were too small in the lateral dimensions for a good containment of a hadron shower. So, HiDRa (∼65 × 65 cm^2 in cross section and 2.5 m long) will be the first fibre-sampling design for a sensible hadronic shower containment. HiDRa has been approved by INFN $CSN5$ in 2021 and it is a

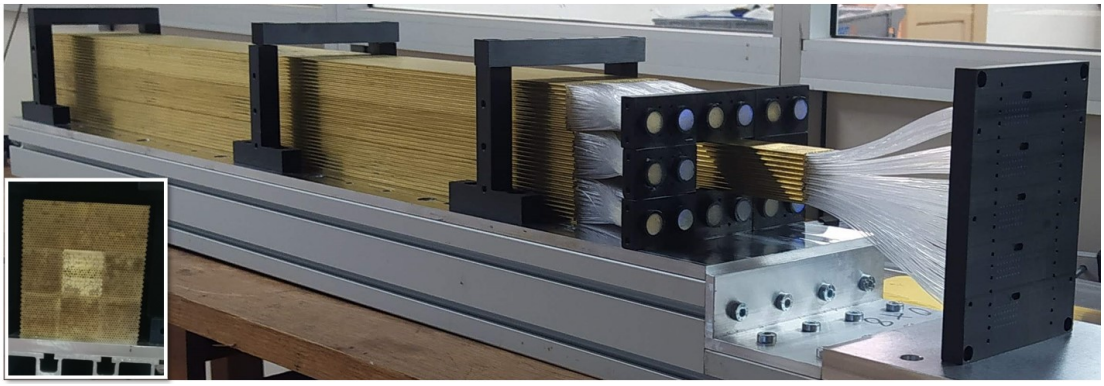

Figure 4.16: The EM-scale 3 × 3 tower structure before coupling with light sensors. 20 cm longer central tower is highly granular as there is one-to-one correspondence between fibres and SiPMs. The fibre bundles in external towers are well separated before coupling with PMT windows. The inset image shows the front face of the 3 × 3 tower structure.

three-year programme with a workplan over the period 2022-2024. An international collaboration is participating to the advancement of this project. It involves six INFN units (Bologna, Catania, Milano, Pavia, Pisa and Rome), the University of Sussex, the UTFSM of Valparaiso, a cluster of universities in South Korea and the CalVision collaboration in the US.

Unlike the EM-scale ptototype, all the mechanical construction activities, from the procurement of capillary tubes and their QAQC tests to the final assembly of the tubes, are going to be performed in Pavia. The proof-of-concept of the new assembly procedure has already been established with 20 cm long stainless-steel capillary tubes. Tubes with different combination of inner and outer diameters have been considered. The final values, 1.1 mm and 2.0 mm for tubes' inner and outer diameters, respectively, were chosend based on physics and technical requirements, that will be described in Chapter 5.

The mean outer diameter of 20 cm long capillary tubes was estimated to be 1.996 mm (2 mm - 4 μm) with a standard deviation of 2 μm (Figure 4.17a). The mean value is compatible with the detector requirements and the standard deviation is well below the needs for reaching the needed mechanical precision. The tools for tube handling with a vacuum system and for tube gluing, are shown, for 20 cm long capillaries, in Figures 4.18a and 4.18b, respectively. A support with reference plates (Figure 4.18c), for the preparation of staggered tube layers, was built. The vacuum system deposits a layer of glued tubes on top of the previous one kept in the reference assembly tool as shown in Figure 4.18d. The design of tools for QAQC studies, gluing and module assembling are qualified and feasible to scale up for large scale production with 2.5 m long tubes.

1250 samples of 2.5 m long stainless-steel capillary tubes, have arrived in Pavia (Figure 4.19a) and amongst them 150 have been inspected so far (October, 2022). The mean outer diameter of these is measured to be 2.022 mm (2 mm + 22 μm) with a standard deviation of 2 μm (Figure 4.17b). These numbers are compatible with expected values of 2.00 $\pm$ 0.05 mm. Large scale production will be taking place on a granite table in a clean room in Pavia. A system for automatic measurement of

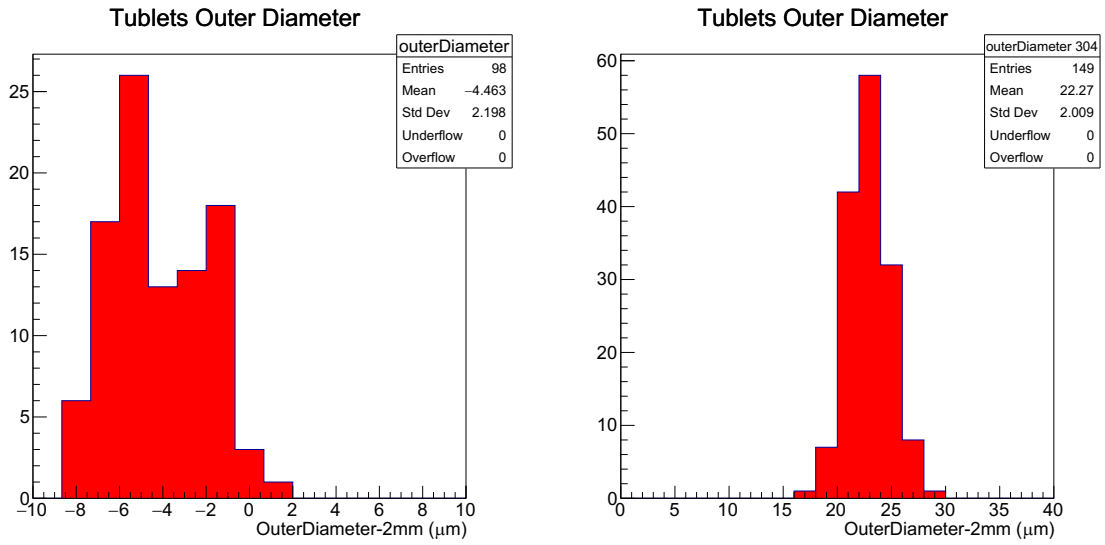

(a) (b)

Figure 4.17: The outer diameter of 20 cm long capillary tubes measured for a sample of 100 tubes. The mean outer diameter is estimated to be 1.996 mm with a standard deviation of 2 μm (a). The outer diameters of 2.5 m long capillary tubes measured for a sample of 150 tubes. The mean outer diameter is measured to be 2.022 mm with a standard deviation of 2 μm (b).

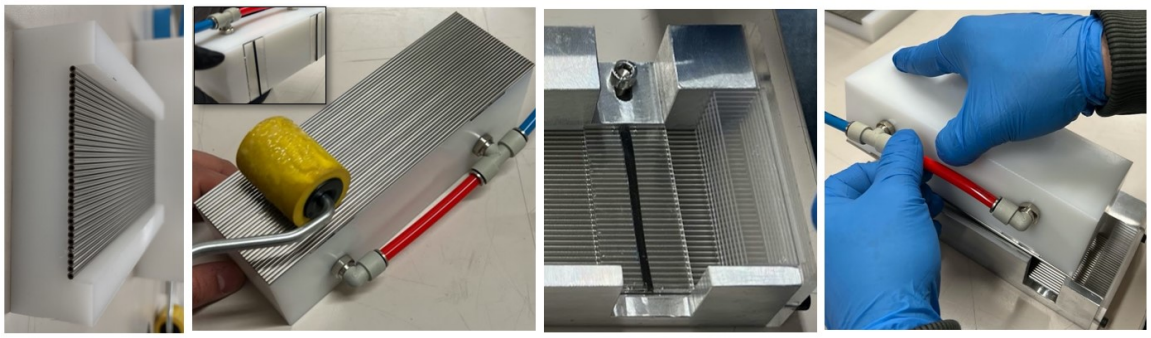

Figure 4.18: Capillaries are aligned on support before gluing (a). Vacuum system picks up the layer of capillaries for glue application. Inset image shows plastic plates prepared with double-sided scotch tape (b). Reference tool with, at one end, plates for staggering tubes along the length in order to couple to SiPMs (c). Vacuum system deposits the layer on top of previous layer to form staggered structure (d).

tubes' diameters (Figure 4.19b), vacuum system for tube handling and glue application and L-shaped support for achieving high mechanical precision in module construction (Figure 4.19c) have been developed. We also installed a system for checking horizontal and vertical alignment within 20 μm (Figure 4.19d).

Figure 4.19: 2.5 m long stainless-steel 304 capillaries arrived in Pavia (a). System for automatic dimension measurement is installed (b). Vacuum system (hanging) for gluing capillaries to form one layer and L-shaped support (laying on granite table) to prepare the calorimeter structure (c). System for horizontal and vertical alignment of the supports (d).

Chapter 5

Simulation and studies for capillary-based modules

A Monte Carlo Geant4 (G4) simulation package[*] has been developed in 2020 in order to study the expected performance of the EM-scale calorimeter, for different conditions, prior to the beam test that has been carried out in 2021. In this simulation, detector dimensions are defined as that of the EM-scale calorimeter (Section 4.1). Scintillation and clear fibres are built with G4-materials, Polysterene and PMMA, respectively. The physics processes in the simulation has been defined by FTFP_BERT physics list that contains all standard em processes and the Fritiof model [74] that is coupled to Bertini-style cascade [75]. FTFP_BERT is the default physics list used in simulations by CMS and ATLAS collaborations. Unlike the real module where both PMTs and SiPMs are used, in this simulation lights from all 2880 fibres are collected by only SiPM photo-sensors. The simulated data are produced for point-like (0.1 mm) electron beams of 10 GeV energy (if not mentioned otherwise) with 10k event statistics for different geometries of the capillaries, different passive absorbers and different detector orientations with respect to the incoming particles.

I performed analysis of simulated data for the EM-scale calorimeter and the results are discussed in Sections 5.1, 5.2 and 5.3. Section 5.4 is a report on my work on the development of Geant4 geometry for scaled up full containment calorimeter module.

5.1 Different geometries

As the EM-scale module (Chapter 4) is a proof-of-concept for construction of a larger-scale full containment module, it is important to explore the effect of different types of geometries of the capillaries on the EM shower energy, leakage energy, sampling fractions and the dual signals. Three different geometries that have been studied are following:

- Capillary tubes without mechanical tolerance and air between tubes (perfect geometry).
- Capillary tubes with 50 μm mechanical tolerance and air between tubes.

[*] https://github.com/lopezzot/DREMTubes

- Capillary tubes with 50 μm mechanical tolerance and copper between tubes.

Implementation of mechanical tolerance causes smearing of diameters of capillaries. The diameter, d, becomes d + δx, where δx can take any value between 0 and 50 μm. Varying diameters have impacts on detector performances. On the other hand, studies with perfect geometry provide the effect of empty space between the capillaries. For these studies capillary tubes are built with copper and the module orientation is 1° with respect to the incoming particles, both in horizontal and vertical planes.

Figures 5.1a and 5.1b show event-by-event distributions of the total energy deposited in the EM-scale module and the energy brought by the particles leaking out the module, respectively, for perfect geometry of the capillaries. The containment is measured to be ∼94.5% with a standard deviation of 87.3 MeV. The leakage energy is ∼5.3% with a standard deviation of 78.17 MeV. These values are as expected according to the detector geometry and dimension. The discrepancy of ∼0.2% is a measure of *albedo* that is the back scattering of soft photons through the front face of the module. These photons are counted neither as deposited particles in the module nor as escaped ones. The containment increases to ∼94.6% for capillaries with 50 μm mechanical tolerance and ∼96.1% for capillaries with 50 μm mechanical tolerance and with presence of Cu between the capillaries, whereas the leakage energy reduces to ∼5.2% and ∼3.7%, respectively. The amount of back scattering of soft photons is measured to be same, ∼0.2%, for all three geometries. The numbers with standard deviations are reported in Table 5.1.

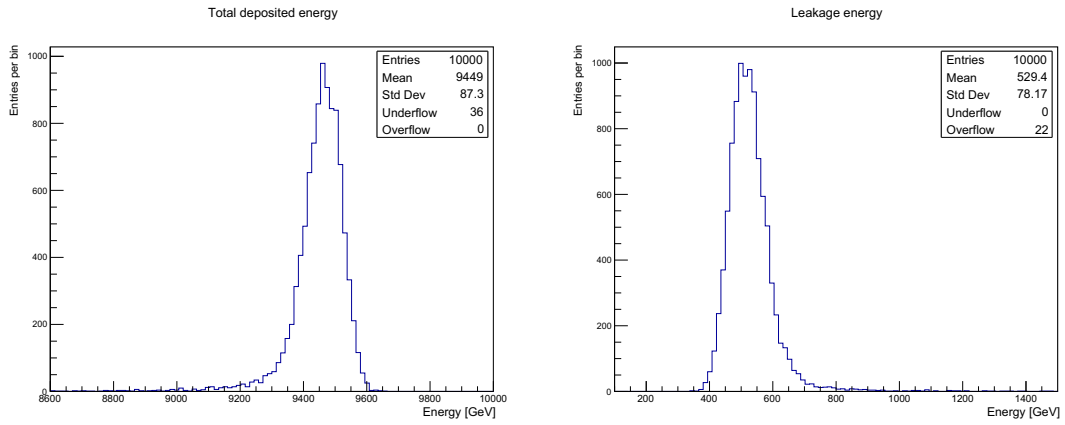

(a) (b)

Figure 5.1: Simulation studies for perfect geometry. Event-by-event distributions of the total energy deposited in the EM-scale module (a) and the energy of particles leaking out the EM-scale module (b).

Figures 5.2a and 5.2b show event-by-event distributions of fraction of the total shower energy sampled by the scintillation fibres and clear fibres, respectively, i.e., a measure of f_{samp}. It is measured to be ∼2.3% and ∼2.9%, respectively for scintillation and Cherenkov channels for perfect geometry of the capillaries. For the other two geometries f_{samp}, for both channels, becomes smaller. In particular, for the presence of Cu between the capillaries, the values are ∼1.8% and ∼2.2% for scintillation and Cherenkov channels, respectively. The numbers are reported in Table 5.2.

Measured quantity	Tolerance		
10k e^- events	[Zero] + air	[50 μm] + air	[50 μm] + Cu
Average shower energy $[MeV]$	9449 ± 87	9457 ± 86	9611 ± 80
Average leakage energy $[MeV]$	529 ± 78	520 ± 76	367 ± 68

Table 5.1: The shower energy and the leakage energy measured from simulation studies are reported for perfect geometry, capillaries with 50 μm mechanical tolerance and capillaries with 50 μm mechanical tolerance plus Cu between the capillaries.

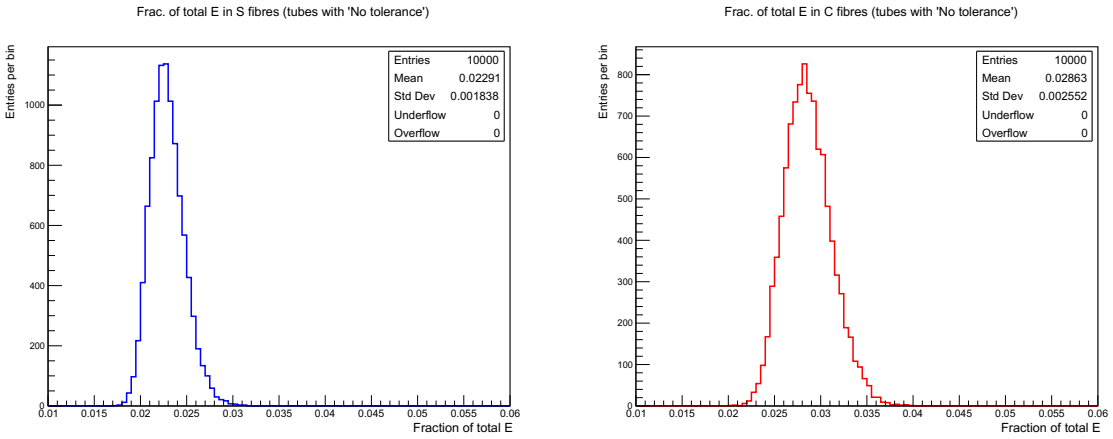

(a) (b)

Figure 5.2: Simulation studies for perfect geometry. Fraction of the total deposited energy sampled by the scintillation channels (a) and Cherenkov channels (b). The mean values of these distributions are estimation of sampling fractions (for e^-), separately, for two the channels.

Measured quantity	Tolerance		
10k e^- events	[Zero] + air	[50 μm] + air	[50 μm] + Cu
$< f_{samp} >$ (S) [%]	2.3 ± 0.0	2.2 ± 0.0	1.8 ± 0.0
$< f_{samp} >$ (C) [%]	2.9 ± 0.0	2.6 ± 0.0	2.2 ± 0.0

Table 5.2: Sampling fractions, separately, for scintillation and Cherenkov channels measured from simulation studies are reported for perfect geometry, capillaries with 50 μm tolerance and capillaries with 50 μm tolerance plus Cu between the capillaries.

Scintillation and Cherenkov signals are separately measured by summing up the individual signals in all fibres. Cherenkov signals are proportional to the number of cherenkov photons. Hence, the number of Cherenkov photoelectrons (C.p.e.) produced by the SiPMs is the measure of Cherenkov signals in the simulation. On the other hand, the number of scintillation photons is less important in measurement of Scintillation signals. These photons are emitted isotropically, hence, the scintillation signals are, approximately, proportional to the amount of energy deposited in these fibres. The problem of light saturation by densely ionising particles, as described by Birks' law (Equation 5.1), is taken into account [76].

$$\frac{dL}{dx} \propto \frac{dE/dx}{1 + k_B \cdot dE/dx} \tag{5.1}$$

where L is the amount of light produced by a particle of energy E and k_B is Birks' constant which is a material property. So, the amount of saturated energy in the fibres is a measure of scintillation signals in the simulation. Figures 5.3a and 5.3b show event-by-event distributions of sum of scintillation signals and sum of Cherenkov signals in all fibres, respectively. For perfect geometry the amount of these signals are 208.6 (a.u) and 225 (C.p.e.). Signals have direct correlation with f_{samp}. So, like f_{samp}, signals also decrease in the other two geometries. The values are reported in Table 5.3.

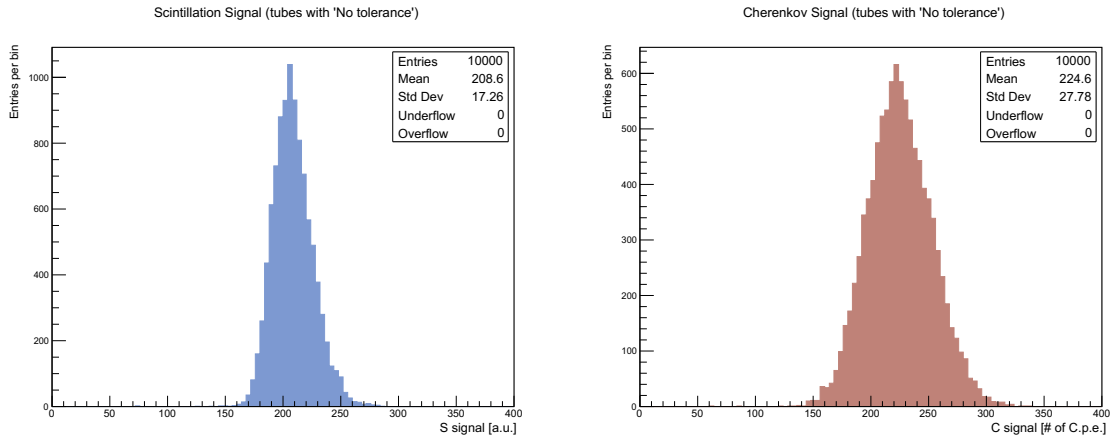

(a) (b)

Figure 5.3: Simulation studies for perfect geometry. Total signals in Scintillation channels (a) and Cherenkov channels (b).

f_{samp} is a determining factor for the acsEM energy resolution (Equation 1.10) of a calorimeter. A better sampling fraction, hence, larger detector response, is an obvious choice for construction. So, with these results the idea of filling the gaps between capillaries with absorber materials for both the EM-scale and large-scale module construction has been discarded. For the studies mentioned in the next sections, mechanical tolerance has not been implemented to the capillaries.

Measured quantity	Tolerance		
10k e^- events	[Zero] + air	[50 μm] + air	[50 μm] + Cu
<Scintillation signal> [*a.u.*]	208.6 ± 17.3	200.6 ± 17.0	169.4 ± 16.4
<Cherenkov signal> [*# of C.p.e.*]	225.0 ± 27.8	210.0 ± 27.1	175.0 ± 24.7

Table 5.3: The dual signals measured from simulation studies are reported for perfect geometry, capillaries with 50 μm tolerance and capillaries with 50 μm tolerance plus Cu between the capillaries.

5.2 Different absorbers

A set of studies have been investigated to select passive detector materials for the construction of EM-scale and hadronic-scale calorimeters. For these studies any tolerance has not been applied to the capillaries. For references, relevant material properties of five passive absorbers and two fibre constituents are listed in Table 5.4.

Material	Composition and Atomic number (Z)	Density [g·cm^{-3}]	X_0 [cm]	R_M [cm]
Brass	Cu(29):Zn(30)::70:30	8.53	1.492	1.64
Cu	29	8.96	1.436	1.568
Fe	26	7.874	1.757	1.719
Inconel718	Fe(26):Cr(24)Ni(28)::33:17:50	8.2	1.634	1.66
S. Steel	Fe(26):Cr(24)Ni(28)::74:18:8	8	1.740	1.689
PMMA	H(1):C(6):O(8)	1.19	34.07	8.422
Polystyrene	H(1):C(6)	1.06	41.31	9.409

Table 5.4: Some material properties of five passive absorbers and two fibre constituents. The values are taken from the Particle Data Group (PDG).

5.2.1 Sampling fraction and stochastic term

Values of f_{samp} for showers developed by MIPs in different absorbers (brass, Cu, Fe, Inconel718 and stainless-steel) as a function of the dimension of capillaries have been calculated analytically. The outer diameter of the capillaries has been increased from 1.6 mm to 3.0 mm in a step of 0.2 mm, whereas the inner diameter is kept fixed at 1.1 mm. In Figures 5.4a and 5.4b calculated f_{samp}, separately and respectively for scintillation and Cherenkov channels, as a function of outer radii of capillary tubes are shown. In these plots, it is seen that for higher diameters of capillaries, f_{samp} for

different absorber materials merges. At 2 mm outer diameter (the dimension selected for prototype construction), f_{samp} for the five materials ranges from $\sim 2.5\%$ to $\sim 2.8\%$ for the scintillation channels and $\sim 2.9\%$ to $\sim 3.2\%$ for the Cherenkov channels.

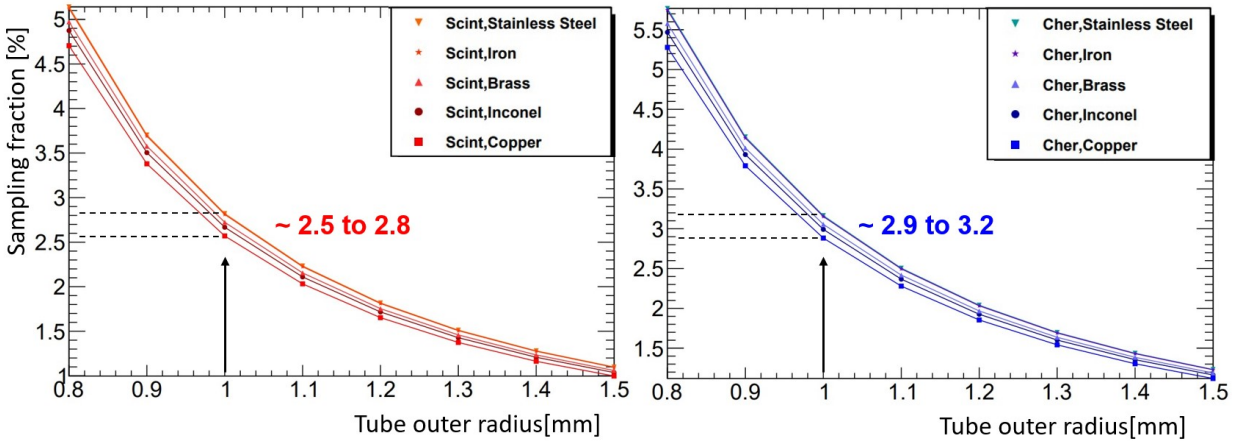

Figure 5.4: Analytical calculations. Sampling fraction for MIPs, in different absorber materials, as a function of outer radius of the capillaries. Sampling fractions are measured separately for the scintillation channels (a) and Cherenkov channels (b).

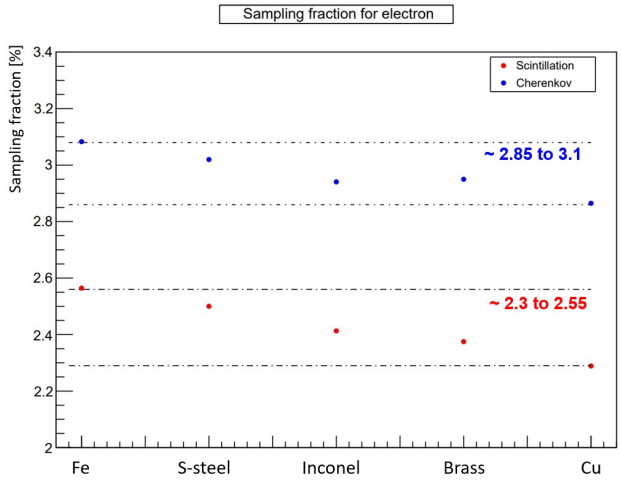

Figure 5.5: Simulation studies for 10 GeV electrons. Sampling fraction for the scintillation and Cherenkov channels as a function of absorber materials with 2 mm outer diameter of the capillaries.

Values of f_{samp} for electrons as a function of different materials have been extracted by the simulation. Figure 5.5 shows this study where f_{samp} ranges from $\sim$ 2.3% to $\sim$ 2.6% for the scintillation channels and $\sim$ 2.8% to $\sim$ 3.1% for Cherenkov channels. These numbers for e^-s are in good agreement with analytical studies for MIPs.

In Section 1.5 we have seen that f_{samp} for MIPs and the dimension of active layers (d), fibre diameter in our case, determine the stochastic term of energy resolution (Equation 1.10). f_{samp} for MIPs is $\sim$3% for both channels (Figure 5.4) and d equals to 1 mm for the EM-scale module. These lead to a stochastic term of $\sim$15.6%. Simulation has been performed for electrons (0.5 GeV to 15 GeV) steering at the centre of the

brass module. Electrons of 10 GeV are used to calculate the calibration constants (K_S, K_C). K_S and K_C, separately and respectively for scintillation and Cherenkov channels, are calculated as:

$$K_{S,C} = \frac{< S_{sum} >_{S,C}}{< E_{dep} >} \tag{5.2}$$

where E_{dep} is the total deposited energy in the calorimeter and S_{sum} is the sum of signals extracted from all the fibres. For other energies (can be considered *unknown* due to the impact of the energy leakage), signals are reconstructed event-by-event using $K_{S,C}$. The reconstructed σ/E as a function of particle energy, for the two channels are shown in Figure 5.6. Linear fits estimate the energy resolution measured by the scintillation and Cherenkov channels as $21\%/\sqrt{E}$ and $23\%/\sqrt{E}$, respectively.

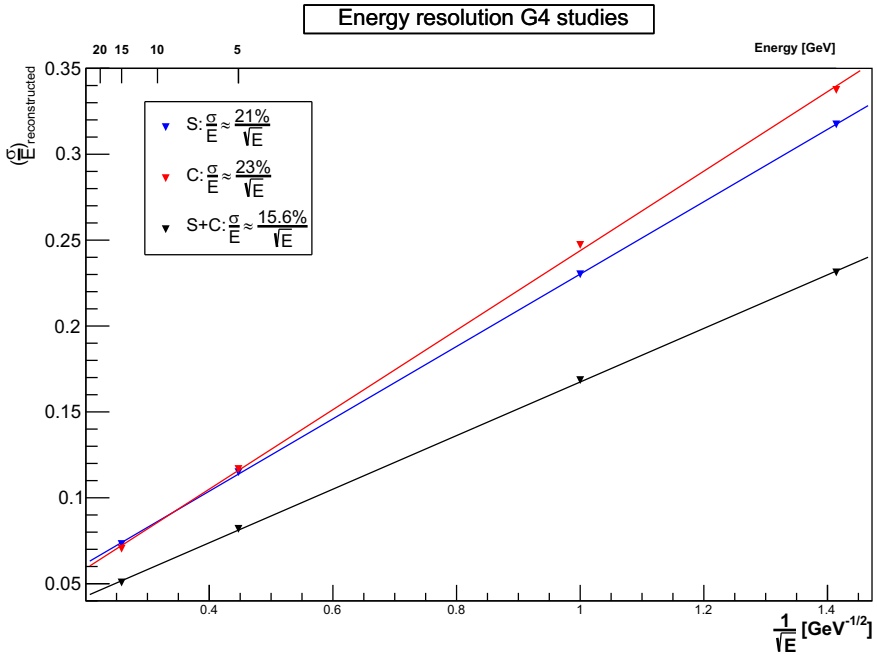

Figure 5.6: Electromagnetic energy resolutions obtained with scintillation and cherenkov channels are measured to be $21\%/\sqrt{E}$ and $23\%/\sqrt{E}$, respectively. The resolution improves significantly to $15.6\%/\sqrt{E}$ when the results from the two independent channels are combined.

The results from these two independent channels are combined by performing a weighted average ($E_{(S+C)}$). Also the weighted standard deviations ($\sigma_{(S+C)}$) are calculated.

$$\begin{aligned} E_{S+C} &= \frac{\frac{E_S}{{\sigma_S}^2} + \frac{E_C}{{\sigma_C}^2}}{\frac{1}{{\sigma_S}^2} + \frac{1}{{\sigma_C}^2}} \\ \sigma_{S+C} &= \frac{1}{\left(\frac{1}{{\sigma_S}^2} + \frac{1}{{\sigma_C}^2}\right)^{1/2}} \end{aligned} \tag{5.3}$$

Reconstructed $\sigma_{(S+C)}/E_{(S+C)}$ are plotted in Figure 5.6 and the linear fit determines a significantly improved energy resolution of $15.6\%/\sqrt{E}$ that is in good agreement with

the analytical observation mentioned before. The stochastic terms, for individual signals (S, C) and the combined signals (S+C), have been measured for absorbers made of Cu, Inconel, Fe and stainless-steel. The values are similar (Figure 5.7) to those found for brass.

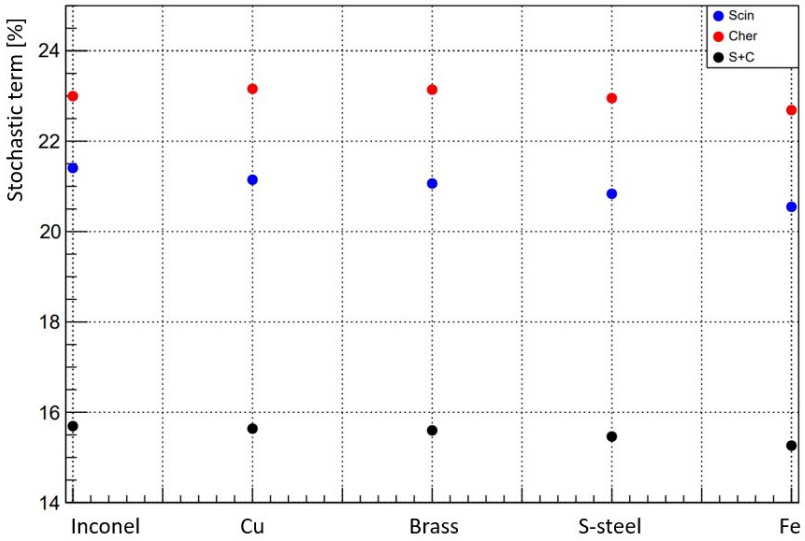

Figure 5.7: The stochastic terms, obtained for scintillation, Cherenkov and the combined signals, are comparable for the chosen different absorber materials.

5.2.2 Activated fibres and signals

The map of activated fibres in the transverse plane of the EM-scale calorimeter and the amount of signals in these fibres are observed. As mentioned in Section 5.1, the amount of energy deposited, taking into account the light saturation in scintillation fibres and the number of C.p.e. in clear fibres, are measures of the scintillation and Cherenkov signals, respectively. In Figures 5.8 and 5.9, the $X-Y$ plane represents the transverse plane of the module and the Z-axis represents the amount of signal, for single event, in fibres. Only the activated fibres are displayed in the plots. Amongst different absorbers, the signal is found to be the maximum in brass for scintillation channels and in stainless-steel (568 C.p.e.) for Cherenkov channels. Here, the $3D$ signal maps are displayed only for brass and stainless-steel, separately for scintillation (Figure 5.8) and Cherenkov (Figure 5.9) channels. It is apparent in these four distributions that a significant amount of EM-shower signal comes from a single fibre. This effect is more evident for scintillation fibres.

The number of activated scintillation and clear fibres as a function of different absorber materials are plotted in Figure 5.10. These numbers are lower for the Cherenkov channels, because the LY is smaller in clear fibres compared to that in scintillation fibres, as shower particles only with v > c/n produce a detectable signal. The ratio of the number of activated scintillation fibres to that of clear fibres is ∼1.3 for the brass module. This ratio varies between 1.3 and 1.5 for Cu, Inconel718, Fe and stainless-steel. For these studies, LYs are calculated analytically. These are determined, typically, by the calibration of photosensors (e.g., SiPMs) with test-beam data. For this simulation,

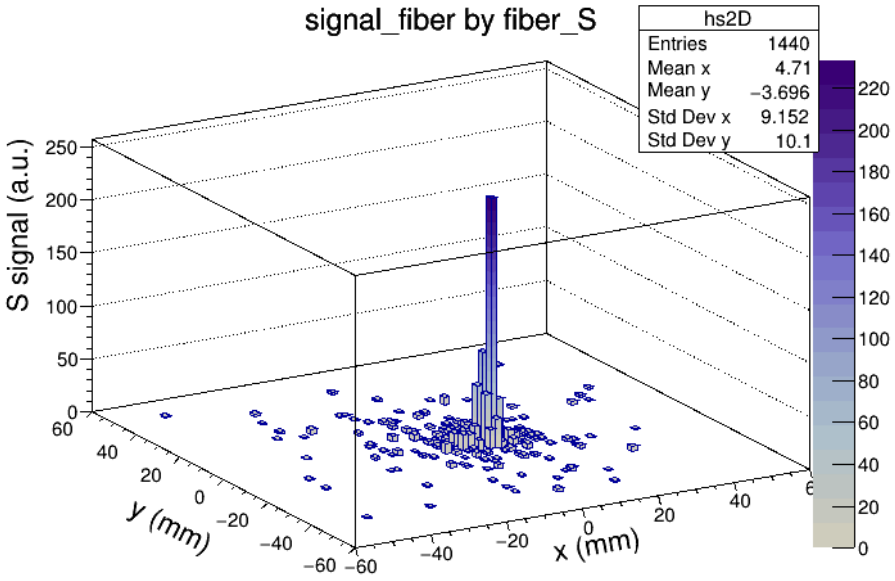

(a) Brass

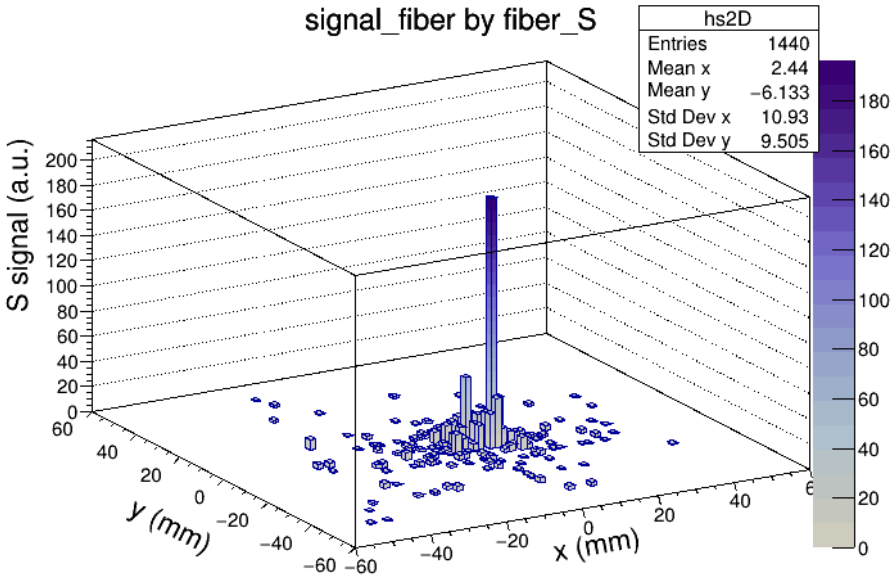

(b) Stainless-steel

Figure 5.8: 3D-maps of scintillation signals for 10 GeV electrons. Activated fibres are illustrated in X-Y plane. Z (color) axis represents the amount of signal, i.e., the energy deposited, taking into account the light saturation, in a fibre. Distributions are shown for brass absorber (a) and stainless-steel absorber (b).

LYs are taken from the previous beam test (Section 2.2.2), and modified taking into account the better efficiency of SiPMs chosen for the EM-scale calorimeter and the reduction in f_{samp}. The plugged-in values in simulation are 80 scintillation ptotoelectrons per GeV and 45 C.p.e per GeV.

Conclusion: f_{samp} and the signals are measured to be little better for stainless-

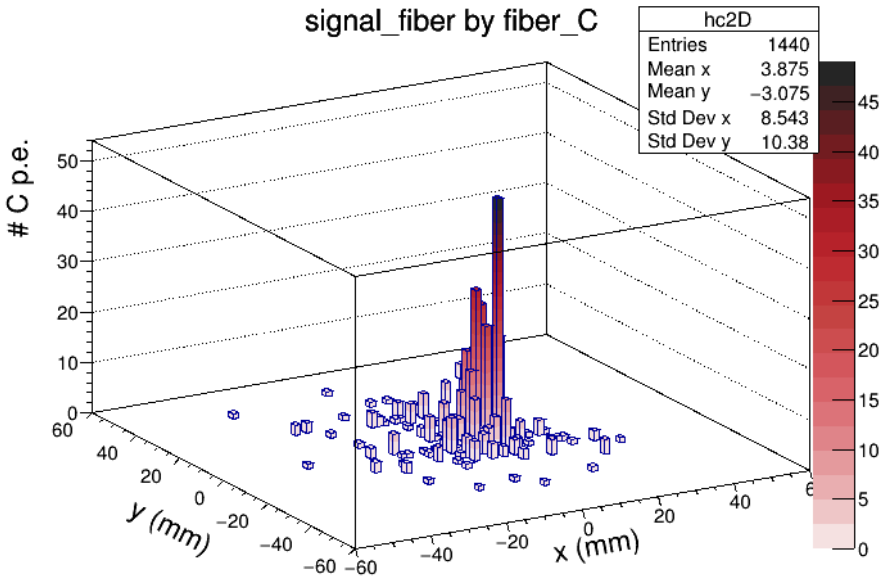

(a) Brass

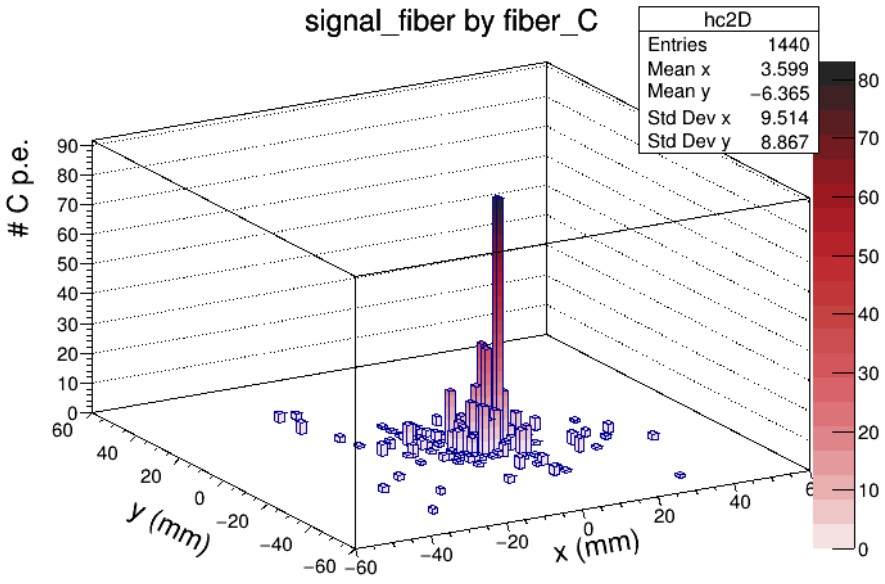

(b) Stainless-steel

Figure 5.9: 3D-maps of Cherenkov signals for 10 GeV electrons. Activated fibres are illustrated in X-Y plane. Z (color) axis represents the amount of signal, i.e., the number of C.p.e. in a fibre. Distributions are shown for brass module (sum of signals is 485 C.p.e.) (a) and stainless-steel module (sum of signals is 568 C.p.e.).

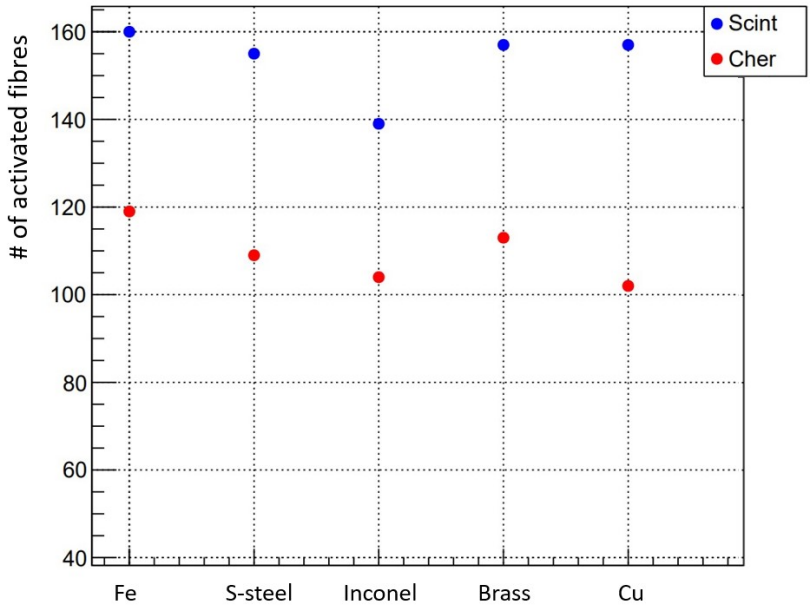

Figure 5.10: Number of activated scintillation and clear fibres as a function of the chosen different absorber materials.

steel and brass, for both scintillation and Cherenkov channels. The measures of the effective X_0 for an EM-scale calorimeter made of stainless-steel and brass are 26.1 mm and 22.7 mm, respectively. A 1.2 m long module contains $\sim 46 \cdot X_0$ and $\sim 53 \cdot X_0$, respectively for stainless-steel and brass absorber. So, brass has been selected as a better candidate than stainless-steel. For the upcoming hadronic-scale full containment module introduced in Section 4.4.2, stainless-steel has been selected as passive absorber. The performances of these two are measured to be comparable and for a cost-effective solution 304 stainless-steel has been the final material choice.

5.3 Angular dependence

For spaghetti type calorimeters, detector performance is sensitive to the angle of incidence of the incoming particles for two main reasons:

- Cherenkov emission is a directional phenomenon. The Cherenkov photons produced in extremely collimated, early shower components, fall outside the NA of the clear fibres. So, the calorimeter response is completely insensitive to these photons.

- The so called *channeling effect* may take place. At the detector front face, if a particle impinges on a fibre at 0° with respect to the fibre axis, instead of producing a shower it may travel through out the fibre and reach the photosensor at detector rear end, causing *oversampling*.

A solution to these problems is to apply rotation to the detector. It will allow to trap the above mentioned Cherenkov photons and channeling (or over sampling) will not happen. Brass is chosen as absorber material for this study. The goal is to observe

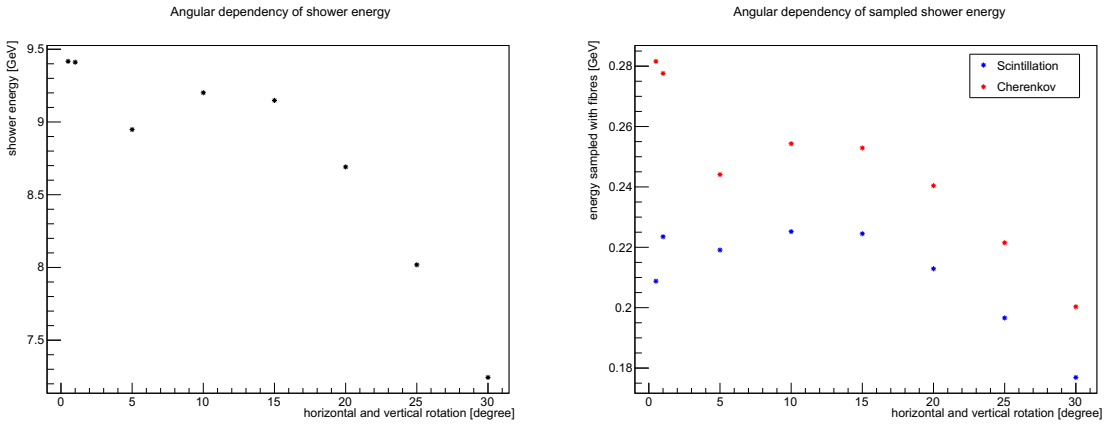

(a) (b)

Figure 5.11: Simulation studies with 10 GeV e^- beams are performed to measure the angular dependence of detector performance. Shower energy (a) and the energy sampled with scintillation and Cherenkov channels (b) as a function of detector rotation both in horizontal and vertical planes are shown.

the angular dependence of detector performance. The shower energy and the energy sampled by scintillation and Cherenkov channels are measured as a function of angle (from 0.5° to 30°) by which the detector is rotated both in horizontal and vertical planes.

In Figure 5.11a it is shown that the energy deposited in the module has higher values at 0.5° and 1° angles. Figure 5.11b shows that the shower energy sampled by the clear fibres also has higher values at smaller angles. On the other hand, the shower energy sampled by the scintillating fibres is comparable at 1° and 10° angles. This behaviour is not yet understood.

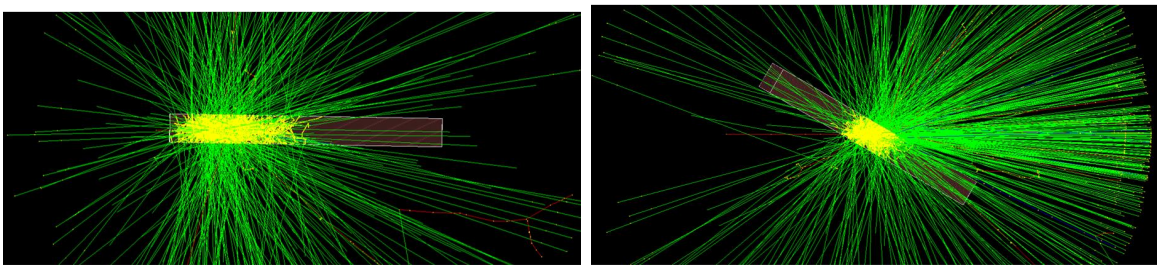

(a) (b)

Figure 5.12: Visualisation from simulation. The effective length of the module seen by the showering particles reduces with increment of angle of rotation applied to the module. Longitudinal shower size is illustrated when the module is rotate by 1° (a) and 30° (b) in both horizontal and vertical planes.

For geometrical reasons, for angles larger than 10° the effective length of the module seen by the showering particles is significantly smaller (Figure 5.12). At these angles, the particles no longer enter the module from the front face but from the side. As a result, the total deposited energy and the energy sampled with two different channels become smaller with increasing angles. In Figures 5.13a and 5.13b, event-by-event

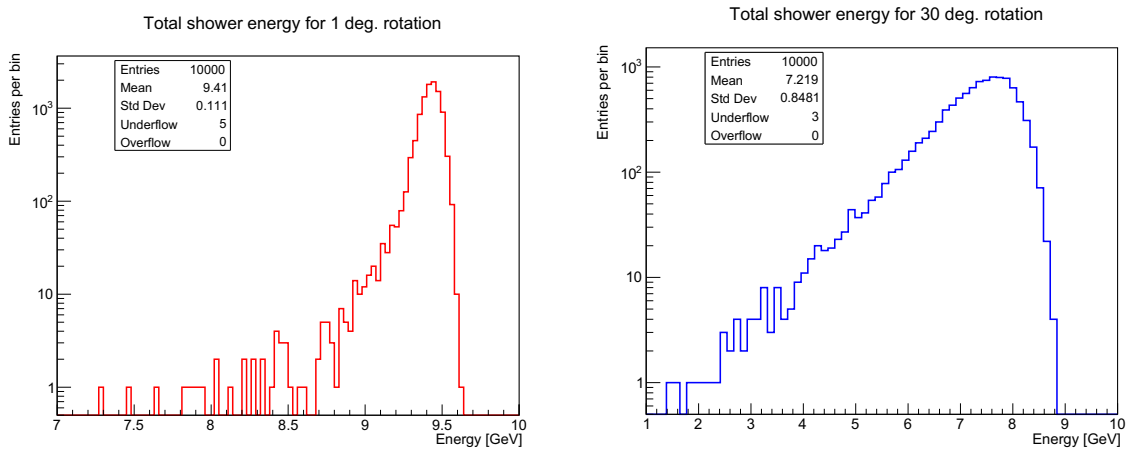

(a) (b)

Figure 5.13: Event-by-event distributions of the shower energy (Monte Carlo truth) developed by 10 GeV e^-s. The mean of the distribution is 9.4 ± 0.1 GeV for 1° rotation of the module (a). For 30° rotation, the mean is 7.2 ± 0.9 GeV. The low energy tail represents significant event-to-event leakage fluctuation (b).

distributions of shower energies developed by 10 GeV e^-s are shown for 1° and 30° rotations, respectively. The mean values of the distributions determine 94% ± 1% and 72% ± 12% containment for 1° and 30° rotations, respectively. The low energy tail of Figure 5.13b represents significant event-to-event leakage fluctuation. The observations from these studies led to apply 1° rotation, with respect to beam axis, in the horizontal plane during beam test data taking (Chapter 6) with the EM-scale calorimeter.

5.4 Geant4 geometry for hadronic-scale module

I started developing the geometry of hadronic-scale module based on the existing Geant4 simulation (version 10.5) for the EM-scale module. I learnt how to build materials, define shapes and sizes and then create logical and physical volumes to place these shapes inside the mother volume of the simulation. I explored the two ways to repeat a volume, through parameterisation using copy number and by creating replica of volumes. The objective of this work was to get familiar with Geant4 simulation and to initiate the R&D activities for the hadronic-scale module.

HiDRa demonstrator is primarily planned to be a composition of 16 modules made up of stainless-steel capillary tubes. The structure has a cross section of $(65 \times 65)\ cm^2$ and is 2.5 m long. Each module ($\sim 13 \times 13 \times 250\ cm^3$) is comprised of ten minimodules. 512 capillary tubes arranged in a staggered architecture of 32 × 16 matrix construct a minimodule. On top of 16 modules, eight extra minimodules may be constructed and equipped at the two edges for better containment of the shower laterally. Figure 5.14 illustrates a visualisation of HiDRa geometry developed by the simulation. Figure 5.14a shows 2.5 m long sixteen modules and eight extra minimodules for better cointainment. Figure 5.14b shows the front face of a minimodule with $(2 \times 256 =)$ 512 channels. Figure 5.14c shows 512 SiPM sensors attached to the back end of the fibres.

Recently, a complete Geant4 simulation package, for detailed assessment of detec-

tor performance for high-energy hadrons (pions and protons), has been developed by dedicated software group of Pavia. In this simulation one unit of volume is defined by a double-minimodule i.e., 1024 channels in a 64 × 16 matrix. In total eighty double-minimodules comprise the hadronic-scale module. The extra (double)-minimodules for better containment have been dropped after several simulation studies.

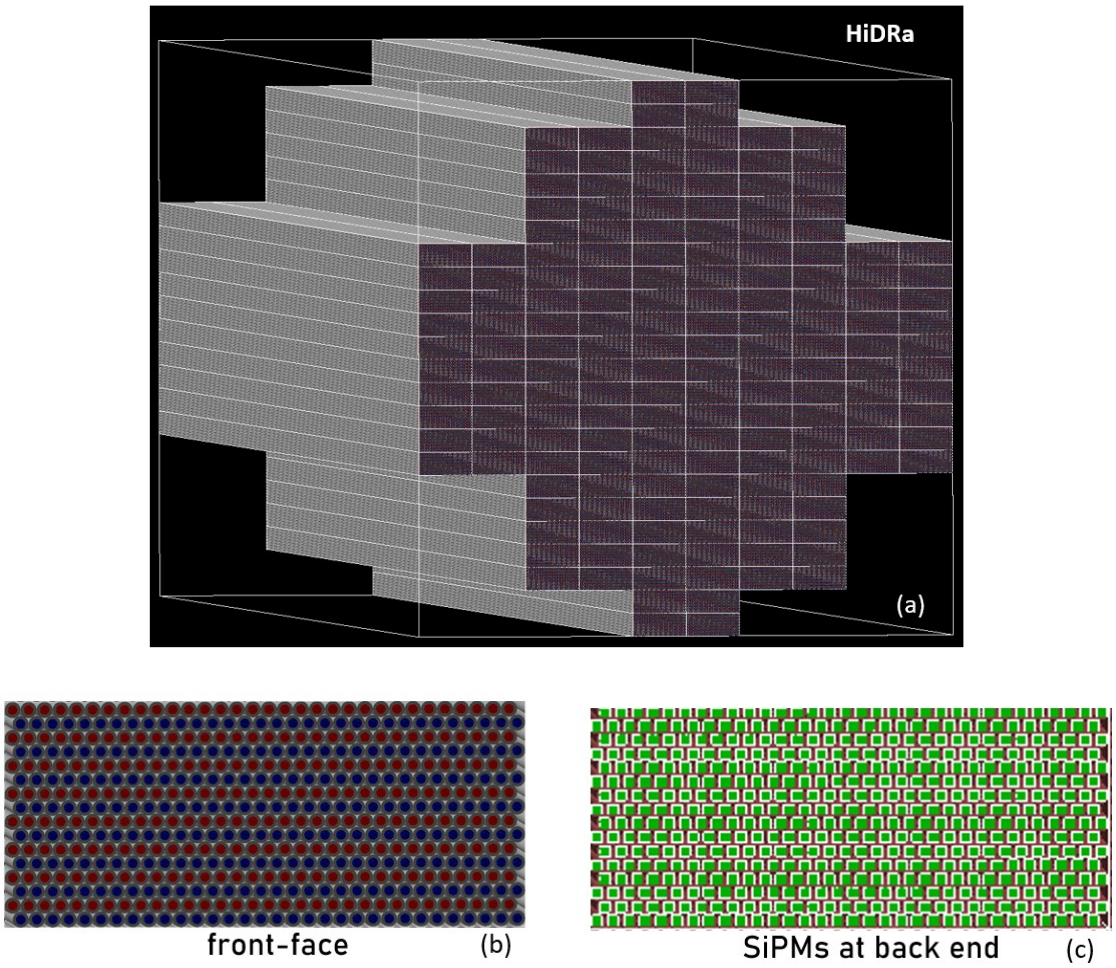

Figure 5.14: Visualisation of HiDRa Geometry with Geant4 simulation. Sixteen modules and eight extra minimodules, made of stainless-steel, to fully contain hadronic showers (a). A minimodule is a composition of (32 × 16 =) 512 capillaries loaded with scintillation and clear fibres in alternating layers (b). 512 SiPMs are attached to fibre tips at detector rear end (c).

Chapter 6

EM-scale module qualification with SPS beam

The EM-scale calorimeter has been exposed to beams at two facilities, DESY and the CERN Super Proton Synchrotron (SPS), in 2021. The purpose of the beam tests were to verify the detector performances and validate the Geant4 simulation for EM shower profiles and tune it for future studies. At DESY, low-energy electron beams of up to 6 GeV have been used, whereas at CERN SPS, we used fixed-target positron beams from 6 to 100 GeV and muon beams of ∼180 GeV. In this chapter we will focus on the latter beam test.

The SPS beam test* has taken place from August 10th to August 25th, 2021, inside the EHN1 experimental surface hall at CERN's North Area, in particular, on the H8 beam line of the SPS. The first week was spent for mounting the EM-scale module and then aligning and setting up the module along with other auxiliary detectors that were involved in the data taking processes, whereas data were taken in the second week. Figure 6.1 shows the calorimeter module, covered with a black cloth for isolation from light sources, some of the upstream auxiliary detectors and the beam pipe in the experimental hall.

In Section 6.1, an overview of the beam line and the auxiliary detectors has been given, whereas in Sections 6.2, 6.3 and 6.4 detailed descriptions of the data acquisition process, the data analysis methods and studies on beams have been reported, respectively. Experimental results are discussed in Section 6.5.

6.1 Beam line and auxiliary detectors

High-intensity, slow-extracted protons from the SPS constituted the primary particle beams of momentum 400 GeV/c for our beam test. The interaction of the primary proton beams on a thin beryllium-plate primary target (T4), located at a ∼15 m underground cavern, produced 180 GeV positive-pion secondary beams. Positron and muon beams, that had been used in our experiment, were derived from these secondary pions. The maximum $\frac{\Delta p}{p}$ acceptance of this line was 1.5%. Two small scintillation counters (S_1, S_2), with a (4×4) cm^2 superimposed area, were used for event selection

*https://twiki.cern.ch/twiki/bin/view/DREAM/DreamTBAugust2021

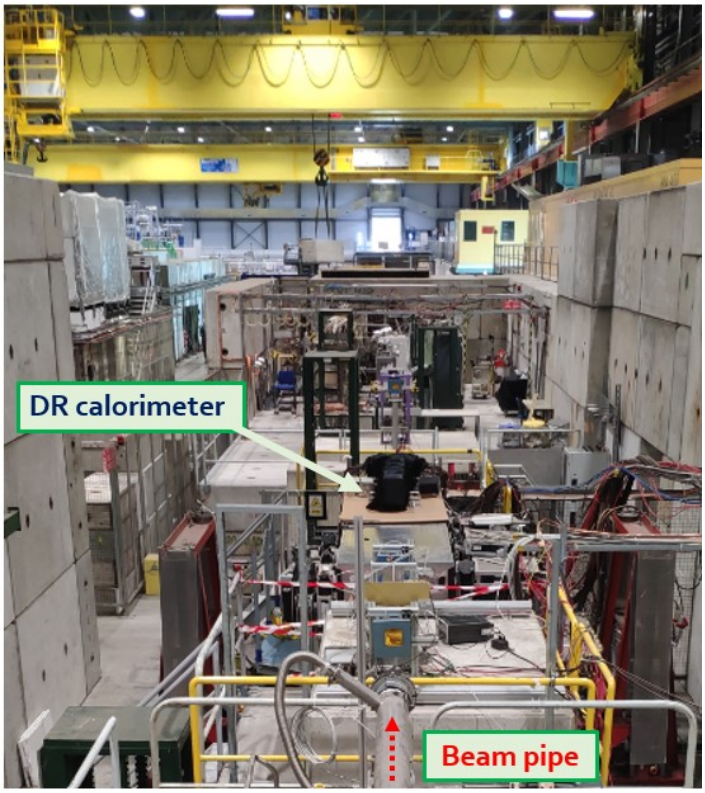

Figure 6.1: The EM-scale calorimeter installed in the H8 beam line inside the EHN1 experimental hall at CERN's North Area. Between the beam pipe and the calorimeter module, some upstream auxiliary detectors are visible. See text for details.

during data taking, whereas a veto detector (V), installed 42 cm upstream the scintillator counters, was used for event rejection. Hence, the (anti-)coincidence between the logic signals from these counters, i.e., $S_1 \cdot S_2 \cdot \overline{V}$, served as the trigger for the data acquisition system. A number of auxiliary detectors were installed to limit and define the effective size of the beam spot, provide tracking information and for PID in order to reject the beam contamination. The system included two Cherenkov threshold counters, two Delay Wire Chambers (DWCs), a PreShower (PS) detector upstream and a Muon Counter (MC) downstream the calorimeter module. Figure 6.2 is the sketch of a schematic top-view of the beam-test setup. The approximate positions along the beam axis of targets, trigger counters, auxiliary detectors and the calorimeter module followed by some amount of concrete absorber, are indicated.

Two Cherenkov threshold counters, that identify relativistic charged particles (typically e^- and e^+) were installed several tens of metres upstream the calorimeter. The counters were implemented as cylindrical volumes filled with CO_2 gas, where gas pressures were tuned typically between 10 mbar and 0.7 bar depending on the energy of the selected beam particles. Two small DWCs, with a (10×10) cm^2 transverse area, were installed, one upstream and the other downstream of the trigger counters. These tracking devices were providing two measurements of the (x, y) coordinates of the beam particle track. A PS was installed 2.85 m upstream the calorimeter module. It was composed of a 5 mm thick lead absorber followed by a 5 mm thick plastic scintillator. Typically, when traversing the PS, muons and hadrons behave as a MIP and leave the

associated (small) signal in the scintillator, while electrons or positrons start producing a shower in the lead slab, and a significantly larger signal is detected in the scintillator. The PS was meant to be used to reject the beam contamination by muons and hadrons. A MC was installed several tens of metres downstream the calorimeter and after the concrete absorber necessary for beam dumping. It was a large paddle of scintillator of dimension (50×50) cm^2 and it was used to select (veto) muon events.

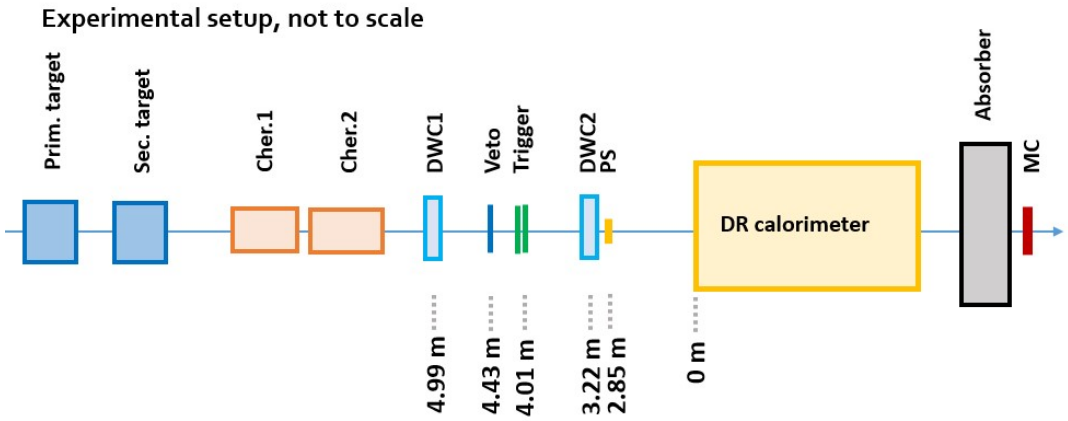

Figure 6.2: Schematic top view of the beam-test setup at the SPS H8 line. The blue arrow from left to right defines the beam axis. The approximate positions along the beam line of the targets, the auxiliary detectors, the EM-scale calorimeter and the downstream concrete absorber, are illustrated. The distances are not to scale.

6.2 Data acquisition

The high-voltage channels required for operating the PMTs were located in the Control Room (CR). For the SiPMs, working at around 40 V, the power was provided through the FERS readout system. To transport the trigger signals from the experimental area to the CR, as fast as possible, low-loss cables of diameter 15 mm and with a signal speed of ∼0.78·c were used. For the *busy* and the trigger validation signals for the SiPMs, two standard 50 Ω coaxial cables with signal speed of ∼0.66·c were used. The signals from sixteen PMTs, two Cherenkov counters, PS and MC were routed to three Analogue-to-Digital Converter (ADC) modules in the CR, via RG58 cables. The ADCs, performing charge integration followed by digitisation, were 12-bit CAEN V792AC QDC modules, with a resolution of 100 fC per count. The signals from the two DWCs were transported to a Time-to-Digital Converter (TDC), a 16-bit CAEN V775N module, working with a resolution of 0.139063 ns per count.

The trigger provided a common 'start signal' to the TDC. Time delays from the common start to the four 'stop signals' of the two DWCs, were measured with the TDC. With respect to a right-handed reference system where the positive z axis represents the direction of the beam, the four 'stop signals' can be referred to as S_{Left}, S_{Right}, S_{Up} and S_{Down}. The time information was used to estimate the relative impact coordinates

(x, y) of the particles on the DWCs, using Equation 6.1.

$$\begin{aligned} x &= (t_{Right} - t_{Left}) \times m_h + c_h \\ y &= (t_{Up} - t_{Down}) \times m_v + c_v \end{aligned} \tag{6.1}$$

where t stands for time of signal, m_h and m_v are the horizontal and vertical slopes, c_h and c_v are the horizontal and vertical offsets. To find the slopes and offset values, the two DWCs were calibrated[†] before the data taking started. For the calibration measurement, a pulse generator was used to provide the trigger signal. The measured time delays, while exciting the chamber at –30 mm, the centre and at +30 mm, are listed in Table 6.1 and the corresponding plots are shown in Figure 6.3. The slopes and offsets, derived from the fitting parameters, are reported in Table 6.2.

Position on DWCs	ΔT at DWC1 [ns]		ΔT at DWC2 [ns]	
	Left-Right	Up-Down	Left-Right	Up-Down
30 mm Left or Up	160	160	158	162
0 mm Centre	0	0	0	3
- 30 mm Right or Down	- 160	- 158	-161	-156

Table 6.1: Time delays between left-right or up-down signals with respect to a common signal provided by a pulse generator at three positions of the chambers. These values are plotted and the linear fits provided the constant slopes and offsets for Equation 6.1.

Fitting	DWC1		DWC2	
parameters	horizontal	vertical	horizontal	vertical
Slope	0.1875	0.1887	0.1881	0.1887
Offset	0	-0.1258	0.1881	-0.566

Table 6.2: Horizontal (left-right) and vertical (up-down) slopes and offsets derived from the linear fits (Figure 6.3) for the conversion of time delays, measured by the TDC, into the coordinates of the impact points of beam particle tracks at the two DWCs.

All signal cables from the experimental area were received via a patch panel and then fed to the electronic modules in the CR. Two standard VME crates were used for hosting the ADC, TDC modules and other electronic control boards.

Several set of *runs* were registered with different purposes, e.g., detector calibration, energy scans, position scans, etc. One run is the integration of several ($\mathcal{O}(50k)$) events. In order to evaluate the electronic noise contribution during the data taking, *pedestal* events (i.e., events with the absence of any physics signal) were recorded with a trigger provided by a pulse generator. ADC and TDC values, from the calorimeter and auxiliary detectors, were recorded for each event of a run. To avoid channeling effects (Section 5.3) the calorimeter module was rotated by 1° in the horizontal plane with respect to the beam axis.

[†] https://cds.cern.ch/record/702443/files/sl-note-98-023.pdf

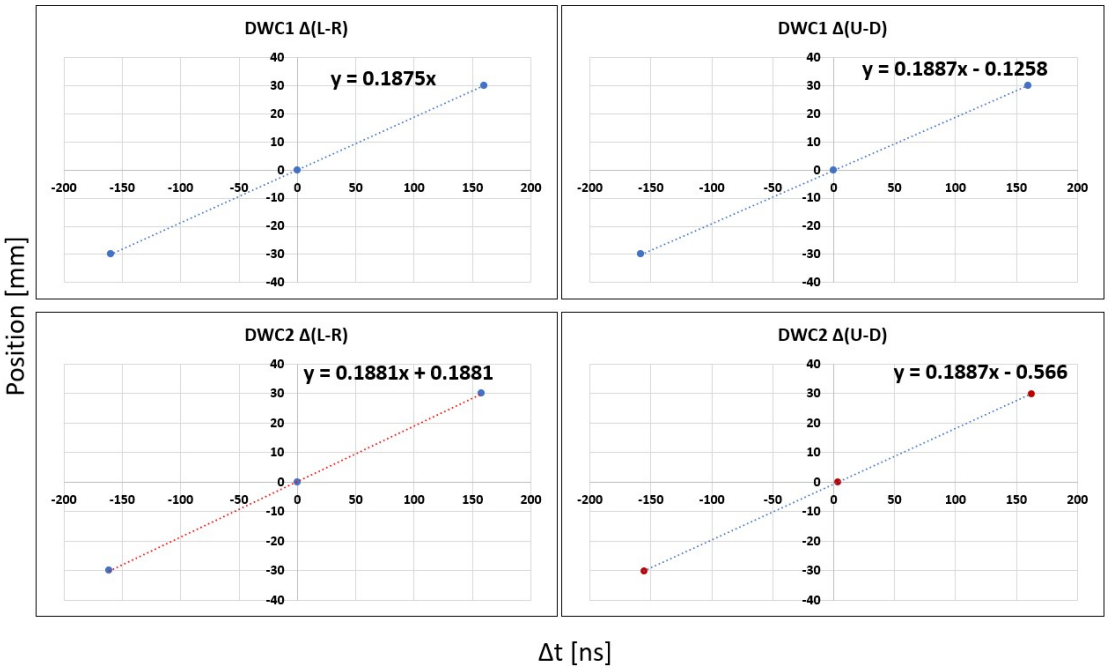

Figure 6.3: Calibration of the DWCs. Time delays between left-right or up-down signals with respect to a common signal provided by a pulse generator at three positions of the chambers. The slopes and offsets extracted by the linear fits are used to calculate the impact points of particle tracks at the two DWCs.

6.3 Data analysis methods

6.3.1 Calibration

The calibration of the SiPM signals has been performed in two steps:

- Equalisation of all SiPM responses (ADC counts).
- Conversion of the ADC counts to number of photoelectrons.

The essence of the procedure is depicted here. A detailed overview of this work has been narrated in Ref. [77]. The SiPM responses were equalised in amplitude, before mounting them on the detector, by tuning the amplifiers. Equal overbreakdown voltages (+7 V) were applied allowing all the SiPMs to operate with roughly the same, stable Photon Detection Efficiency (PDE). The equalisation in amplitude was necessary because one FERS board was serving a unique threshold for 64 SiPMs under the self-triggering readout system.

Figures 6.4a and 6.4b illustrate the High Gain (HG) and Low Gain (LG) spectra, respectively, in ADC counts of one SiPM, for the data taken at DESY beam test with a 6 GeV electron beam. The pedestal peak and the multiphoton peaks of Figure 6.4a are clearly visible in the zoomed-in Figure 6.4c, where the Gaussian fits provide the pedestal peak position and the average peak-to-peak distance for three consecutive multiphoton peaks. These values are used to calculate the calibration constant for the HG spectrum of the SiPM. On the other hand, a correlation of the number of photoelectrons

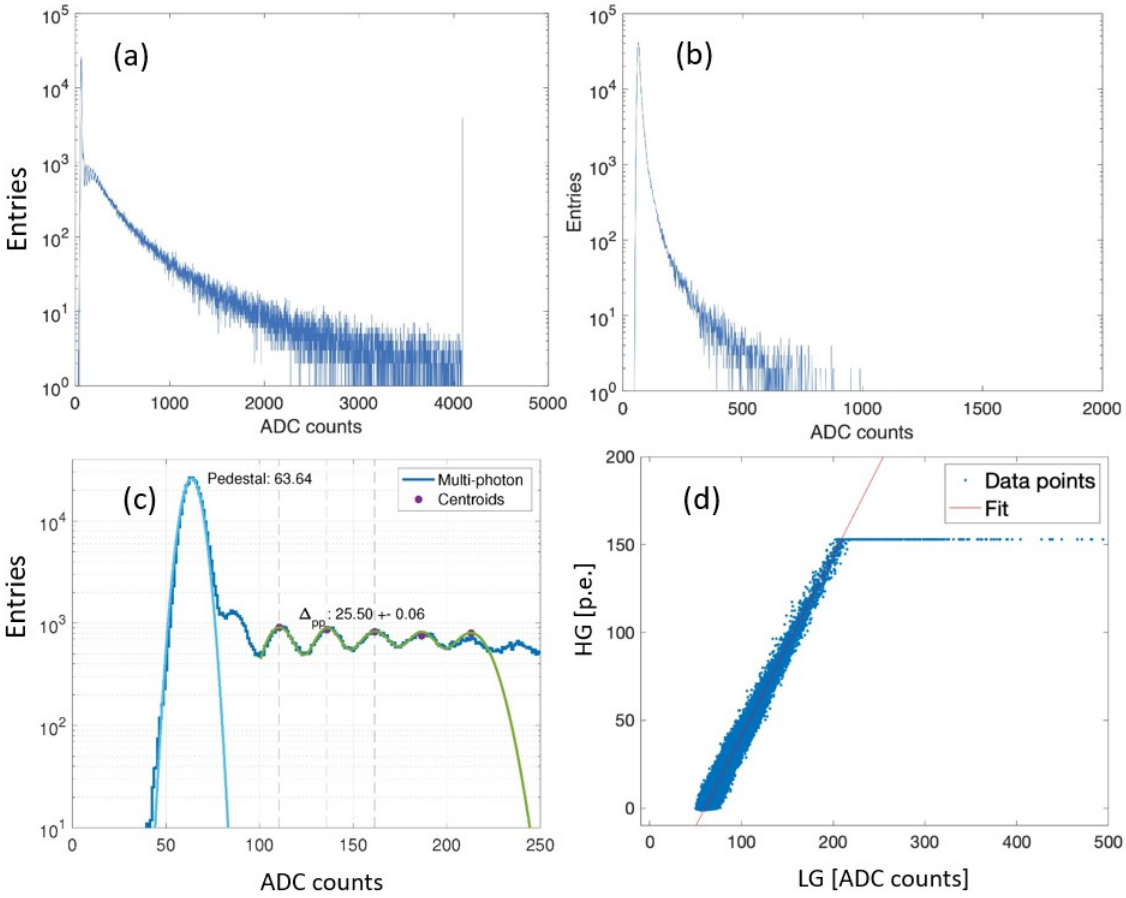

Figure 6.4: Spectra of one SiPM response for the HG amplifier (a) and the LG amplifier (b) for 6 GeV electrons at the DESY beam test. Gaussian fits of the HG spectrum provide the pedestal peak position and the average peak-to-peak distance for the multiphoton peaks (c). Number of photoelectrons extracted from the HG spectrum as a function of the ADC counts of the LG spectrum. The slope provides the conversion factor for the conversion of the LG ADC measurement (pedestal subtracted) to photoelectrons (d). Ref. [77].

extracted from the HG spectrum and the ADC counts of the LG spectrum is shown in the scatter plot of Figure 6.4d. Parameters from the linear fit provide the conversion factor for the pedestal-subtracted LG ADC measurement to photoelectrons.

The calibration of the PMT signals has been performed in two steps:

- Equalisation of PMT signals (ADC counts) of each surrounding tower with respect to the central tower.
- Conversion of the ADC counts in energy scale (GeV) by calculating two fixed scaling factors, one for the scintillation channels and one for the Cherenkov ones, for the full EM-scale module. This step also calculates the LYs, i.e., number of photoelectrons per GeV deposited energy for the SiPM signals.

These two steps are explained hereafter. Given the fact that the central and surrounding towers were read out independently, a normalisation of the signal amplitudes

for the nine towers has been performed. At the beginning of the beam-test period, the PMT signals were roughly normalised, separately for the scintillation and Cherenkov channels, by tuning their operating high voltages. The PMT towers were equalised with respect to the central tower in analysis. Runs with 20 GeV positron beams have been used to perform this step. 20 GeV positron beams have been steered, separately, at each one of the nine towers. A combination of tight cuts, C1-tight OR C2-tight (Section 6.3.2), in the two upstream Cherenkov counters has been applied for flagging positron events. The pedestal peak positions and Most Probable Values (MPVs) of the pedestal-subtracted signal distributions, in ADC counts, are noted for these nine runs. Figures 6.5a and 6.5b show for tower # 8 the pedestal peaks for the scintillation and Cherenkov channels, whereas Figures 6.5c and 6.5d show pedestal-subtracted signal distributions for the respective channels. The MPVs of pedestal-subtracted signals

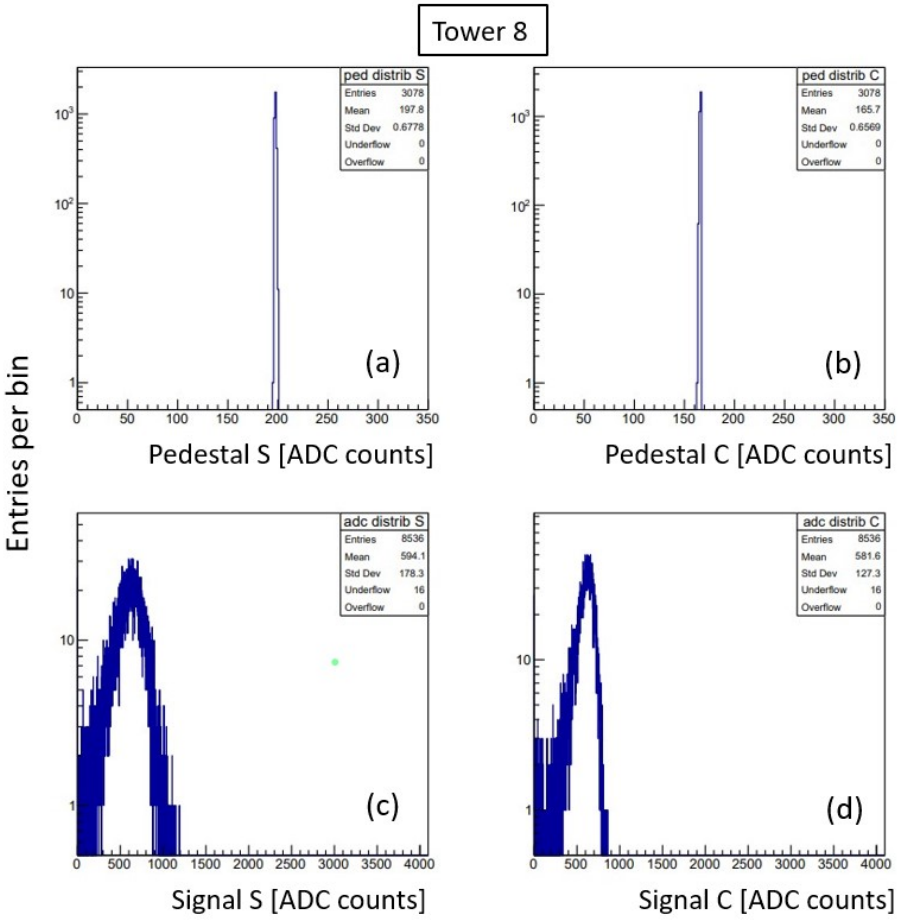

Figure 6.5: A 20 GeV positron beam has been steered at tower # 8. Pedestal peak positions for the scintillation (a) and Cherenkov (b) channels. Pedestal-subtracted signal distributions for scintillation (c) and Cherenkov (d) channels.

of the nine towers have been equalised with respect to that of the central tower. This exercise, performed separately for the scintillation and Cherenkov signals, provides 9×2 equalisation constants, for the external (T_n) and central (T_0) towers.

$$EQ_{S,C}(T_n) = \frac{PMT_{S,C}(T_n)}{SiPM_{S,C}} \quad \text{and} \quad EQ_{S,C}(T_0) = \frac{SiPM_{S,C}}{SiPM_{S,C}} = 1 \tag{6.2}$$

where S is the scintillation signal and C the Cherenkov one. The numerators and denominators of Equations 6.2 are in ADC counts. Numbering of the towers in the transverse plane of the module from the front face is shown in Figure 6.6. The equal-

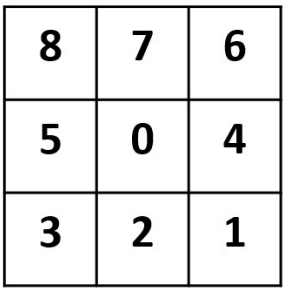

Figure 6.6: Numbering of the towers in the transverse plane of the EM-scale module from the front face.

isation constants, for the scintillation and Cherenkov channels, are listed in Table 6.3. For a 20 GeV positron beam steered at the central tower, event-by-event equalised signal distributions for the nine towers are shown in Figures 6.7 and 6.8 for the scintillation and Cherenkov channels, respectively.

As a second step, with a 20 GeV positron beam steered at the central tower, the equalised signals produced in all towers are summed up event by event as shown in Figure 6.9. The MPVs of these distributions ($ADC_{S,C}$) are ∼5210 and ∼902.5 for the scintillation and Cherenkov channels, respectively. These values are defined as 18.8 GeV i.e., the estimated containment (94%) for 20 GeV electron showers for the EM-scale module. Two fixed scaling factors, $f_S = 277.13$ and $f_C = 48.01$, for the module are calculated through Equation 6.3.

$$f_{S,C} = \frac{ADC_{S,C}}{18.8} \quad \text{where} \quad ADC_{S,C} = \sum_{n=1}^{8} \frac{PMT_{S,C}(T_n)}{EQ_{S,C}(T_n)} + SiPM_{S,C} \tag{6.3}$$

The LYs for the SiPMs of the central tower and the calibration constants for the PMT signals of the external towers are calculated using Equation 6.4.

$$K_{S,C}(T_n) = f_{S,C} \cdot EQ_{S,C}(T_n) \tag{6.4}$$

The obtained values are reported in Table 6.3. As the equalisation constants are 1 for the central tower, the light yields ($K_{S,C}(T_0)$) coincide with the scaling factors ($f_{S,C}$). The subtraction of the pedestal position, a constant offset, is included in the calibration process. For any chosen run, the calibration constants are applied to the pedestal-subtracted ADC counts.

6.3.2 Event selection and efficiency of cuts

CERN SPS beams are not 100% pure. Cleaning the data before using them for physics analysis is a primary step to perform. A significant percentage of other particles (muons, pions, protons etc.) was present in positron beams. In particular, the hadron contamination was dominant at higher energies. DWCs are used to select event samples that

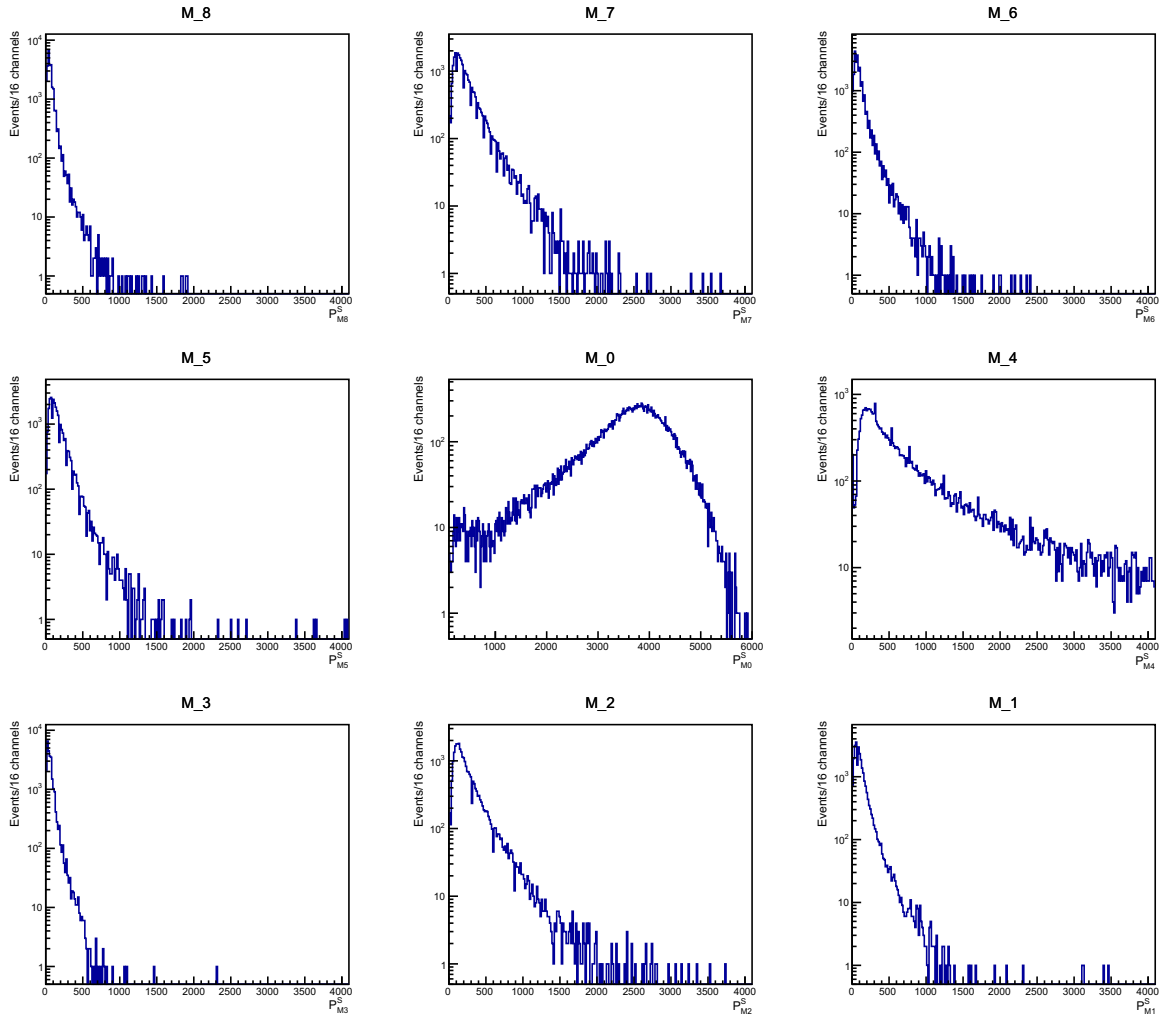

Figure 6.7: Equalised-signal distributions for the scintillation channels in the nine towers obtained with a 20 GeV positron beam.

Tower number	EQ_S	EQ_C	K_S	K_C
0	1	1	277.13 ± 3.36	48.01 ± 1.53
1	0.125 ± 0.001	0.822 ± 0.029	34.52 ± 0.64	39.48 ± 0.91
2	0.122 ± 0.002	0.756 ± 0.027	33.73 ± 0.70	36.27 ± 0.88
3	0.145 ± 0.002	0.895 ± 0.031	40.15 ± 0.81	42.98 ± 0.99
4	0.130 ± 0.002	0.808 ± 0.028	35.89 ± 0.81	38.77 ± 0.91
5	0.114 ± 0.002	0.769 ± 0.026	31.63 ± 0.61	36.91 ± 0.83
6	0.157 ± 0.001	0.975 ± 0.032	43.46 ± 0.76	46.83 ± 0.96
7	0.114 ± 0.001	0.775 ± 0.027	31.63 ± 0.53	37.20 ± 0.86
8	0.155 ± 0.002	0.889 ± 0.030	43.03 ± 0.87	42.69 ± 0.93

Table 6.3: The LYs for the SiPMs of the central tower and the calibration constants for the PMT signals of the external ones, for both the scintillation and Cherenkov channels are listed.

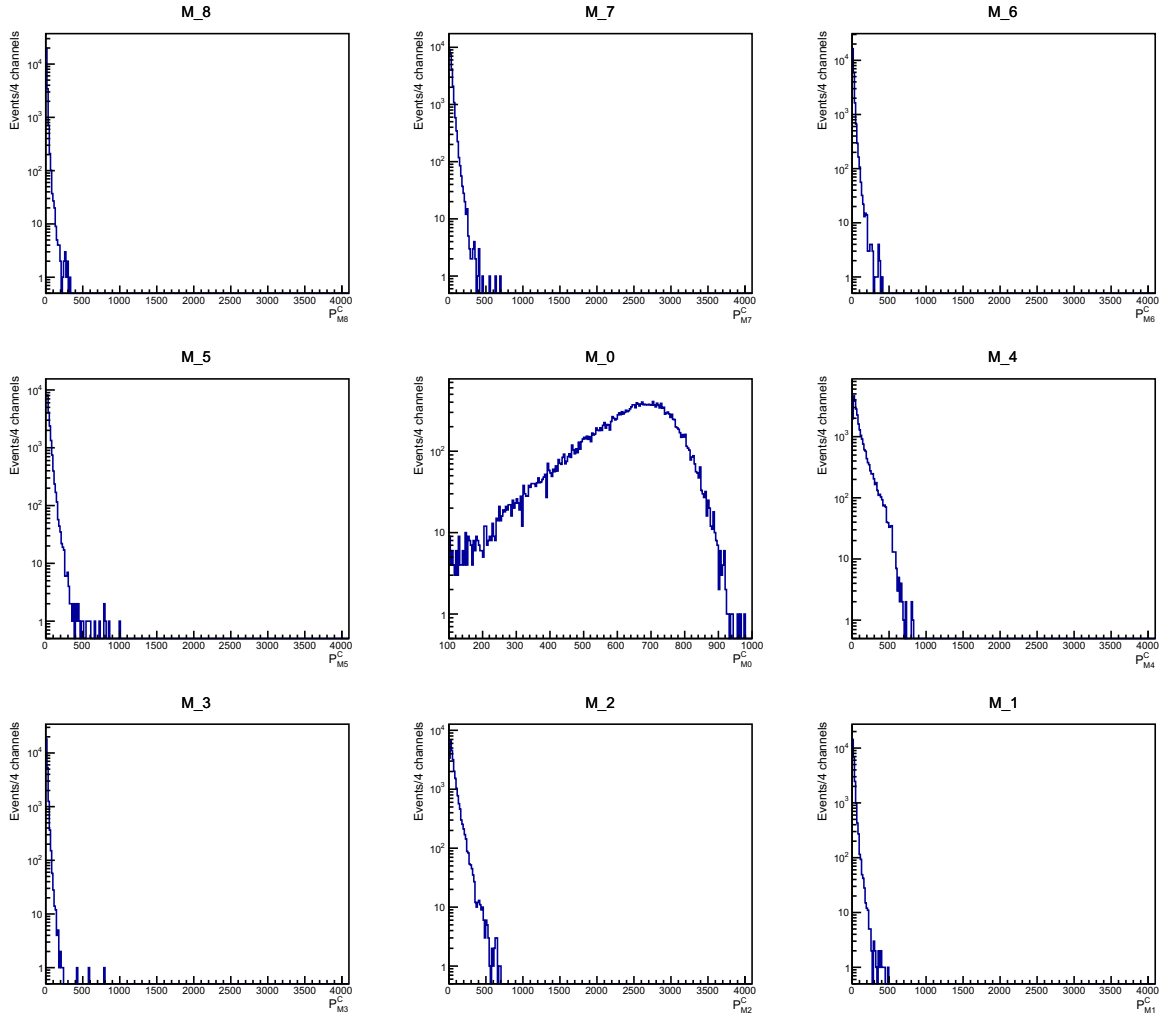

Figure 6.8: Equalised-signal distributions for the Cherenkov channels in the nine towers obtained with a 20 GeV positron beam.

come within a precise beam spot radius, i.e., ∼less than 1 cm around the geometrical centre of the calorimeter front face. Two upstream Cherenkov counters and the PS play vital roles for tagging positron events. Muon and hadron events contribute to the MIP peak of the signal distribution for the PS. In principle, positrons can be selected with a high cut, e.g., greater than 3 MIPs, in the PS signal distribution. The distance between the PS and the calorimeter module was quite large (∼2.85 m). When a positron shower is produced in the lead of the PS, particles in the shower tail are emitted at a large angle with respect to the positron direction. As a result, the shower is only partially sampled in the calorimeter and the measured signal is heavily affected by lateral leakage fluctuations (Figure 6.10). So, unless otherwise specified, the two upstream Cherenkov counters are used to flag positrons in my analysis. The cuts applied in the two signal distributions for the Cherenkov counters (C1 and C2) are written in Table 6.4. The cuts, for C1 and C2, are justified and shown for a run with 20 GeV positrons in Figures 6.11 and 6.12, respectively. Signals at the PS and the downstream MC for the same run are shown in Figures 6.13 and 6.14, respectively.

Systematic studies have been performed for positron beams ranging from 10 GeV

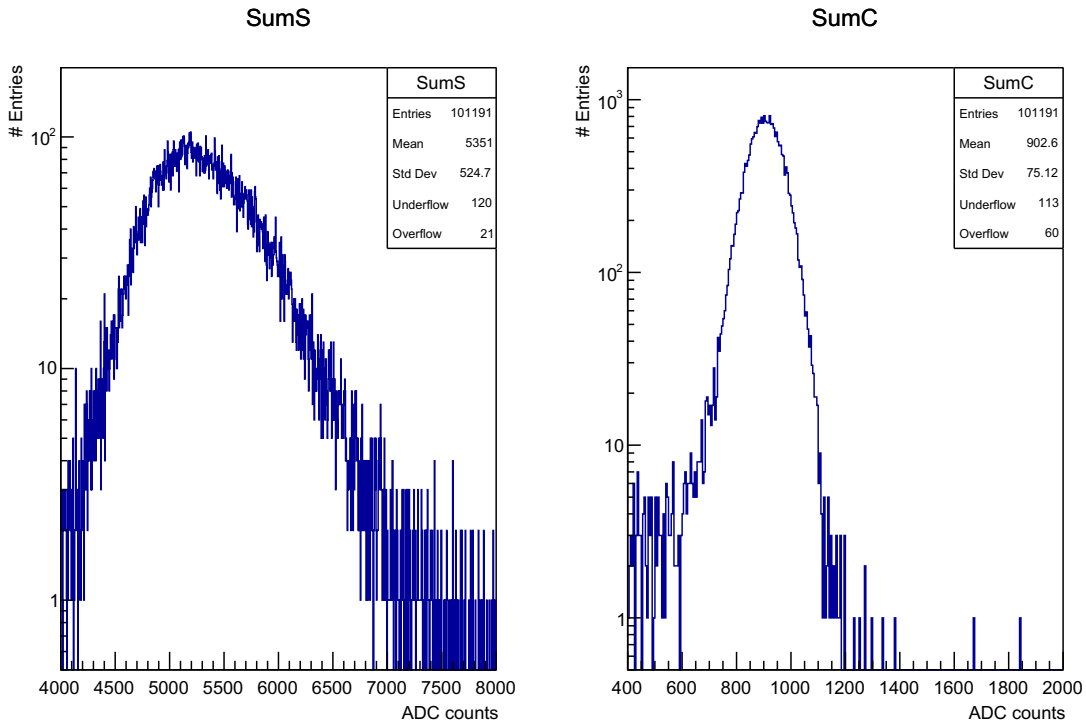

Figure 6.9: Event-by-event distributions of the sum over the nine towers of the scintillation (left) and the Cherenkov (right) signals, for a 20 GeV positron beam steered at the central tower.

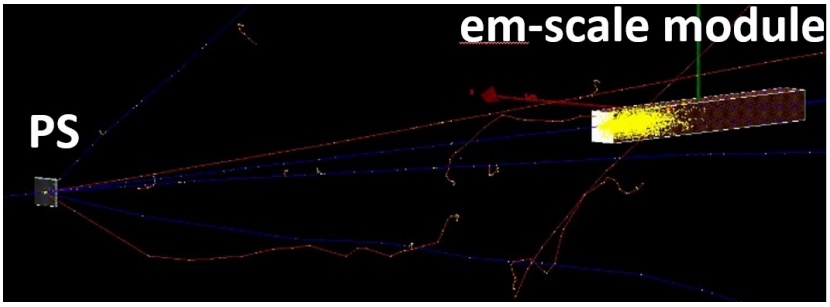

Figure 6.10: The distance between the EM-scale prototype and the upstream PS is ∼2.85 m. Due to such a distance, most positron showers that start to develop in the lead slab of the PS, are only partially contained in the calorimeter.

Cherenkov counter	Loose (L) cut [ADC counts]	Tight (T) cut [ADC counts]
C1	> 2	> 5
C2	> 10	> 18

Table 6.4: Definition of loose and tight cuts in the upstream Cherenkov counters.

to 60 GeV to choose the best cuts for analysis. Figures 6.15a and 6.15b show superimposed signal distributions for seven different cuts, separately for the scintillation and Cherenkov signals. It can be observed that for both channels, selection efficiencies are

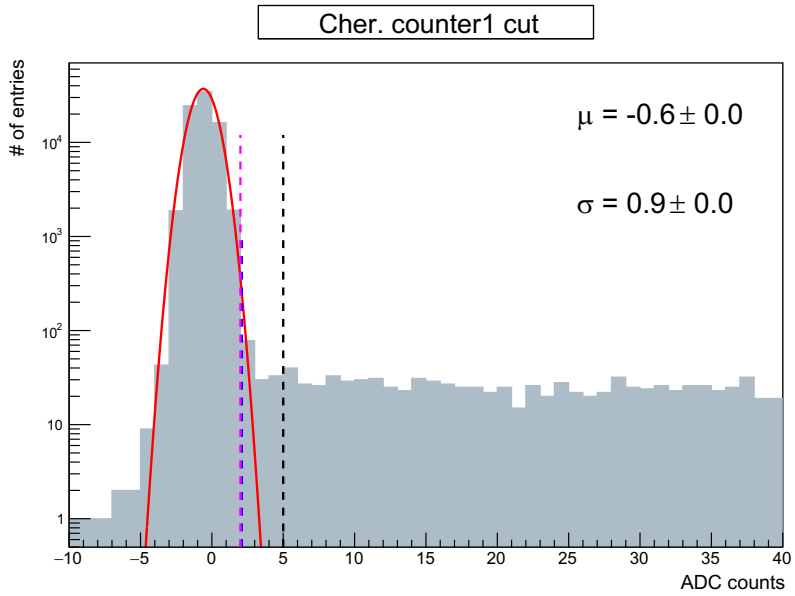

Figure 6.11: The loose and tight cuts, indicated by the pink and black vertical lines, are applied almost at and after $\mu + 3\sigma$ of the pedestal distribution for the Cherenkov counter1. The blue vertical line represents $\mu + 3\sigma$ obtained by the Gaussian fit.

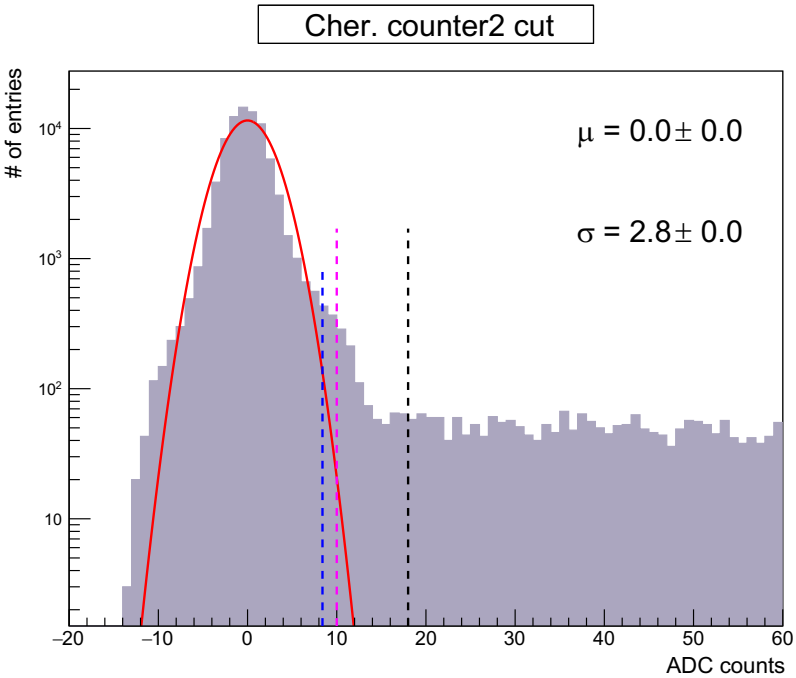

Figure 6.12: Both the loose and tight cuts, indicated by the pink and black vertical lines, are applied after $\mu + 3\sigma$ of the pedestal distribution for the Cherenkov counter2. The blue vertical line represents $\mu + 3\sigma$ obtained by the Gaussian fit.

maximum for a combination of loose cuts, namely (C1T OR C2T) and a combination of tight cuts, namely (C1T OR C2T), in the two Cherenkov counters. These cuts, in particular (C1T OR C2T), has been chosen for performing data analysis. Cuts involv-

ing more than one auxiliary detectors have been preferred over the single cuts, e.g., C1L, C1T, C2L or C2T.

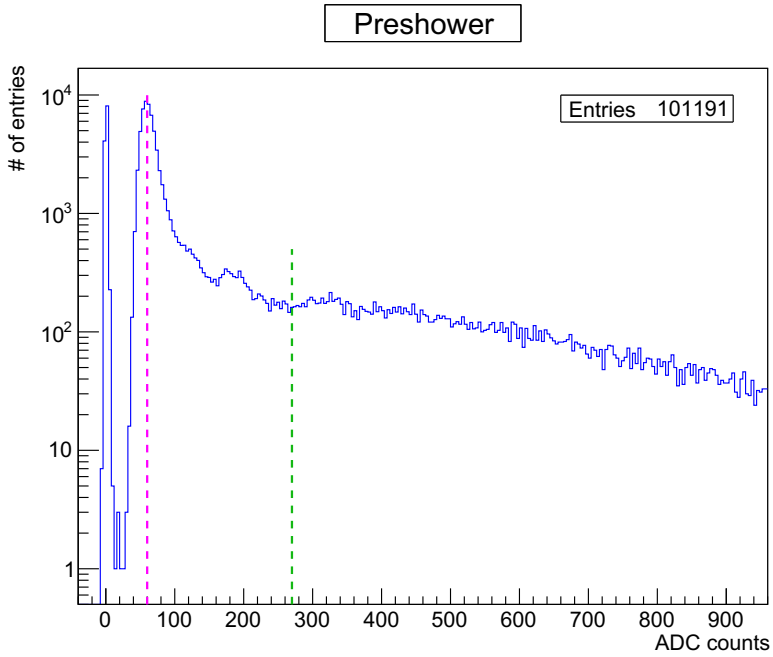

Figure 6.13: Signal distribution at the upstream Preshower. The pedestal peak is at 0 whereas the MIP peak, indicated by the pink vertical line, appears at 60 ADC counts. The high cut at 4.5 MIPs that is used in the analysis is indicated by the green vertical line.

A high cut in the PS signal distribution, PS > 4.5 MIPs (Figure 6.13), is applied to estimate the efficiency of the chosen cuts. In Equations 6.5 and 6.6, the numerators in the Right Hand Side (RHS) provide the number of events selected by the indicated cuts, whereas the denominators are the number of total events taken for the run. These values, for different energies of positron beams, together with the pressure setting for the Cherenkov counters, are reported in Table 6.5. The two parameters at the Left Hand Side (LHS) of Equations 6.5 and 6.6, are the fraction of events passing the respective selection requirements. The request on the PS signal is used to select a subsample of pure electrons. Equation 6.6 defines the fraction of events that satisfy both a request (X) on the Cherekov signals and the high request on the PS signal.

$$f\left(PS > 4.5\,MIPs\right) = \frac{N\left(PS > 4.5\,MIPs\right)}{N_{tot}} \tag{6.5}$$

$$f\left(X \;\; AND \;\; PS > 4.5\,MIPs\right) = \frac{N\left(X \;\; AND \;\; PS > 4.5\,MIPs\right)}{N_{tot}} \tag{6.6}$$

where X = (C1L OR C2L) or (C1T OR C2T). In the RHS of Equation 6.7, the effect of the PS request cancels out since it appears in both the numerator and the denominator. Hence, the efficiency for positrons of the chosen cut (ε_{X^e}) on the Cherenkov signals is determined by Equation 6.7.

$$\varepsilon_{X^e} = \frac{f\left(X \;\; AND \;\; PS > 4.5\,MIPs\right)}{f\left(PS > 4.5\,MIPs\right)} \tag{6.7}$$

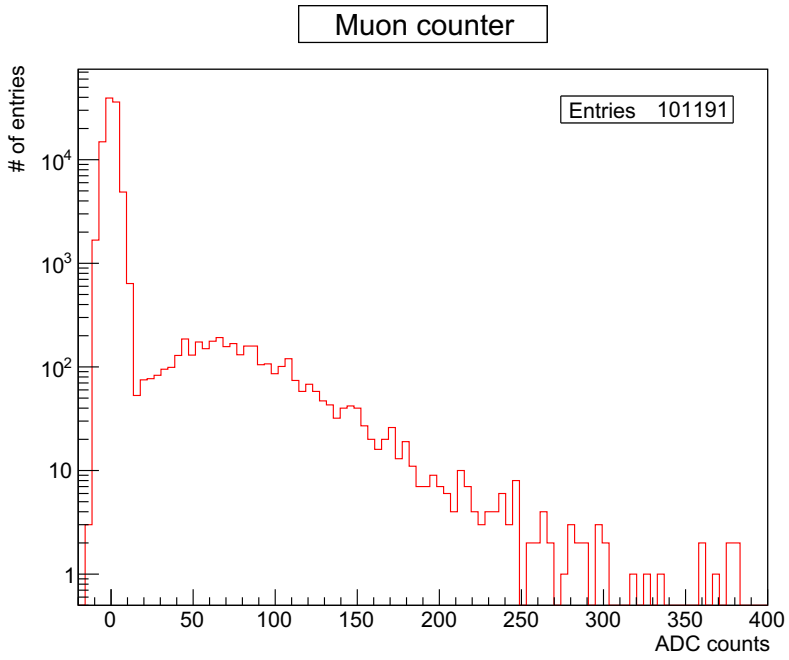

Figure 6.14: Signal distribution at the downstream Muon Counter. The pedestal peak is at 0.

E $[GeV]$	P_{gas} $[mbar]$	Total events	N(PS>4.5MIPs)	N(C1L OR C2L AND PS>4.5MIPs)	N(C1T OR C2T AND PS>4.5MIPs)
6	700	31244	3127	2819	2817
10	700	51640	17918	17520	17518
20	350	101191	20047	17143	17057
30	150	101844	10999	4883	4718
40	80	501857	34324	4878	4494
60	40	101451	4405	231	177

Table 6.5: Gas pressures set at the two Cherenkov counters, the total number of events, number of events selected with the PS cut and a combination of the PS and chosen (X) cuts for analysis are listed for different beam energies.

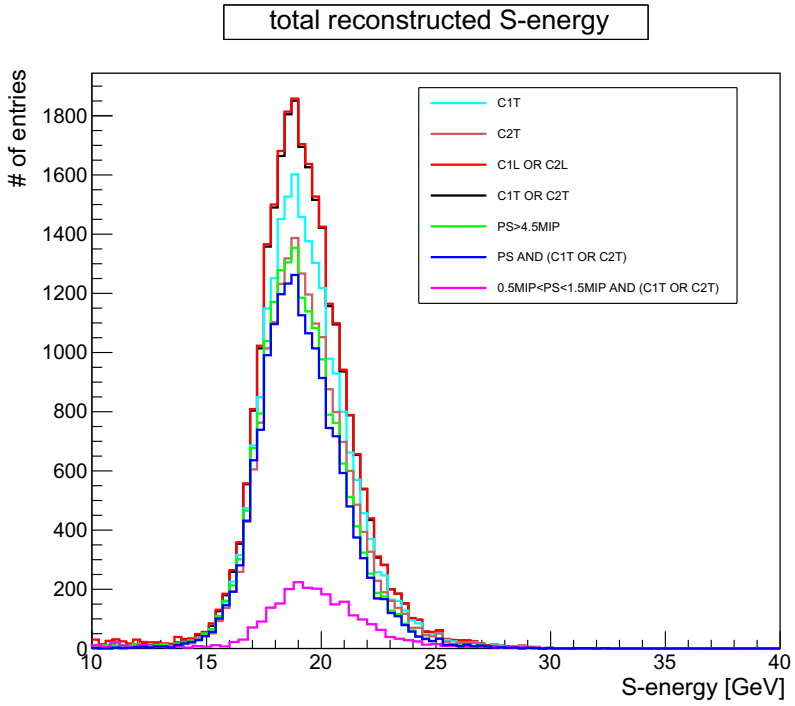

(a)

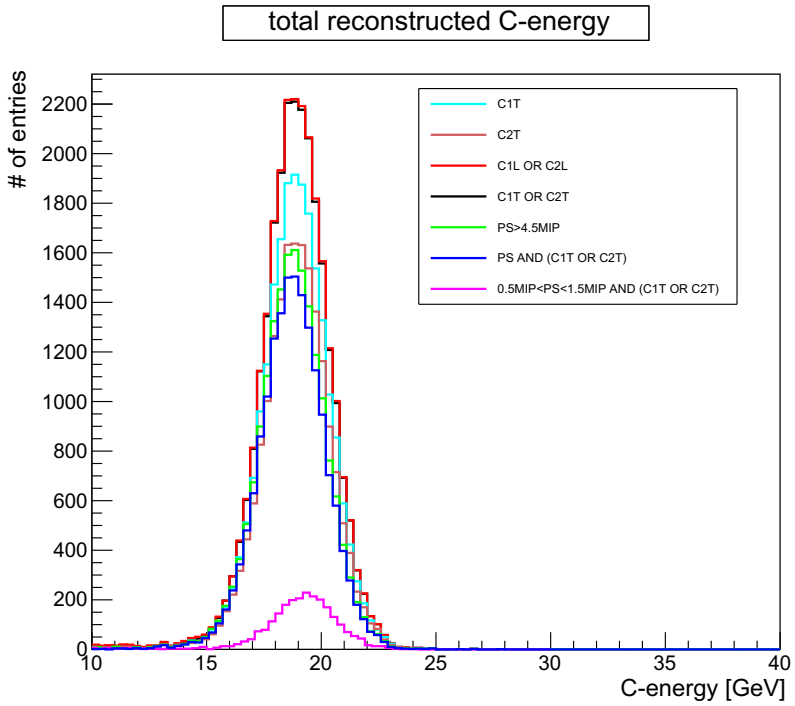

(b)

Figure 6.15: Systematic studies with 20 GeV positron beams to choose the best cuts for analysis. Superimposed reconstructed energies, using different cuts on signal distributions at the auxiliary detectors, for the scintillation channels (a) and Cherenkov channels (b). The distortion in the shape of these distributions comes from the opening of the shower due to the PS position in the line, the impact point dependency of the signals and the too small impact angle of the beam.

In order to cross-check the results about the efficiency for electrons of the Cherenkov cuts, a second sample of pure electrons was selected by requiring that at least 80% of the beam energy (well above a MIP signal) is reconstructed with the calorimeter signals. So, for this case, Equations 6.8, 6.9 and 6.10 are used. Equation 6.8 defines the fraction of events for which reconstructed scintillation and Cherenkov signals, separately, are 80% of the beam energy. As for the PS cut, Equation 6.9 defines the fraction of events that is selected by requiring both the chosen cut (X) and the calorimetry cut.

$$f(E_{CALOR} > 0.8 \cdot E) = \frac{N\left(E_{CALOR} > 0.8 \cdot E\right)}{N_{tot}} \tag{6.8}$$

$$f(X \;\; AND \;\; E_{CALOR} > 0.8 \cdot E) = \frac{N\left(X \;\; AND \;\; E_{CALOR} > 0.8 \cdot E\right)}{N_{tot}} \tag{6.9}$$

Finally, Equation 6.10 provides an independent estimate of the efficiency of the Cherenkov selection cut (X) for positrons.

$$\varepsilon_{X^e} = \frac{f(X \;\; AND \;\; E_{CALOR} > 0.8 \cdot E)}{f\left(E_{CALOR} > 0.8 \cdot E\right)} \tag{6.10}$$

where, E is the beam energy, E_{CALOR} is the energy reconstructed, independently, by the scintillation and Cherenkov channels. So, $E_{CALOR} > 0.8 \cdot E$ really means ($E_S > 0.8 \cdot E$ AND $E_C > 0.8 \cdot E$). The results, for different energies of positron beams, are reported in Table 6.6. The efficiencies calculated with Equations 6.7 and 6.10, for positron beams of energies up to 60 GeV, look to be compatible with each other, as shown in Figures 6.16a and 6.16b for (C1L OR C2L) and (C1T OR C2T), respectively. The comparable numbers tell that the contribution of hadrons, in shower formation with at least 80% of beam energy, is negligible for any given energies. For further higher energies the statistics of selected positron samples are too low.

E $[GeV]$	Total events	N(E_{CALOR} >0.8·E)	N(C1L OR C2L AND E_{CALOR} >0.8·E)	N(C1T OR C2T AND E_{CALOR} >0.8·E)
6	31244	4713	4167	4166
10	51640	23742	23260	23255
20	101191	28702	24487	24359
30	101844	16045	6756	6519
40	501857	52711	6626	5999
60	101451	6920	333	227

Table 6.6: The total number of events, number of events selected with cuts in the reconstructed shower energy and number of events selected with a combination of cuts in the reconstructed shower energy and chosen cuts (X) for analysis are listed for different beam energies.

Another important verification, in the context of efficiency of chosen cuts, has been done using Formulae 6.11.

$$\begin{aligned} \varepsilon_{(C1L \quad OR \quad C2L)} &= 1 - (1 - \varepsilon_{(C1L)}) \cdot (1 - \varepsilon_{(C2L)}) \\ \varepsilon_{(C1T \quad OR \quad C2T)} &= 1 - (1 - \varepsilon_{(C1T)}) \cdot (1 - \varepsilon_{(C2T)}) \end{aligned} \tag{6.11}$$

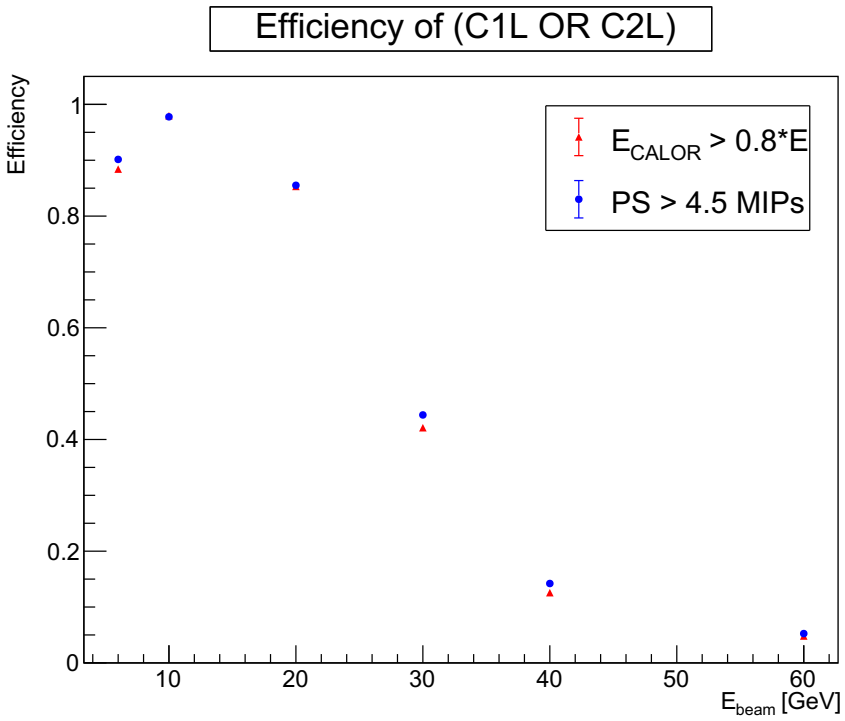

(a)

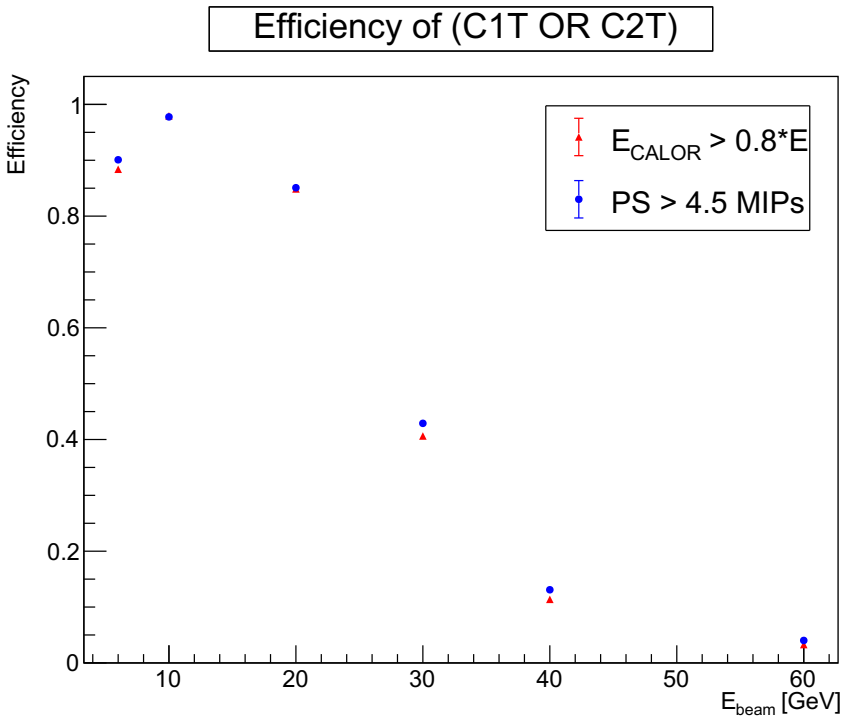

(b)

Figure 6.16: Efficiency of combination of loose cuts (a) and tight cuts (b) are compatible, when calculated with respect to PS $>$ 4.5 MIPs and $E_{CALOR} > 0.8 \cdot$E, as a function of beam energy.

These relations should hold as soon as there are no correlations among the signals in the different Cherenkov counters (as it should be). All efficiencies in these formulae are calculated using Equation 6.7. The numbers of selected events and the efficiencies are reported, for different beam energies, in Tables 6.7 and 6.8, respectively. The efficiency of the combined cuts in the two Cherenkov counters has been expressed in terms of individual efficiencies of cuts in the single Cherenkov counters. The differences for some energy values (e.g., for 20 GeV electrons) are not fully understood and seems to point to some correlated inefficiency. The associated errors are calculated with a binomial approximation.

The Purity of the selection and the beam contamination, with the two chosen cuts, were estimated as discussed in Section 6.4.1.

E [GeV]	N(PS>4.5MIP)	N(C1L AND PS>4.5MIP)	N(C1T AND PS>4.5MIP)	N(C2L AND PS>4.5MIP)	N(C2T AND PS>4.5MIP)
6	3127	2758	2756	2751	2741
10	17918	17196	17185	16862	16809
20	20047	14673	14609	12928	12623
30	10999	3167	3119	2722	2543
40	34324	2847	2769	2345	1981
60	4405	64	57	176	125

Table 6.7: The number of events selected with a cut on the PS signal and with a combination of cuts on the PS signal and signals at individual Cherenkov counters is listed for different beam energies.

Energy [GeV]	$\varepsilon_{(C1L\,OR\,C2L)}$ [%]	1–[(1-$\varepsilon_{(C1L)}$) ×(1-$\varepsilon_{(C2L)}$)][%]	$\varepsilon_{(C1T\,OR\,C2T)}$ [%]	1–[(1 - $\varepsilon_{(C2T)}$) ×(1 - $\varepsilon_{(C2T)}$)][%]
6	90.2 ± 0.2	98.6 ± 0.1	90.1 ± 0.2	98.5 ± 0.1
10	97.8 ± 0.1	99.8 ± 0.0	97.8 ± 0.1	99.8 ± 0.0
20	85.5 ± 0.1	90.5 ± 0.1	85.1 ± 0.1	90.0 ± 0.1
30	44.4 ± 0.2	46.4 ± 0.2	42.9 ± 0.2	44.9 ± 0.2
40	14.2 ± 0.1	14.6 ± 0.1	13.1 ± 0.1	13.4 ± 0.1
60	5.2 ± 0.1	5.4 ± 0.1	4.0 ± 0.1	4.1 ± 0.1

Table 6.8: The efficiencies of the combined cuts on the two Cherenkov counters and these as a function of the individual efficiencies of cuts in the single Cherenkov counters are listed for different beam energies.

To select events within a precise beam spot area, a cut on the beam spot radius, r ($= \sqrt{x^2 + y^2}$) < 1 cm, measured with the DWCs is also applied for data analysis.

6.4 Studies on beam

6.4.1 Beam composition

Based on the estimation of efficiency of the two chosen cuts, measurements of beam composition and purity, as a function of energy, have been performed. The selected positron beam that was derived from a secondary pion beam, is a composition of several particles. The real beam purity is defined by

$$P_{real} = \frac{total\,number\,of\,positrons}{total\,number\,of\,all\,particles} = \frac{T_p}{N} \tag{6.12}$$

The denominator in Equation 6.12 is simply the number of total events taken for a run. Let us define N_{sel} as the number of events selected with a given cut on the Cherenkov signals. If a given cut has an efficiency ε_X and assuming that the selected (positron) sample has a very little contamination, the total number of positron events present in the full data sample can be estimated as

$$N_P = \frac{N_{sel}}{\varepsilon_X} \tag{6.13}$$

But in reality this number would be lower, because the purity of the selection procedure is never 100%, i.e., also the selected sample is contaminated by events due to particles other than positrons. In the assumption that the selection is very pure, a first order approximation of beam purity can be determined by Equation 6.14:

$$P_{beam} = \frac{N_{sel}}{\varepsilon_X \times N} \tag{6.14}$$

The beam purity can be defined as the number of positrons present in the data sample (N_{sel}/ε) over the number of all particles (N). Figure 6.17a illustrates the beam purity, defined by Equation 6.14 for the two chosen cuts, as a function of the energy. The values (Table 6.9), comparable for the two cuts, fall exponentially from ∼60% for 10 GeV to ∼15% for 40 GeV. The data points for 6 GeV and 60 GeV do not fit in the picture, because we have taken less statistics for 6 GeV data and only a limited sample of events survive after the selection for runs with 60 GeV.

However, the selection cuts are not sufficient to extract pure samples of positrons. The selected samples also contain a fraction of muons and hadrons. As a consequence, the beam purity is overestimated. Since the selection purity is expected to be higher with tight cuts than with looser ones, the overestimation is larger in the second case (as seen in Figure 6.13a). So, the definition given by Equation 6.14 must be improved. A better approximation of beam purity can be provided by Equation 6.15, which takes into account the efficiencies of cuts in Cherenkov counters for selection of muons. This approximation would be correct in the case the beam contamination is dominated by muons. However, since the efficiency of the Cherenkov counters for hadrons is lower than for muons, the beam purity, in this case, is expected to be underestimated. The efficiency for muons of the Cherenkov counters can be estimated by Equation 6.16 that is similar to Equations 6.7 and 6.10. Muons are selected using the response in the

Beam energy	C1L OR C2L			C1T OR C2T		
$[GeV]$	N_{sel}	ε	P_{beam} [%]	N_{sel}	ε	P_{beam} [%]
6	6655	0.902	23.6 ± 0.2	6479	0.901	23.0 ± 0.2
10	29595	0.978	58.5 ± 0.2	29457	0.978	58.3 ± 0.2
20	26824	0.855	31.0 ± 0.1	26158	0.851	30.4 ± 0.1
30	8666	0.444	19.2 ± 0.1	7575	0.429	17.3 ± 0.1
40	12944	0.142	18.1 ± 0.1	8885	0.131	13.5 ± 0.1
60	2573	0.052	48.5 ± 0.2	1338	0.040	32.8 ± 0.1

Table 6.9: Samples selected with cuts only in Cherenkov counters, the efficiency of these cuts calculated by Equation 6.7 and the beam purity estimated by Equation 6.14 are listed for positron beams of different energies.

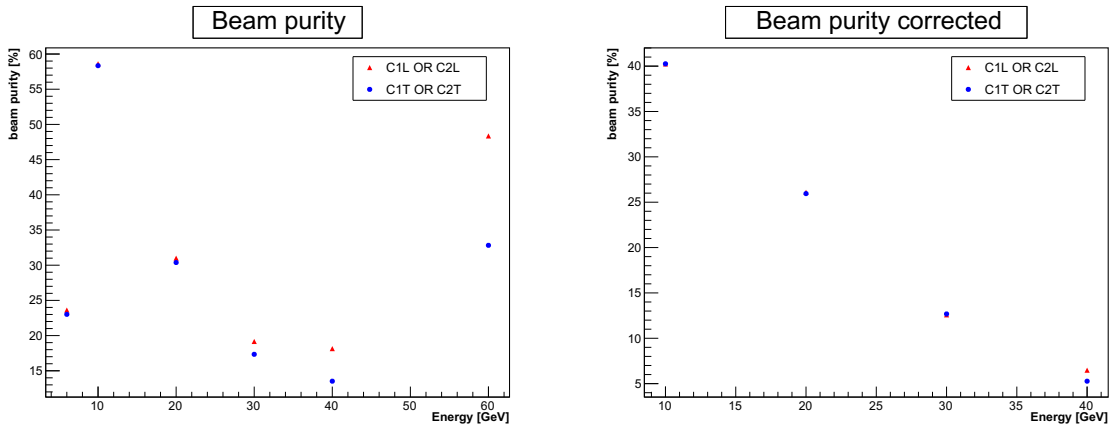

(a) (b)

Figure 6.17: Beam purity calculated by Equation 6.14 that gives a first order approximation (a) and Equation 6.15 taking into account the efficiency of Cherenkov counters for muon selection (b) for cuts C1L OR C2L and C1T OR C2T as a function of beam energy.

downstream MC. A low cut, MC > 20 ADC counts, has been applied to select a reasonable number of muons.

$$P_{beam}(modified) = \frac{\frac{Nsel}{N} - \varepsilon_{X^\mu}}{\varepsilon_{X^e} - \varepsilon_{X^\mu}} \tag{6.15}$$

$$\varepsilon_{X^\mu} = \frac{\varepsilon\,(X \;\; AND \;\; MC > 20)}{\varepsilon(MC > 20)} \tag{6.16}$$

The modified beam purity, as shown in Figure 6.17b, has been dropped significantly, as expected, for different beam energies. Data points for tight cuts appearing below that for loose cuts is recovered for 10, 20 and 30 GeV, whereas for 40 GeV the difference between the two values has dropped to 1% from 5%. All relevant numbers including efficiencies of cuts in Cherenkov counters for selection of muons and the associated errors calculated with Binomial approximation are reported in Table 6.10.

E $[GeV]$	N(MC >20)	N(C1L OR C2L AND MC>20)	$\varepsilon_{(C1L\ OR\ C2L)^{\mu}}$ [%]	N(C1T OR C2T AND MC>20)	$\varepsilon_{(C1T\ OR\ C2T)^{\mu}}$ [%]
6	1516	725	47.8 ± 1.3	721	47.6 ± 1.3
10	875	263	30.1 ± 1.6	259	29.6 ± 1.5
20	3592	204	5.7 ± 0.4	183	5.1 ± 0.4
30	4457	149	3.3 ± 0.3	102	2.3 ± 0.2
40	22618	401	1.8 ± 0.1	258	1.1 ± 0.1
60	3722	115	3.1 ± 0.3	79	2.1 ± 0.2

Table 6.10: Number of muon samples selected with a low cut in the MC, number of muon samples that survived a combination of MC cut and the selection cuts chosen to tag positrons, efficiency for muons of the selection cuts estimated with Equation 6.16 are listed for different beam energies.

An underestimation of beam contamination, N_{cont}, is calculated by subtracting the estimated number of positrons from the total number of events. The numbers are reported in Table 6.11 for different beam energies, as calculated with Equation 6.17 (first order approximation for the beam purity). On the other hand, an overestimation of true beam contamination is calculated using Equation 6.15 and the numbers are reported in Table 6.12.

$$\begin{aligned} N_{cont} &= N - \left(\frac{N_{sel}}{\varepsilon}\right) \\ N_{cont}[\%] &= 1 - P_{beam} \end{aligned} \tag{6.17}$$

Beam energy	C1L OR C2L		C1T OR C2T	
$[GeV]$	N_{cont}	$N_{cont}[\%]$	N_{cont}	$N_{cont}[\%]$
6	23862	76.4	24052	77.0
10	21373	41.4	21510	41.7
20	69823	69.0	70448	69.6
30	82324	80.3	84185	82.7
40	410776	81.9	433996	86.5
60	52386	51.6	68152	67.2

Table 6.11: Contamination of the SPS positron beams calculated with two cuts chosen to flag positrons is listed for different beam energies.

As mentioned already, the selections made with cuts (C1L OR C2L) and (C1T OR C2T) are not 100% pure. It is important to make an assessment of purity of these selections for different beam energies. In order to do so, the rejection factor (R) is determined for each energy. R, given by Equation 6.18 and hence, the inverse of

Beam energy $[GeV]$	C1L OR C2L		C1T OR C2T	
	$P_{beam}(modified)$ [%]	$N_{cont}(modified)$ [%]	$P_{beam}(modified)$ [%]	$N_{cont}(modified)$ [%]
10	40.2	59.8	40.2	59.8
20	26.1	73.9	25.9	74.1
30	12.6	87.4	12.7	87.3
40	6.5	93.5	5.3	94.7

Table 6.12: The underestimated purity (calculated by Equation 6.15) and the corresponding true values of overestimated contamination of the SPS positron beams, calculated with the two cuts chosen to flag positrons, are listed for different beam energies.

Equation 6.16, is defined as the ratio of number of muons in the beam, selected with the MC, to the number of muons survived with a given cut. It would be expected that very few muons survive with chosen cuts in the Cherenkov counters. The purity of selection is proportional to R. Figure 6.18 illustrates the exponential drop of R^{-1} i.e., the muon efficiency of the two chosen cuts for selection of positron samples with increasing beam energy. Finally, the contamination of selection (C_{sel}) and purity of selection (P_{sel}) are derived using Equations 6.19 and 6.20.

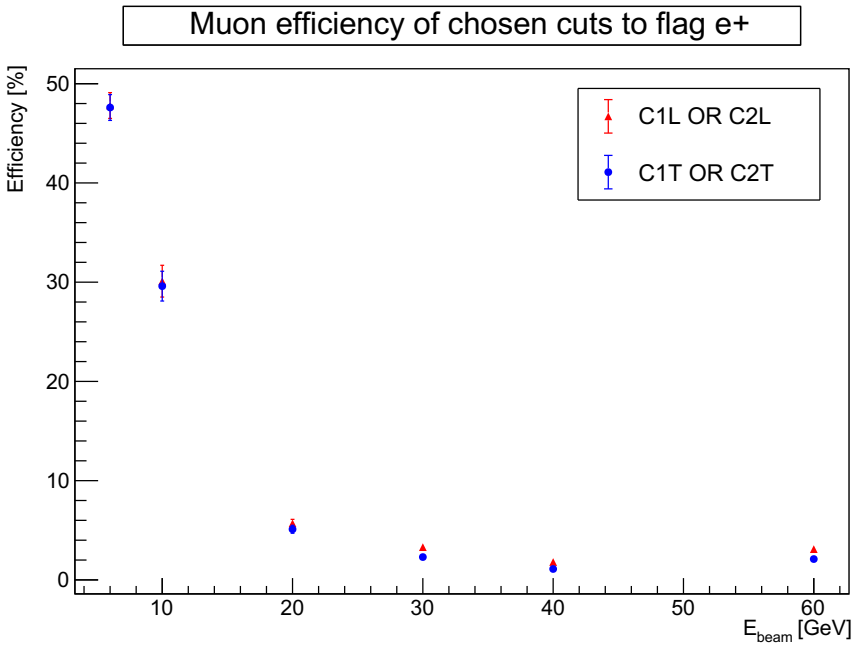

Figure 6.18: Efficiency for muons of the two chosen selection cuts to flag positron samples (i.e., $\varepsilon^{\mu}_{(C1L\ OR\ C2L)}$ and $\varepsilon^{\mu}_{(C1T\ OR\ C2T)}$) as a function of beam energy.

$$R = \frac{1}{\varepsilon_X(muons)} = \frac{\varepsilon(MC > 20)}{\varepsilon\,(X\ \ AND\ \ MC > 20)} \tag{6.18}$$

$$C_{sel} = \frac{N_{cont}}{R} \tag{6.19}$$

$$P_{sel} = 1 - \left(\frac{C_{sel}}{N_{sel}}\right) \tag{6.20}$$

Figure 6.19 shows the upper bound of selected-sample purity as a function of beam energy. All relevant numbers are put together in Table 6.13. On the other hand, selected-sample contamination estimated with N_{cont}(modified) and hence the lower bound of true selected-sample purity are calculated and reported in Table 6.14.

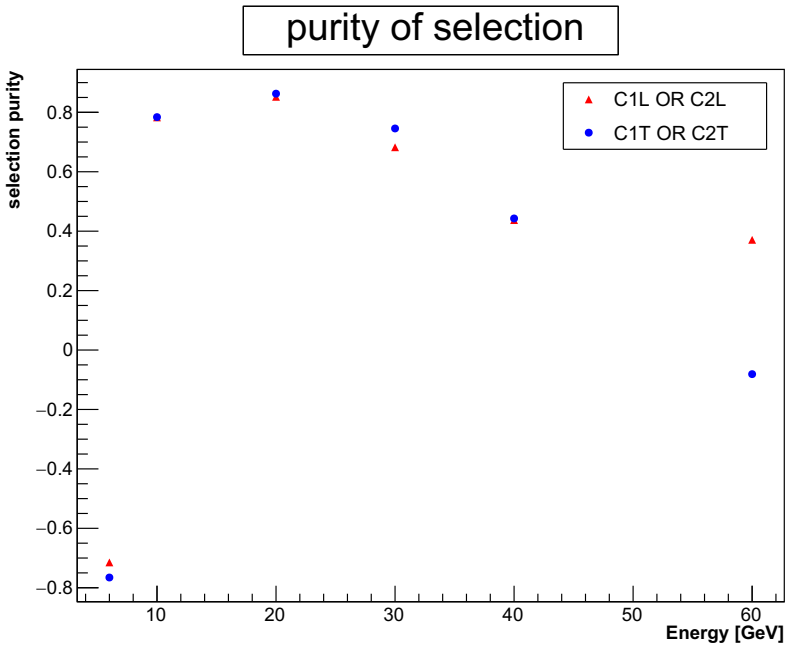

Figure 6.19: Purity of selection of cuts C1L OR C2L and C1T OR C2T as a function of energy.

Beam energy	C1L OR C2L			C1T OR C2T		
$[GeV]$	R	C_{sel}	P_{sel} [%]	R	C_{sel}	P_{sel} [%]
6	2.1	11411	-	2.1	11439	-
10	3.3	6424	78.0	3.4	6367	78.4
20	17.61	3966	85.2	19.63	3589	86.3
30	29.91	2752	68.2	43.70	1927	74.6
40	56.40	7283	43.7	87.67	4951	44.3
60	32.37	1619	37.1	47.11	1447	-

Table 6.13: Rejection factor, contamination of selection and purity of selection for different beam energies are listed. Selection purities for 6 GeV with both cuts and for 60 GeV with C1T OR C2T are unphysical due to low statistics as mentioned before.

Beam energy [GeV]	C1L OR C2L		C1T OR C2T	
	C_{sel}(modified)	P_{sel}(modified) [%]	C_{sel}(modified)	P_{sel}(modified) [%]
10	9358	68.4	9083	69.2
20	4246	84.2	3820	85.4
30	2976	65.7	2035	73.1
40	8320	35.7	5421	39.0

Table 6.14: Selection-sample contamination estimated with modified beam contamination (Equation 6.15) and true selected-sample purity, for different beam energies, are listed.

6.4.2 Beam divergence and positioning

Beam with low divergence allows the particles to be fully contained in the calorimeter module. Angular measurements on particle tracks provide the amount of beam divergence. If (X_1, Y_1, Z_1) and (X_2, Y_2, Z_2) are the coordinates of impact points of a beam particle on DWC1 and DWC2 as illustrated in Figure 6.20, then θ_X and θ_Y are the measures of beam divergence, where $tan\ \theta_X = \frac{X_2 - X_1}{Z_2 - Z_1}$, $tan\ \theta_Y = \frac{Y_2 - Y_1}{Z_2 - Z_1}$ and $Z_2 - Z_1 =$ 1.77 m, is the distance between two wire chambers. Figure 6.21a shows the distribu-

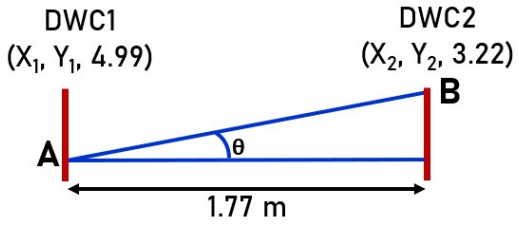

Figure 6.20: The particle track AB makes an angle θ with the straight line joining the two wire cambers. Measurements of θ in both the horizontal and vertical planes provide the amount of beam divergence.

tions of θ_X and θ_Y, separately, for 20 GeV positron beam. Figure 6.21b is an event by event correlation between θ_X and θ_Y, where the core of the scatter plot is confined within 0.1°. These show that the beam divergence was not significant.

The mean values of the X and Y coordinates of impact points of the tracks on the wire chamber, that was installed closer to the calorimeter module, along with the standard deviations, are measured for different energies of positron beams from 6 GeV to 100 GeV. Figure 6.22a shows scatter plot of the X and Y coordinates of impact points for a 60 GeV positron beam and Figure 6.22b shows a good positioning of beams throughout different energies.

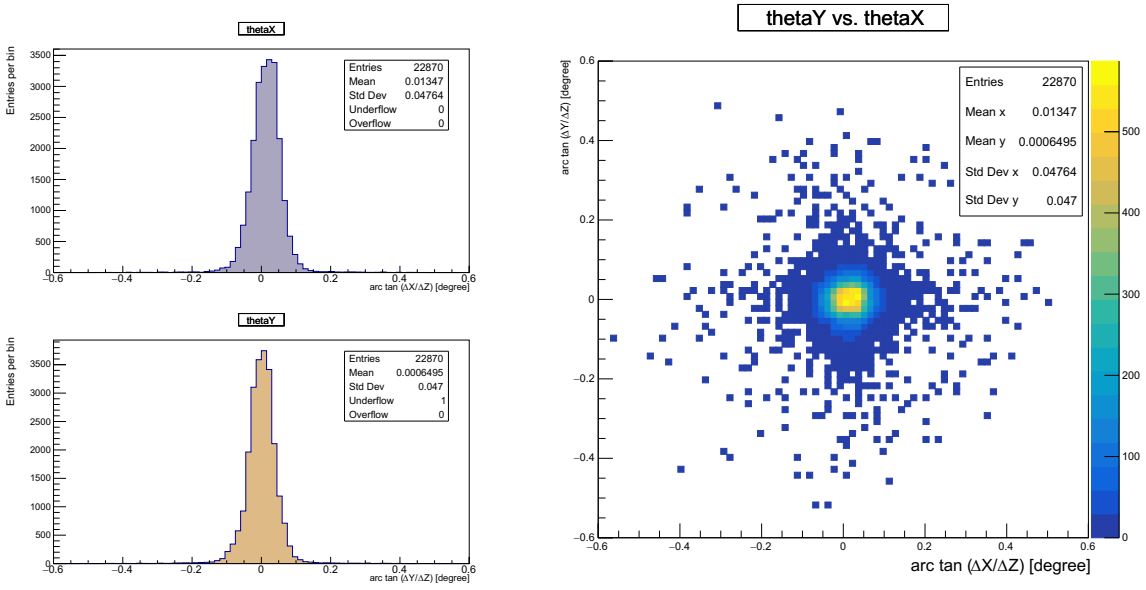

(a) (b)

Figure 6.21: The distribution of θ_X, in top, and θ_Y, at bottom (a). The scatter plot of θ_X and θ_Y shows a significant beam divergence only for less than a hundred events out of $\sim$ 23k samples of 20 GeV positrons.

6.5 Experimental results

6.5.1 Reconstructed energy and shower map

The total scintillation or Cherenkov signals, i.e., the sum of signals from eight PMTs and 160 SiPMs at nine towers, provide an estimate of the total shower energy. The total shower energy has been reconstructed by converting the PMT and SiPM signals to energy values using calibration constants (Section 6.3.1). For a 30 GeV positron beam, the total shower energy reconstructed, event by event, independently by the scintillation and Cherenkov channels are shown in Figures 6.23a and 6.23b, respectively. The mean reconstructed energies obtained with Gaussian fits are 28.86 $\pm$ 0.04 GeV and 28.55 $\pm$ 0.03 GeV for the scintillation and Cherenkov channels, respectively. In Figure 6.23a, the very few events around 0 GeV miss the calorimeter totally. On the other hand, the scatter plot in Figure 6.24 shows the correlation between the energy reconstructed by the scintillation channels and that by the Cherenkov ones, for 20 GeV positron beams steering the tower # 5. Few tens of events, that appear at less than 15 GeV for both channels, represent the energy leakage due to the large divergence of shower particles for showers started in the PS.

Nine energy scan runs, each of 30k events and with a 20 GeV positron beam steered at the center of each individual tower, have been taken. For these runs, the percentage of the total shower energy deposited in the tower at which beam was steered, has been measured separately for the scintillation and Cherenkov channels. Figure 6.25 shows these measurements as a function of the tower number (Figure 6.6). From 66 to 90% of the total shower energy, for both channels, is deposited in the tower hit by the beam. For any given energy, the total shower energy is lower, due to leakage, when the beam is

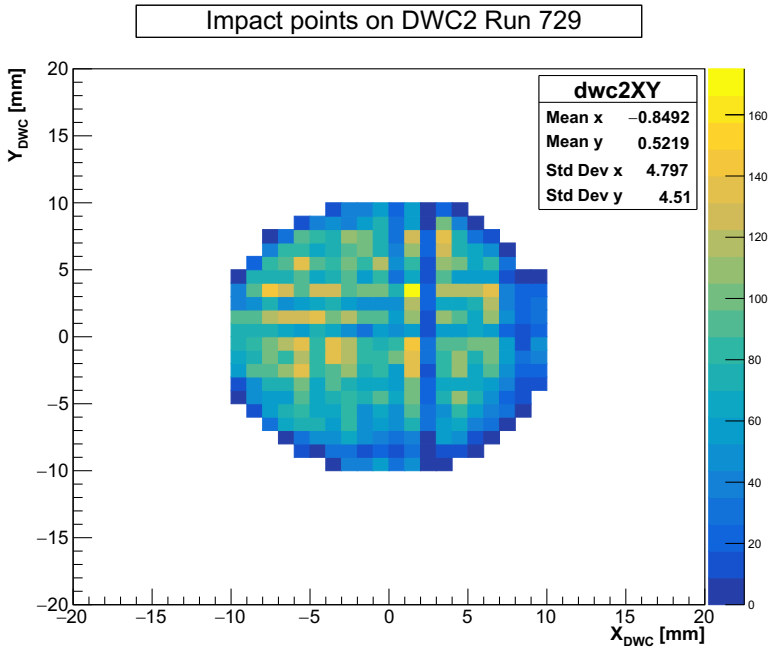

(a)

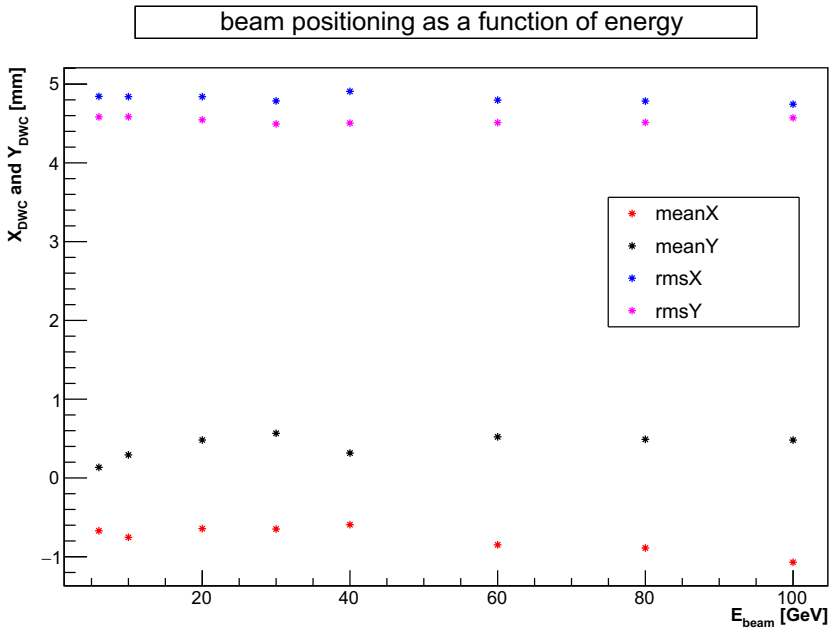

(b)

Figure 6.22: Scatter plot of the X and Y impact points for 60 GeV particle tracks measured with a Delay Wire Chamber is illustrated (a). Mean and standard deviation values of the X and Y impact points for particle tracks of different energies show good positioning of the beams (b).

steered at any external tower compared to that when the beam is steered at the central one. As a result, the fraction of the total shower energy deposited in any external tower is measured to be higher than that in the central one. Figure 6.26 shows the distributions of the total shower energy when beam is steered, separately, at the tower

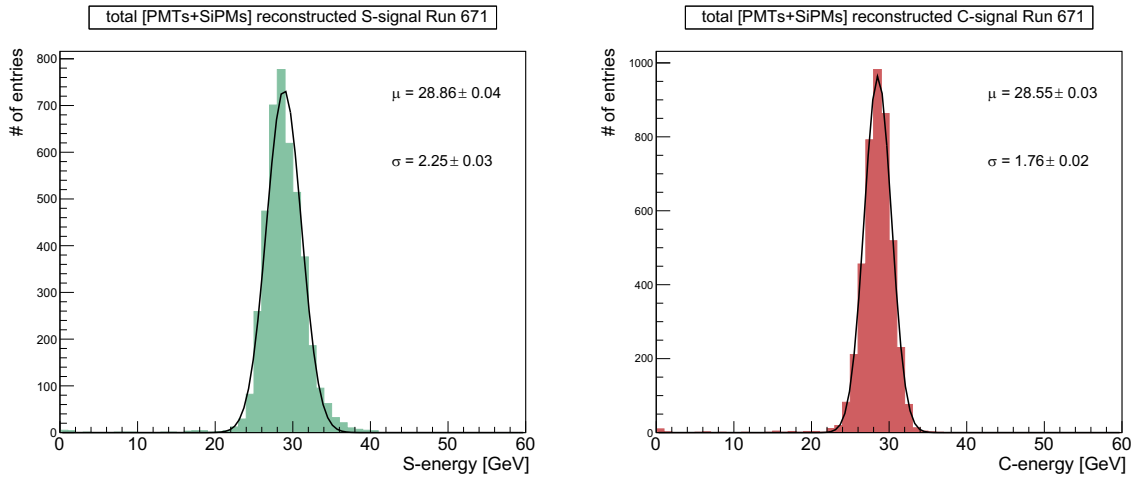

(a) (b)

Figure 6.23: The shower energy reconstructed by the scintillation channels (a) and the Cherenkov channels (b) for a 30 GeV positron beam steered at the central tower.

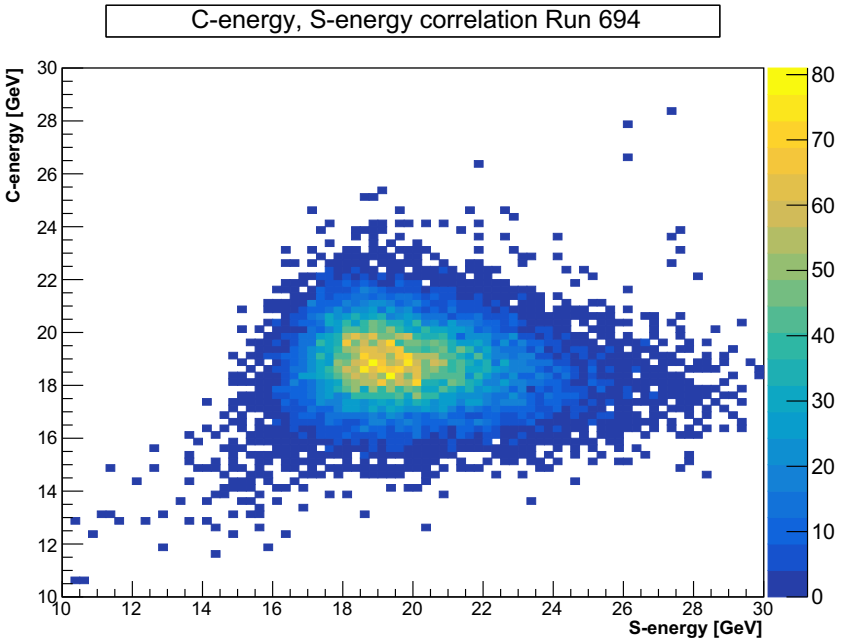

Figure 6.24: Correlation between the shower energy reconstructed by the scintillation and Cherenkov channels for a 20 GeV positron beam steered at the tower # 5. The events, at less than 15 GeV for both channels, represent the energy leakage due to the large divergence of shower particles for showers started in the PS.

0 and tower # 5 and the mean values are measured to be 19.10 ± 0.01 GeV and 17.50 ± 0.03 GeV, respectively.

The highly granular readout of the central tower allows to produce maps of activated fibres in the transverse plane of the EM-scale calorimeter module. In Figures 6.27a and 6.27b, the X-Y plane represents the transverse plane of the module, whereas the z axis represents the signal amplitude in fibres. In these scatter plots, the coordinates of

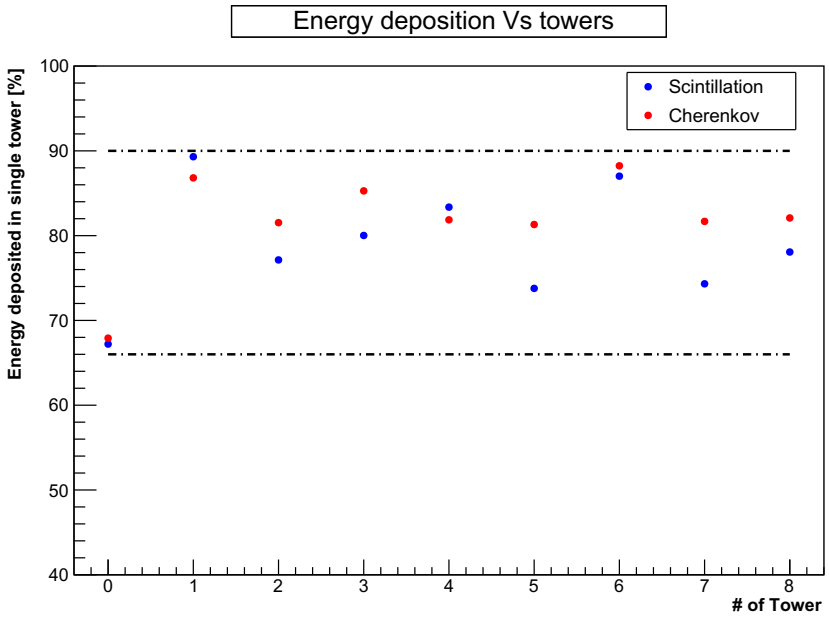

Figure 6.25: Percentage of the total shower energy deposited in a single tower where beam has been steered at. This study has been performed with 20 GeV positron beams steered, one by one, at the nine towers.

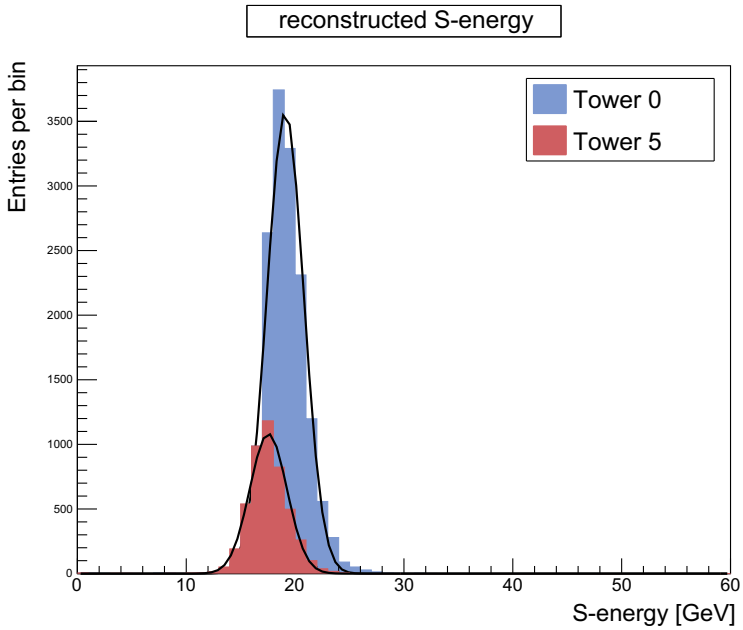

Figure 6.26: The shower energy reconstructed by the scintillation channels for beams steered at the central tower and tower # 5. The mean values extracted from the Gaussian fits are 19.10 ± 0.01 GeV and 17.50 ± 0.03 GeV, respectively.

activated scintillation and clear fibres along with the number of photoelectrons in the corresponding channel are illustrated for an integration of ∼25k selected events of a 20 GeV positron run. One Cherenkov fibre in the bottommost row has been taken off (Figure 6.27b) as the associated SiPM is turned out to be a *hot* one. These two fibre

maps show that most of the EM-shower is contained within a cylinder with a radius of less than 1 cm.

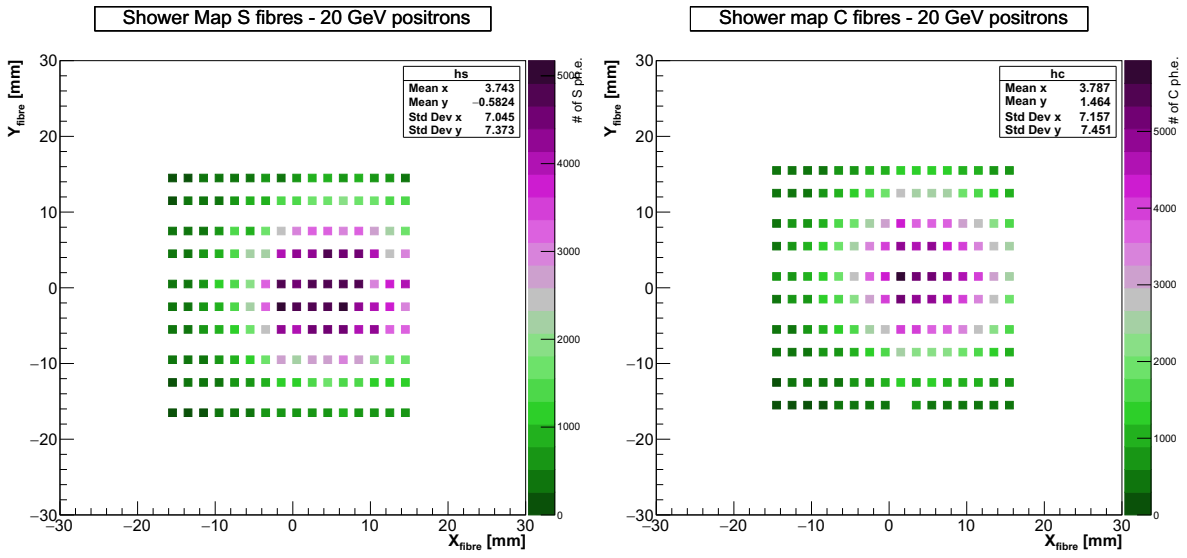

(a) (b)

Figure 6.27: Maps of activated scintillation (a) and clear (b) fibres for a 20 GeV positron beam. X-Y values represent the fibre coordinates in the transverse plane of the calorimeter and the Z (colour) axis depicts the number of photoelectrons in the corresponding channel. Most of the EM-shower is contained within a cylinder of radius < 1 cm.

6.5.2 Response linearity

The response linearity is one of the most important properties of any EM calorimeter. The energy of an incoming particle (photon or electron) gets transferred in the interaction with a dense medium, by creating a shower of electrons, positrons and photons. An active medium produces a detectable response to the charged-particle shower component. In a homogeneous calorimeter, the absorber and the active media coincide. Hence all deposited energy contributes to signal development, whereas in a sampling calorimeter, only a small fraction of the shower contributes to signal formation. As mentioned in the previous chapters, the detector response is defined as the signal per unit of deposited energy. For an ideal case, the response is fixed for EM showers of any energy developed in a particular calorimeter module. In the data analysis, the ratio between the shower energy reconstructed, independently, by the scintillation and Cherenkov channels, and the beam energy, as a function of the beam energy, provides a measure of the response linearity. This ratio has been measured for positron beams with energies ranging from 10 to 100 GeV. A correction for the energy deposition in the upstream PS has been included in the analysis. A correlation has been established between the positions of the MIP peaks in MPVs, observed with beam data (60 ADC counts) and with simulations (7.5 MeV).

Figure 6.28 illustrates the response linearity, separately for the scintillation and Cherenkov channels. For the Cherenkov channels, the response is closer to 1 at higher

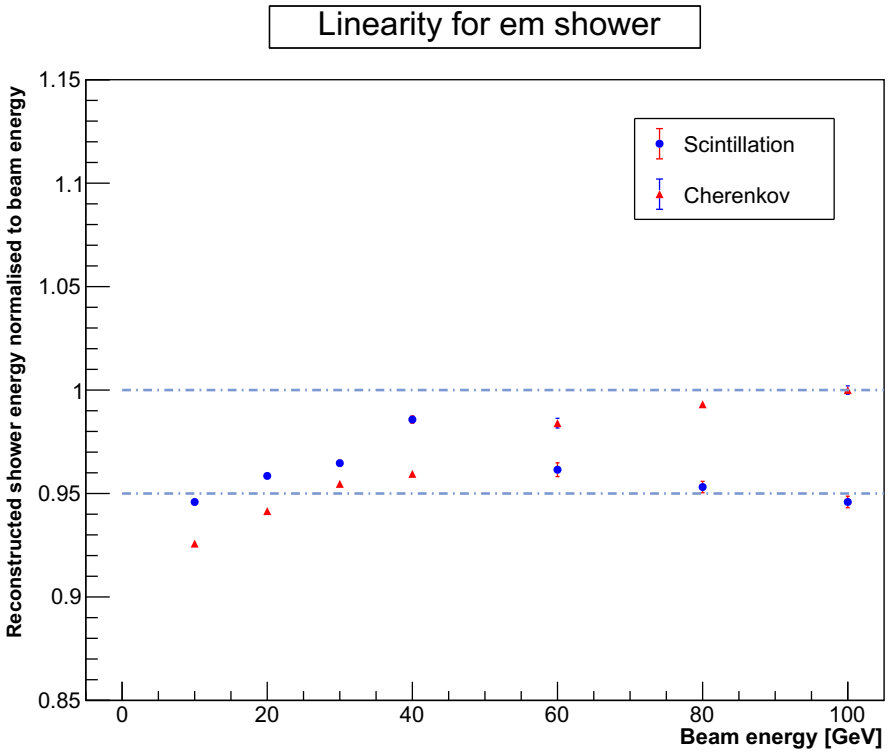

Figure 6.28: The response linearity of the EM-scale calorimeter, separately for the scintillation and Cherenkov channels, is measured to be ∼5%.

energies, whereas for the scintillation channel, the response achieves a maximum at 40 GeV. Most of the data points are within a band with a 5% of variation. The reason for this broader variation is assumed to be the incomplete shower containment due to the shower opening when starting in the PS.

6.5.3 Uniformity scan

The response uniformity over the transverse surface of the calorimeter has been measured. Two independent uniformity scans and the corresponding results will be discussed here. In the first one, ∼50k positrons with an energy of 40 GeV were steered at the corners of four towers, namely 0, 2, 3 and 5 as shown in Figure 6.29a. For event selection, apart from previously discussed cuts for analysis, (C1T OR C2T) and r_{beam} < 1 cm, another cut $E_{CALOR} > 30$ GeV has been applied to discard the bumps, shown in Figure 6.29b, likely due to muons and hadrons. E_{CALOR} is the energy reconstructed, independently, by the scintillation and Cherenkov channels. Both measurements are required to be greater than 30 GeV. A few thousand positron events survived after all these cuts.

The illuminated area, four quadrants in four towers, is subdivided in (2×2) mm^2 cells and the sum of the energy deposited in the four towers has been taken into account to build the maps of the energy reconstructed, independently, by the scintillation and Cherenkov channels as shown in Figures 6.30a and 6.30b, respectively. The energy deposited in other towers is minor and is neglected at this stage. The X-Y plane represents the coordinates of the impact point reconstructed on the DWC that is closer to

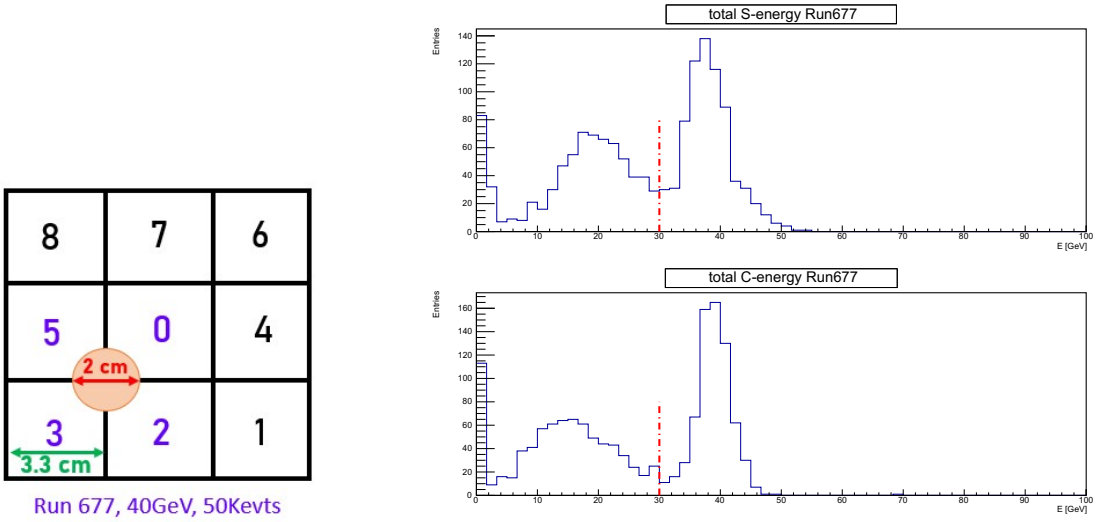

(a) (b)

Figure 6.29: Beam is steered at the corners of four towers to perform a uniformity scan (a). Additional cuts, $E_{CALOR} > 30$ GeV, are applied to discard muons and hadrons (b).

the calorimeter module. The Z axis represents the reconstructed average shower energy. Figures 6.30c and 6.30d illustrate the corresponding histograms of these maps. The relative spread (σ over mean) is calculated to be 6.2% and 5.0% for the scintillation and Cherenkov channels, respectively, and is clearly affected by geometrical non-uniformity effects. The results from the two independent measurements are combined in calculating the weighted average and weighted standard deviation with Equation 5.3. The spread is improved and measured to be 3.8%. The energy reconstructed by the two independent channels are also combined by performing an unweighted average of the two. The map of the unweighted-average energy is shown in Figure 6.31a, whereas the corresponding histogram, illustrated in Figure 6.31b, shows a 4.3% response spread. The impact point dependence of the signal and the mentioned lateral leakage of the shower have been considered as the main sources of these fluctuations. At present, we understand that the most significant contributions to the fluctuations are due to geometrical effects: a too small impact angle and the discrete, and alternate, fibre structure. A larger impact angle and a PS much closer to the calorimeter should allow to largely cancel them.

A special run has been acquired to repeat the signal uniformity studies with a statistics more than 20 times higher than the one mentioned above. ∼100k positrons of energy 20 GeV were steered at the central tower as shown in Figure 6.32a. For the event selection, apart from (C1T OR C2T) and $r_{beam} < 1$ cm, another cut $E_{CALOR} > 11$ GeV (for both scintillation and Cherenkov measurements) has been applied to discard part of the long low energy tails, as shown in Figure 6.32b. 22k positron events were selected after these cuts.

In this study, the granularity of the maps of the reconstructed energy has been improved by subdividing the illuminated area in (1×1) mm^2 cells. The energy deposited in the whole calorimeter module has been taken into account to build the maps of the

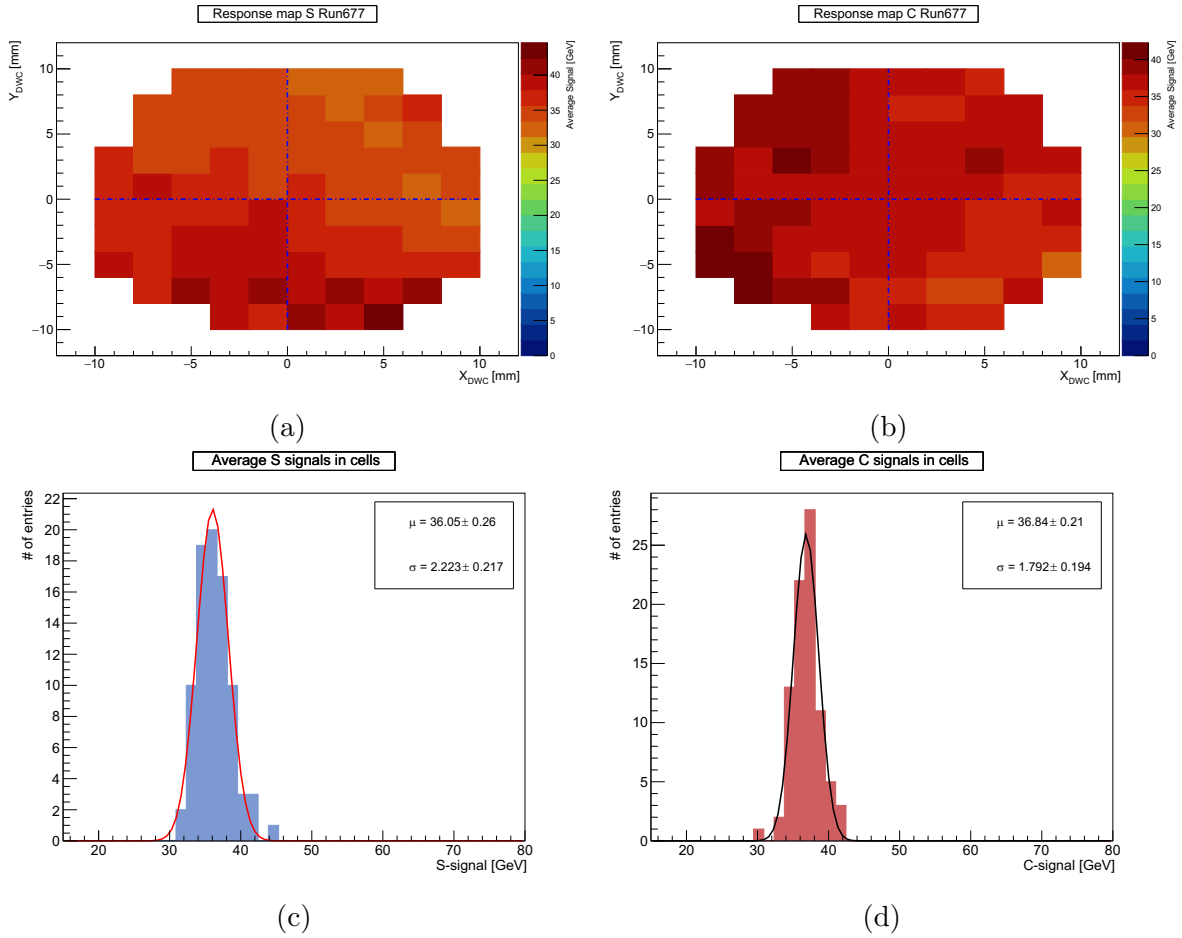

Figure 6.30: Uniformity scan with a 40 GeV positron beam steered at the corner of four towers. Maps of the average energy reconstructed by the scintillation (a) and Cherenkov (b) channels are displayed. The histograms of these maps are illustrated for the scintillation channels that show a 6.2% spread (c) and the Cherenkov channels that show a 5.0% spread (d) in the reconstructed energy.

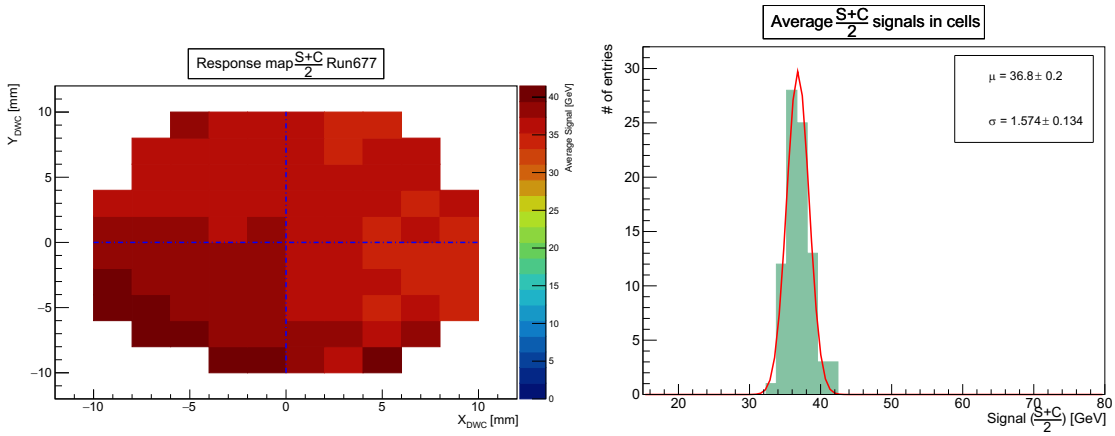

(a) (b)

Figure 6.31: Uniformity scan with a 40 GeV positrons steered at the corners of four towers (Figure 6.29a). The map of the energy reconstructed with the unweighted-average of the two (scintillation and Cherenkov) measurements, is displayed (a). The histogram of the combined reconstructed energy (b) that shows a 4.3% spread.

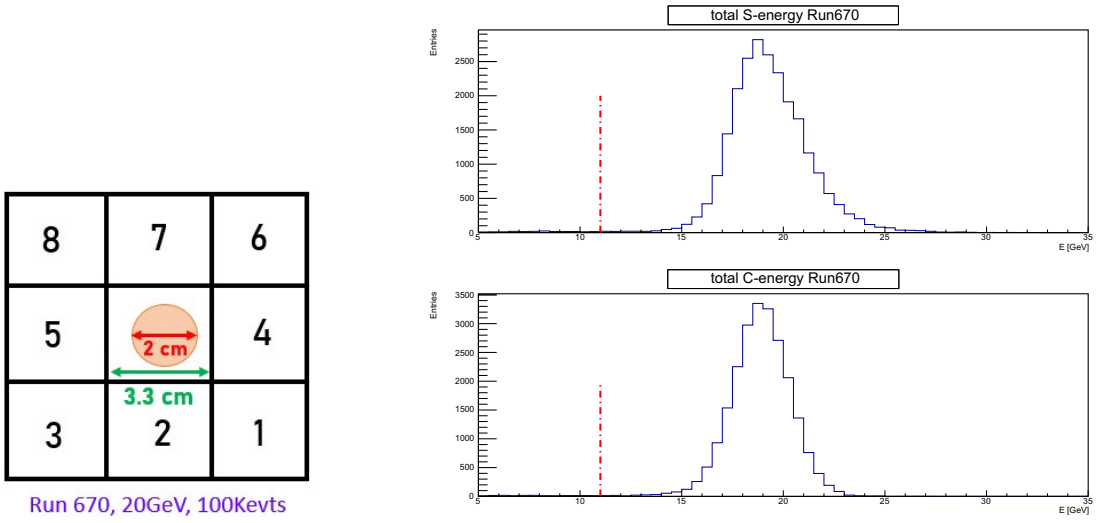

(a) (b)

Figure 6.32: The beam is steered at the central tower (a). An additional cut, $E_{CALOR} > 11$ GeV for both the scintillation and Cherenkov measurements, is applied to reject the low energy tails (b).

energy reconstructed, independently, by the scintillation and Cherenkov channels as shown in Figures 6.33a and 6.33b, respectively. An anticorrelation between the two maps can be observed. Figures 6.33c and 6.33d illustrate the corresponding histograms of these maps. The relative signal spread (σ over mean) is calculated to be 2.0% and 1.6% for the scintillation and Cherenkov channels, respectively. The non-uniformity ob-

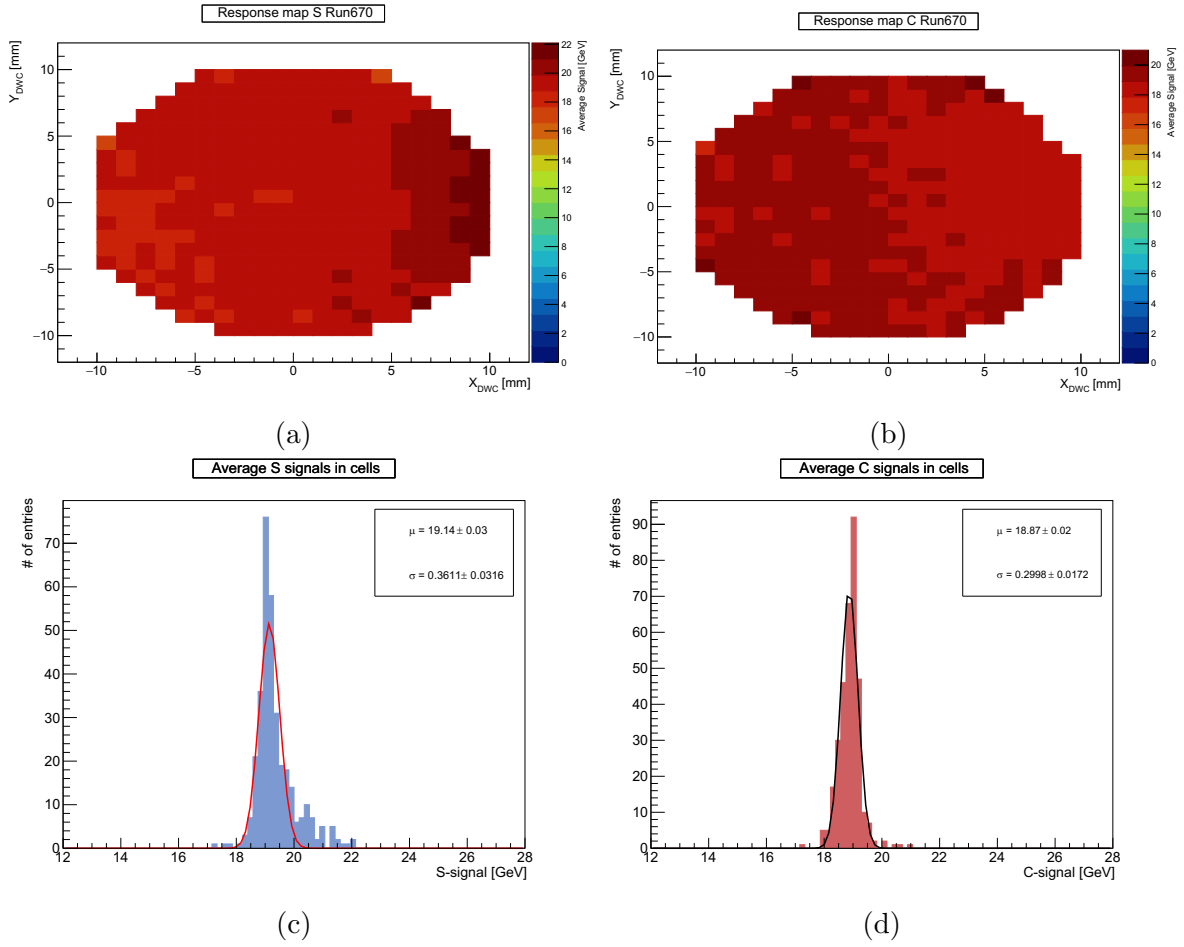

Figure 6.33: Uniformity scan with a 20 GeV positron beam steered at the central tower. Maps of the average energy reconstructed by the scintillation (a) and Cherenkov (b) channels are displayed. An anticorrelation between these two maps can be inferred. The histograms of these maps are illustrated for the scintillation channels (c), showing a 2.0% spread, and the Cherenkov channels (d), showing a 1.6% non-uniformity in the reconstructed energy.

tained by performing a normal average of the two independent channels (Figure 6.34a) is 1% as illustrated by the histogram in Figure 6.34b. The pattern obtained in the map of Figure 6.33a is dominant in that of Figure 6.34a.

6.5.4 Energy Resolution

In most cases, the EM energy resolution given by Equation 1.11 can be approximated as

$$\frac{\sigma}{E} = \frac{a}{\sqrt{E}} + constant \tag{6.21}$$

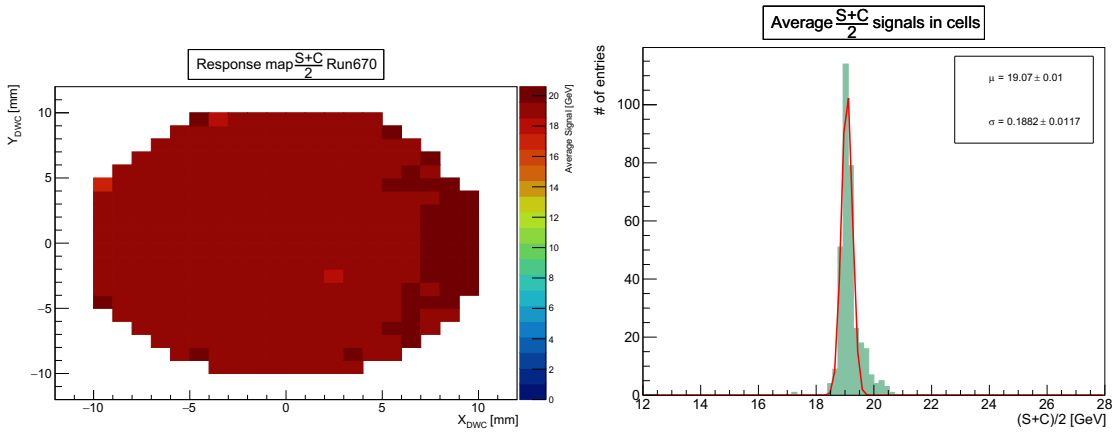

(a) (b)

Figure 6.34: Uniformity scan with a 20 GeV positron beam steered at the central tower. The map of the energy reconstructed by the unweighted average of the scintillation and Cherenkov measurements, is displayed (a). The histogram of this map shows a 1.0% spread of the combined reconstructed energy (b).

Figures 6.35a and 6.35b show distributions of shower energies, for a 20 GeV positron beam steering at the central tower, reconstructed by the scintillation and Cherenkov channels, respectively. The mean values of these distributions are 19.09 ± 0.01 GeV and 18.76 ± 0.01 GeV. The calibration constants, calculated by Equation 6.22, are 0.9545 (K_S) and 0.938 (K_C).

$$K_{S,C} = \frac{< E_{S,C}(reco) >}{E_{beam}} \tag{6.22}$$

where $< E_{S,C}(reco) >$ is the average reconstructed shower energy and E_{beam} is 20 GeV. $K_{S,C}$ has been used to reconstruct beam energies, independently, with the scintillation

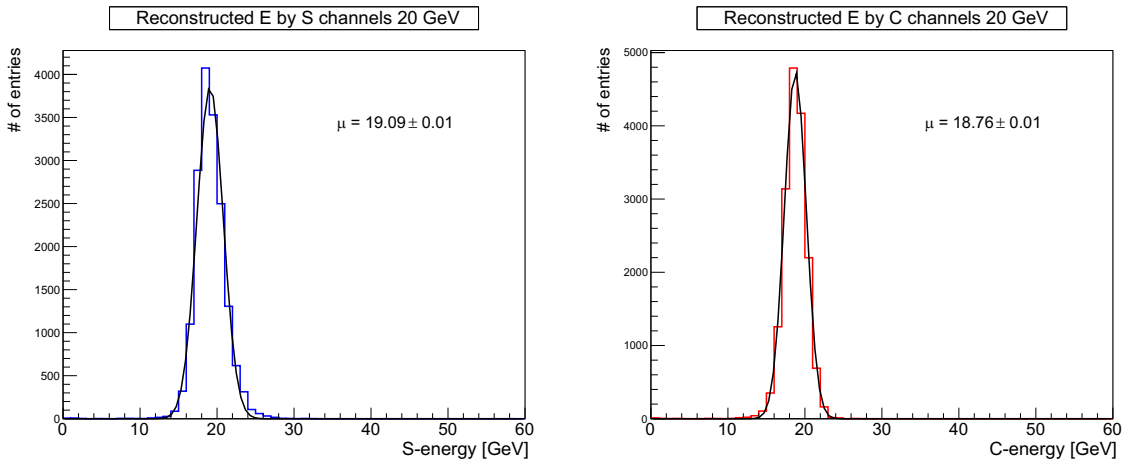

(a) (b)

Figure 6.35: The shower energy reconstructed by the scintillation (a) and Cherenkov channels (b) for a 20 GeV positron beam steered at the central tower.

and Cherenkov channels, for different positron runs ranging from 10 GeV to 60 GeV.

The Monte Carlo corrections mentioned in Section 6.5.2 are applied here too. For the event selection, a high cut on the PS signals is included with the combination of cuts on the Cherenkov counters, i.e., (C1T OR C2T) AND PS $>$ 4.5 MIPs, in order to obtain good Gaussian fits on the reconstructed energy distributions, in particular for 40 and 60 GeV runs. The mean values, $E_{beam|S,C}$(reco), and standard deviations, $\sigma_{S,C}(reco)$, of the distributions of the reconstructed beam energies have been extracted for both channels. The results of the two independent channels are combined by calculating, event by event, the weighted averages of $E_{beam|S,C}$(reco) and weighted standard deviations, using Equation 5.3. The resolutions, $\sigma_{S+C}(reco)/E_{beam|(S+C)}$(reco), have been calculated and plotted as a function of $1/\sqrt{E_{beam}}$, where E_{beam} is in GeV. It is shown in Figure 6.36. The linear fit provides an EM energy resolution of $24\%/\sqrt{E}$. A reference straight line, indicating a stochastic term of 15% that is the goal for the EM-scale module, has been drawn. It is seen that a constant term of 0.006, i.e., the intercept of the y axis by the fitting line, is present. The position dependence of calorimeter signals and the lateral leakage of the shower energy, due to the shower opening after starting in the PS, are supposed to be the cause of this intercept. A simulation study shows that the constant term can be substantially reduced by applying larger rotations, e.g., 2.5°, to the calorimeter module with respect to the beam axis, in both the horizontal and vertical planes. A little amount of rotation also helps in reducing channeling effects, i.e., the contribution of individual fibres in developing detector signals.

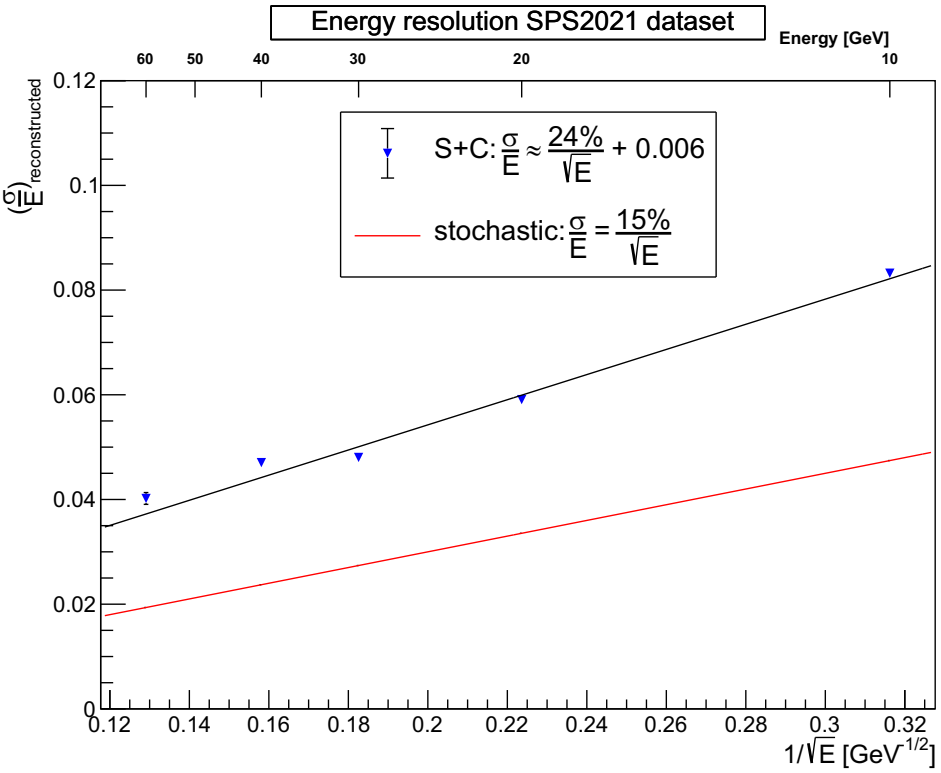

Figure 6.36: The electromagnetic energy resolution, by combining the independent scintillation and Cherenkov measurements, is estimated to be $24\%/\sqrt{E} + 0.6\%$. The red line indicates an EM energy resolution of $15\%/\sqrt{E}$.

6.5.5 Impact point dependence

An interesting feature, mentioned before, of any EM shower developed in a fibre-sampling DRO calorimeter, is the extremely collimated shower core that develops a significant amount of calorimeter signals. This core reconstructed with the Cherenkov signals is slightly broader compared to that reconstructed with the scintillation signals. This is due, as understood so far, to geometrical differences in the production and trapping of the scintillation and Cherenkov photons. While the emission of scintillation photons is isotropic, highly relativistic particles radiate Cherenkov photons at a well defined angle with respect to their flight direction. Since the shower core develops along the primary particle direction, the Cherenkov emission has an angular correlation with the beam axis. In case the beam angle with respect to the fibre axis is too small, many photons fall out of the NA of the fibres. This is particularly true for the early part of the shower. Moreover, there is a modulation of the signal depending on the impact point position. The primary beam particle can indeed impinge either on a fibre or on the brass absorber at the calorimeter front face. For the same angular effects depicted above, this may produce oversampling only in the scintillation fibres, since in the Cherenkov ones the photons are emitted out of the NA of the fibre. So, there are systematic fluctuations in the signals that are larger for the scintillation channels compared to the Cherenkov channels.

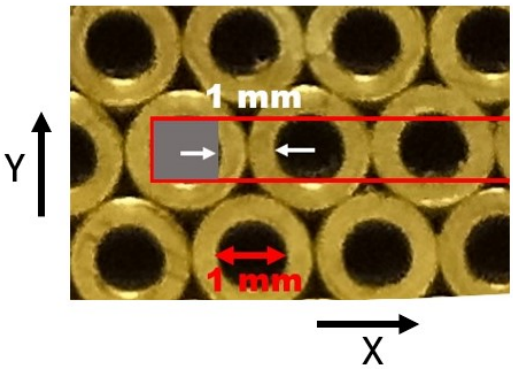

Figure 6.37: An area (grey squared cell) of (1×1) mm^2 is selected to see the average signal in all the towers for events hitting this area. This area is slided from -8 mm to +8 mm in steps of 1 mm along the X-axis in order to select events impinging either on fibres or on the brass absorber.

In order to observe this feature in the novel EM-scale module, an area of (1×1) mm^2, from the distribution of impact points of particles, has been selected using the upstream DWC2. The average signal in nine towers is measured for the selected events. The area has been slided from -8 mm to +8 mm along the X-axis, in steps of 1 mm, on the calorimeter front face. This should allow to select events impinging either on fibres or on the brass absorber as illustrated in Figure 6.37. The average signal in the calorimeter module, as a function of the X coordinate of the impact point, is measured. This study has been performed for different ranges of the Y coordinate of the impact point. The ones obtained for the range $-1\ mm < \mathrm{y} < 0\ mm$, for a 20 GeV positron data sample, are shown here. Figures 6.38 and 6.39, respectively, show the average energy reconstructed independently with the scintillation and cherenkov signals as a

function of the X coordinate of the impact point for the mentioned y range. The trends of the plots show a clear oscillating pattern with a period of ∼2 mm that is indeed the fibre-to-fibre distance along the X axis. This impact point dependency of the signals is higher for the scintillation channels compared to that in the Cherenkov channels. On the other hand, the combined reconstructed energy, i.e., the weighted average of the scintillation and Cherenkov independent measurements, has a behaviour very close to the Cherenkov one as shown in Figure 6.40. The trend of this plot shows the same oscillating pattern with a period of ∼2 mm. With the present setup, the response in the scintillation channels is strongly depending on the x coordinate of the impact point and this effect can be only partially recovered with the Cherenkov response. At present, the only further step that we can envisage, would be to introduce a parametric correction as a function of X. On the other hand, a better geometrical setup should be able to provide significant improvements.

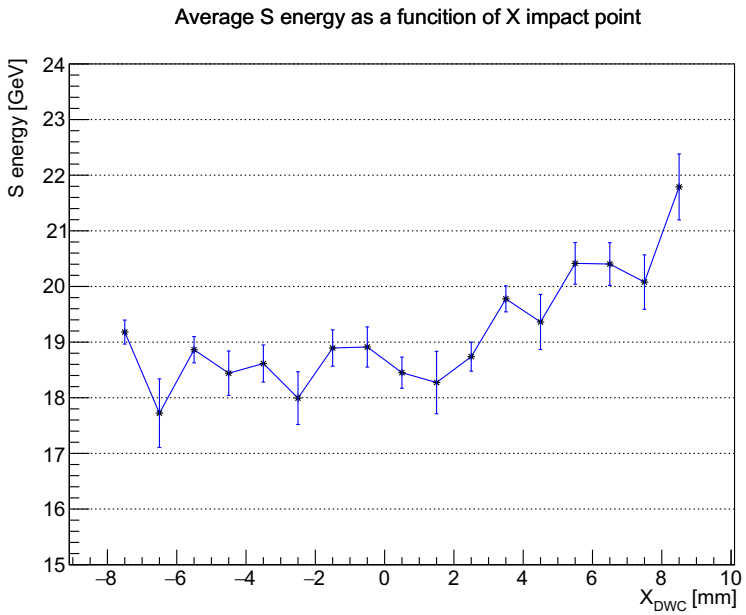

Figure 6.38: The average energy reconstructed with the scintillation channels as a function of the X coordinate of the impact point for $-1\,mm < \mathrm{y} < 0\,mm$. The impact points are measured in the upstream DWC2. The oscillating pattern with a period of ∼2 mm shows the impact point dependency of scintillation signals.

To cancel, or at least reduce, the impact point dependency of the signals, the shower axis (i.e., the beam axis) must form some finite angle with respect to the direction of the fibres. This can be achieved by positioning the calorimeter during data taking, at some predefined angle, preferably in both the horizontal and vertical planes, with respect to the beam axis. Some simulation studies, with muons, have been performed in this direction (Section 6.5.6).

The analysis of SPS positron data has been going on. In particular, some recent studies show that an EM energy resolution below $\sim 20\%/\sqrt{E}$ can be achieved for the capillary based EM-scale prototype by implementing fine corrections to suppress the impact point dependency of the scintillation signals. On the other hand, the radial profiles of EM showers are important features to be observed with data. Some results

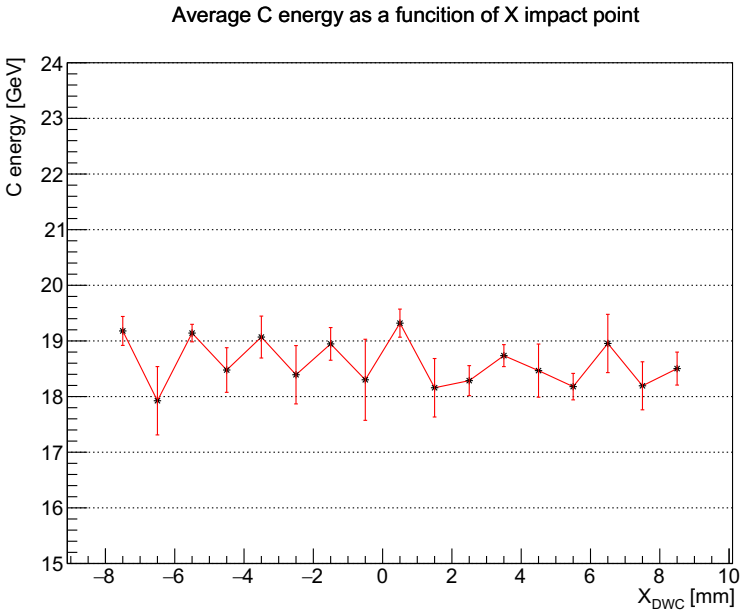

Figure 6.39: The average energy reconstructed with the Cherenkov channels as a function of the X coordinate of the impact point for $-1\,mm < \mathrm{y} < 0\,mm$. The impact points are measured in the upstream DWC2. The oscillating pattern with a period of ∼2 mm shows the impact point dependency of the Cherenkov signals that is moderate compared to that of the scintillation signals.

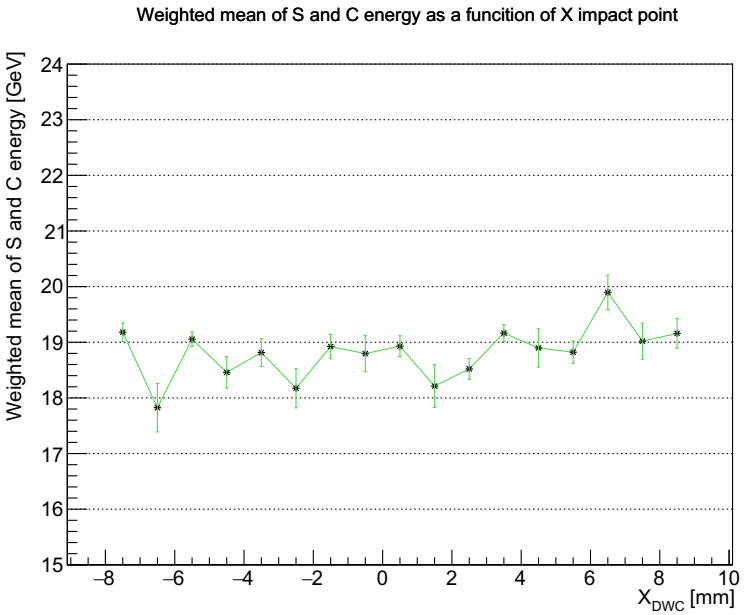

Figure 6.40: The combined reconstructed energy, i.e., a weighted average of the energies reconstructed by the scintillation and Cherenkov channels as a function of the X coordinate of the impact point for $-1\ mm < \mathrm{y} < 0\ mm$. The oscillating pattern with a period of ∼2 mm shows the impact point dependency of the signals.

in this direction can be found in [77].

6.5.6 Muon detection

Event selection

Calorimeter systems in HEP experiments play a vital role in detecting muons and measuring their properties. Muons have the characteristic feature that they can traverse a long quantity of dense material and deposit a small fraction of their energies in it. Muons follow their way through the calorimeter and the beam dump concrete. Hence, a correlated information must be present in all ancillary detectors (as well as in the calorimeter). In our beam test, high-energy muons were derived from 180 GeV/c pion beams. So, what we received was a muon beam with a spectrum ranging from ∼60% to ∼100% of the original hadron energy, i.e., from ∼108 GeV/c to ∼180 GeV/c, peaking around ∼165 GeV/c. Muon samples are selected by observing MIP signals in the downstream MC. The presence of MIP signals as well in the upstream PS makes the muon tagging even more robust. To maximise the number of muon events, a reasonably low cut (> 15 ADC counts) is applied to the MC signal as shown in Figure 6.41. Out

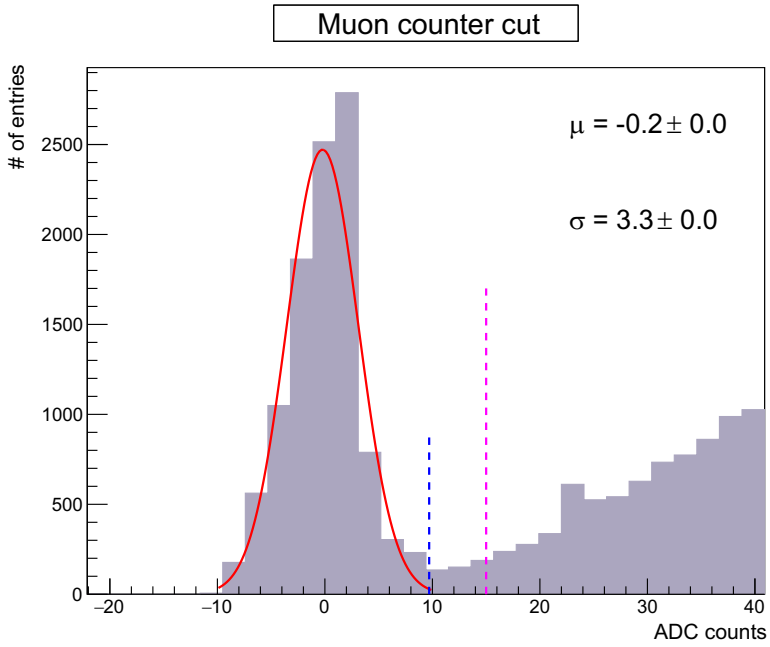

Figure 6.41: MC > 15 ADC counts, between $\mu + 3\sigma$ of the pedestal distribution and the signal peak, has been chosen to select ∼91k muon events. The blue and pink vertical lines are at $\mu + 3\sigma$ of the Gaussian fit and at 15 ADC counts.

of ∼102k total events of this run, a sample of ∼91k muon candidates is selected. MIP signals are observed at upstream PS for these events (Figure 6.42 left-top). The signal distributions at two Cherenkov counters are also shown in Figures 6.42 left-bottom and 6.42 right-top. On the other hand, the distribution of all events (∼ 102k) at the downstream MC is shown in Figure 6.42 right-bottom). During the data taking with the muon beam settings, the detector orientation was the same as during the runs witn positron beams, i.e., 1° in the horizontal plane with respect to the beam axis. For muon data analysis, we have used the PMT and SiPM calibrations performed with positrons (Section 6.3.1).

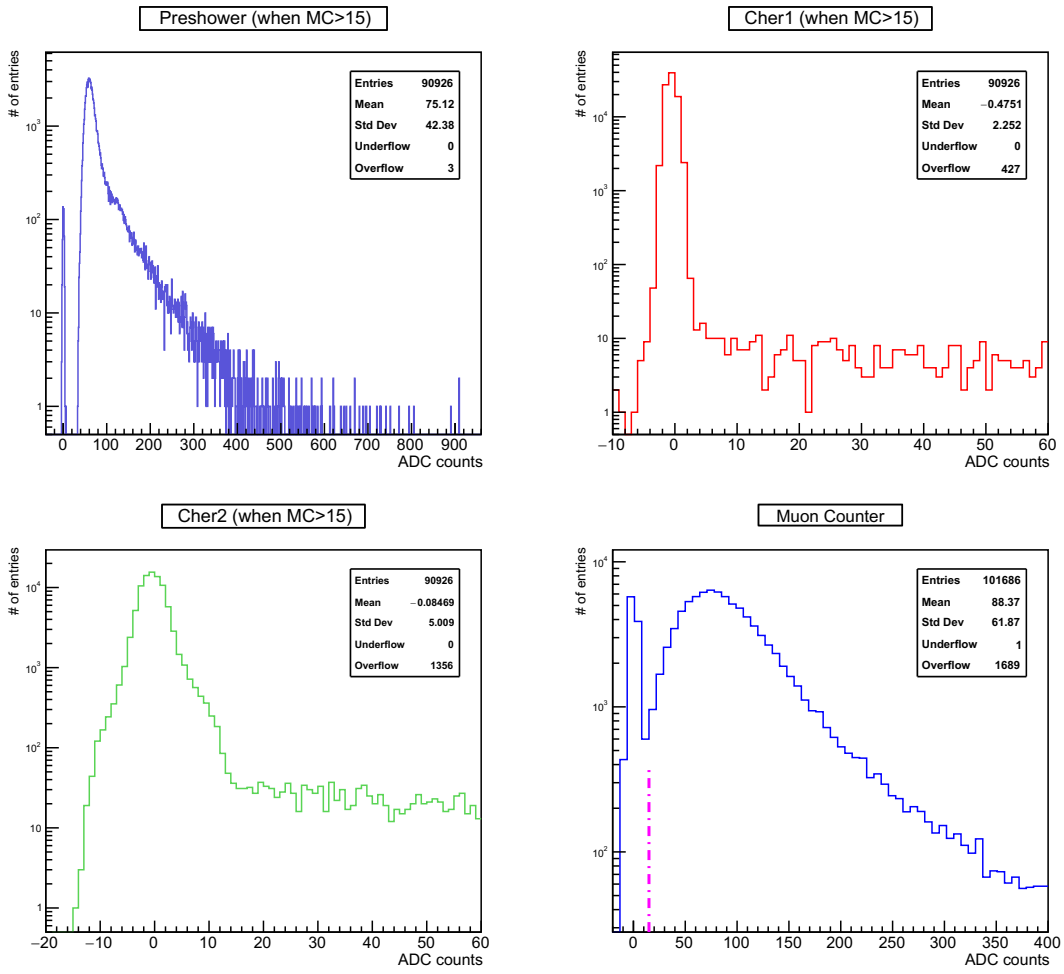

Figure 6.42: The distribution of muon samples (∼91k events), selected by the cut MC > 15 ADC counts, at the preshower (left-top), the Cherenkov counter1 (right-top) and Cherenkov counter2 (left-bottom) which are upstream of the calorimeter. The distribution of all events (∼ 102k) for this run at the downstream muon counter. The low cut to flag muons is indicated (right-bottom).

Reconstructed muon loss

Muons lose energy mainly by ionising the absorber material of the calorimeter. Muons start producing bremsstrahlung radiation only at extreme energies. The muon energy losses has been reconstructed, independently, with the scintillation and Cherenkov channels and the corresponding distributions are shown in Figures 6.43a and 6.43b. The long tails of the two distributions are results of large event-to-event fluctuations in the ionisation energy loss. Those fluctuations are primarily caused by the rare but measurable occurrence of knock-on electrons (called δ-rays), which gain enough energy from the interaction to become ionising particles themselves. In the two distributions the tails look identical but the peak positions differ from each other. The average muon energy loss is measured by fitting the spectrum with a Landau distribution and extracting the Most Probable Value (MPV). These values are measured to be 1.499 $\pm$ 0.002 GeV and 0.522 $\pm$ 0.002 GeV, respectively for the scintillation and Cherenkov

channels. Geant4 simulation studies show that a point-like monochromatic beam of 180 GeV μ^+, steeered on the central tower of the module that is oriented at 1° in the horizontal plane with respect to the beam axis, deposits as MPV 1.232 ± 0.001 GeV of its energy (Figure 6.44) in the EM-scale module. This is the MPV provided by the fit of the the spectrum of 80k simulated events with a Landau distribution. The difference with respect to the measured values for both the scintillation and Cherenkov channels, is likely due to the fact that the energy calibration for ionisation processes is different from the energy calibration for electromagnetic showers.

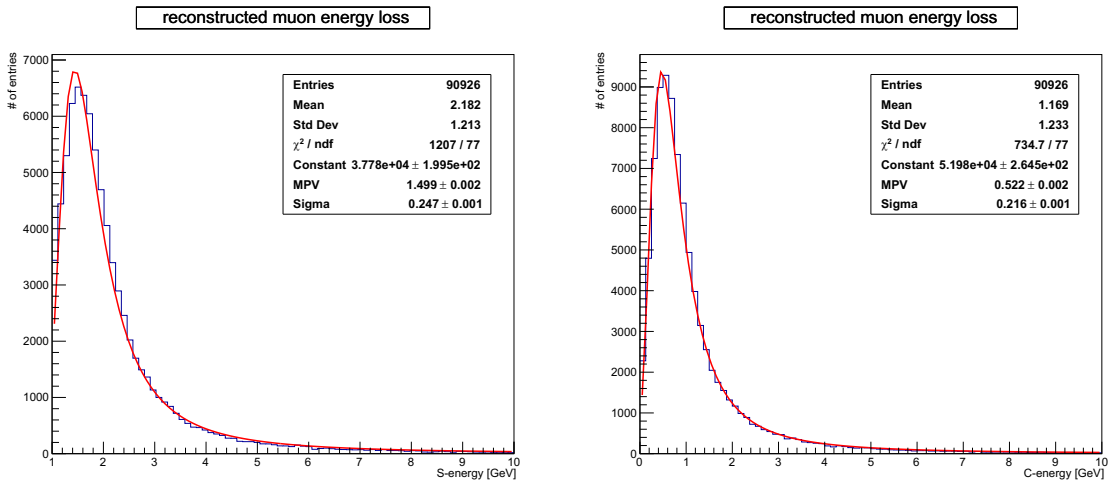

(a) (b)

Figure 6.43: Energy loss of a ∼180 GeV SPS muon beam in the EM-scale calorimeter, reconstructed by the scintillation (a) and Cherenkov (b) channels.

SPS data shows that the MPV of the Cherenkov signal is ∼35% of the MPV of the scintillation signal. Measurements with the DREAM calorimeter[23] showed that the energy loss for 200 GeV muons reconstructed with the Cherenkov channels was measured to be ∼50% of that reconstructed with the scintillation channels, both calibrated at the EM scale. How much Cherenkov radiation is generated (and can be detected) in the ionisation processes of a MIP (or by the primary particle) is still matter of discussion. Further studies, with both Monte Carlo simulations and beam data, need to be done. The DREAM calorimeter ($99X_0$) had ∼2 times more X_0 than the EM-scale module ($\sim 53X_0$). Hence, the reconstructed muon energy loss obtained with EM-scale capillary-based module does not look in good agreement with the results from DREAM. The orientation of DREAM module for these measurements was different, 6° in the horizontal plane and 0.7° in the vertical plane with respect to the beam axis. For a better comparison of results, the correlation between scintillation and Cherenkov signals for ∼108 Gev to ∼180 GeV muons traversing the EM-scale module and that for muons ranging from 40 GeV to 200 GeV traversing the DREAM module, have been observed. For the former case, an event-by-event scatter plot (Figure 6.45a) has been observed, whereas for the latter, the MPVs of reconstructed signal distributions (Table 1, [23]) are plotted (Figure 6.45b). All energies have been reconstructed at the EM-scale. The correlations between the dual-readout signals are given by Equation 6.23 for the EM-scale module and by Equation 6.24 for the DREAM calorimeter. The slopes

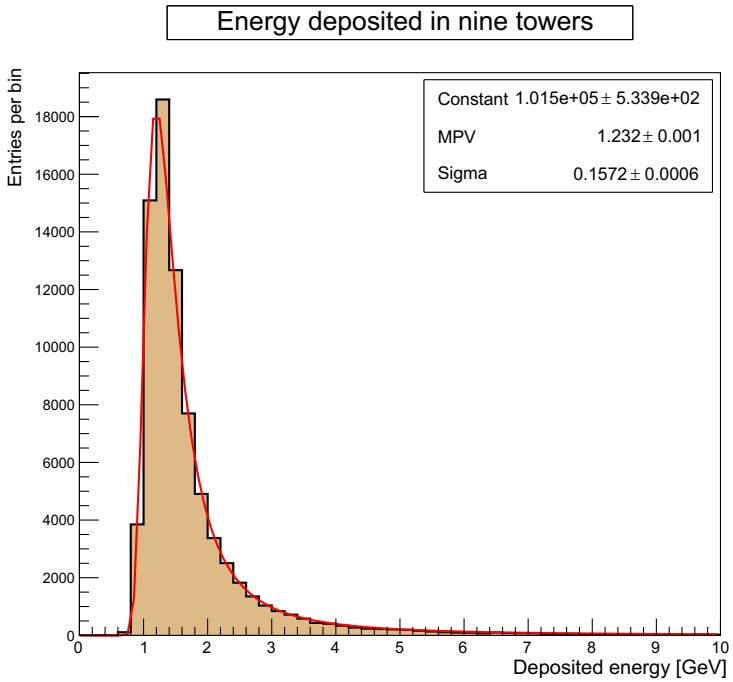

Figure 6.44: Simulation studies with a point-like monochromatic beam of 180 GeV muons. Event-by-event distribution of the energy deposited by the muons in the EM-scale calorimeter. The most probable value provided by the Landau fit is measured to be 1.232 ± 0.001 GeV.

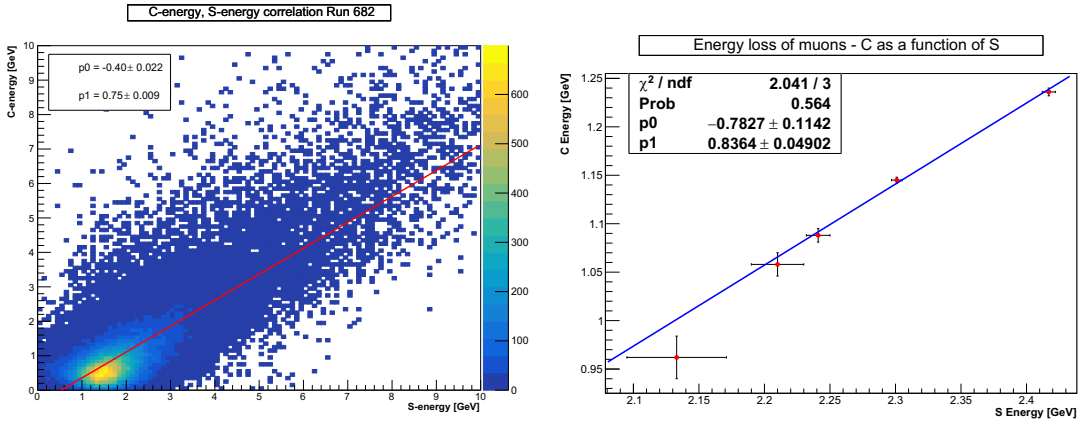

(a) (b)

Figure 6.45: Event-by-event scatter plot of the scintillation and Cherenkov signals for ∼108 GeV to ∼180 GeV muons traversing the EM-scale calorimeter (a). The correlation between scintillation and Cherenkov signals for 40 GeV to 200 GeV muons traversing the DREAM calorimeter (b).

and offsets are the results of two linear fits:

$$C = 0.75 \cdot S - 0.40 \tag{6.23}$$

$$C = 0.84 \cdot S - 0.78 \tag{6.24}$$

where C and S are the muon loss reconstructed by the Cherenkov and scintillation signals, respectively. The two slops are comparable but the factor ∼2 larger offset in Equation 6.24 still lacks a clear explanation.

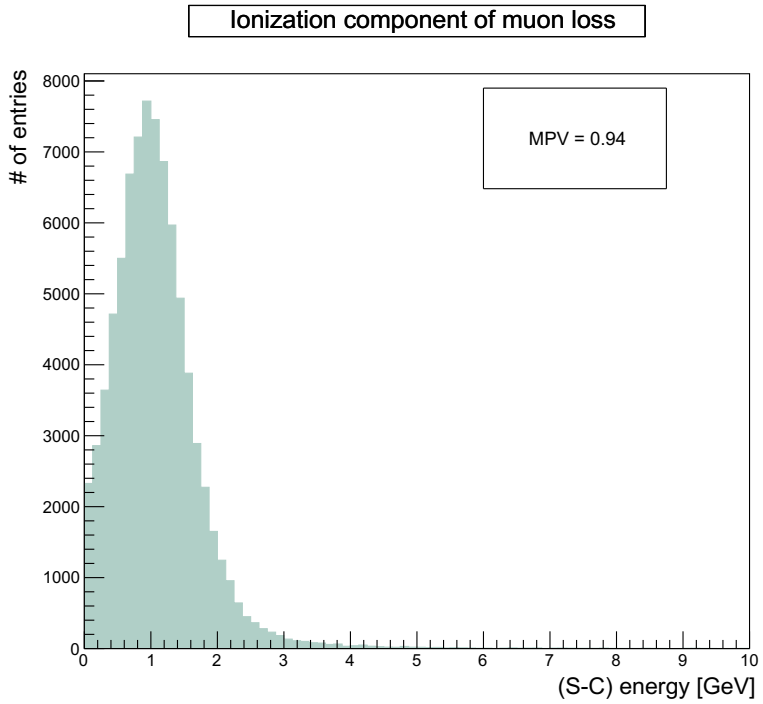

Figure 6.46: Event-by-event distribution of the difference in the scintillation and Cherenkov signals measured with the EM-scale calorimeter.

An event-by-event distribution of the difference between the scintillation and Cherenkov signals, measured with the EM-scale module has been observed. This is illustrated in Figure 6.46. In the assumption that the Cherenkov signal is only due to radiative losses (assumption that is probably too simplistic), the MPV of this distribution, 0.94 GeV, would provide an estimation of the ionisation loss by muons. Results obtained with the DREAM module provided a measure of (S-C), as the difference of the two MPVs, ranging from 1.171 to 1.181 GeV as a function of the muon-beam energy. This appears to be hardly compatible with our observed value (0.947 GeV), because of the 100% larger depth of the DREAM module. Finally, the absolute value of (S-C) was found, by the DREAM collaboration, to be largely independent of the muon energy. Unfortunately we could not have muon beams with different energies (and not even monocromatic). The result is that, at present, there are more open questions than answers but, when hopefully clarified, it should probably be possible to estimate, with a DRO calorimeter, the difference between the ionisation and radiative components of energy loss by muons. Dedicated data taking with muon beams of different energies is required to improve in this direction.

Shower shape

The numbers of produced photoelectrons in SiPM sensors, separately for the scintillation and Cherenkov channels, have been measured fibre by fibre. In Figures 6.47a and

6.47b, the X-Y plane depicts the fibre coordinates in the transverse plane of the module. The Z-axis provides a measure of the number of photoelectrons for an integration of a sample of ∼91k muons with energy ranging from ∼108GeV to ∼180 GeV. The signal in one clear fibre, at the bottom row, is set to zero (Figure 6.47b,) because of the "hot" SiPM sensor associated with that fibre.

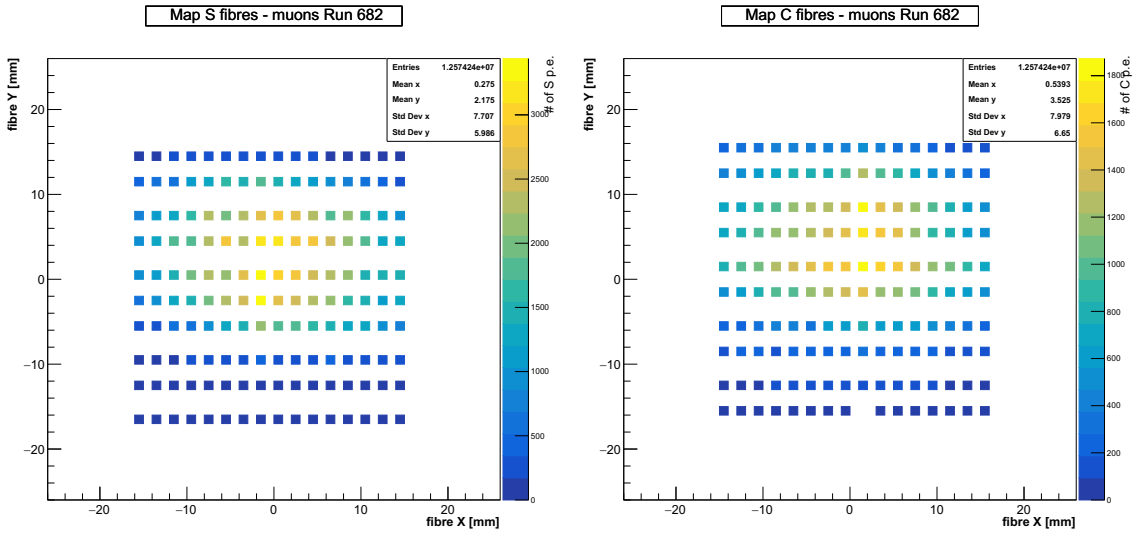

(a) (b)

Figure 6.47: In the transverse plane of the EM-scale calorimeter, the positions of the scintillation (a) and clear fibres (b) of the central tower are shown. The Z (colour)-axis represents the amount of signals in terms of number of photoelectrons in SiPM sensors for an integration of ∼91k events.

Shower barycentre

The *barycentre* of a shower is defined by a pair (X, Y) of coordinates where X and Y are the sum of fibre coordinates weighted with signals developed in the fibres, divided by the sum of signals in all fibres, as given by Equation 6.25.

$$X = \frac{\Sigma X_i E_i}{\Sigma E_i}$$
$$Y = \frac{\Sigma Y_i E_i}{\Sigma E_i} \tag{6.25}$$

A shower has two independent barycentres, one for the scintillation and another for the Cherenkov channel. Figure 6.48a shows a scatter plot of the X and Y coordinates of the barycentres for the scintillation channels for the selected muon sample (∼79k events). For this study, muons within a beam spot radius of less than 1 cm were selected. Along the Y direction an over population of events at a distance of ∼3 mm is observed. To understand the reason behind this, the average signal extracted from the SiPM sensors associated to the scintillation fibres i.e., only from the central tower, is measured as a function of Y coordinate of the barycentre for scintillation channels. It is shown in Figure 6.48b. An oscillating pattern with a period of ∼3-4 mm has been observed. This observation can be explained as an effect of the following facts:

- The maximum signal comes from a single fibre.
- Channeling effects may give rise to oversampling.
- The present design of the dual sampling i.e., same type of fibres appears in alternating layers.

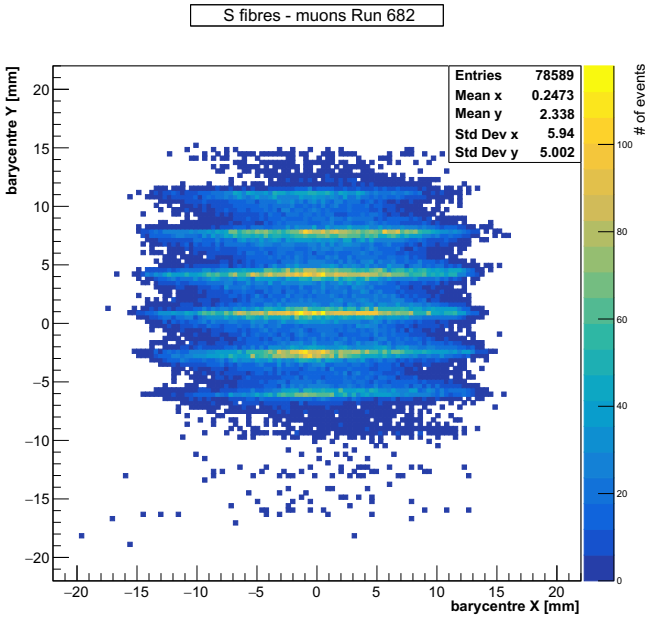

(a)

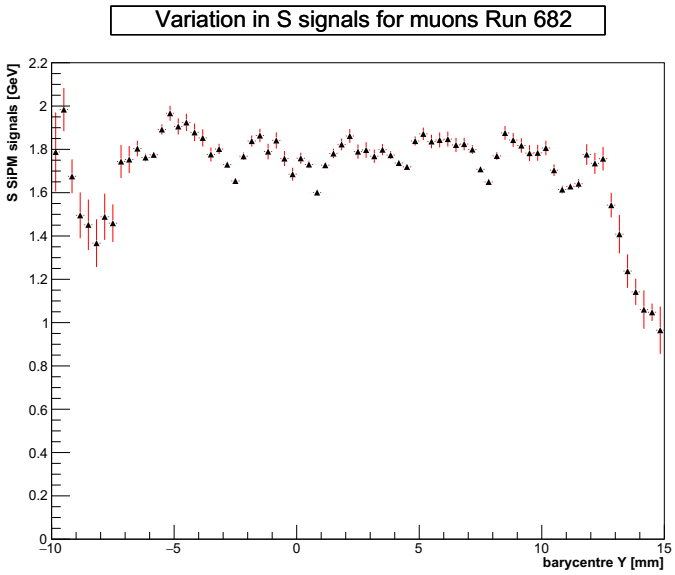

(b)

Figure 6.48: A scatter plot of the X and Y coordinates of the shower barycentre for the scintillation channels (a). The variation of the average total (SiPM) signals with Y coordinates of the barycentre for scintillation channels. An oscillating pattern with a period of ∼3-4 mm is observed (b).

A feature of SPACAL-type fibre sampling of showers is that the signal in one particular fibre is the largest for an event. It is true also for the case of channeling, hence, oversampling of the shower. From Equation 6.25, it can be understood that a specific scintillating-fibre coordinate (X_i, Y_i) becomes the barycentre (X, Y) of shower for an event due to largest value of the signal in that fibre. The spacing between two layers of same type of fibres is ∼3.5 mm (Figure 6.49). As, for most of the events, the barycentre coordinates coincide with (or are very close to) the scintillating-fibre coordinates, the plot 6.48a is overpopulated at gaps of ∼3-4 mm.

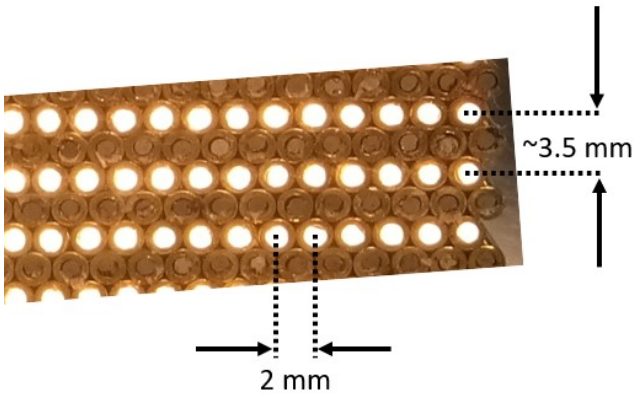

Figure 6.49: A small portion of the front face of the EM-scale calorimeter. The ∼3.5 mm spacing between two illuminated scintillation layers is indicated. The ∼2 mm spacing between two consecutive scintillation fibres in the same layer is also indicated.

Simulation studies for vertical tilt

The effect of channeling on the barycentre distributions and the muon energy losses reconstructed by scintillation and Cherenkov signals have been observed in simulation studies for a 180 GeV point-like muon beam steering the front face of the calorimeter. The calorimeter is oriented at some angle in the vertical plane and at 1^0 in the horizontal plane with respect to the direction of the incoming particles. For module orientation at 1^0 and 0.4^0 in horizontal and vertical planes, respectively, the distributions of X and Y coordinates of shower barycentres for scintillation and Cherenkov signals are illustrated in Figures 6.50a and 6.50b. The distributions have non-symmetric short tails in either sides. But the smoothness of the distributions or the absence of overpopulation of events at equally spaced distances of Y coordinate of shower barycentre represent the fact that channeling of a particle or development of significant amount of signals in a single fibre can be avoided by implementing vertical tilts to the calorimeter. Figure 6.51 shows the absence of modulation in the average Scintillation signals extracted from the SiPMs when plotted as a function of Y coordinates of barycentre for scintillation channels. Also, the amount of muon energy losses, reconstructed individually with the scintillation and Cherenkov signals, increases. This better sampling leads to a better energy resolution.

Figure 6.52 shows the muon energy losses reconstructed with the scintillation and Cherenkov channels as a function of the vertical tilt, with respect to the beam axis, applied to the module. A scan on the vertical tilt from 0.2^0 to 2.5^0 with a fixed horizontal

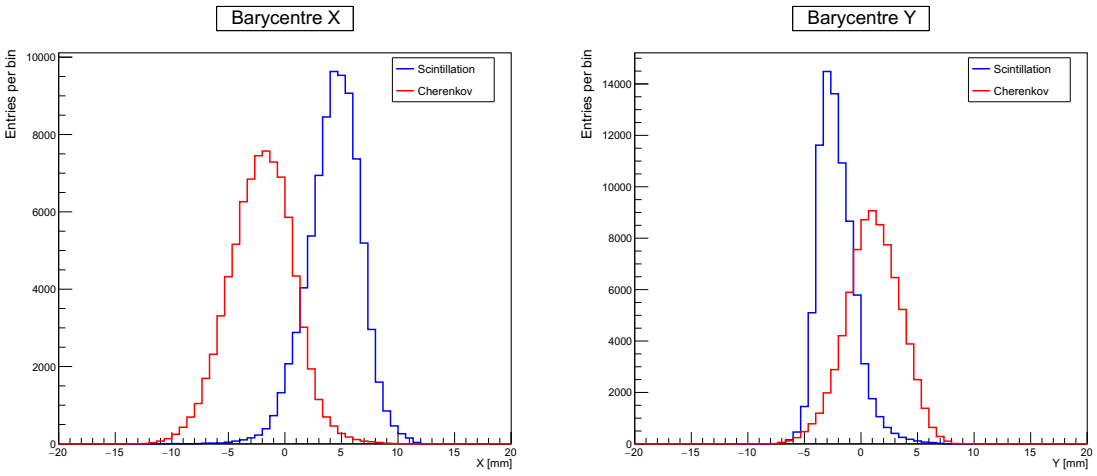

(a) (b)

Figure 6.50: The distributions of X (a) and Y (b) coordinates of shower barycentres for scintillation and Cherenkov channels for 180 GeV muons steering the front face of the EM-scale module. The module is rotated at 1^0 and 0.4^0 in horizontal and vertical planes, respectively, with respect to the direction of the incoming particles.

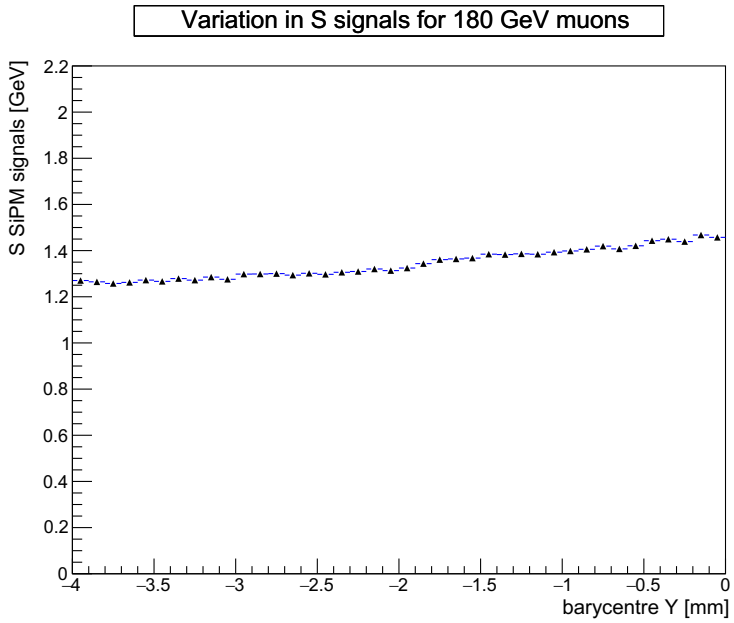

Figure 6.51: Simulation studies. The absence of modulation in the average Scintillation signals, for 180 GeV muons, extracted from the SiPMs when plotted as a function of Y coordinates of barycentre for scintillation channels.

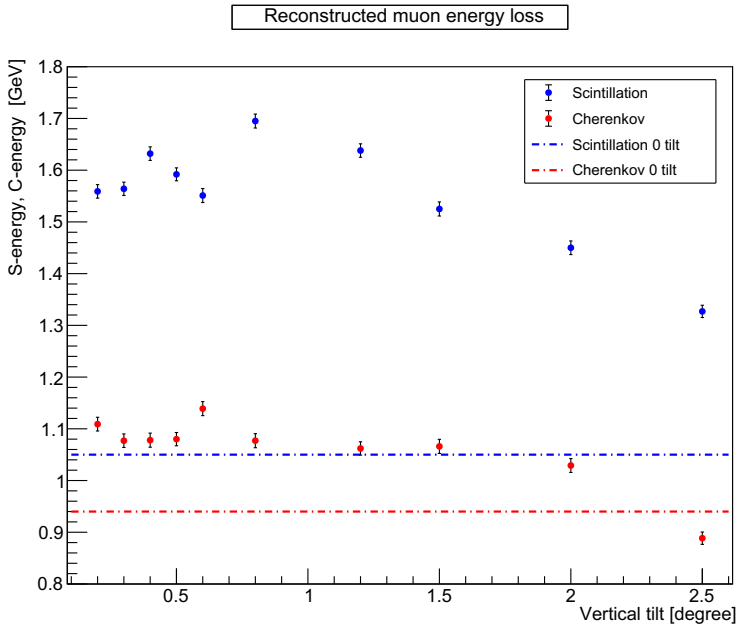

Figure 6.52: Muon energy losses reconstructed by the scintillation and Cherenkov channels as a function of the vertical tilt, with respect to the beam axis, applied to the module.

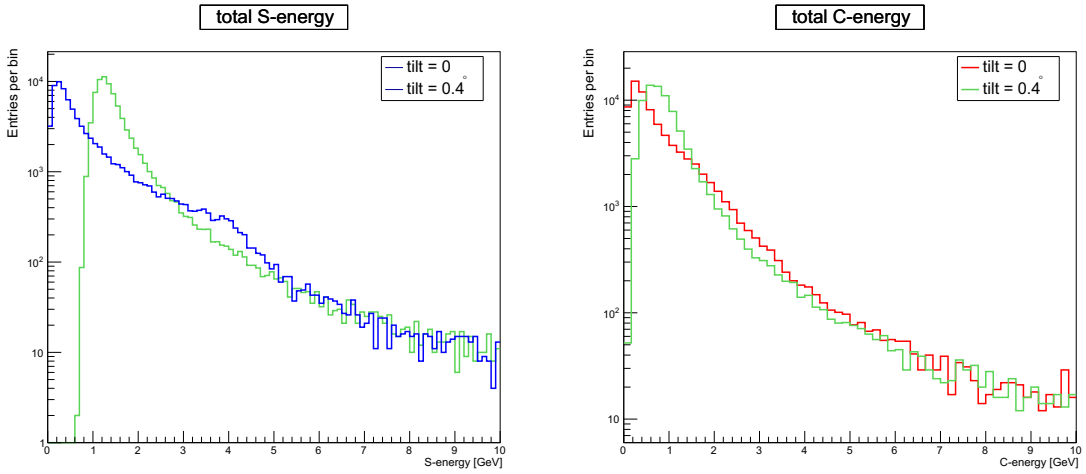

(a) (b)

Figure 6.53: The MPVs of the muon energy losses reconstructed by the scintillation (a) and Cherenkov (b) channels appear at higher values for a 0.4^0 tilt compared to the ones at 0^0.

rotation of 1^0 has been performed. 80k muons of energy 180 GeV were used for this study. The horizontal lines represent the nominal muon energy losses reconstructed by the scintillation and Cherenkov channels in the absence of any vertical tilt. The nominal values appear at lower energies compared to the ones that are obtained with vertical tilts. This can also be observed in the distributions of Figures 6.53a and 6.53b where the MPVs of the muon energy losses reconstructed, respectively, with the scintillation

and Cherenkov channels appear at higher values for a 0.4^0 tilt compared to the ones at 0^0.

Chapter 7

Conclusion and outlook

The primary purpose of this thesis work was to understand the performance of a DRO fibre-sampling EM-scale calorimeter prototype, for the first time built starting from capillary tubes. Following the resolution of all the technical issues for the construction and assembly of the prototype, tests with positron and muon beams were performed in DESY and at the CERN SPS North Area. The main observations and learning derived from the SPS data analysis (Sections 6.3, 6.4 and 6.5) are briefed in Section 7.1. Objectives on a scalable HiDRa readout are shortly described in Section 7.2.

7.1 Lessons from the EM-scale prototype tests

The EM-scale prototype has dimensions of $\sim 2 \cdot R_M$ (R_M = 23.8 mm) and $\sim 44 \cdot X_0$ and $\sim 53 \cdot X_0$ (X_0 = 22.7 mm) for the surrounding and central towers, respectively. When hit at the centre, it has a nominal containment of ∼94%, estimated with simulation studies, independently for both the scintillation and Cherenkov channels. About 50% of the EM-shower energy is contained within a cylinder with a radius of 1 cm. As expected, the containment is the highest when the beam is steered at the central tower rather than at the surrounding ones, because the number of shower particles leaking out the module is comparatively lesser. However, during the tests with beam at the CERN SPS, the shower containment was distorted as a consequence of the presence of the upstream PS. Due to its distance from the calorimenter, the opening of the showers starting in the PS was causing both more leakage and larger leakage fluctuations, as well as a ∼5% variation in the linearity of the reconstructed shower energy normalised to the beam energy. Among other studies, the response uniformity over the transverse surface of the calorimeter was studied with a 40 GeV positron beam steered at the common corner of four towers. The relative spread (σ over mean) was calculated to be 6.2% and 5.0% for the scintillation and Cherenkov channels, respectively. The spread was improved and measured to be 3.8% and 4.3% when the results from the two independent measurements were combined by weighted and unweighted average, respectively. These fluctuations are dominated by geometrical effects, a too small impact angle of the beam particles and the discrete and alternate fibre pattern. Also the lateral leakage due to distant positioning of the PS contributes to these spreads. An EM energy resolution of $24\%/\sqrt{E} + 0.006$ was estimated for the combined signals. The prototype aims to achieve an EM energy resolution of $\sim 15\%/\sqrt{E}$. Further analysis is ongoing to

implement corrections in order to try to account for the geometrical effects mentioned before.

It is clear that most of the above problems can be avoided with a better geometrical arrangement. It appears that, for the beam tests of the EM-scale prototype, the standard setup used for the RD52 prototype tests was followed. Due to the much larger dimensions of the RD52 prototype, $\sim(28 \times 28)\ cm^2$, the fact that the PS was installed at 2.8 m upstream, was not causing significant issues. For the EM-scale prototype, this was a mistake that caused significant energy leakage and even more significant leakage fluctuations. On top of that, a too small impact angle (1^0) of the beam particles in the horizontal plane and the no impact angle (0^0) in the vertical plane introduced geometrical effects that were reflected in the measurements of response uniformity and EM energy resolution. Last but not least, the quality of the measurements was also affected by issues due to the tracking devices (the two DWCs not properly working) and the very poor purity of high-energy positron beams on the SPS beam line.

In order to acquire data with less beam contamination and improved systematic arrangements (PS mounted close to the calorimeter module, a properly working tracking system, etc.), the DRO collaboration has decided to test the EM-scale calorimeter at the CERN SPS again in 2023, in case on a different beam line. Significant and different combination of the horizontal and vertical orientation of the module with respect to the beam axis will be thoroughly studied. In addition, experimental data are needed to better understand the response of the calorimenter to MIP particles. In all cases, the comparison with Geant4 predictions and their validation, will constitute a stepping stone for detector development. The fibre SiPM readout indeed can provide measurements with an unprecedented granularity so that the energy deposition pattern can be analysed with great details.

7.2 Some objectives on HiDRa

The above work is setting the ground for building a hadronic-scale prototype. As briefly discussed in Section 4.4.2, the HiDRa project is the next potential step (already started), towards building a calorimeter for IDEA, capable of fulfilling the detector requirements for future circular leptonic colliders. HiDRa aims to exploit the following:

- Validation of a feasible solution for the technical and mechanical construction.
- Design and validation of a compact and scalable readout architecture based on SiPM sensors.
- Validation of the Geant4 hadronic shower simulation models.
- Assessment of hadronic performance of the calorimeter.
- Assessment of the longitudinal shower position reconstruction through timing measurements.
- Exploitation of Deep Neural Network (DNN) algorithms [78, 79] in final-state identification and reconstruction.

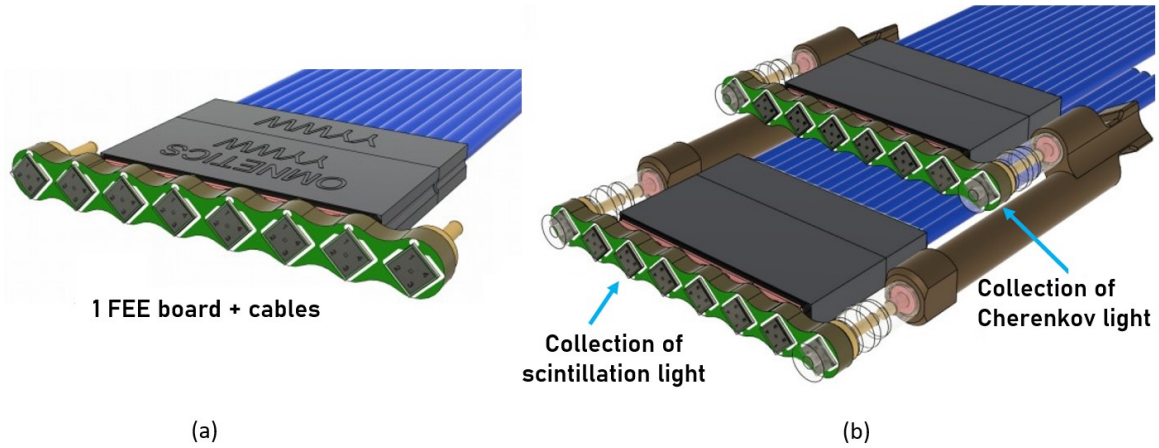

Figure 7.1: One FEE board reads eight SiPMs that are interspaced by 2 mm. Blue strips represent cabling (a). Scintillation and Cherenkov light collections are well separated to fully avoid optical crosstalk. Two FEE boards are attached by clips (b).

The scalable readout solution that is under studies and that will be adapted for HiDRa, is briefly outlined here. Amongst the 86 016 channels of HiDRa, 10 240 fibres in the two central modules will be read out by SiPMs and thus a highly granular core will be formed. The rest of modules will be read out by 150 PMTs. Handling such a large number of SiPMs is a challenge for the design of the detector rear end and FEE boards. For the two highly granular modules, 2×10 FEE boards are required. Custom designed module (from HAMAMATSU) with 8 SiPMs, each of area (1×1) mm^2, 2 mm interspaced and 10 or 15 μm cell size, are under studies. Signals from eight SiPMs will be summed up in a grouping board and read by one FEE board.

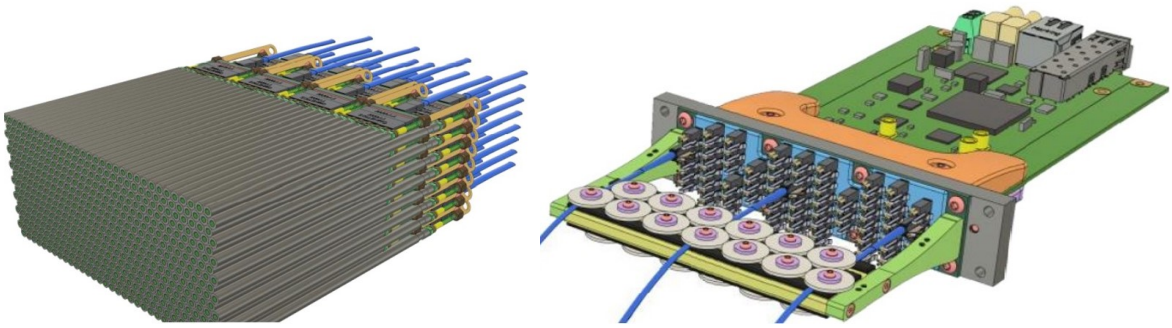

Figure 7.2: In one minimodule each fibre is equipped with a single SiPM. 64 FEE boards (one board per eight SiPMs) serve one minimodule (a). With 8-channel grouping, one FERS card serves 64 FEE boards, i.e., 512 channels (b).

Figure 7.1a shows the mechanical drawing of one FEE board and the cables. Two modules are well separated to fully avoid optical crosstalk, i.e., the contamination between scintillation and Cherenkov lights (Figure 7.1b). A minimodule (512 channels) requires 64 $(512 \div 8)$ FEE boards that, with the grouping of the signals of 8 FEE channels, are served by one FERS board (Figure 7.2b). The option for using digital SiPMs

is also under discussion. Recently, the qualification of PMTs has started in Catania and Pisa.

Appendix A

Construction and data quality of Micromegas for NSW

A.1 The ATLAS experiment

The ATLAS detector is designed to exploit the full physics potential of the proton-proton collisions at the LHC. Hence, it is hermetic and covers nearly the full 4π solid angle around the IP. Its subsystems, the Inner Detector [80, 81, 82], the electromagnetic, hadronic and forward calorimeters [83, 84] and the outermost Muon Spectrometer [85, 86], are designed for the identification of particles and measurements of their kinematic properties. ATLAS has concentric detector layers in the so called *barrel* region and is sealed by the two *endcap* structures where the detector layers are in form of disc shapes. The subsystems are cylindrically symmetric as the particles produced in the collisions have no preferred direction in the plane transverse to the beamline. Hence, ATLAS is roughly cylindrical with the LHC beampipe as its longitudinal central axis and is about 44 m long and 25 m in diameter. The overall weight of the detector is approximately 7000 tonnes. An overview of the ATLAS detector is shown in Figure A.1. The subsystems are capable to tolerate high-intensity radiation doses from the LHC and use radiation-hard, fast electronics which provide distinct readout for a 25 ns *bunch crossing* rate. ATLAS makes use of four superconducting magnets [87]; an inner solenoid, a barrel toroid and two endcap toroids. These are cooled with liquid helium and maintained at an operating temperature of ∼4.7 K.

A huge amount of data (∼1.6 MB raw data per event) is produced at a 40 MHz collision rate of proton bunches with around 30 collisions (*pile-up*) per bunch crossing (i.e., 10^9 collisions per second). The ATLAS Trigger and Data Acquisition (TDAQ) system [89] handles the online event selection based on physics processes of interest (e.g., the production of Z bosons) and the readout of data for the selected events. The hardware based Level-1 (L1) trigger reduces the rate of 40 MHz down to ∼100 kHz and the software based High Level Trigger (HLT) reduces it even further to about 1 kHz in average. The selected events are sent for full reconstruction at the CERN on-site computing center called Tier-0. A detailed description about the operation of the ATLAS trigger system in Run 2 can be found in Ref. [90].

The ATLAS data taking is a collection of *runs* which typically correspond to one *LHC fill* [90, 91]. Each run is split into small sections of time, referred to as Luminosity

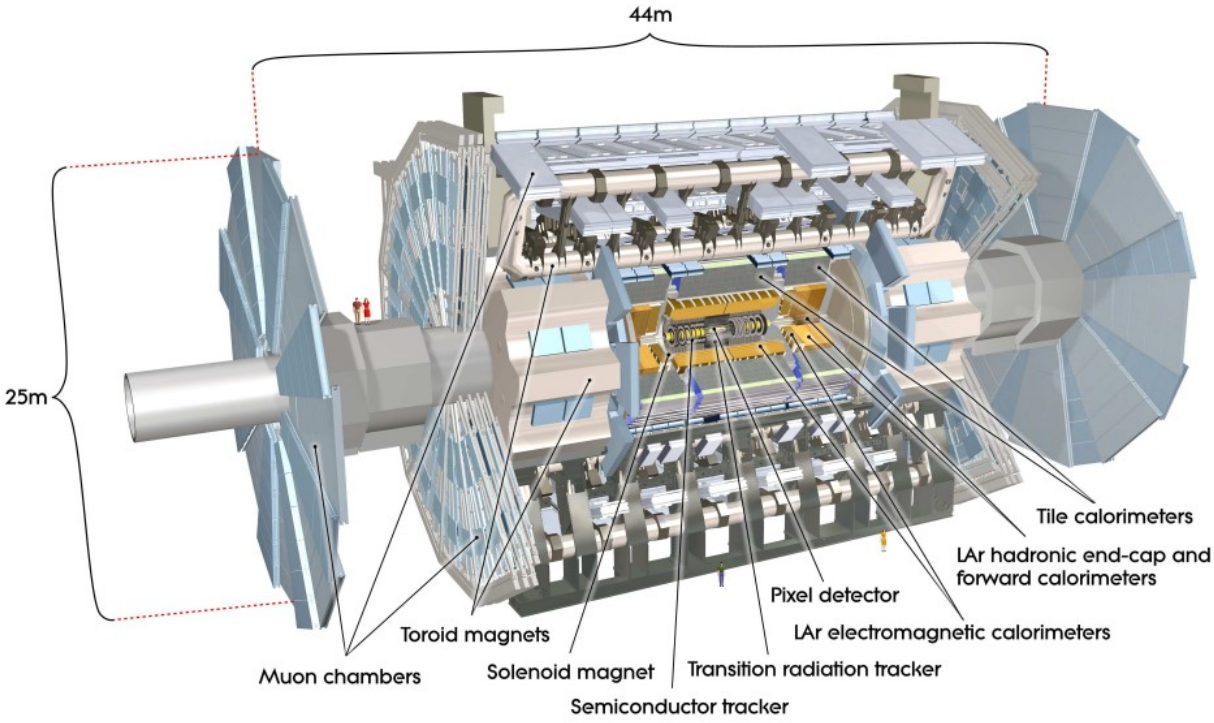

Figure A.1: Overview of the ATLAS detector with labelled subsystems and magnets. Ref. [88]

Blocks (LBs). A LB has a length of $\sim$ 60 s and is identified by an integer unique within a given run. The instantaneous luminosity is approximated to be constant within a LB interval. Data events inside a LB are recorded under the stable detector conditions (including the trigger system and its configuration). The integrated luminosity can then be expressed as:

$$L = \sum_{LBs} \mathcal{L}_{LB} \cdot \Delta t_{LB} \tag{A.1}$$

where $\mathcal{L}_{LB}$ is the constant luminosity inside the LB, Δt_{LB} is the duration of the LB and the sum runs over all the LBs in the considered time window. After data taking in Run 2 (2015-2018), an integrated luminosity of 139 fb^{-1} is available for data analysis after rejecting those LBs where essential detector components were malfunctioning. A complete description of the ATLAS experiment can be found in Ref. [88].

A.2 LHC Phase-I upgrade and NSW

The LHC and its experiments have gone through several upgrades [92] during the Long Shutdown 2 (LS2) in order to increase the instantaneous luminosity of $10^{34} cm^{-2} s^{-1}$ and deal with it in Run 3 (2022 - 2025). One of the main upgrades of the ATLAS experiment was the replacement of the innermost station of its muon endcap system, the Small Wheel (SW), by the New Small Wheel (NSW) [93], as indicated in Figure A.2. The SW was not designed to exceed the original design luminosity of the LHC, whereas the NSW has been designed to cope with high background radiation environment upto $\sim$15 kHz/cm^2.

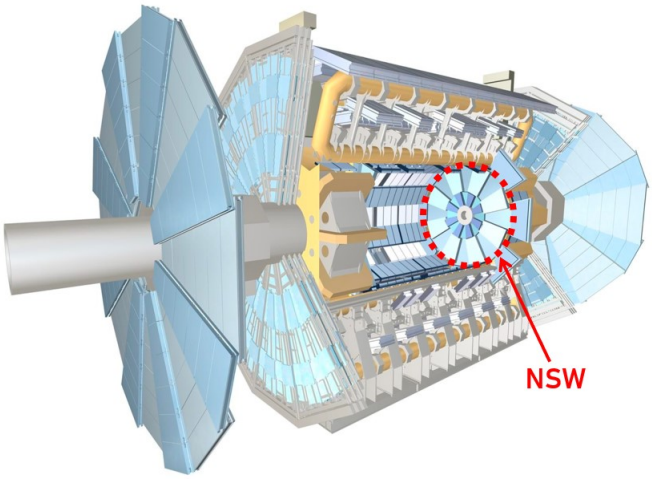

Figure A.2: One of the two NSWs, the innermost station of the muon endcap system, is indicated.

The two SWs were equipped with Cathode Strip Chambers (CSCs) and Monitoring Drift Tubes (MDTs), whereas the two NSWs are equipped with MicroMegas (MM) and small-strip Thin Gap Chamber (sTGC). Because of the small gap and strip pitches (Section A.4.1), the MM serves as the primary precision tracking detector. On the other hand, the sTGC acts as the primary trigger system (L1), because of the single bunch crossing identification capability. The MM can also confirm the existence of track segments online and the sTGC can measure muon tracks with good precision offline. So, the sTGC - MM combination is a redundant detector for triggering and tracking. The main performance criteria of the NSW are listed below:

- The angular resolution of ∼1 mrad for online reconstruction of track segments (for L1 trigger).
- 100 μm spatial resolution for precision reconstruction of tracks for offline analysis.
- 0.4 mm granularity in track-separation.

These requirements demand the following mechanical precision:

- Knowledge of the absolute position of each detector unit at the level of 60 µm or better.
- Planarity of all detector surfaces with RMS below 37 µm.

And, these numbers bring enormous complexity in the construction.

A.3 A Micromegas double wedge

The NSW is a composition of eight small and eight large trapezoidal, multi-layer sectors (Figure A.3a). Each sector (Figure A.3b) comprises of two sTGC quadruplets and two MM quadruplets i.e., a MM double wedge or eight MM detection layers. For the first time, MM detectors of large size (up to 3 m^2) have been employed in a HEP experiment.

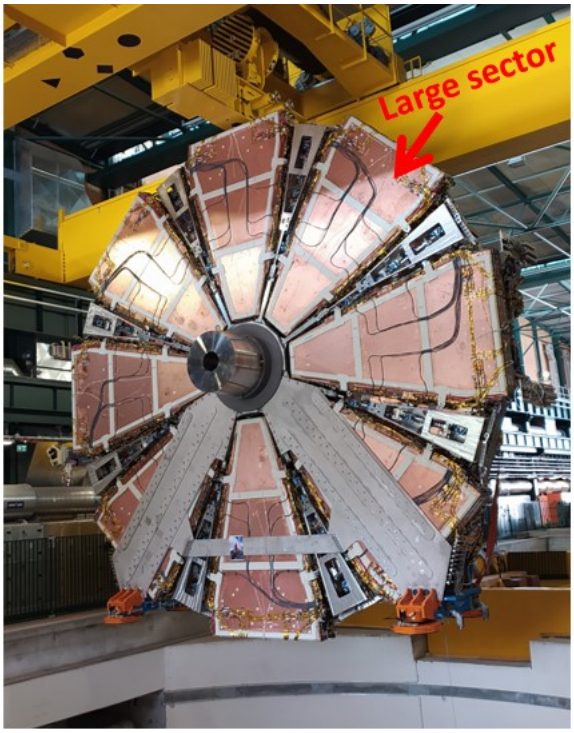

(a)

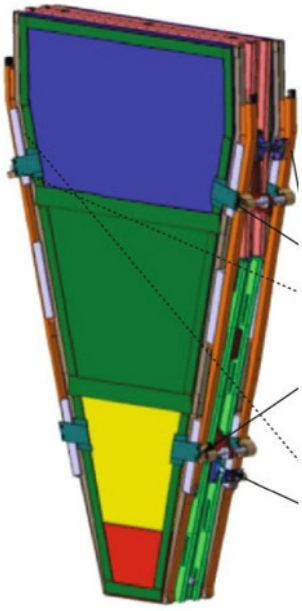

(b)

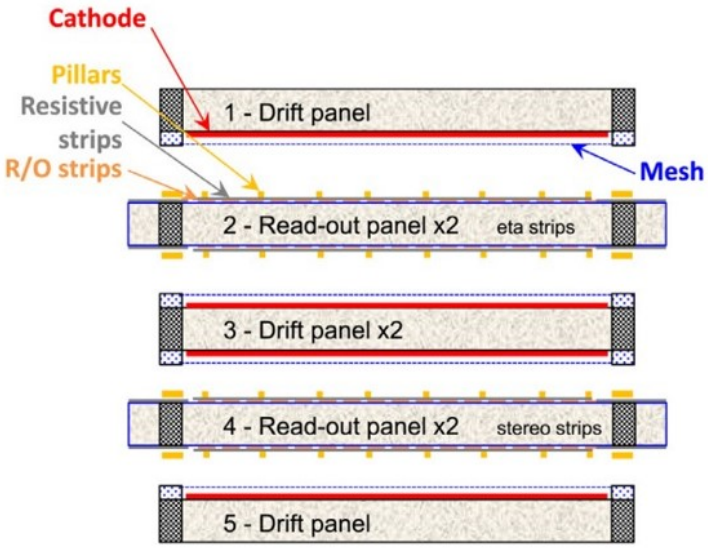

(c)

Figure A.3: All sixteen sectors are installed and the NSW-A is ready to be transported inside the cavern for commissioning. One large sector is indicated (a). A schematic sketch of one sector (b). A sketch of five panels (multiplets) that are assembled to form a MM quadruplet i.e., four MM detection layers (c). Ref. [94]

Each MM quadruplet [94] is a composition of five certified panels forming a multiplet (Figure A.3c). Two of these five panels are double faced ReadOut (RO) panels that consist of Printed Circuit Boards (PCBs) with carbon resistive strips, Cu RO strips and pillars to support and stretch the micro-mesh. These mentioned components of the PCBs will be introduced in the next Section A.4. The RO panels are of two types, namely eta and stereo. In eta panels, the resistive and readout strips run parallel to the trapezoid bases. In stereo panels the resistive and readout strips run with $\pm 1.5^{\circ}$ angles with respect to the direction of the bases. The two cases reconstruct and measure two different coordinates of the experimental coordinate system [94].

The constructions of 4 types of Small (S) and Large (L) MM Modules (M), namely SM1, SM2, LM1, LM2, were distributed over different countries: Italy, Germany, France, Russia/Greece, respectively. Two MM quadruplets of a small (large) sector is a combination of SM1 (LM1) and SM2 (LM2) panels. SM1 and SM2 (also LM1 and LM2) RO panels are composed of five and three trapezoidal PCBs, respectively. The two NSWs are integration of 128 quadruplets (32 of each type). Italy took the responsibility of SM1 panel construction. INFN-Pavia, in particular, was responsible for the construction of 64 SM1 RO panels for the two NSWs. One RO panel is made of 10 (2×5) PCBs on both surfaces. So, one RO panel supports two micro-meshes and builds two MM detection layers.

A.4 Micromegas

My ATLAS Qualification Tasks (QTs) (Sections A.5 and A.6) were solely focused on Micromegas. So, the working mechanism and dimensions of the detector are described here.

A.4.1 Operating principle

Micro mesh gaseous structure (Micromegas) or MM [95] is an MPGD. It consists of a planar drift electrode, a thin metallic micro-mesh and a readout electrode (Figure A.4a). The gas gap of a few millimetres between the drift electrode and the mesh acts as the conversion and drift region, whereas the thin amplification region of $\sim 128\mu$m is formed between the mesh and the electrode. A sketch of the Micromegas operating principle is shown in Figure A.4b. The HV potentials have been chosen to create a relatively low electric field of ~0.6 kV/cm in the drift region and of 40 - 50 kV/cm in the amplification region. Charged particles traversing the drift gap ionise the gas (typically, Ar:CO_2 :: 93:7). The liberated electrons drift towards the mesh and as the electric field of the amplification gap is $\sim$ 100 times stronger than the drift gap, the mesh becomes transparent for most of the electrons. In the amplification gap avalanche of electrons takes place in a fraction of nanosecond and charge clusters are formed. Positive ions produced in the process move back towards the mesh. Due to relatively low drift velocity, it takes ~100 ns for the ions to reach the mesh. Still it is quite faster compared to other gas detectors.

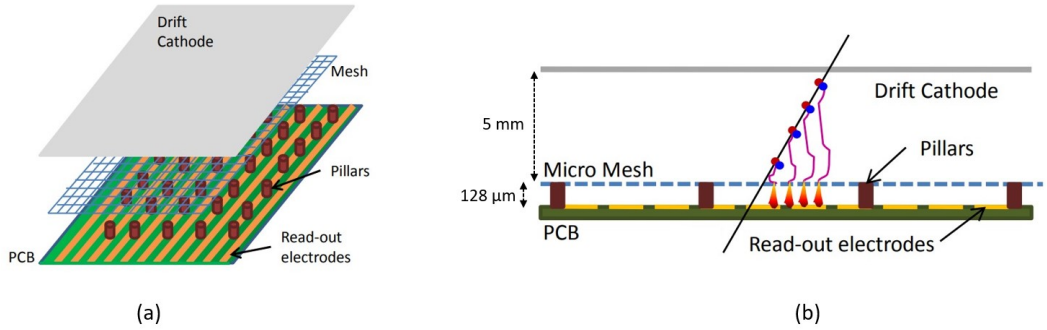

Figure A.4: A layout (not to scale) of the Micromegas is illustrated (a). Operating principle of the Micromegas: the muon track, its ionisation and cluster formations are depicted (b). Ref. [93]

A.4.2 Spark protection

Micromegas detectors are vulnerable to sparking. Sparks occur when the total number of electrons in the avalanche reaches a few 10^7. To avoid the risks of detector and readout damaging or large dead time, a spark protection system [96, 97] has been developed. A carbon resistive strip layer is added on top of a thin insulator (kapton foil) layer just above the readout copper electrode as shown in Figures A.5a and A.5b. The strip pitch

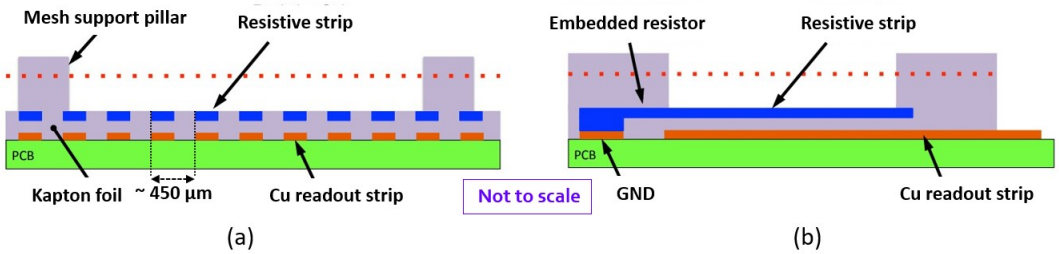

Figure A.5: Schematic diagram of spark protection principle. Two cross-sections at 90° angles are shown. Parallel resistive and Cu strips (a). One resistive strip is embedded on top of kapton foil above one readout Cu strip (b). Ref. [93]

and width are ∼450 μm and ∼300 μm, respectively. The heights of carbon resistive and Cu RO strips are ∼15 μm and ∼17 μm, respectively. The resistance of the carbon strips is a few MΩ/cm. So, the detector can operate at high gas gain and the readout strips are not directly exposed to charges created in the amplification gap. Rather, signals are induced via capacitive coupling to the readout strips. A detailed overview of the construction of Micromegas for the ATLAS NSWs is narrated in Ref. [98].

Two tasks, a hardware activity and a software development, have been assigned to me for being qualified as an ATLAS author. The hardware activity was participation in the construction of SM1 RO panels, in particular, the electrical tests of the PCBs and constructed RO panels for QAQC. The software activity was developing the tools for monitoring (online) the data quality of Micromegas during Run 3.

A.5 Electrical tests and construction

The main components of the SM1 RO panels are PCBs. The electrical properties of the PCBs are critical for the electrical stability and performance of the detector. So, several point-to-point impedances were measured for each PCB produced by Eltos*. The resistive strips and RO Cu strips are already described in Section A.4.2. Another important element for electrical connection is the silverline. It provides the HV connection to the resistive strips. The resistive and Cu strips are disconnected in the middle of a PCB. So tests were performed on both sides of a PCB. Figure A.6 illustrates a sketch of all electrical contact points on a PCB, whereas Figure A.7a shows the largest PCB of a SM1 RO panel and the electrical connections at one side are indicated. The tools used were an automated insulation tester (Megger BM 25) (Figure A.7b), a plexiglass tool with probes (Figure A.7c), multimeters, cables with banana plugs, metal bars and single probe tools. The following resistances were checked PCB by PCB:

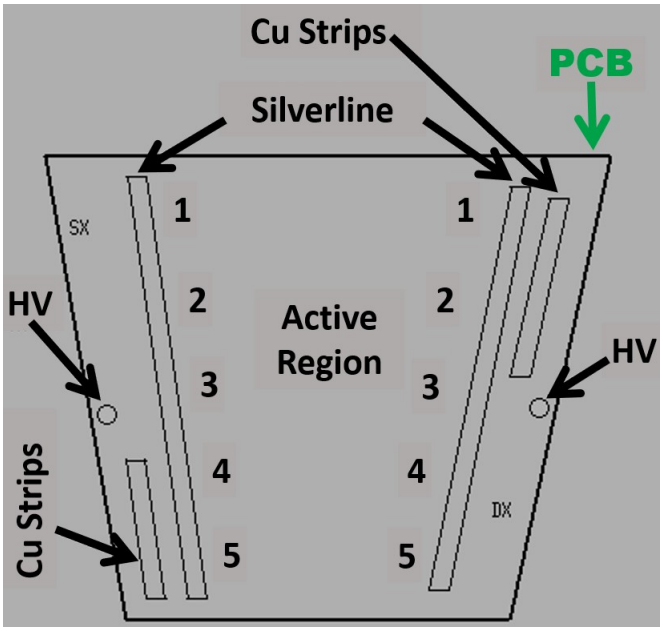

Figure A.6: A schematic sketch of different electrical contact points on a PCB.

- Resistances of the resistive strips at borders and main active region of a PCB with respect to the HV were measured to be a few MΩ.
- Silverline isolation with respect to the resistive strips provided a measure of HV stability. Most of the tested silverlines were very well insulated ($\sim$ 1 TΩ). Isolation was measured at 1000 V of insulation tester for 2 minutes.
- Insulation of the resistive strips with respect to the RO Cu strips (due to presence of kapton foil) was measured to be $\sim$ 3 GΩ.
- Resistance of the resistive strips along the borders of the active region was measured to be greater than 0.8 MΩ to confirm the HV stability. Otherwise, PCBs

*https://eltos.com/

were sent back to CERN for passivation or deactivation of the border regions. After passivation the resistances were measured to be 100 GΩ.

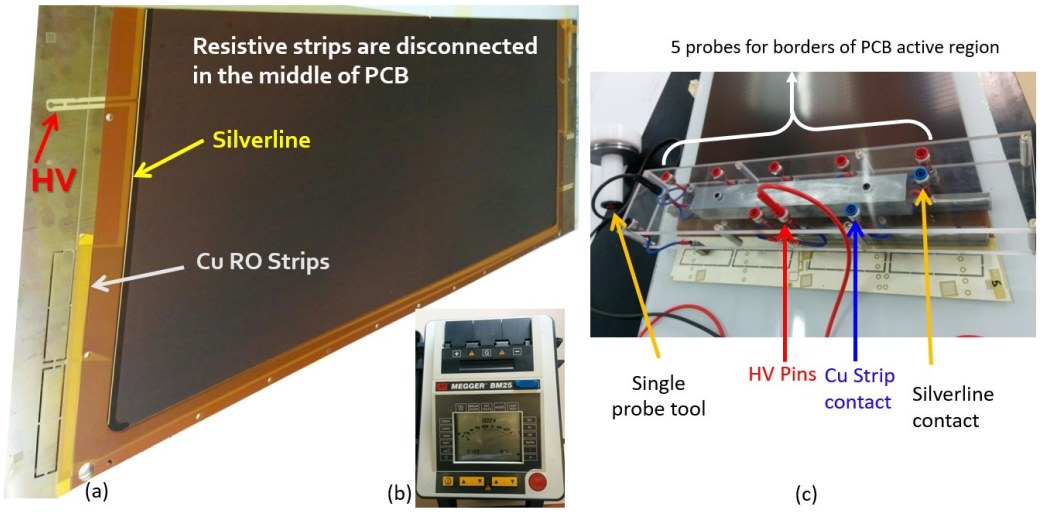

Figure A.7: The largest PCB of a SM1 RO panel. The HV connection, the Cu RO strip connection and the silverline at one side of the PCB are indicated (a). The automated insulation tester (Megger BM 25) used to measure high resistances e.g., ∼GΩ or more (b). A plexiglass tool placed on one side of a PCB. The probes are indicated. The single probe tool for connecting the resistive strips in the active area of the PCB is shown (c).

After the electrical tests on the PCBs were carried out, five PCBs of different sizes were placed on high-precision aluminium plates, mounted on a granite table. The granite table, having a planarity with a certified maximum deviation of 8 μm, was used as reference for both the construction tools and the measurement system. The aluminium

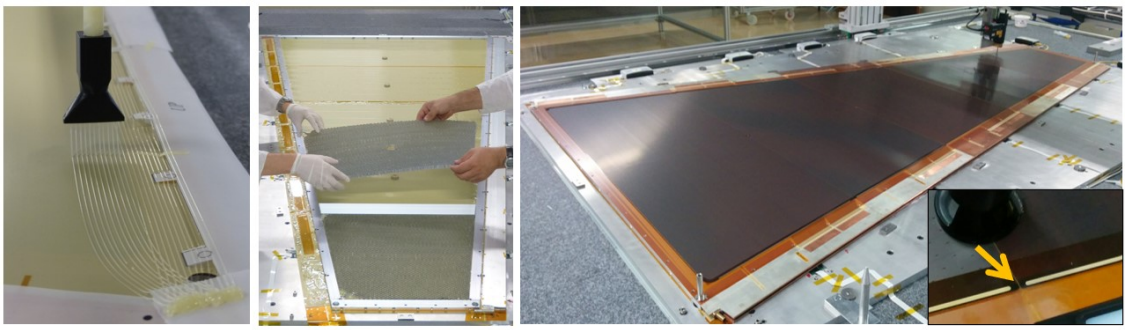

Figure A.8: An automatic glue dispenser was installed (a). Honeycomb structures and aluminium bars are placed on the top of glued PCBs before placing another layer of PCBs (b). One assembled SM1 readout panel that has two back-to-back layers of readout PCBs with pillars for the mesh. The inset image indicates the insulation (>30 GΩ) of the junction glue at the silverline position that has been measured with respect to the HV inputs of both PCBs (c).

plates were equipped with vacuum suction systems. For each Micromegas layer, the fine positioning of the PCBs were achieved by exploiting the vacuum technique. An automatic glue dispenser was installed (Figure A.8a). Two Micromegas layers, brought back-to-back using a stiff-back plate, were separated by glued honeycomb structures and aluminium frames (Figure A.8b). Figure A.8c shows one assembled SM1 RO panel i.e., two back-to-back Micromegas layers. The use of reference holes on plates and calibrated Contact-CCDs (C-CCDs) assured the quality of alignment that was measured to be excellent and within requirements.

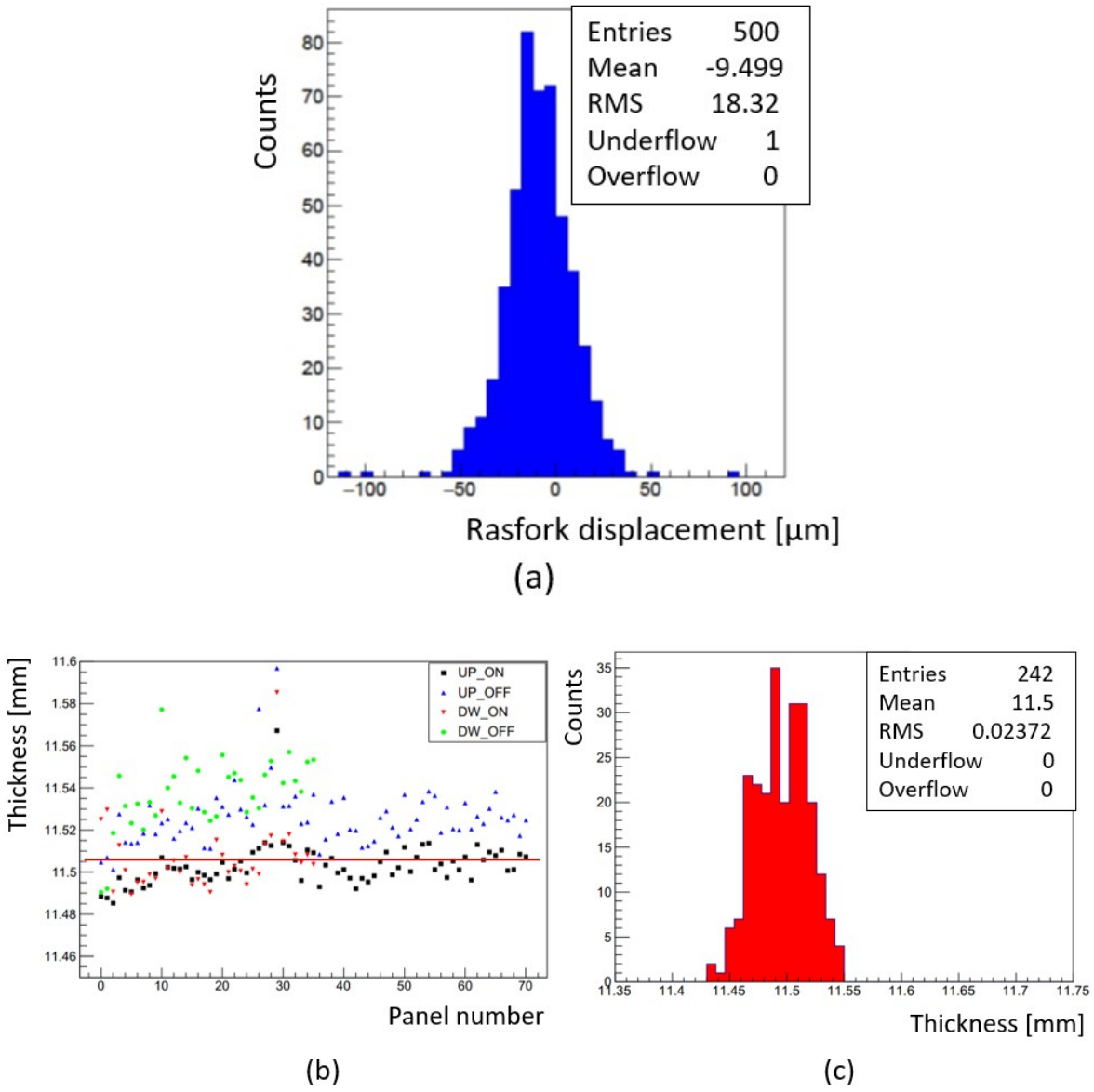

Figure A.9: The distribution of the Rasfork mask displacement. The standard deviation of ∼18 μm shows an excellent alignment (a). The average thickness of all panels for both sides, with vacuum sucking either ON or OFF (b). The distribution of thickness for all panels. The standard deviation of 24 μm shows an excellent planarity (c). Ref. [99]

Figure A.9a shows the distribution of the calibrated mask (Rasfork tool [100]) displacement measured by the C-CCDs. The standard deviation of ∼18 μm shows a good positioning and alignment. Figure A.9b shows the thickness measurement of 70 (64 + 6 spares) RO panels as a function of the panel number. The corresponding histogram is shown in Figure A.9c. The nominal value of the thickness was measured to be 11.5 mm, whereas a standard deviation of ∼24 μm shows an excellent planarity below the upper limit of 37 μm that was required to guarantee the constant gain of the detector.

As mentioned before, the electrical tests were performed again on the assembled RO panel, as a step of finalisation, before transportation to the INFN Laboratori Nazionali di Frascati where assembling of the quadruplets took place. The previously mentioned first three electrical tests performed on each PCB were repeated on both surfaces of the constructed RO panels. The excellent results obtained are shown in Figure A.10. One more electrical test was carried out on the junction of two PCBs at the silverline position (Figure A.8 inset image). The insulation of this junction glue was measured with respect to the HV inputs of both PCBs and for most of the tests it was greater than 30 GΩ. A pen-like tool with probe and the automated insulation tester were used for these measurements. A detailed description of the construction procedure of the SM1 RO panels along with all the quality control tests, e.g., electrical tests, gas tests etc., can be found in Ref. [99].

A.6 Online-DQ monitoring for Micromegas

The Data Quality Monitoring (DQM) [101] is an integral part of the data taking process of the ATLAS experiment. It can occur both in online and offline environment. The online DQM in the ATLAS Control Room (ACR) is the first line of defense to catch and mitigate data loss. It provides the shift personnel with live information about the ongoing run. If the data taken is determined to be faulty, the run is marked accordingly as not to be used for physics analysis. The online DQM involves analysis of monitoring data through predefined and user defined DQM Algorithms and then display of analysis results, while the data is being processed. This information is used by the shift operators and the detector experts to make an assessment on the quality of the current run and is then archived for future reference. The DQM provides XML files that constitute the Good Runs Lists (GRL) that are certified for use in physics analysis. These files are fully integrated into the analysis tools used by the ATLAS collaboration.

A.6.1 Configuration database and DQMF

For developing the online DQM of Micromegas, *partition*, a self-contained TDAQ system, has been configured. Configuration database includes files for the TDAQ release 09-01-00. The database describes all the parameters, that are spread over multiple files located in different sub-folders (e.g., schema, sw, hw, segments and partitions), of a TDAQ system. The configuration has been set up in the ATLAS TDAQ Test Bed machines that are connected to the CERN General Public Network (GPN).

The Data Quality Monitoring Framework (DQMF) [103, 104] interacts with the online monitoring services as well as some other online services provided as part of the ATLAS TDAQ software infrastructure, in order to fulfill its objectives. Figure

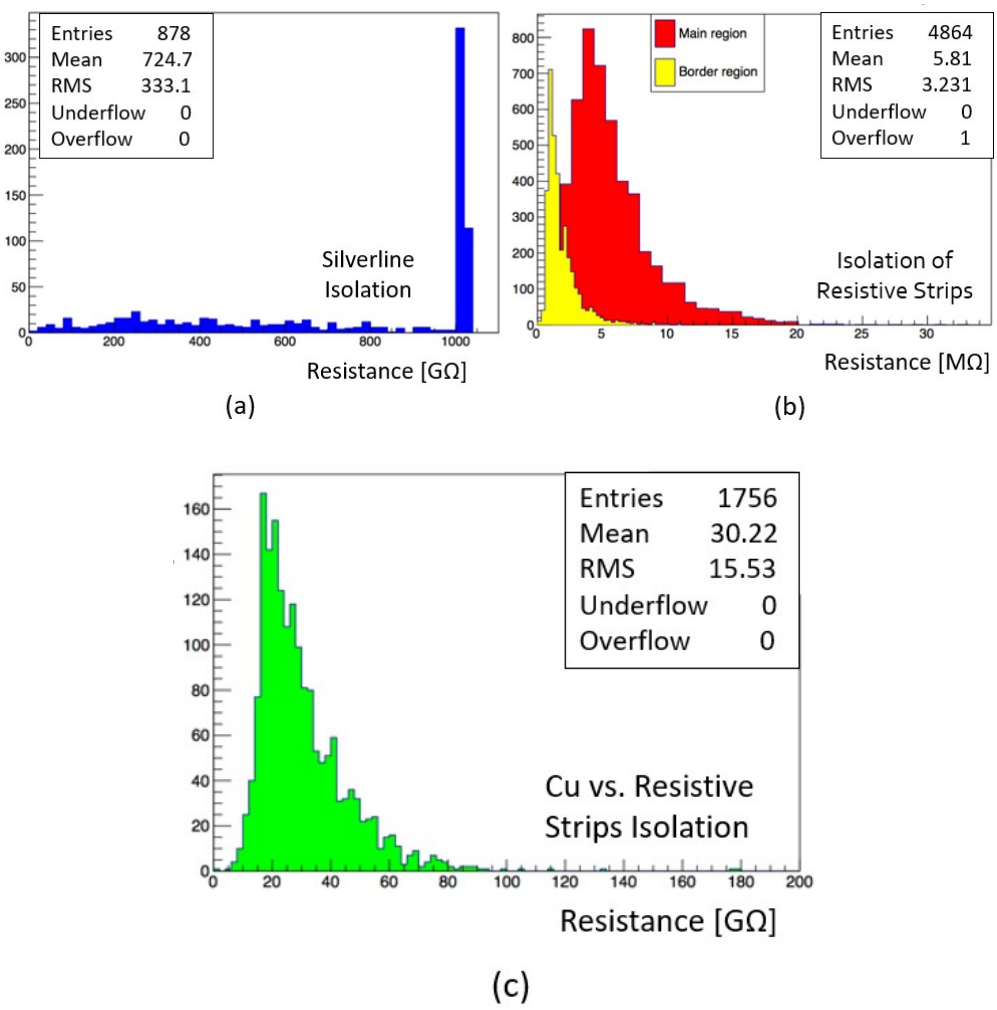

Figure A.10: Results of the electrical tests for the SM1 RO panels. Most of the tested silverlines are very well insulated. The peak of the distribution is at $\sim$ 1TΩ (a). The distribution of the resistive strip isolation with respect to the HV has a peak at $\sim$2 MΩ for the borders and at $\sim$5 MΩ for the main active regions (b). The distribution of isolation of the resistive strips with respect to the RO Cu strips has a peak at $\sim$30 GΩ (c). Ref. [99]

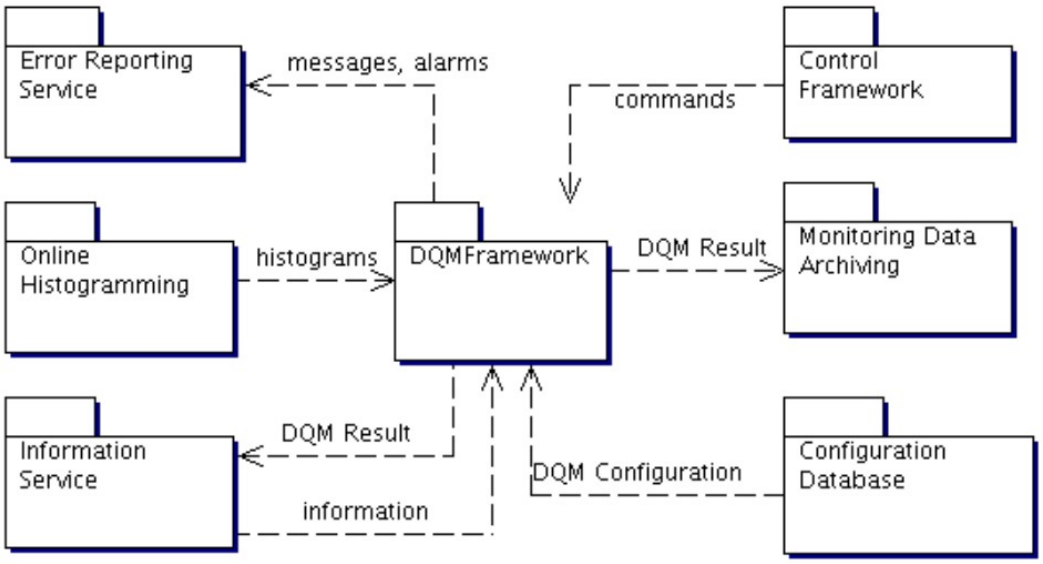

Figure A.11: Interaction of the DQMF with the TDAQ online services. Ref. [102]

A.11 shows a graphical representation of these interactions between the DQMF and the TDAQ online services. We have included GNAM [105] framework in the configuration database for event (raw data) analysis. The GNAM produces results for the current run in forms of histograms that are published to the Information Service (IS) via the Online Histogramming service (OH). Data quality assessments have been performed based on the analysis of these histograms. The DQMF executes DQM Algorithms on the input histograms and provides DQM Results as output. The results are presented to the shift operators by the Data Quality Monitoring Display (DQMD) [106].

A.6.2 DQM Algorithms

The DQMF provides ∼150 predefined DQM Algorithms[†] in a form of shared library. These are used for the most common checks for histograms, like whether all bins are filled, number of underflows/overflows, fittings, threshold application, etc. Figure A.12 shows that the predefined DQM Algorithm, "All Bins Filled", has been defined as an instance of the 'DQAlgorithm' class in an XML file of the configuration database. In addition to predefined algorithms, user defined DQM Algorithms are also developed and used in the system on the fly without modifying the core software.

```
<obj class="DQAlgorithm" id="All_Bins_Filled">
 <attr name="LibraryName" type="string" val="libdqm_algorithms.so"/>
 <attr name="ParametersNames" type="string" num="0"/>
 <attr name="ThresholdsNames" type="string" num="0"/>
</obj>
```

Figure A.12: The predefined DQM Algorithm, "All Bins Filled", has been defined as an instance of the 'DQAlgorithm' class in a configuration database file.

[†]https://gitlab.cern.ch/atlas/athena/-/tree/master/DataQuality/dqm_algorithms

The two NSWs have been tested, sector by sector, at the cosmic test stand of Building 899 at CERN (BB5) [107, 108]. The GNAM framework of the configured partition has used the data files from the cosmic tests for event analysis and produced histograms. Some of these histograms, listed below, have been analysed using predefined and user defined DQM Algorithms.

1. Cluster occupancy, i.e., the distribution of the Centre Of Gravity (COG) position of clusters for each layer.
2. Cluster charge, i.e., the distribution of charge collected in each cluster.
3. Layer timing, i.e. the drift time of each channel in a layer.
4. The number of packets per event for a sector.
5. Occupancy eLink, i.e. the distribution of number of packets from each elink.
6. The distribution of relative Bunch Crossing IDentifier (BCID) for all channels. This parameter was mimicked by the electronics for the cosmic tests.
7. Missing VMM[‡], i.e., the missing VMM bit pattern for all elinks.

User defined DQM Algorithms have been developed in C++ language and using the ROOT[§] framework for some of these histograms. These algorithms for the first two distributions in the mentioned list are discussed below.

Cluster occupancy

A charge particle traversing the gas gaps of Micromegas leaves a signal, referred to as a hit, on a readout strip. On a Micromegas layer, hits on nearby strips are grouped into clusters. Figure A.13 illustrates a distribution of cluster occupancy, i.e., number of hits per readout strip, for layer 6 of sector A03. Each layer, made up of eight PCBs, has total 8192 (8×1024) channels. "ClusterAlgorithm.cxx" has been written in order to perform four tasks:

- Calculation of the percentage of dead channels.
- Calculation of the percentage of noisy channels.
- Checking the uniformity of hit statistics for the eight PCBs.
- Application of the DQM flags.

For counting the number of dead channels, i.e., the RO strips with no hits, the zero bin content channels are counted. For noisy channels, a mean value of the number of hits per channel for the eight PCBs has to be defined. The non-zero bin contents are normalised with respect to area of the corresponding PCB. A vector, filled with these normalised values, has been sorted in the algorithm. The average value of the cell contents, from the middle of the sorted vector, has been registered as 'Mean Hit from All PCBs' (M_{8192}). If the ratio of a cell content of the vector and M_{8192} is greater

[‡]Application Specific Integrated Circuit for Micromegas

[§]https://root.cern.ch/

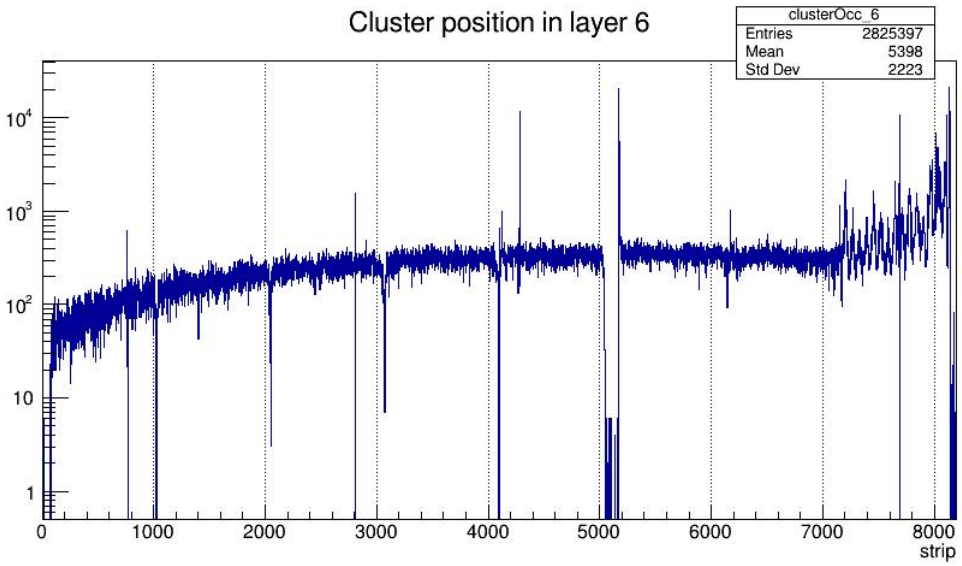

Figure A.13: The distribution of cluster occupancy for layer 6 of sector A03.

than or equal to 20, then the corresponding channel has been counted as a noisy one. In a similar way, 'Mean Hit Single PCB' (M_{1024}) has been calculated separately for the eight PCBs. If $M_{1024} \leq \left(M_{8192} \pm 5\sqrt{M_{8192}}\right)$, then the corresponding PCB is considered as 'Good'.

Debugging of any user defined DQM Algorithm has been performed outside the GNAM partition and the DQM environment. A running partition generates ROOT files where histograms of the run are written. The algorithms have been implemented on these histograms in order to debug the codes. Debugging of the user defined algorithm "ClusterAlgorithm.cxx" with the cluster occupancy histogram of layer 4 (sector A03) is discussed here. The number of empty bins is counted to be 479 out of 8192. Hence, ∼5.8% channels are dead. The algorithm calculates M_{8192} to be ∼283 as shown in Figure A.15a. It is represented by the red line in Figure A.14 that is a distribution of number of hits normalised with PCB areas for all the channels of the Micromegas layer. The noisy channels are those having the number of hits ≥ (20×283). The 33 channels which appear above the green line in Figure A.14 are detected as noisy. Hence, 0.4% channels are noisy for this layer. The average hit statistics is measured for each PCB. Figure A.15b shows the distribution of hit statistics for PCB 8 and the average is measured to be ∼202. This average, individually, for PCB 1 and 4 is below $283 - 5 \cdot \sqrt{(283)}$. So these PCBs are identified as problematic ('Not Good'). The non-uniform hit statistics of this Micromegas layer is clearly visible in Figure A.14. The lower and upper thresholds are defined in the algorithm to process the analysis outcome as the DQM Result. This is described in the next Section A.6.3.

Cluster charge

The number of hits per cluster is a measure of charge in a cluster. The amount of charge (in fC), event by event, forms a cluster charge distribution. It is mentioned in Section A.5 that the readout strips are disconnected at the middle of the PCBs. Hence, for each PCB, there are two cluster charge distributions and for a Micromegas layer, there are sixteen (8×2) cluster charge distributions. Figure A.16 shows one of the two

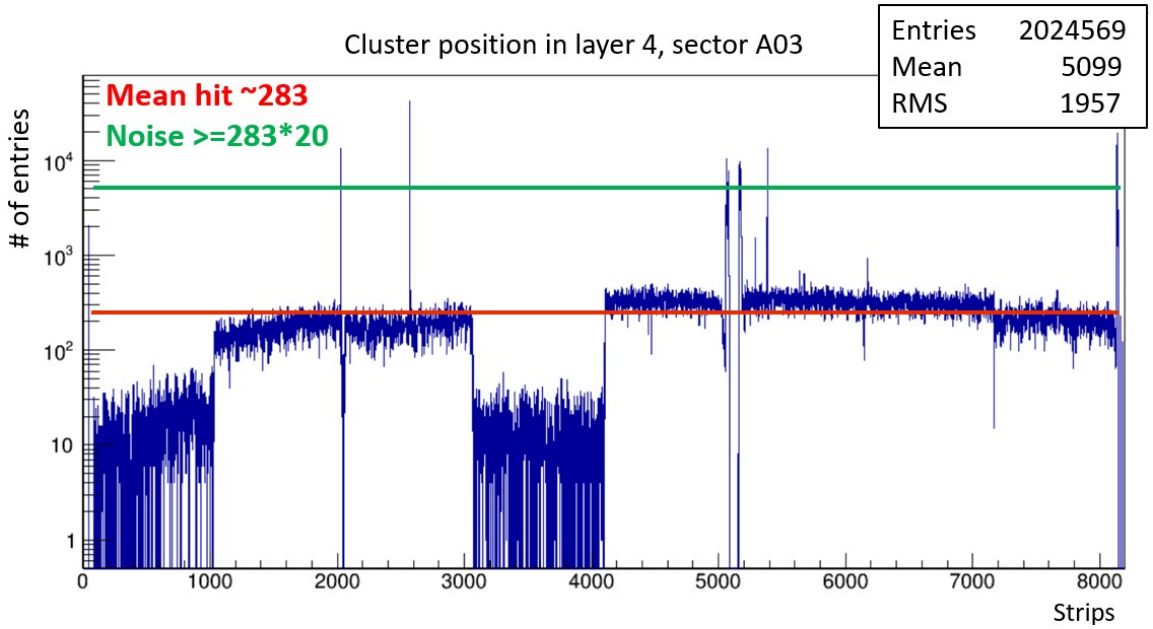

Figure A.14: Debugging of the user defined DQM Algorithm "ClusterAlgorithm.cxx" on a cluster occupancy distribution. The algorithm calculates the average number of hits, ∼283, that is represented by the horizontal red line. The noisy channels are those having the number of hits $\geq (20 \times 283)$. The 33 channels which appear above the horizontal green line, are found to be noisy. For PCB 1 and 4, the hit statistics are comparatively lower.

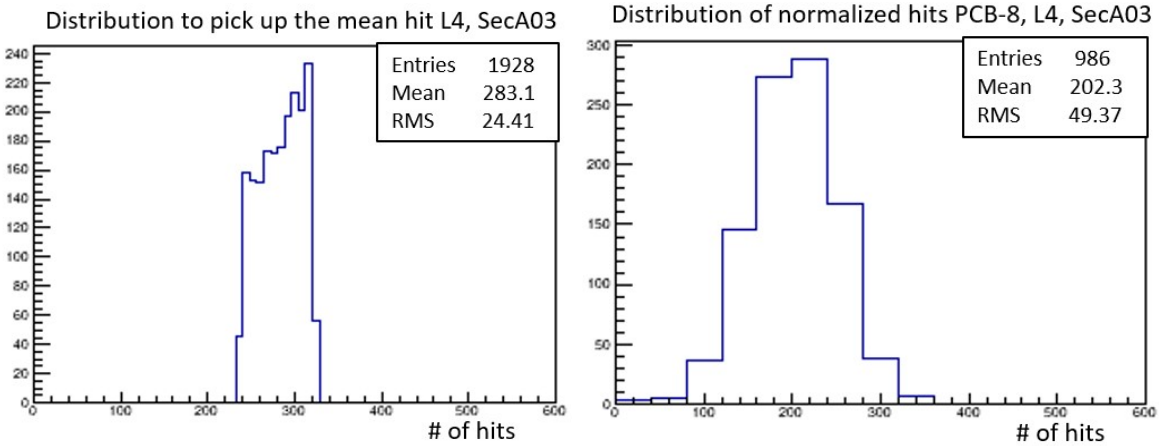

(a) (b)

Figure A.15: The distribution of the number of hits per channel from the middle (1928 cells) of the sorted vector of size 8192. The mean (M_{8192}) of this histogram is ∼283 (a). The distribution of the number of hits, normalised by the PCB area, for PCB 8. The mean is ∼202 (b).

cluster charge distributions of PCB 4 for a Micromegas layer. The DQM Algorithm "ClusterCharge.cxx" first fits the distribution with the Landau function. The MPV of the fitted distribution (C_{MPV}) has been noted. The values, that are defined in the algorithm as the lower and upper thresholds of the MPV, are 15 fC and 45 fC, respectively. The algorithm checks whether C_{MPV} falls within the range from 15 fC to 45 fC or not. Accordingly, the DQMF will show either the Green or Red status as the DQM Result for the histogram.

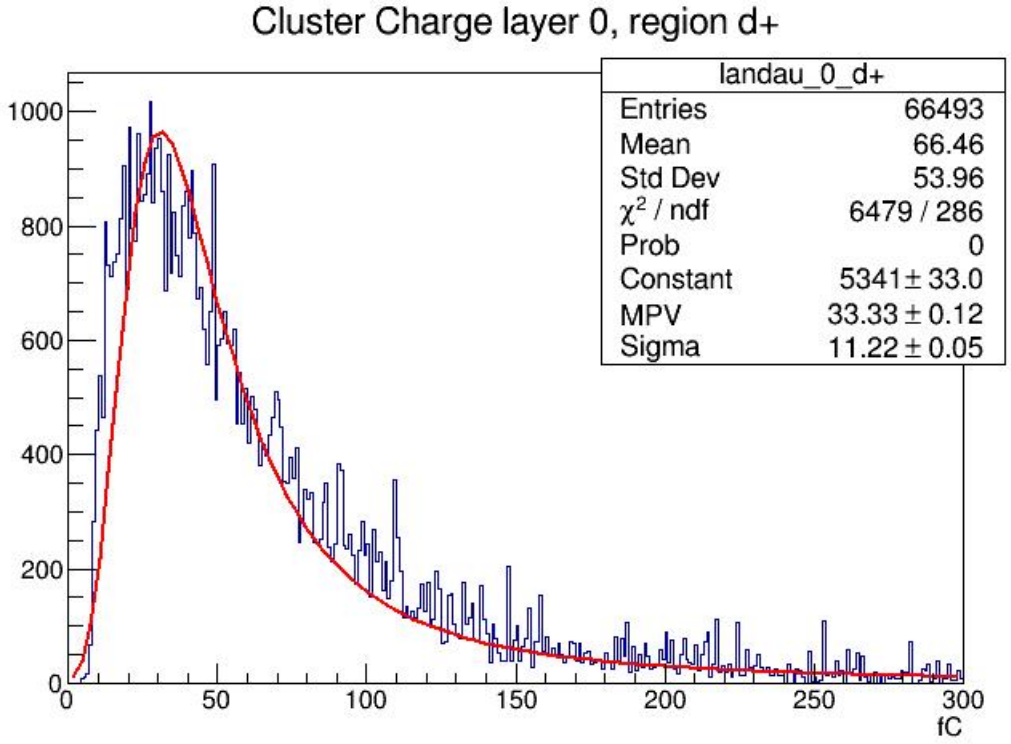

Figure A.16: One of the two cluster charge distributions of PCB 4 for a Micromegas layer. The MPV of the distribution, 33.33 ± 0.12, is extracted from the Landau fit parameters.

A.6.3 DQM Result and Display

The DQM Result object contains a colour code value (Red, Yellow, Green, Grey or Black) that represents the data quality status (Bad, Warning, Good, Undefined or Disabled, respectively) for a given element of the DAQ system. In addition to that it may also contain a reference to the detailed numerical results or histograms that have been produced by the DQM Algorithm.

In previously mentioned algorithm, "ClusterAlgorithm.cxx", "Green" and "Red" thresholds are defined for the three evaluations, i.e., percentage of dead channels, percentage of noisy channels and number of 'bad' PCBs. Figure A.17 shows values of thresholds for this algorithm. The final colour code, as an expression of the DQM Result, is implemented by combining the results of the three evaluations with the following logic:

- **RED:** At least, one of the three evaluations is above the Red threshold.

- **GREEN:** All three evaluations are equal or below the Green thresholds.
- **YELLOW:** At least, one evaluation is between the Green and the Red threshold (i.e., one or two checks may be $\leq$ Green threshold).

For the previously chosen cluster occupancy histogram, the two checks (∼5.8% dead channels and two 'Bad' PCBs) are between the Green and Red thresholds and the other one (0.4% noisy channels) is below the Green threshold. So, the final state of the DAQ element, i.e., the given histogram, is represented by a Yellow flag applied by the DQMF. Figure A.17 shows part of the DQM Display that prints the name of the DQM Algorithm, the parameter(s) and the RED/GREEN thresholds, the description of what the algorithm checks and a troubleshooting message. The parameter(s) and values of the RED/GREEN thresholds are defined in an XML data file of the DQMF. This allows, as mentioned before, implementation of changes in algorithms without modifying the core code.

Result	Configuration	Description	Troubleshooting
2021-Apr-25 11:31:51	**cluster_occupancy_6** Histogram(s): Histogramming.Gnam2./SHIFT/clusters/clusterOcc_6 Weight: 1 Algorithm: ClusterAlgorithm Parameters: minimum noise_hit/average_hit=20 Thresholds: 3<Th_%_of_DeadChn<8; 3<Th_%_of_NoisyChn<8; 0<Th_Nof_Bad_PCB<3;	It is cluster occupancy. The code checks percentage of dead channels, percentage of noisy channels and the unformity of hit statistics for 8 PCBs.	Log it and ask NSW expert

Figure A.17: Part of the DQM Display is shown. It prints the name of the DQM Algorithm, the parameter(s) and values of RED/GREEN thresholds defined in XML data file of the DQMF, the description of what the algorithm checks and a troubleshooting message.

DQM Parameter objects and DQM Region objects are defined in XML data file of the DQMF. A DQM Parameter is an element of the DAQ system, e.g., a histogram, whereas the DQM Region class is a self-contained part of the DAQ system, like a detector or a sub-detector. The display DQMD allows easy navigation between all DQM Regions and Parameters, providing flexibility for visualisation of DQM Results produced by the DQMF. All DQM Regions, sub-Regions and Parameters are organised in a tree where each element is coloured according to the result of the applied algorithm. For each DQM Region the status colour is inferred from the status of underlying DQM Parameters.

After testing the predefined and user defined algorithms on histograms of individual sectors, these algorithms are implemented on histograms of all the sectors of the two NSWs. The DQM display, illustrated in Figure A.18, shows the sixteen sectors as DQM sub-Regions of the higher DQM Region NSW-C. Each sector sub-Region is branched in further sub-Regions that are eight layers. On the other hand, Figure A.19 shows a more complete view of the DQM Display with two panels. The left panel displays an organised tree of the DQM Regions (e.g., NSW-A), the sub-Regions (e.g., sector A01), and all the DQM Parameters (e.g., ClusterOccupancy_L1_A09) with the root node "nsw". It can be observed that the Green status of the Region 'Event_A09' is derived

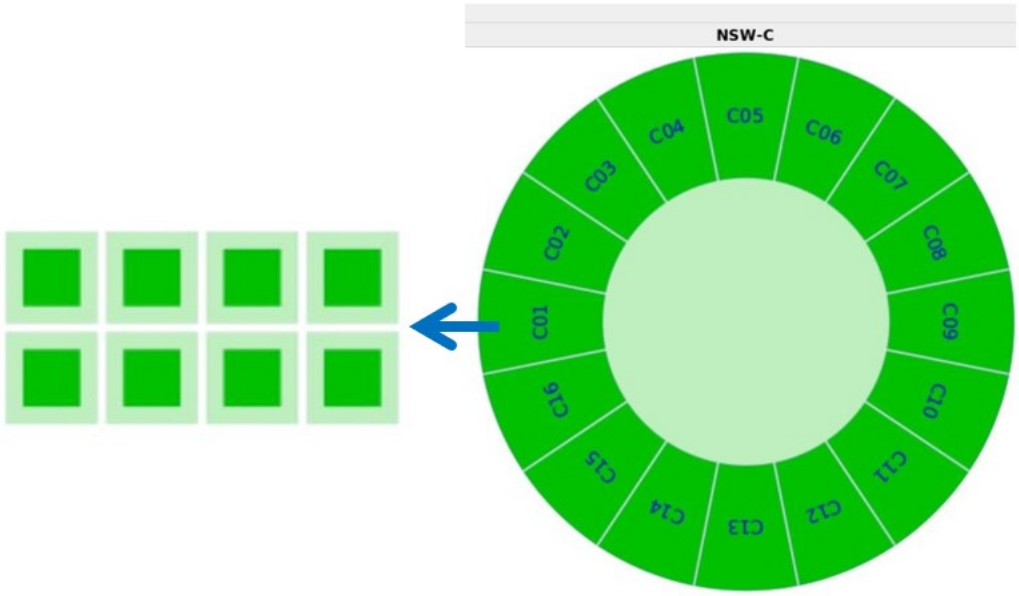

Figure A.18: The DQM Display: NSW-C as the DQM Region and its sixteen sectors as DQM sub-Regions are displayed. Each sector sub-Region has eight layer sub-Regions.

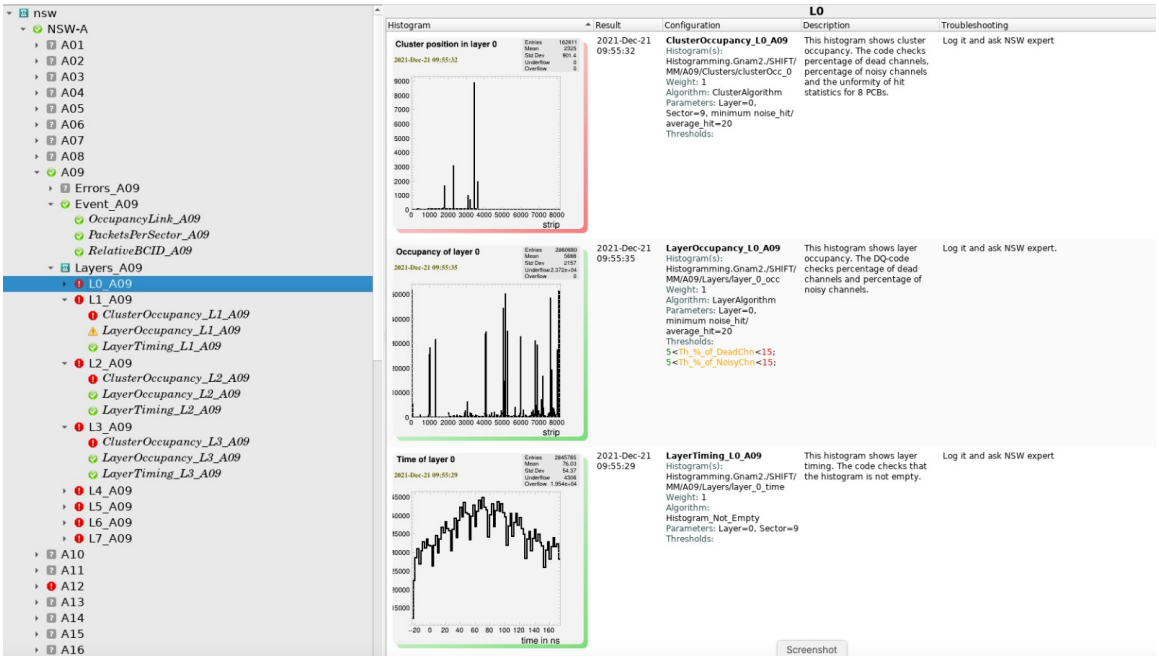

Figure A.19: The DQM Display: The left panel displays DQM Regions, sub-Regions and DQM Parameters organised into a tree with the root node "nsw". The right panel displays histograms as DQM Parameters, colour codes as DQM Results along with configuration, description and troubleshooting messages.

from the Green status of its three Parameters. The right panel displays the detail of all parameters of the Region that has been clicked. Histograms as DQM Parameters are shown with colour icons as DQM Results. For each histogram the DQM Algorithm description, parameters, threshold values and other messages are also displayed.

List of Figures

List of Tables

Bibliography

[1] Richard Wigmans. *Calorimetry: Energy Measurement in Particle Physics*. Oxford University Press, International Series of Monographs on Physics, 2nd edition, September 2017.

[2] Fabiola Gianotti and Christian W. Fabjan. Calorimetry for particle physics. *Review of Modern Physics*, 75, Oct 2003. URL https://cds.cern.ch/record/692252/files/RevModPhys.75.1243.pdf.

[3] F. Nessi-Tedaldi. Overview of PbWO4 calorimeter in CMS. *Production site visit CEA Saclay*, 408, 1998. URL https://doi.org/10.1016/S0168-9002(98)00321-0.

[4] Richard Wigmans. Calorimetry. *Lecture in 2006: Dottorato di Ricerca in Fisica dell' Università di Pavia*, 2008. URL http://siba.unipv.it/fisica/ScientificaActa/volume_2_1/Wigmans.pdf.

[5] W. R. Nelson, H. Hirayama, and D. W. O. Rogers. EGS4 code system. *Technical Report*, Dec 1985. URL https://www.osti.gov/biblio/6137659.

[6] Lawrence E. Price and Paul Lebrun. Report of the working group on detector simulation. *ANL-HEP-CP–86-126*, 1986. URL https://www.osti.gov/servlets/purl/6834826.

[7] Christine V. Scheel. *The spaghetti calorimeter research, development, application.* PhD dissertation, NIKHEF-H, Amsterdam, 1994. URL http://inis.iaea.org/search/search.aspx?orig_q=RN:27032174.

[8] L. An et. al. Performance of a spaghetti calorimeter prototype with tungsten absorber and garnet crystal fibres. *Nuclear Instruments and Methods in Physics Research A*, 1045:167629, Jan 2023. ISSN 0168-9002. URL https://doi.org/10.1016/j.nima.2022.167629.

[9] Donald E. Groom. Energy flow in a hadronic cascade: Application to hadron calorimetry. *Nuclear Instruments and Methods in Physics Research A*, 572:633–653, Jan 2007. URL https://doi.org/10.1016/j.nima.2006.11.070.

[10] Tony A. Gabriel and James E. Brau. Theoretical studies of hadronic calorimetry for high luminosity high energy colliders. *ORNL/TM-10903*, 1989. URL https://www.osti.gov/servlets/purl/6563244.

[11] Sehwook Lee, Michele Livan, and Richard Wigmans. Dual-readout calorimetry. *Rev. Mod. Phys.*, 90:025002, Apr 2018. URL https://link.aps.org/doi/10.1103/RevModPhys.90.025002. [arXiv:1712.05494].

[12] Sehwook Lee and Richard Wigmans. On the energy measurement of jets in high-energy physics experiments. *Journal of Physics : Conference Series*, 404 (1):012051, Dec 2012. URL https://dx.doi.org/10.1088/1742-6596/404/1/012051.

[13] Richard Wigmans. New developments in calorimetric particle detection. *Progress in Particle and Nuclear Physics*, 103:109–161, Nov 2018. URL https://doi.org/10.1016/j.ppnp.2018.07.003.

[14] J. Colas et al. Position resolution and particle identification with the ATLAS EM calorimeter. *Nuclear Instruments and Methods in Physics Research A*, 550: 96–115, Sept 2005. URL https://doi.org/10.1016/j.nima.2005.05.041.

[15] R. Wigmans. Misconceptions about calorimetry. *Instruments*, 1(1), May 2017. ISSN 2410-390X. URL https://doi.org/10.3390/instruments1010003.

[16] G. Opher. On the calibration of longitudinally segmented calorimeter systems. *Nuclear Instruments and Methods in Physics Research A*, 409:621–628, May 1998. ISSN 0168-9002. URL https://doi.org/10.1016/S0168-9002(97)01337-5.

[17] M. Albrow. Intercalibration of the longitudinal segments of a calorimeter system. *Nuclear Instruments and Methods in Physics Research A*, 487:381–395, July 2002. ISSN 0168-9002. URL https://doi.org/10.1016/S0168-9002(01)02190-8.

[18] D. Buskulic. Performance of the ALEPH detector at LEP. *Nuclear Instruments and Methods in Physics Research A*, 360, 1995. URL https://doi.org/10.1016/0168-9002(95)00138-7.

[19] The CMS Collaboration. The CMS experiment at the CERN LHC. *Journal of Instrumentation*, 3, 2008. URL https://iopscience.iop.org/article/10.1088/1748-0221/3/08/S08004.

[20] Richard Wigmans. The dual-readout approach to calorimetry. *Nuclear Instruments and Methods in Physics Research A*, 732:475–479, Dec 2013. URL https://doi.org/10.1016/j.nima.2013.04.005.

[21] Vladimir Nagaslaev, Alan Sill, and Richard Wigmans. Beam tests of a thin dual-readout calorimeter for detecting cosmic rays outside the earth's atmosphere. *Nuclear Instruments and Methods in Physics Research A*, 462:411–425, April 2001. URL https://doi.org/10.1016/S0168-9002(01)00185-1.

[22] N. Akchurin et al. Electron detection with a dual-readout calorimeter. *Nuclear Instruments and Methods in Physics Research A*, 536(1):29–51, 2005. ISSN 0168-9002. URL https://doi.org/10.1016/j.nima.2004.06.178.

[23] N.Akchurin et al. Muon detection with a dual-readout calorimeter. *Nuclear Instruments and Methods in Physics Research Section A*, 533:305–321, Nov 2004. URL https://doi.org/10.1016/j.nima.2004.05.134.

[24] N. Akchurin et al. Hadron and jet detection with a dual-readout calorimeter. *Nuclear Instruments and Methods in Physics Research A*, 537(3):537–561, 2005. ISSN 0168-9002. URL https://doi.org/10.1016/j.nima.2004.07.285.

[25] K. C. Chandler, T. W. Armstrong, and N. Poveda. Operating instruction for the High-Energy Nuclear-Meson Transport Code HETC. *ORNL-4744*, 1972. URL https://technicalreports.ornl.gov/1972/3445600501473.pdf.

[26] E. A. Straker et al. The MORSE code - a multigroup neutron and gamma ray Monte Carlo transport code. *ORNL-4585*, 1970. URL https://digital.library.unt.edu/ark:/67531/metadc866427/.

[27] N. Akchurin et al. Neutron signals for dual-readout calorimetry. *Nuclear Instruments and Methods in Physics Research A*, 598:422–431, 2009. URL https://doi.org/10.1016/j.nima.2008.09.045.

[28] N. Akchurin et al. Contributions of Cherenkov light to the signals from lead tungsten crystals. *Nuclear Instruments and Methods in Physics Research Section A*, 582:474–483, 2007. URL https://doi.org/10.1016/j.nima.2007.08.174.

[29] N. Akchurin et al. New crystals for dual-readout calorimetry. *Nuclear Instruments and Methods in Physics Research Section A*, 604:512–526, 2009. URL https://www.roma1.infn.it/~pinci/Articles/NIMA_604_512.pdf.

[30] N. Akchurin et al. Optimization of crystals for applications in dual-readout calorimetry. *Nuclear Instruments and Methods in Physics Research Section A*, 621:212–221, 2010. ISSN 1-3. URL https://doi.org/10.1016/j.nima.2010.05.063.

[31] Richard Wigmans. New results from the RD52 (DREAM) project. *Nuclear Instruments and Methods in Physics Research A*, 718:43–47, 2013. URL https://doi.org/10.1016/j.nima.2015.09.069.

[32] N. Akchurin et al. The electromagnetic performance of the RD52 fiber calorimeter. *Nuclear Instruments and Methods in Physics Research Section A*, 735:130–144, 2014. ISSN 0168-9002. URL https://doi.org/10.1016/j.nima.2013.09.033.

[33] N. Akchurin et al. Particle identification in the longitudinally unsegmented RD52 calorimeter. *Nuclear Instruments and Methods in Physics Research Section A*, 735:120–129, 2014. URL http://dx.doi.org/10.1016/j.nima.2013.09.024.

[34] F.G. Hartjes and R. Wigmans. Scintillating plastic fibres for hadron calorimetry. *Nuclear Instruments and Methods in Physics Research Section A*, 277:379–385, 1989. URL https://doi.org/10.1016/0168-9002(89)90766-3.

[35] D. Lazic. Fundamentals of Cherenkov fiber calorimetry. *RD40*, 1997. URL http://cds.cern.ch/record/349395.

[36] S. Lee et al. Hadron detection with a dual-readout fiber calorimeter. *Nuclear Instruments and Methods in Physics Research Section A*, 866:76–90, 2017. URL https://10.1016/j.nima.2017.05.025.

[37] Chen Xu. *Study of the Silicon Photomultipliers and Their Applications in Positron Emission Tomography*. PhD dissertation, DESY, 2014. URL https://bib-pubdb1.desy.de/record/168988/files/DESY-2014-02771.pdf.

[38] Erika Garutti. Silicon photomultipliers for high energy physics detectors. *Journal of Instrumentation*, 6, Oct 2011. URL https://doi.org/10.1088/1748-0221/6/10/C10003.

[39] M. Antonello et al. Tests of a dual-readout fiber calorimeter with SiPM light sensors. *Nuclear Instruments and Methods in Physics Research Section A*, 899: 52–64, 2018. ISSN 0168-9002. URL https://doi.org/10.1016/j.nima.2018.05.016.

[40] Richard Wigmans. 25 years of dual-readout calorimetry. *Instruments (Selected Papers from the 19th International Conference on Calorimetry in Particle Physics (CALOR 2022))*, 6(3), 2022. ISSN 2410-390X. URL https://www.mdpi.com/2410-390X/6/3/36.

[41] Lyndon Evans. The Large Hadron Collider. *34th SLAC Summer Institute On Particle Physics (SSI)*, 2006. URL https://www.slac.stanford.edu/econf/C060717/papers/L003.PDF.

[42] Burkhard Schmidt. The High-Luminosity upgrade of the LHC. *Journal of Physics: Conference Series*, 706, 2016. URL https://doi.org/10.1088/1742-6596/706/2/022002.

[43] O. E. Casas, A. M. Raba, and N. Poveda. An approach to the formalism of the Standard Model of Particle Physics. *arXiv physics.gen-ph*, 2010. URL https://doi.org/10.48550/arXiv.1004.3331.

[44] H. Baer et al. The International Linear Collider Technical Design Report - Volume 2: Physics. *ILC-REPORT-2013-040*, 2013. URL https://doi.org/10.48550/arXiv.1306.6352.

[45] L. Linssen et al. Physics and Detectors at CLIC: CLIC Conceptual Design Report. *CERN Yellow Report (CERN-2012-003)*, 2012. URL https://doi.org/10.48550/arXiv.1202.5940.

[46] A. Blondel et al. Report of the ICFA Beam Dynamics Workshop "Accelerators for a Higgs Factory: Linear vs. Circular" (HF2012). *FERMILAB-CONF-13-037-APC IHEP-AC-2013-001 SLAC-PUB-15370*, 2013. URL https://arxiv.org/abs/1302.3318.

[47] CEPC Study Group Collaboration. CEPC Conceptual Design Report: Volume 2 - Physics & Detector. *IHEP-CEPC-DR-2018-02*, 2018. URL https://doi.org/10.48550/arXiv.1811.10545.

[48] K.R. Long et al. Muon colliders to expand frontiers of particle physics. *Nature Physics*, 17:289–292, 2021. URL https://doi.org/10.48550/arXiv.1901.06150.

[49] M. Koratzinos et al. FCC-ee: Energy calibration. *Poster presented at IPAC'15, Richmond, VA, USA*, 2015. URL https://doi.org/10.48550/arXiv.1506.00933.

[50] J.P. Delahaye et al. Muon Colliders. *The European Particle Physics Strategy Update*, 2019. URL https://doi.org/10.48550/arXiv.1901.06150.

[51] K.M. Black et al. Muon Collider Forum Report. *hep-ex*, 2022. arXiv:2209.01318.

[52] The FCC Collaboration. FCC-ee: The Lepton Collider. *European Physical Journal Special Topics*, 228:261–623, 2019. URL https://link.springer.com/article/10.1140/epjst/e2019-900045-4.

[53] M. Benedikt et al. Future Circular Colliders succeeding the LHC. *Nature Physics*, 16:402–407, 2020. URL https://www.nature.com/articles/s41567-020-0856-2.

[54] R. G. Suarez et al. The Future Circular Collider (FCC) at CERN. *Proceedings Of Science*, 2022. URL https://doi.org/10.48550/arXiv.2204.10029.

[55] A. Abada et. al. FCC-ee: The Lepton Collider. *The European Physical Journal Special Topics*, 228:261–623, 2019. URL https://doi.org/10.1140/epjst/e2019-900045-4.

[56] David d'Enterria. Physics at the FCC-ee. *Proceedings, 17th Lomonosov Conference on Elementary Particle Physics:Moscow, Russia*, pages 182–191, 2016. URL https://arxiv.org/pdf/1602.05043.pdf.

[57] The FCC Collaboration. FCC-hh: The Hadron Collider. *The European Physical Journal Special Topics*, 228:755–1107, 2019. URL https://link.springer.com/article/10.1140/epjst/e2019-900087-0.

[58] The FCC Collaboration. FCC Physics Opportunities. *The European Physical Journal C*, 79(474), 2019. URL https://link.springer.com/article/10.1140/epjc/s10052-019-6904-3.

[59] Stéphane Monteil and Guy Wilkinson. Heavy-quark opportunities and challenges at FCC-ee. *The European Physical Journal Plus*, 136(837), 2021. URL https://doi.org/10.1140/epjp/s13360-021-01814-0.

[60] Alexander L. Kagan et. al. An Exclusive Window onto Higgs Yukawa Couplings. *Physical Review Letters*, 114:101802, 2015. URL https://doi.org/10.1103/PhysRevLett.114.101802.

[61] P. Azzi et al. Exploring requirements and detector solutions for FCC-ee. *The European Physical Journal Plus*, 136(1195), 2021. URL https://link.springer.com/article/10.1140/epjp/s13360-021-02141-0.

[62] N. Bacchetta et al. Tracking and vertex detectors at FCC-ee. *The European Physical Journal Plus*, 137(231), 2022. URL https://link.springer.com/article/10.1140/epjp/s13360-021-02323-w.

[63] CERN Linear Collider Detector Collaboration. CLD - A Detector Concept for the FCC-ee. *LCD-Note-2019-001*, 2019. URL https://cds.cern.ch/record/2697140?ln=it.

[64] M. Antonello. IDEA: A detector concept for future leptonic colliders. *Colloquia: IFAE 2019*, 2020. URL https://cds.cern.ch/record/2770999/files/10.1393_ncc_i2020-20027-2.pdf.

[65] F. Bedeschi. Overview of Idea detector. *3rd FCC Physics and Experiments Workshop, CERN*, 2020. URL https://indico.cern.ch/event/838435/contributions/3658345/attachments/1968063/3273039/Bedeschi_IDEA.pdf.

[66] G. Bencivenni et. al. The μ-RWELL detector. *Journal of Instrumentation*, 12:C06027, June 2017. URL https://iopscience.iop.org/article/10.1088/1748-0221/12/06/C06027.

[67] et. al. N. Akchurin. Dual-Readout calorimetry for future experiments probing fundamental physics. *White Paper for the 2021 Snowmass process*, June 2022. URL https://doi.org/10.48550/arXiv.2203.04312.

[68] M.T. Lucchini et al. New perspectives on segmented crystal calorimeters for future colliders. *Journal of Instrumentation*, 15(11):P11005, Nov 2020. URL https://doi.org/10.1088/1748-0221/15/11/P11005.

[69] A. Karadzhinova-Ferrer et al. Novel prototype tower structure for the dual-readout fiber calorimeter. *Journal of Instrumentation*, 17(09):T09007, Sept 2022. URL https://doi.org/10.1088/1748-0221/17/09/t09007.

[70] *Position sensitive photomultiplier tubes R8900-00-C12, R8900U-00-C12*. Hamamatsu, 2006. URL https://www.hamamatsu.com/content/dam/hamamatsu-photonics/sites/documents/99_SALES_LIBRARY/etd/R8900(U)-00-C12_TPMH1299E.pdf.

[71] *A SiPM-based dual-readout calorimeter for future leptonic colliders*. VCI2019 - The 15th Vienna Conference on Instrumentation, 2019. URL https://indico.cern.ch/event/716539/contributions/3245930/attachments/1798238/2932528/MAn_VCI_19_02_19.pdf.

[72] *BC-600 optical cement*. Saint-Gobain, 2005. URL https://vepp2k.inp.nsk.su/~inest/halometer/SGC%20BC600%20Data%20Sheet%200105.pdf.

[73] Roberto Ferrari. Open call 2021 - HiDRa. *Scientific Proposal*, 2021. URL https://indico.cern.ch/event/1039239/attachments/2244390/3805972/HiDRa_2020_proposal.pdf.

[74] B.Andersson et al. A model for low-p_T hadronic reactions with generalizations to hadron-nucleus and nucleus-nucleus collisions. *Nuclear Physics B*, 281:289–309, Jan 1987. URL https://doi.org/10.1016/0550-3213(87)90257-4.

[75] Dennis H. Wright and John Apostolakis. An Overview of the Geant4 Toolkit. *AIP Conference Proceedings*, 896, Jan 2007. URL https://doi.org/10.1063/1.2720452.

[76] J.B. Birks. *The theory and practice of scintillation counting*. Pergamon, Oxford, 1964. Link to the book.

[77] Romualdo Santoro. SiPMs for dual-readout calorimetry. *Instruments*, 6(4):59, Oct 2022. URL https://doi.org/10.3390/instruments6040059.

[78] Kim Albertsson et al. Machine learning in high energy physics community white paper. *Journal of Physics: Conference Series*, 1085:022008, 2018. URL https://iopscience.iop.org/article/10.1088/1742-6596/1085/2/022008.

[79] Dimitri Bourilkov. Machine and deep learning applications in particle physics. *International Journal of Modern Physics A*, 34(35), 2019. URL https://doi.org/10.1142/S0217751X19300199.

[80] The ATLAS Collaboration. ATLAS inner detector : Technical Design Report, 1. *CERN-LHCC-97-016 ; ATLAS-TDR-4*, 1997. URL https://cds.cern.ch/record/331063.

[81] The ATLAS Collaboration. ATLAS inner detector : Technical Design Report, 2. *CERN-LHCC-97-017 ; ATLAS-TDR-5*, 1997. URL https://cds.cern.ch/record/331064.

[82] A. Salzburger. Tracking tutorial, in Artemis School on calibration and performance of ATLAS detectors. *CERN-LHCC-97-017 ; ATLAS-TDR-5*, 2008. URL https://indico.cern.ch/event/34087/contributions/802944/attachments/669263/919934/IDTracking_A_Salzburger.pdf.

[83] The ATLAS Collaboration. ATLAS liquid-argon calorimeter : Technical Design Report. *CERN-LHCC-96-041 ; ATLAS-TDR-2*, 1996. URL https://cds.cern.ch/record/331061.

[84] The ATLAS Collaboration. ATLAS tile calorimeter : Technical Design Report. *CERN-LHCC-96-042 ; ATLAS-TDR-3*, 1996. URL https://cds.cern.ch/record/331062.

[85] The ATLAS Collaboration. ATLAS muon spectrometer : Technical Design Report. *CERN-LHCC-97-022 ; ATLAS-TDR-10*, 1997. URL https://cds.cern.ch/record/331068.

[86] The ATLAS Collaboration. Muon reconstruction performance of the ATLAS detector in proton–proton collision data at $\sqrt{s}$=13 tev. *The European Physical Journal C*, 76, 2016. URL https://doi.org/10.1140/epjc/s10052-016-4120-y.

[87] The ATLAS Collaboration. ATLAS magnet system : Technical Design Report, 1. *CERN-LHCC-97-018 ; ATLAS-TDR-6*, 1997. URL https://cds.cern.ch/record/338080.

[88] The ATLAS Collaboration. The ATLAS experiment at the CERN Large Hadron Collider. *Journal of Instrumentation*, 3, 2008. URL https://iopscience.iop.org/article/10.1088/1748-0221/3/08/S08003.

[89] Catrin Bernius. The ATLAS Trigger and Data Acquisition system. *ATL-DAQ-SLIDE-2020-356*, 2020. URL https://cds.cern.ch/record/2730760?ln=bg.

[90] The ATLAS Collaboration. Operation of the ATLAS trigger system in Run 2. *Journal of Instrumentation*, 15, 2020. URL https://iopscience.iop.org/article/10.1088/1748-0221/15/10/P10004/pdf.

[91] The ATLAS Collaboration. Standard filling schemes for various LHC operation modes. *LHC-PROJECT-NOTE-323*, 2003. URL https://cds.cern.ch/record/691782.

[92] Burkhard Schmidt. The High-Luminosity upgrade of the LHC. *Journal of Physics: Conference Series*, 706, 2016. URL https://cds.cern.ch/record/2263093/files/10.1088_1742-6596_706_2_022002.pdf.

[93] The ATLAS Collaboration. New Small Wheel Technical Design Report. *CERN-LHCC-2013-006*, 2013. URL https://cds.cern.ch/record/1552862/files/ATLAS-TDR-020.pdf.

[94] M. Balikina et. al. Developing production technology and control methods for Micromegas detectors. *Physics of Particles and Nuclei Letters*, 18, 2021. ISSN 1547-4771. URL https://link.springer.com/content/pdf/10.1134/S1547477121030055.pdf.

[95] I. Giomataris et. al. Micromegas in a bulk. *Nuclear Instruments and Methods in Physics Research Section A*, 560, May 2006. URL https://doi.org/10.1016/j.nima.2005.12.222.

[96] T.Alexopoulos et. al. A spark-resistant bulk-micromegas chamber for high-rate applications. *Nuclear Instruments and Methods in Physics Research Section A*, 640, June 2011. URL https://doi.org/10.1016/j.nima.2011.03.025.

[97] M. Iodice et. al. Small-pad resistive Micromegas: Comparison of patterned embedded resistors and DLC based spark protection systems. *Journal of Physics: Conference Series*, 1498, 2020. URL https://iopscience.iop.org/article/10.1088/1742-6596/1498/1/012028/pdf.

[98] Marco Sessa. Design and construction of Micromegas detectors for the ATLAS Muon Spectrometer upgrade. *NUOVO CIMENTO C*, 39, 2016. URL https://cds.cern.ch/record/2282365/files/fulltext.pdf.

[99] J. Agarwala et. al. Construction and test of the SM1 type Micromegas chambers for the upgrade of the ATLAS forward muon spectrometer. *Nuclear Instruments and Methods in Physics Research Section A*, 1040, 2022. URL https://doi.org/10.1016/j.nima.2022.167285.

[100] P. F. Giraud. The RASFORK tool for checking MM alignment quality. *Production site visit CEA Saclay*, 2017. URL https://indico.cern.ch/event/633240/contributions/2560619/subcontributions/230270/attachments/1469151/2275232/rasfork_PFG.pdf.

[101] G. Aad et. al. ATLAS data quality operations and performance for 2015-2018 data-taking. *Journal of Instrumentation*, 15, April 2020. URL https://doi.org/10.1088/1748-0221/15/04/P04003.

[102] S. Kolos et. al. ATLAS TDAQ data quality monitoring architectural design. *Document ID: ATL-DQ-ON-0024*, Aug 2006. URL https://twiki.cern.ch/twiki/.

[103] A Corso-Radu et. al. Data quality monitoring framework for the ATLAS experiment at the LHC. *IEEE Transactions on Nuclear Science*, 55, March 2008. URL https://ieeexplore.ieee.org/stamp/stamp.jsp?tp=&arnumber=4448489.

[104] A Corso-Radu et. al. Data Quality Monitoring Framework for the ATLAS experiment: Performance achieved with colliding beams at the LHC. *Journal of Physics: Conference Series*, 331, 2011. URL https://iopscience.iop.org/article/10.1088/1742-6596/331/2/022027.

[105] P. Adragna et al. The GNAM monitoring system and the OHP histogram presenter for ATLAS. *IEEE*, 331, 2005. URL https://ieeexplore.ieee.org/document/1547412.

[106] Y. Ilchenko et. al. Data Quality Monitoring Display for ATLAS experiment at the LHC. *Journal of Physics: Conference Series*, 219, 2010. URL https://iopscience.iop.org/article/10.1088/1742-6596/219/2/022035/pdf.

[107] Gabriel Rabanal Bolaños. Cosmic results with the final Micromegas sectors for the ATLAS muon upgrade. *40th International Conference on High Energy physics - ICHEP2020*, 2020. URL https://pos.sissa.it/390/773/pdf.

[108] Athina Kourkoumeli-Charalampidia and Dimitrios Fassouliotis. The Micromegas surface commissioning for the ATLAS New Small Wheel. *Journal of Physics: Conference Series*, 2105, 2021. URL https://iopscience.iop.org/article/10.1088/1742-6596/2105/1/012020/pdf.